| | |
|---|---|
| **Titre:** Title: | Hollow Core Photonic Bragg Fibers for Industrial Sensing Applications |
| **Auteur:** Author: | Jingwen Li |
| **Date:** | 2017 |
| **Type:** | Mémoire ou thèse / Dissertation or Thesis |
| **Référence:** Citation: | Li, J. (2017). Hollow Core Photonic Bragg Fibers for Industrial Sensing Applications [Ph.D. thesis, École Polytechnique de Montréal]. PolyPublie. https://publications.polymtl.ca/2472/ |

UNIVERSITÉ DE MONTRÉAL

# HOLLOW CORE PHOTONIC BRAGG FIBERS FOR INDUSTRIAL SENSING APPLICATIONS

JINGWEN LI

DÉPARTEMENT DE GÉNIE PHYSIQUE

ÉCOLE POLYTECHNIQUE DE MONTRÉAL

THÈSE PRÉSENTÉE EN VUE DE L'OBTENTION

DU DIPLÔME DE PHILOSOPHIAE DOCTOR

(GÉNIE PHYSIQUE)

FÉVRIER 2017

UNIVERSITÉ DE MONTRÉAL

ÉCOLE POLYTECHNIQUE DE MONTRÉAL

Cette thèse intitulée:

# HOLLOW CORE PHOTONIC BRAGG FIBERS FOR INDUSTRIAL SENSING APPLICATIONS

présentée par : LI Jingwen

en vue de l'obtention du diplôme de : Philosophiae Doctor

a été dûment acceptée par le jury d'examen constitué de :

M. FRANCOEUR Sébastien, Ph. D., président

M. SKOROBOGATIY Maksim A., Ph. D., membre et directeur de recherche

M. LEBLOND Frédéric, Ph. D., membre

M. ADAMCHUK Viacheslav I., Ph. D., membre externe

# DEDICATION

*I would like to dedicate this thesis to my parents and my sister for their love and support.*

# ACKNOWLEDGEMENTS

I would like to express my deepest and heartfelt gratitude to my supervisor and research director, Prof. Maksim Skorobogatiy, for offering me the opportunity to pursue my scientific dream, and for encouraging and supporting me during my Ph. D study.

I would like to thank all my friends and colleagues in Engineering Physics Department, Ecole Polytechnique de Montreal. Especially, I want to thank Dr. Hang Qu, Kathirvel Nallappan, Hichem Guerboukha, Tian Ma, Xin Lu, for invaluable discussion and assistance in my projects.

I want to thank the technicians in our group, Francis Boutet and Yves Leblanc for providing technical assistance, as well as many useful advices.

Finally, I wish to thank my family and friends for their support during my doctoral study.

# RESUME

Le rôle de plus en plus important des senseurs optiques dans une multitude d'applications scientifiques et industrielles, incluant la détection biologique, le diagnostic médical, l'industrie alimentaire, le contrôle des procédés et le monitoring environnemental, a mené à un regain de vitalité dans les efforts de recherche et développement dans ce domaine. Pour ces senseurs, la fibre optique peut être une technologie prometteuse en raison de ses nombreux avantages tels que la portabilité, la protection face l'interférence électromagnétique, la possibilité de les utiliser dans des environnements explosifs, ou encore celle d'avoir une mesure quantitative et qualitative continue. Aujourd'hui, une vaste gamme de senseurs à fibre optique a été proposée et développée. Cependant, la plupart de ces senseurs fonctionnent sur la base d'un couplage évanescent des modes de réflexion totale interne (RTI) à proximité de l'analyte. Ceci comporte plusieurs désavantages, tels que le faible chevauchement du mode avec l'analyte, une distance de sensibilité plus petite, le besoin d'apporter des modifications complexes à la fibre, ainsi qu'une faible robustesse mécanique de la fibre.

Afin de surmonter ces limitations et simplifier l'implémentation pratique, dans cette thèse, nous proposons l'utilisation de fibres de Bragg à cœur creux opérant dans des plages fréquentielles distinctes (le visible et les térahertz) pour effectuer de la réfractométrie dans des analytes liquides et de surface. Nous mènerons des analyses théoriques et des caractérisations expérimentales des guides d'onde proposés et nous étudierons leur potentiel d'applications dans une variété de domaines industriels.

Dans la première partie de la thèse, nous explorerons la capacité d'utiliser des fibres de Bragg à cœur creux dans le visible pour simultanément détecter la partie réelle et imaginaire de l'indice de réfraction d'analytes liquides. Ce senseur de Bragg est constitué d'un large cœur creux (diamètre d'environ 0.7 mm) entouré de couches alternantes de polymethyl methacrylate (PMMA) et de polystyrènse (PS) qui agissent essentiellement comme des réflecteurs de Bragg. Nous utiliserons ce senseur pour le monitoring de la concentration de liquides de refroidissement commerciaux. La stratégie de détection s'appuie sur une double mesure de la position spectrale du centre de la bande interdite et sa transmission en amplitude. Les deux mesures sont hautement sensibles à l'indice de réfraction de l'analyte qui sera introduit dans le cœur creux du guide d'onde. Ceci permettra de déterminer la concentration des liquides de refroidissement. La fibre

proposée intègre intrinsèquement la détection optique et la microfluidique, permettant d'ouvrire la voie au monitoring en temps réel de la concentration de plusieurs fluides industriels tels que les liquides de transmission de chaleur ou les fluides de sciage avec une précision de moins de 1% en volume.

Dans la deuxième partie de la thèse, nous démontrerons une fibre de Bragg à cœur creux dans le visible pour une détection en surface. En utilisant une modalité spectrale, le senseur est capable de détecter des changements dans l'épaisseur d'un analyte déposé dans la surface interne du cœur. En effet, les spectres de transmission sont grandement modifiés en raison du phénomène d'évitement du croisement, à proximité de la longueur d'onde qui satisfait la condition de phase entre le mode du cœur guidé et celui de la couche d'analyte. Ceci permet donc de mesurer les changements de propriétés de cette dernière. Comme démonstration pratique, nous appliquerons le guide d'onde pour observer la dynamique de dissolution d'un film de polyvinyl butyral (PVB) déposé sur la surface interne du cœur. Nous observerons un fort shift spectral durant la dissolution du film et nous déterminerons expérimentalement une sensibilité d'environ 0.052 nm/nm avec des échantillons aqueux. De plus, nous démontrerons qu'une pression physique de la fibre mène à une augmentation du chevauchement des modes guidés et de surface, menant à une augmentation significative de la sensibilité de surface du senseur. Ce guide d'onde ouvre de nouvelles applications des guides d'ondes à bande interdite dans la détection en temps réel des dynamiques des liaisons et affinités chimiques, pour un large éventail d'échantillons chimiques et biologiques.

Dans la troisième partie de la thèse, nous étendrons l'étude des fibres de Bragg à cœur creux aux fréquences térahertz pour la détection des larges constituants biologiques tels que les bactéries et les  cellules ou des échantillons sous forme de poudre. En utilisant un guide d'onde THz opérant en régime monomode, nous démontrerons une amélioration de la limite de détection de senseurs similaires. Le principe d'opération repose sur le suivi de la fréquence d'anticroisement entre le mode de cœur et le mode de défaut. Cette fréquence se manifeste par un minimum étroit de transmission dans le spectre THz qui est relativement large. Ceci est accompli en introduisant un défaut géométrique dans la première couche du réflecteur de Bragg. La largeur du minimum (3 GHz) est parmi les plus étroites jamais réalisées pour un résonateur THz. La position spectrale du minimum est hautement sensible aux propriétés optiques de la couche de défaut (son épaisseur et son indice de réfraction). Pour calibrer le senseur, nous déposerons des

couches de PMMA de différentes épaisseurs sur la surface interne du cœur. Nous déterminerons ainsi une sensibilité de 0.1 GHz/μm. Nous utiliserons également une poudre de α-lactose monohydratée comme échantillon. Le phénomène d'anticroisement entre le mode du cœur guide et le mode de défaut sera expérimentalement vérifié en imageant directement le mode à la sortie de la fibre de Bragg à l'aide d'un système de microscopie THz fibré. Le senseur sera caractérisé en utilisant un système de spectrocopie THz (TDS) dans le domaine du temps et un système continue (CW). Ceci nous permettra de conclure que le système CW est plus approprié pour notre guide d'onde, car il a une meilleure résolution spectrale. La possibilité de modifier les propriétés spectrale du guide d'onde de Bragg en concevant une géométrie particulière implique qu'il devient un outil versatile pour plusieurs applications industrielles, tels que la détection de poudres, le monitoring en temps réel des polluants environnementaux ou la détection de bactéries.

# ABSTRACT

The expanding role of optical sensors in numerous scientific and industrial applications，including biosensing, medical diagnostics, food industry, process control, and environmental monitoring, has led to a growth of research and development efforts in this field. Optical fibers can be used as a very promising platform for these applications, due to many appealing properties such as compactness, high degrees of integration, safety in explosive environments and potential to provide real time and remote analysis. To date, a wide range of fiber-optic sensors have been proposed and developed. Most of these sensors, however, use an evanescent coupling of total internal reflection guided modes to the test analytes, which typically suffers from many disadvantages, such as poor modal overlap with the analytes, limited probing length, as well as complicated fiber modifications and poor mechanical robustness in fiber structures.

In order to circumvent these limitations and simplify the practical sensing implementation, in this thesis, we study using hollow-core Bragg fiber sensors operating in different frequency ranges (i.e., visible and terahertz range) for bulk refractometry of liquid analytes and surface sensing applications. We then carry out the theoretical and experimental characterizations of the proposed sensors, and study their applications in various industrial fields.

In the first part of the thesis, we explore the capability of using the hollow-core Bragg fibers operating in the visible range to simultaneously monitor both the real and imaginary parts of liquid analyte refractive index. The Bragg fiber sensor features a large hollow core (diameter: ~0.7mm) surrounded by an alternating polymethyl methacrylate (PMMA)/polystyrene (PS) multilayer as a Bragg reflector. We then apply this fiber sensor to monitor the concentrations of various commercial cooling oils. The sensing strategy relies on a two-channel sensing modality that simultaneously interrogates the bandgap center position of the Bragg fiber as well as the fiber transmission amplitude at the bandgap center. Both measurands are highly sensitive to the complex refractive index of the analyte filled in the fiber core, thus enabling efficient determination and cross correlation with the concentration of cooling oils. The presented fiber sensor inherently integrates optical detection with microfluidics without any fiber modifications, thus allowing for real time monitoring of the concentrations of many industrial fluids, such as heat transfer fluids, sawing fluids, and other industrial dilutions with sub-1%v accuracy.

In the second part of the thesis, we demonstrate the hollow-core Bragg fibers operating in the visible range for surface sensing applications. The fiber sensor operates using a spectral sensing modality to monitor changes in the thickness of an analyte layer deposited on the inner surface of the fiber core. Due to the phenomenon of avoided crossing in the vicinity of the phase matching wavelength between the core-guided and the analyte layer bound modes, fiber transmission spectra are significantly modified, thus allowing for monitoring the changes in the analyte layer properties. As a practical demonstration, we apply the sensor to monitor the dissolution dynamics of a polyvinyl butyral (PVB) film coated on the inner surface of the fiber core. Strong spectral shift is observed during the dissolution of the PVB film, and a surface sensitivity of ~0.052nm/nm is achieved experimentally with aqueous analytes. Moreover, we demonstrate that squeezing a section of the Bragg fiber can effectively increase the overlap between the core-guided modes and the analyte layer, which, in turn, significantly enhances the surface sensitivity of the fiber sensor. The proposed fiber sensor opens up new sensing applications of photonic bandgap fibers such as real time detection of binding and affinity, study of kinetics, etc. for a wide range of chemical and biological samples.

In the third part of the thesis, we extend the operation of the hollow-core Bragg waveguide sensor into terahertz range for the detection of larger targets, such as bacteria and cells, as well as other analytes in powder forms. More importantly, by using THz waveguide sensors operating in an effectively single mode regime, we have significantly improved the detection limit of such sensors by directly tracking the anticrossing frequency between the core-guided mode and the defect mode, which manifests itself as a sharp transmission dip in the relatively broad transmission window. This is accomplished by introducing a geometrical defect in the first layer of the Bragg reflector. The experimentally achieved linewidth (3GHz) of the resonant dip is among the narrowest measured for any resonator in the THz range. Spectral position of the resonant dip is found to be highly sensitive to the optical properties of the defect layer (i.e., thickness and refractive index). In order to calibrate the sensor, we use PMMA layers of different thicknesses attached to the waveguide inner surface, and the surface sensitivity is found to be 0.1GHz/μm. Moreover, an example of THz resonant surface sensing using α-lactose monohydrate powder as the analyte is demonstrated experimentally. The anticrossing phenomenon between the core-guided mode and the defect mode is confirmed by imaging of the modes propagated in the waveguide using a fiber-coupled THz imaging setup. The waveguide

sensor is characterized using both a time domain spectroscopy (TDS) setup and a continuous wave (CW) setup. We conclude that the CW setup with higher frequency resolution is more suitable for applications that require high sensitivity and precision. The ability to tailor the spectral properties of the Bragg waveguides by properly designing their geometrical parameters means that the proposed sensors become a viable platform for many industrial sensing applications, such as detection of various powders and online monitoring of environmental pollutants, as well as detection of bacteria.

# TABLE OF CONTENTS

# LIST OF TABLES

# LIST OF FIGURES

# LIST OF SYMBOLS AND ABBREVIATIONS

| | |
|---|---|
| $\alpha$ | Absorption coefficient |
| $\alpha_{rad}$ | Radiation loss |
| $c$ | Volume concentration of oil |
| $C_{in}$ | Input coupling coefficient |
| $C_{out}$ | Output coupling coefficient |
| $d_a$ | Thickness of the analyte layer |
| $d_h$ | Thickness of high-index layer in the Bragg reflector |
| $d_l$ | Thickness of low-index layer in the Bragg reflector |
| $\varepsilon$ | Dielectric constant |
| $\varepsilon_o$ | Complex dielectric constant of pure bulk oil |
| $\varepsilon_w$ | Complex dielectric constant of water |
| $n_h$ | Refractive index of the high-index layer in the Bragg reflector |
| $n_l$ | Refractive index of the low-index layer in the Bragg reflector |
| $n_a$ | Refractive index of the analyte layer |
| $n_c$ | Refractive index of the fiber core |
| $\lambda_g$ | Bandgap center wavelength |
| $\lambda$ | Wavelength of light |
| $I$ | Intensity of light |
| $L$ | Fiber length |
| $T$ | Transmission |
| $\Gamma$ | Confinement factor |
| $Q$ | Quality factor |

| | |
|---|---|
| $S$ | Sensitivity of the sensor |
| $\omega$ | Frequency |
| ARRHW | Anti-resonant reflecting hollow waveguide |
| ARROW | Anti-resonant reflecting optical waveguide |
| CCD | Coupled charge device |
| CW | Continuous wave |
| DFB | Distributed feedback |
| FBG | Fiber Bragg grating |
| FEM | Finite element method |
| FP | Fabry perot |
| GHz | Gigahertz |
| HC | Hollow core |
| LPG | Long period grating |
| LED | Light emitting diode |
| MOF | Micro-structured optical fiber |
| PMMA | Polymethyl methacrylate |
| PS | Polystyrene |
| PCF | Photonic crystal fiber |
| PVB | Polyviny butyral |
| PPWG | Parallel plate waveguide |
| PBGF | Photonic bandgap fiber |
| PM | Parabolic mirror |
| RIU | Refractive index unit |
| RPM | Revolutions per minute |

| | |
|---|---|
| RI | Refractive index |
| SPR | Surface plasmon resonance |
| SPW | Surface plasmon wave |
| TDS | Time domain spectroscopy |
| TE | Transverse electric |
| TEM | Transverse electromagnetic |
| THz | Terahertz |
| TIR | Total internal reflection |

# LIST OF APPENDICES

# CHAPTER 1 INTRODUCTION

Biosensors are electrical, optical, chemical, or mechanical devices that are capable of detecting various biological and chemical species. During the past several decades, biosensors have been extensively studied for a variety of industrial applications, such as biochemical sensing, medical diagnosis, food quality control, and environmental monitoring. Particularly, these applications include liquid refractive index sensing, detection of analyte layer thickness or trace amounts of molecules, study of antigen-antibody interaction, and monitoring of surface dynamics, as well as detection of particles or cells.

In order to convert the analyte information or the biochemical process into a quantifiable signal, several kinds of transducers (e.g., electrochemical, optical, piezo-electrical, acoustic, and calorimetric transducers) have been proposed and demonstrated. Among these configurations, optical transducers are powerful analysis tools to address these applications by investigating the changes in the optical properties of the sensors such as phase, intensity and frequency, manifested because of the presence of the biological samples. Due to many desirable advantages including high sensitivity, immunity to electromagnetic interference, safety in explosive and hazardous environments, and potential to provide real time and remote analysis, a wide range of optical biosensors based on different principles and configurations has been proposed and demonstrated.

Optical fibers or waveguides constitute a very promising platform to build optical biosensors, as they offer miniaturization, high degree of integration, as well as distributed sensing possibilities. Typically, in such sensors, the spectral properties of the fibers are sensitive to the effective refractive index changes caused by the binding of biomolecules onto the fiber surface, or due to the refractive index changes of the bulk analyte solution. Variations in the effective refractive index of the surrounding medium cause changes in the light propagation conditions, leading to changes in the properties of the reflected or transmitted optical waves. This sensing modality is of particular interest in numerous industrial applications. First, since the refractive index values of materials are related to their compositions, measurement of the analytes refractive indices can be used for the determination of material purity and concentration, as well as physical/chemical process monitoring [1-4]. Particularly, on-line monitoring of the solution concentrations, including heat transfer fluids, coolant, or other dilutions, is of significant importance in many industrial processes [5]. Second, detection of analytes refractive indices is

one of the most important chemical/biological analysis methods used in biosensors, because many specimens can be identified by measuring their refractive indices [6-8]. Moreover, binding events occurring on the fiber surface can be detected by analyzing the variations in the effective refractive index of the surrounding medium. This kind of sensing mechanism is especially relevant for biosensing applications, such as precise detection of analyte layers or trace amounts of biomolecules, study of antigen-antibody interactions, and monitoring of surface dynamics, as well as identification of bacteria pathogens [9-11]. Additionally, another highly attractive feature of refractive index sensors is potentially being able to detect various analytes in powder forms including illicit drugs, explosive or hazardous powders, and suspended powder pollutants, because of changes of the refractive index in the vicinity of the fiber surface. This sensing strategy has important applications in the pharmaceutical and food industry, as well as environmental pollution control [12-14].

In general, fiber-based refractive index sensors can be categorized into two classes according to different detection strategies, namely, an amplitude-based detection strategy and a spectral-based detection strategy [15]. Each class has its own advantages and limitations. In an amplitude-based detection strategy, one typically operates at a fixed wavelength and records changes in the amplitude of an optical signal, which are then reinterpreted in terms of variations in the analytes refractive indices. The principal advantages of the refractive index sensors based on this strategy are low cost, ease of fabrication and simple signal acquisition and processing, as well as compactness since no bulky spectral analyzers are required. An alternative detection strategy is based on the spectral interrogation. This sensing modality is commonly employed in resonant sensing configurations that feature sharp transmission peaks (or dips) in the fiber transmission or reflection spectra. Perturbations of the refractive index of an analyte in the vicinity of certain resonant structures (e.g., Bragg gratings [74], interferometers [186], and whispering-gallery-mode resonator [16, 17]) would modify the resonant property of the structure, thus leading to spectral shifts in the fiber spectra. There are several advantages offered by the spectral-based detection modality. Firstly, the resonant peaks (or dips) used to infer the changes in the analyte refractive index can be made very narrow via proper design of the resonator structure, thereby allowing for resolving minute spectral shift caused by small variations in the analyte refractive index, or the bio-layer thickness. Secondly, the sensors operating on a spectral-based modality are generally less influenced by the fluctuations in the intensity of the light

sources and environmental conditions, which guarantees higher accuracy in the refractive index measurements.

To date, many fiber-optic refractive index sensors based on different detection strategies and configurations have been developed. One of the most commonly used configurations is using an evanescent coupling of the total internal reflection (TIR) guided modes to the test analytes. The evanescent wave arises when electromagnetic waves traveling in a medium undergo total internal reflection at its boundary. Although the light propagates along the fiber by total internal reflectance, there is energy penetrating into the cladding, with its electric field amplitude decaying exponentially from the core-cladding interface. When this region is surrounded by a test analyte, the transmission property of the fiber is modified due to coupling of the optical mode to the analyte. However, these sensors generally have limitations when addressing liquid or gaseous samples. Particularly, in a typical TIR-based fiber-optic sensor, to ensure an efficient overlap between the analyte and the evanescent field of the fiber core modes, certain fiber modifications such as stripping off a section of the fiber cladding or tapering the fibers into microfibers, have to be first carried out. In practice, these laborious modifications of the fiber structure not only undermine the mechanical robustness of these sensors, but also limit their effective sensing lengths. Moreover, since the penetration depth of the evanescent field of the core-guided modes is typically less than a single wavelength, these sensors suffer from a low sensitivity due to a poor modal overlap with the test analytes, as well as difficulty in the detection of relatively larger targets (such as bacteria with sizes of 0.5μm-10μm).

Another alternative is to use liquid-core capillary fiber sensors [18-19], where the refractive index of the fiber core is higher than that of the cladding material. While these sensors are advantageous due to the enhanced interaction overlap between the optical field and the test analytes, as well as the simplicity in their structures and sensing principle, the difficulty in finding suitable cladding material with a refractive index lower than those of aqueous solutions (n~1.33) limits the application range of the TIR-based liquid-core sensors.

Photonic crystal fibers (PCFs), also known as micro-structured optical fibers (MOFs), have enormous potential for chemical and biological sensing. The micron-sized holes running along the length of PCFs enable hosting of the biological/chemical samples in liquid or gaseous forms inside the air holes in the immediate vicinity of the fiber core, thereby significantly

enhancing light-analyte coupling and ensuring high sensitivity. Of particular interest is the ability of PCFs to guide in the analyte-filled hollow cores using a photonic bandgap effect. In such fibers, guidance is possible with analytes of any refractive indices. Additionally, PCFs offer a number of other unique benefits compared to the conventional TIR-based sensors. First, PCFs naturally integrate optical detection with microfluidic channels, thus, allowing for continuous monitoring of dangerous samples in real-time without exposing the personnel to danger. Second, only a small volume of samples is required for sensing, due to the micro-sized holes of the fluidic channels. Third, PCF-based sensors can be coiled into long sensing cells, thus dramatically increasing the interaction lengths and their sensitivities, while the same is impossible to achieve with traditional TIR-based fiber sensors, as the side-polishing step limits sensor length to only several centimeters. Fourth, PCFs can be mass-produced using a commercial fiber drawing tower in a cost-effective way, while traditional TIR-based fibers require significant post-processing procedures before they can be used for sensing applications.

Generally, PCFs can be divided into two classes, i.e., solid-core PCFs and hollow-core PCFs [15]. Solid-core PCFs typically guide with a modified total internal reflection principle, which is similar to the guidance of traditional step-index fibers. Proposed by Monro et al. [92], the holes in the cladding of an index-guiding PCF can be filled with liquid or gaseous analytes, which are then detected by the evanescent field propagating in these holes. Careful design of the geometry parameters such as core size, air-filling fraction allows an enhanced overlap between the modal field of the fiber and the test analyte. When the cladding holes are filled with liquid analytes with refractive indices higher than that of the fiber material, the guidance of the solid-core PCFs turns into the photonic bandgap guidance. These sensors generally use a spectral-based detection modality. Variations in the refractive index of a liquid analyte filling the fiber would modify the bandgap guidance of the solid-core PCFs, leading to strong spectral shifts in the fiber transmission spectra. Thus, the spectral shifts can be used to extract the changes in the refractive indices of the test analytes. For example, D. K. C. Wu et al. [105] reported a solid-core PCF refractive index sensor, which achieved very high sensitivity of 30100nm/RIU. However, this design requires a complicated selective filling method to introduce the liquid analytes into the porous cladding. Moreover, such sensors can only be used for the detection of analytes with refractive indices higher than the fiber structure material, which limits their applications in chemical/biological fields where $n_{analyte}$ is ~1.33.

Another alternative is using hollow-core PCFs. In this case, the hollow-core is filled with liquid samples. A highly attractive aspect of this configuration is that the modal field is almost completely confined to the liquid samples. The sensing mechanism of these sensors is based on the interrogation of spectral shifts in response to changes in the refractive indices of the liquids filling the fiber core. For example, in [107], the authors experimentally demonstrated a liquid-core refractive index sensor that features a hollow core surrounded by a porous cladding. A sensitivity of ~5000 nm/RIU was reported. However, fabrication of the hollow-core PCFs requires a sophisticated drawing technique, and the fiber is very expensive (thousands of dollars per meter). Moreover, these sensors require a relatively long response time to introduce the test analytes into the micron-sized holes of the PCFs.

Hollow-core photonic bandgap Bragg fibers (or simply hollow-core Bragg fibers) can also be used for sensing the analytes refractive indices. In the cross section of such fibers, a hollow core is surrounded by a periodic sequence of micron-sized layers of different materials in the cladding, as shown in Fig. 1.1. This configuration avoids the problems of selective filling, at the same time, achieves almost complete modal overlap with the test analytes. Due to the possibility of having a relatively large core size (~1mm), the response time of introducing the test analyte into the fiber core could be shortened to ~1s, thus allowing for continuous on-line monitoring of liquid samples in a contained, highly integrated manner. In [110], K. J. Rowland et al. reported a hollow-core high-refractive-index-contrast Bragg fiber sensor with a sensitivity ~330nm/RIU. More recently, our group reported a hollow-core low-refractive-index-contrast Bragg fiber sensor operating on a spectral modality [111]. We showed that such Bragg fiber sensors offer superior performance in detection of changes in the real part of the analyte refractive index by monitoring the spectral shifts in the transmission spectra. The sensitivity of our sensor, compared to that of the sensor reported in [110], is considerably improved (~1400nm/RIU). In fact, we have argued in [111], that low-refractive-index-contrast Bragg fibers are most suitable for liquid-core sensors, while high-refractive-index-contrast Bragg fibers are most suitable for gas-core sensors.

Figure 1.1 A Bragg fiber featuring a large hollow core surrounded by a periodic sequence of high and low refractive index layers.

In this thesis, we explore the capability of the hollow-core Bragg fibers operating in the visible range to simultaneously monitor both the real and imaginary parts of the analyte refractive index by interrogating the spectral modality and amplitude modality. Moreover, we demonstrate the hollow-core Bragg fibers for surface sensing applications. The fiber sensor operates using a spectral sensing modality to monitor changes in the thickness of an analyte layer deposited on the inner surface of the fiber core. Finally, we extend the operation wavelength of the hollow-core Bragg waveguide sensors into THz range, with a goal to improve the detection limit of such sensors and, at the same time, enrich their sensing scenarios for the detection of larger targets such as bacteria and cells, as well as other analytes in powder forms. The hollow-core Bragg fibers can be directly integrated into the sensing systems without any fiber modifications, which significantly simplifies the practical sensing implementations, and greatly enhances the robustness of such systems. Other advantages of the proposed sensors include high sensitivity, short response time, label-free detection, good repeatability and stability, cost-effective mass production, and re-usability. We then carry out the theoretical and experimental characterizations of the proposed sensors and study their applications in various industrial fields. In particular, the objective of this thesis can be sub-divided into three parts.

In the first part of this thesis (Chapter 4), we investigate the capability of the hollow-core Bragg fiber to simultaneously monitor both the real and imaginary parts of the analyte refractive index. We then apply the fiber sensor to monitor the concentrations of various commercial cooling oils. The sensing strategy relies on a two-channel sensing modality that simultaneously

interrogates the bandgap center position of the Bragg fiber as well as the fiber transmission amplitude at the bandgap center. Both measurands are highly sensitive to the complex reflective index of the anlyte filled in the fiber core, thus enabling efficient determination and cross-correlation with the concentration of cooling oils. The main advantages of the two-channel sensor compared to a single channel sensor is that, in principle, the measurement error can be significantly improved if the two channels are independent and they offer comparable detection errors. The presented fiber sensor can be used for on-line monitoring of concentration of many industrial fluids such as heat transfer fluids, sawing fluids, and other industrial dilutions with sub-1%v accuracy. We note that this accuracy is frequently used as a benchmark for evaluating the performance of sensors [256].

In the second part of this thesis (Chapter 5), we demonstrate the hollow-core Bragg fibers for surface sensing applications. The fiber sensor operates using a spectral sensing modality to monitor changes in the thickness of an analyte layer deposited on the inner surface of the Bragg fiber core. When a thin analyte layer is deposited on the inner surface of the fiber core, the analyte layer supports its own-guided modes with their optical properties strongly affected by the layer refractive index and thickness. Due to the phenomenon of avoided crossing in the vicinity of the phase matching wavelength between a particular pair of the core-guided and the analyte layer bound modes, fiber transmission spectra (bandgap shape) can be significantly modified, thus allowing for monitoring of changes in the analyte layer properties. One of the design challenges when using Bragg fibers for surface sensing is a weak overlap between the modal fields of the core-guided and the analyte layer bound modes. This is due to the fact that the fields of the core guided modes of a Bragg fiber decrease rapidly from the core center towards the core inner surface where the analyte layer is located. In order to increase the field overlap and promote hybridization between the core-guided modes and the analyte layer bound modes, we propose squeezing of the Bragg fiber. Squeezing of the fiber decreases the fiber core size in one dimension, which, in turn, leads to the field enhancement and mode overlap in the direction of squeezing. As a demonstration of the surface sensing modality, we apply the fiber sensor to monitor the dissolution dynamics of a polyvinyl butyral (PVB) film coated on the inner surface of the fiber core. Simulations based on the transfer matrix method are conducted to validate the experimental results. The proposed fiber sensor opens a new approach for a wide range of

applications, such as detection of molecular interaction and study of surface kinetics, as well as bacteria detection and other applications involving surfaces.

In the third part of this thesis (Chapter 6), we extend the operation wavelength of the hollow-core Bragg waveguide sensor into THz range, which is an asset for the detection of larger targets such as bacteria and cells, as well as other analytes in powder forms. More importantly, by using such a THz waveguide operating in an effectively single mode regime, we have significantly improved the detection limit of such sensors by directly tracking the anticrossing frequency between the core mode and the defect mode, which manifests itself as a sharp transmission dip (3GHz) in the relatively broad high transmission window (45GHz). This is accomplished by introducing a geometrical defect in the first layer of the Bragg reflector. Spectral position of the loss peak is found to be highly sensitive to the optical properties of the defect layer such as thickness and refractive index. In order to realize such sensors, we use 3D stereolithography. The Bragg waveguide used in this work features a hollow core surrounded by a periodic sequence of high/low refractive index multilayers, namely, printing resin (PlasClear, Asiga), and air. As a practical demonstration, we apply this sensor for detecting PMMA films with different thicknesses loaded on the inner surface of the waveguide core. Target film thickness can be directly correlated to the position of the anticrossing frequency. Moreover, an example of THz resonant surface sensing using α-lactose monohydrate powder as the analyte is demonstrated experimentally using a fast rotating setup, where the powders are conveniently spread on the waveguide core surface via the action of centrifugal force. The anticrossing phenomenon between the core-guided mode and the defect mode is directly confirmed by imaging the modes propagated in the waveguide using a THz microscopy setup. The Bragg waveguide sensor is characterized using both a terahertz time-domain (TDS) spectroscopy setup and continuous wave spectroscopy (CW) setup, and we conclude that the CW setup with higher frequency resolution is more suitable for applications that require high sensitivities. The ability to tailor the spectral properties of the sensors by properly designing their geometric parameters means that the Bragg waveguides become a viable platform for a wide range of applications, such as detection of various powder analytes including drugs, hazard powders and granular pollutants.

The rest of this thesis is organized as follows:

In Chapter 2, we review several types of fiber-optic sensors, and briefly summarize their advantages and limitations. We then focus in particular on the research and development of PCF-based sensors. Finally, we provide an up-to-date review of scientific reports that describe various types of THz waveguide sensors.

In Chapter 3, we introduce two sensing modalities commonly used by fiber-optic sensors, which are the spectral-based detection modality and the amplitude-based detection modality. Then, we present the Bragg fiber design and the techniques used for the fabrication of the hollow-core Bragg fibers. Finally, we briefly introduce the experimental setup used in this thesis to characterize the transmission spectra of the proposed Bragg fiber sensors.

Chapter 4 is based on our research paper "Simultaneous monitoring the real and imaginary parts of the analyte refractive index using liquid-core photonic bandgap Bragg fibers", which is published in Optics Express in 2015. In this chapter, we experimentally demonstrate a hollow-core Bragg fiber sensor for bulk refractometry of liquid analytes. We detail the two-channel sensing modality that simultaneously interrogates the bandgap center position of the Bragg fiber, as well as the fiber transmission amplitude at the bandgap center. As a practical application, we apply the fiber sensor to monitor the concentrations of various commercial cooling oils.

Chapter 5 is based on our research paper "Squeezed hollow-core photonic Bragg fiber for surface sensing applications", which is published in Optics Express in 2016. In this chapter, we propose and demonstrate a hollow-core Bragg fiber for surface sensing applications. We demonstrate theoretically and confirm experimentally that squeezing a section of the Bragg fiber can significantly enhance the surface sensitivity of the fiber sensor. As a practical demonstration, we apply the fiber sensor for *in situ* monitoring of the dissolution dynamics of a sub-micron-thick polyvinyl butyral film coated on the surface of the liquid-filled Bragg fiber core.

Chapter 6 is based on our research paper "3D printed hollow-core terahertz Bragg waveguides with defect layers for resonant surface sensing applications", which is published in Optics Express in 2017. In this chapter, we demonstrate that by using Bragg waveguides with defect layers, we can significantly enhance the sensitivity and detection limit of such sensors. As a practical application, we apply the sensor to detect PMMA films and lactose powders loaded on the waveguide inner surface.

In Chapter 7, we summarize the distinctive features of the proposed Bragg fiber sensors, provide a general discussion of the achieved results, and indicate future research directions and perspectives for this project.

Finally, in Chapter 8, the thesis is concluded with a summary of all the results.

# CHAPTER 2 LITERATURE REVIEW

In this Chapter, we review several of the most commonly used fiber-optic refractive index sensors and briefly summarize their advantages and limitations. Then, we focus in particular on the research and development of PCF-based optical sensors, and conclude that PCFs offer many advantages for sensing of samples in liquid and gaseous forms, compared to conventional step-index fibers. Finally, we review several waveguide sensors operating in the THz regime. Considering that a prerequisite of fiber-optic sensors to function in industrial sensing applications is the ability to detect the refractive index variations and surface binding events, we will review these two sensing scenarios in parallel.

## 2.1 Review of fiber-optic sensors

### 2.1.1 Fiber-optic sensors based on the evanescent field detection

The evanescent wave, first described by Hirschfeld [21], arises when electromagnetic waves traveling in a medium undergo total internal reflection at its boundary. Based on the principle of total internal reflectance, light launched into a waveguide placed in a dielectric medium with lower refractive index is totally internally reflected when the angle of light incidence is greater than the critical angle. Although the light propagates along the fiber by total internal reflectance, there is energy penetrating into the cladding, with its electric field amplitude decaying exponentially from the core-cladding interface. The exponentially decaying evanescent field in the cladding region is frequently used for developing different types of optical transductions such as fluorescence or absorption [22-25, 66]. In a fiber with uniform diameter, the evanescent field decays to almost zero within the cladding. Therefore, to create an efficient overlap between the evanescent field of the core modes and the test analyte, the cladding of the fibers should be partially or completely removed, as shown in Fig. 2.1.

In a fluorescence-based sensor, the fluorescence is excited and coupled back to the fiber by the evanescent field [24-29]. Since the evanescent wave is a near-surface phenomenon, sensors employing the evanescent wave to generate fluorescent signal are by nature surface detections. Only the fluorescent molecules near the surface are excited, thereby enabling discrimination of specific binding from non-specific absorption of sample components. In the

case of absorption as optical transducer, the output light intensity is interrogated with the complex refractive index of the surrounding medium. When the fiber core is exposed to the test analyte, the evanescent field strength is influenced by the extinction coefficient of the analyte, and the concentrations of the analyte can be detected by measuring the loss of the output power of the sensing fiber. By immobilizing the biological receptor close to the optical fiber, or directly on its surface, one can detect the binding of analytes that absorb the propagating light, thus enabling detection of specificity [30-32]. For example, in [32], an evanescent wave absorption sensor based on a multimode fiber is demonstrated for DNA concentration detection.

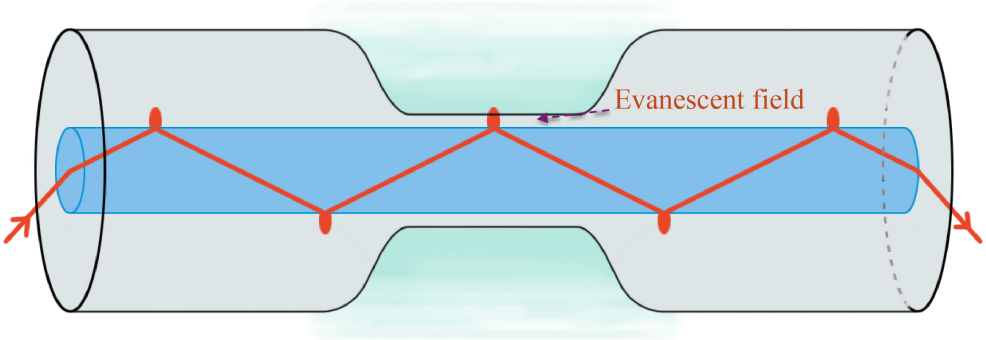


Figure 2.1 Schematic of fiber optic sensors based on the evanescent-field detection.

Moreover, refractive index sensors based on the evanescent field detection have also been reported [33, 34]. In such sensors, the presence of liquid analytes with different refractive indices in the unclad region of the fiber can modify the modal confinement condition, thus leading to changes in the transmission amplitude of the fiber. In [33], M. Sheeba et al. demonstrated a side-polished evanescent-field fiber refractometer for the detection of adulterant traces in coconut oil with a refractive index resolution of $10^{-3}$ RIU. In [34], a refractometer based on a tapered fiber was demonstrated, with the resolution in this case being found to be $10^{-4}$ RIU.

One critical parameter related to evanescent-field based sensing strategy is the penetration depth of the core mode, $d_p$, which is defined as the distance where the electric field amplitude decreases to *1/e* of its value at the core-cladding interface. The penetration depth is mathematically given by [23]:

$$d_p = \frac{\lambda}{2\pi\sqrt{n_{co}^2 \cdot \sin^2\theta - n_{cl}^2}} \tag{2.1}$$

where, $\lambda$ is the wavelength of the light source, $\theta$ is the incident angle of light at the core/cladding interface, and $n_{co}$ and $n_{cl}$ are the refractive index of the fiber core and the cladding, respectively.

For example, analytes in biosensing applications usually have a refractive index of 1.33-1.34. The fiber core typically has a refractive index of ~1.45, and the penetration depth is estimated to be ~140nm for a light source with wavelength of 470nm [23]. Generally speaking, the greater the penetration depth is, the higher the sensor sensitivity is, due to an increased modal overlap with the test analyte. In this respect, the evanescent-field based fiber-optic sensors become more sensitive to analytes with refractive indices closer to that of the fiber core [36, 37]. Other methods that can enhance overlap between the evanescent field and the test analyte include employing different geometric designs, such as tapering fibers into microfibers [38, 39], U-shaping of the unclad fibers [30, 31], or using side-polished fibers [35, 40-42].

The merits of sensors in this category are the simplicity of the structure, low cost, small footprint, and a simple sensing mechanism, while the main disadvantages of such sensors are their poor modal overlap between the evanescent field and the analyte (less than 1%), as well as the poor mechanical robustness due to the cladding-stripping or fiber-tapering process. Moreover, since the penetration depth of the evanescent field is typically less than a wavelength, fiber-optic sensors employing evanescent wave excitation are, by their nature, surface-sensitive measurements. Therefore, they can only detect the surface events rather than the bulk events.

### 2.1.2 Fiber-optic sensors based on the surface plasmon resonance (SPR)

Surface plasmons are the collective charge oscillation modes localized on the interface between a metal and dielectric layer with unique light interaction properties. Propagating at the metal/dielectric interface, surface plasmons are extremely sensitive to changes in the refractive index of the dielectric medium. Typically, these sensors are implemented in the Kretschmann-Raether prism geometry, where a p-polarized light is launched through a glass prism and reflected from a thin metal (Au, Ag) film deposited on the prism facet, as shown in Fig. 2.2. The presence of a prism allows phase matching of an incident light wave with a plasmonic wave at the metal/dielectric interface, by properly choosing the light wavelength and the incident angle.

Changes in the refractive index of an analyte adjacent to the metallic layer would modify the phase-matching condition, thus leading to variations in the spectrum of the reflected beam.

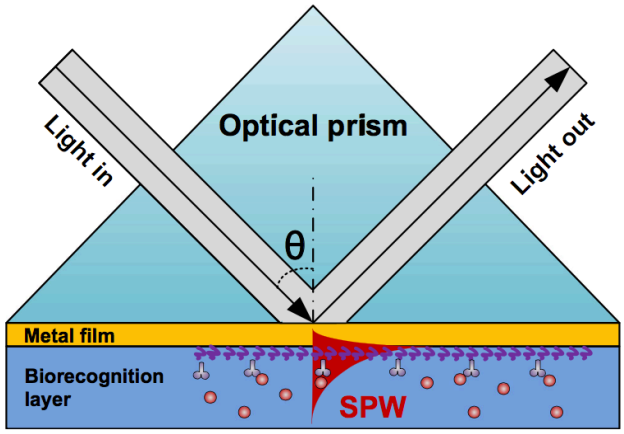


Figure 2.2 Sketch of the operating principle of the Kretschmann-Raether prism (SPW surface plasmon wave) [Fig. 1 in Ref. 43]

Using optical fibers instead of the bulk prisms in plasmonic sensors offers miniaturization, high degree of integration, and remote sensing capabilities. Fiber-optic SPR sensors operate near the frequency of phase matching between a core-guided fiber mode and a high lossy plasmon mode propagating at the metallized core/cladding interface. Being extremely sensitive to the variations in the refractive index of the dielectric surrounding the metal film, fiber-optic sensors based on surface plasmon resonance have attracted much attention, and they have been implemented in many sensing structures [44-49]. In the simplest case (as shown in Fig. 2.3), similar to the case of the evanescent field based fiber sensors, a small portion of the fiber cladding is removed and subsequently coated with a thin metal layer (10-50nm). When this region is surrounded by an analyte, the transmission spectrum of the fiber-based SPR sensor features a spectral dip at a resonant frequency due to efficient excitation of lossy surface plasmons. Variations in the analyte refractive index or the anlyte layer thickness adjacent to the metal layer would result in the spectral shifts of the resonant wavelength, which constitutes the operation principle of the fiber-based SPR sensors.

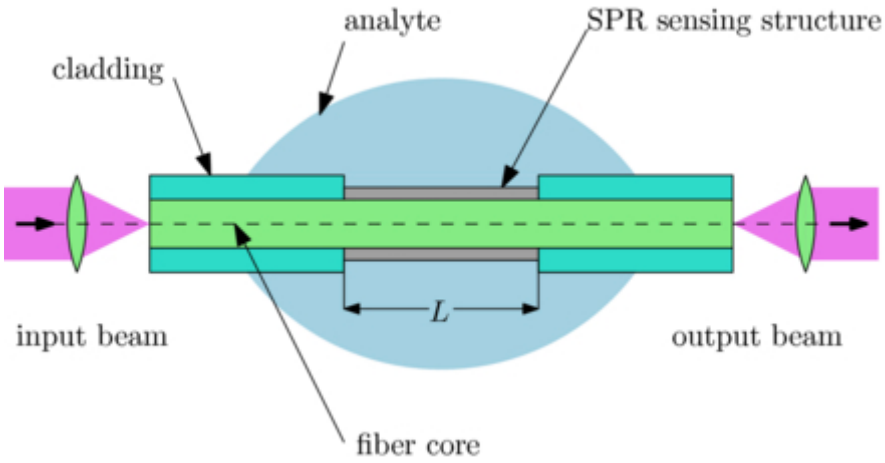


Figure 2.3 Schematic of the fiber-based SPR sensor (Fig. 1 from Ref. [64])

Y. Lin et al. [50] reported a refractive index sensor based on SPR with a side-polished multimode fiber. The experimentally demonstrated sensitivity was ~1570 nm/RIU. In Ref. [51], a similar fiber-based SPR sensor with an improved sensitivity of ~2400nm/RIU was reported, by optimizing the thickness of the metal layer. Several researchers fabricated an additional high-index dielectric layer on the metal film to protect the metal coating and improve its sensitivity [52]. By optimizing the thickness and the refractive index of the dielectric layer, the sensitivity was significantly improved from ~2800 nm/RIU to ~5200 nm/RIU. Additionally, J. H. Ahn et al. [53] demonstrated a fiber-based SPR configuration, in which a metal-dielectric-metal multilayer was deposited on top of a side-polished fiber. The presence of dielectric layer sandwiched between two metal layers allows precise tuning of the resonance wavelength and generation multiple modes. These modes can be selectively chosen for suitable applications. In Ref. [54], the authors demonstrated a tapered fiber-optic SPR sensor (waist diameter as small as 30 μm) with a semi-cylindrical shape thin metal layer. This configuration leads to the excitation of several hybrid SPR modes, thereby generating several resonance dips in the fiber transmission spectrum. The sensitivity of this sensor was found to be $1.2\times10^{5}$ nm/RIU, with an equivalent resolution as high as $7\times10^{-7}$ RIU. Another important application of the fiber-optic SPR sensors is to monitor the thickness variations of thin films deposited on the fiber surface. For example, in Ref. [55], M. Mar et al. used a fiber-optic SPR probe for *in situ* characterization of a multi-layered-Langmuir-Blodgett film. Experimental results show constant shifts in the resonance wavelength as the number of monolayers was increased. Similar configurations of using fiber optic SPR sensors for

real-time monitoring of the growth of titanium-dioxide thin films [56], and nano-scale polymer films [57], as well as formation of polyelectrolyte coatings [58], have also been reported.

Currently, fiber-based SPR sensors are among the most sensitive sensors, and thus, are particularly suitable for biomedical sensing applications including monitoring the analytes refractive indices, detection of the surface binding events and DNA hybridization, as well as study of antigen-antibody interactions [59-65]. The advantages of the fiber-based SPR sensors include ultra high sensitivity, label-free and real-time sensing capabilities, flexible sensing structure designs, miniaturized sensor systems, and remote sensing capability, while the drawback of this technique is a complicated fabrication process that requires fiber cladding stripping and polishing, and precisely controlled metal-layer deposition. Moreover, since the probing length of surface plasmon in the visible range is only on the order of 100nm, detection of larger targets (such as bacteria with sizes of 0.5μm-10μm) is problematic using SPR-based fiber sensors.

### 2.1.3 Fiber-optic sensors based on the fiber gratings

Fiber gratings can be generally categorized into fiber Bragg gratings (FBGs) and long-period gratings (LPGs); both of them have been intensively studied for sensing applications. A FBG, which features a grating constant on the sub-micron level, is usually inscribed in the core of a single-mode fiber. It is able to couple a forward-propagating core mode of the optical fiber into the backward, counter-propagating mode at the resonant wavelength of the Bragg grating, thereby generating a spectral peak in the reflection spectrum or a spectral dip in the transmission spectrum, as shown in Fig. 2.4. FBGs are usually used as physical sensors for monitoring the temperature, strain, and pressure [67-69]. Some researchers also demonstrate sensors based on FBGs for the detection of analyte refractive index or biolayer thickness. The operation relies on a spectral-based sensing modality. Variations in the analyte refractive index or layer thickness adjacent to a FBG would modify the effective refractive index of the fiber core mode, thus shifting the resonant wavelength of the FBG. One typical implementation of such a sensor is by partially etching the fiber cladding, so that the evanescent field of the fiber core mode could couple with the test analyte [70-72]. In Ref. [71], A. Asseh et al. demonstrated a FBG refractometer in which the cladding of the FBG is stripped using a chemical etching method. The sensitivity of this FBG refractometer was calculated to be ~220 nm/RIU at a refractive index

value of ~1.45. Since only a small portion of the evanescent wave interacts with the material under test, the sensitivities of such devices are limited. To improve the modal overlap with the samples, Zhou et al. [73] demonstrated a liquid-core fiber sensor fabricated by a chemical etching assisted femtosecond-laser milling technique. A micro-slot engraved along the fiber Bragg grating was used to construct liquid-core waveguide by filling the slot with index matching oils. Experimental sensitivity was reported to be ~945nm/RIU, although the operation range of this sensor is limited to analyte with a refractive index larger than 1.44. In recent years, FBG sensors have also been proposed for biochemical sensing applications. By monitoring the changes of refractive index, one can effectively study the binding events and surface interaction occurring in the evanescent field of the core mode. In 2005, A. N. Chryssis et al. demonstrated an etched FBG sensor for *in situ* monitoring of DNA hybridization [74]. Later, in 2008, S. Maguis et al. [75] presented a biosensor based on a tilted fiber Bragg grating refractometer that enabled real-time detection of target molecules, and the study of antigen-antibody reaction kinetics. A pronounced advantage of the FBG sensor is that the linewidth of the spectral feature is relatively narrow, which allows for measuring minute spectral shift due to small changes in the refractive index of the surrounding medium.

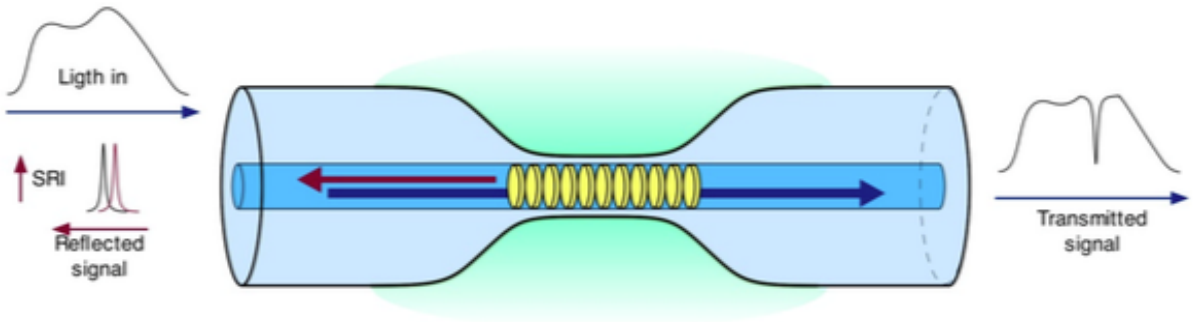


Figure 2.4 Schematic of the operation principle of fiber Bragg grating sensors [Fig. 4 in Ref. 88]

A long period grating typically has a grating constant ranging from ten to several hundred micrometers, as shown in Fig. 2.5. A LPG can couple a fiber core mode into multiple forward-propagating cladding modes. Therefore, sensors based on LPGs generally do not require fiber-cladding stripping. The transmission spectrum of a LPG normally features multiple spectral dips corresponding to the distinct cladding modes. The propagation constants of the cladding modes are very sensitive to the surrounding medium, which constitutes the operation principle of LPG sensors. In 1997, V. Bhatia et al. [77, 78] demonstrated a LPG sensor based on a single-mode

fiber for measuring the variations of the analytes refractive indices, and they achieved a sensitivity of ~400nm/RIU in the refractive index range of 1.33-1.43. To improve the sensitivity, LPG sensors fabricated on D-shaped fibers [79, 80], or tapered fibers [81-83] were reported, and the experimentally demonstrated sensitivity was found to be 2733nm/RIU in the measuring range of 1.45-1.454. Moreover, LPG-based biosensors have also been developed for the detection of overlayer thickness [84, 85], chemical concentrations [76, 86], and study of specific antigen-antibody interaction on the LPG surface [87-90].

We note that LPGs potentially could be developed into compact, highly sensitive sensors. However, LPG-based sensors usually have broader resonance bands, as compared to those of FBGs, which would make determination of the peak positions in fiber transmission spectrum considerably less precise, which, in turn, makes such a sensor less sensitive compared to their FBG counterparts. Moreover, sensors based on FBG or LPG generally have a relatively moderate accuracy due to the cross sensitivity to the fiber strain, bending, and temperature, which is the most pronounced disadvantage. Additionally, these sensors normally suffer from poor mechanical robustness due to the fiber cladding modifications or tapering process.

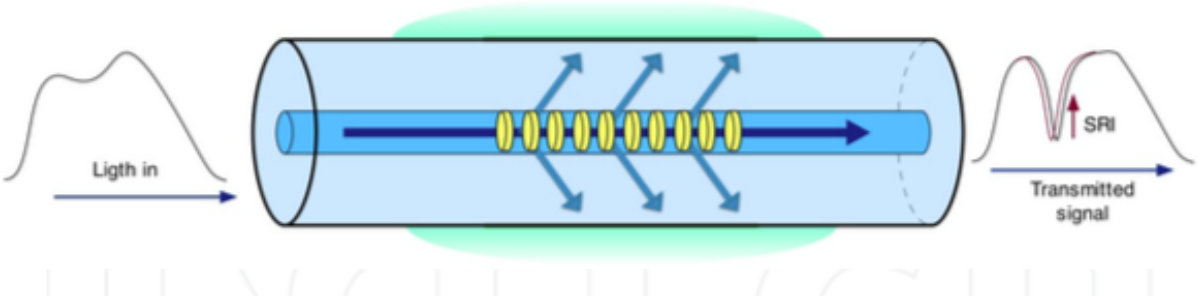


Figure 2.5 Schematic of the operation principle of long period grating sensors [Fig. 6 in Ref. 88].

## 2.2 Review of the PCF-based sensors

Photonic crystal fibers (PCFs), and photonic bandgap fibers (a subset of PCFs), refer to optical fibers that have specially patterned, micro-sized holes running along the fiber length, or a periodic sequence of materials in their structures. In general, PCFs can be divided into two classes, i.e., solid-core PCFs [Fig.2.6 (a)] and hollow-core PCFs (HC-PCFs) [Figs. 2.6 (b) and (c)]. Solid-core PCFs typically guide with a modified total internal reflection principle, which is similar to the guidance of traditional step-index TIR fibers. HC-PCFs feature a hollow core

surrounded by a periodically micro-structured region (e.g., several rings of small air holes or a periodic sequence of high and low refractive index layers) designed such that certain wavelengths cannot propagate through this region and are hence confined to the hollow core by photonic bandgap effect [91]. PCF-based platforms offer numerous advantages for bio-sensing applications. First, the test analytes can be probed by the guided light inside the holes without removing the fiber claddings, thus maintaining the robustness of the sensors. Second, the air holes of the PCF can hold a biological sample with a small volume (only a few nanolitres per centimeter of the fiber), while achieving high sensitivity. This is a significant advantage for biosensing applications. In addition, geometrical manipulation of the fiber cross-section gives PCFs the flexibility to increase the interaction of the guided light with the test sample. There are several types of sensing schemes using PCFs, according to different configurations and working principles.

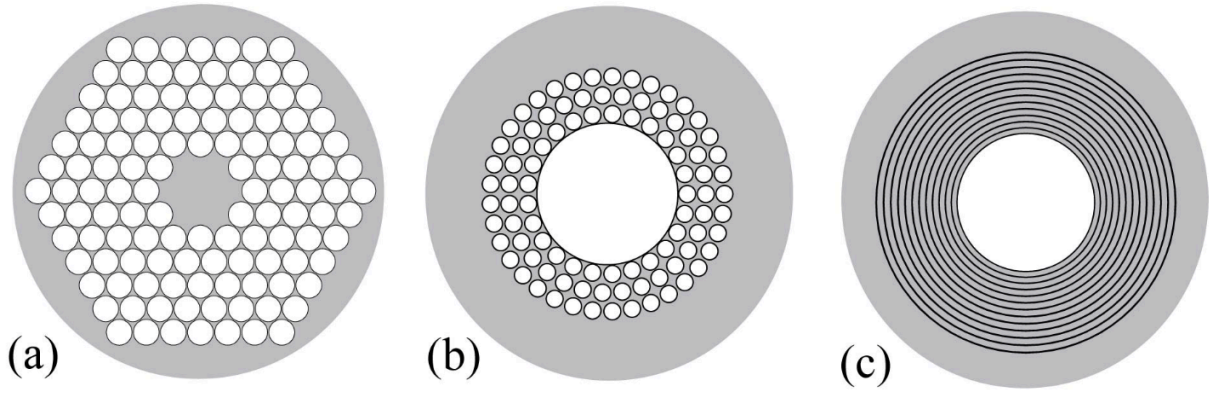


Figure 2.6 Various types of PCFs. (a) Solid-core PCF featuring a solid core surrounded by a periodic array of air holes. (b) Hollow-core PCF featuring a hollow core surrounded by several rings of small air holes. (c) Bragg fiber featuring a large hollow core surrounded by a periodic sequence of high and low refractive index layers. (Fig. 2 in Ref. [91])

### 2.2.1 Solid-core PCF sensors

Proposed by T. M. Monro et al. [92, 93] in 1990s, the cladding holes of a solid-core PCF can be filled with liquid or gas analytes, and the samples are detected by the evanescent field that propagates in these holes. Careful design and optimization of the PCF features, such as core size, pitch, and air-filling fraction in the micro-structured cladding, allows an improved overlap

between the mode field and the test samples (more than 20%), whilst circumventing the problems of short interaction length and fragility associated with traditional stripped claddings or tapered fiber structures in evanescent field based fiber-optic sensors. After this pioneering work, many PCF-based sensors have been designed and reported. For example, evanescent field based absorption spectroscopy for aqueous samples in the holes of a PCF [94, 95], and qualitative detection of aqueous solutions of fluorophore-labelled biomolecules positioned in the air holes [96-99], have been demonstrated. Another demonstration of label-free biosensing was using a silica PCF with a long-period grating (LPG) in order to measure the thickness of double-stranded DNA [100, 101]. A spectral shift of 1.4nm in the resonance wavelength per nm of double-stranded DNA layer was demonstrated.

Solid-core PCFs typically guide with a modified total internal reflection principle. However, when they are used for the sensing of liquid analytes with refractive indices higher than that of the fiber materials (e.g. $n_{analyte}$>1.45 for silica PCFs), the guidance of the solid-core PCFs turns into the photonic bandgap guidance. In Ref. [103], a solid-core PCF sensor was theoretically proposed for sensing of high-index liquid analytes, and the sensitivity was calculated to be ~1200 nm/RIU with the analyte refractive index value of 1.58. X. Yu et al. [104] experimentally demonstrated a solid-core PCF with high index infiltrations for refractive index sensing. Strong shifts in the fiber bandgap positions are observed with the refractive index variations of the infiltrated liquids. A sensitivity of~1500 nm/RIU was achieved experimentally. In [105], D. K. C. Wu et al. reported a microfluidic refractive index sensor based on a solid-core PCF. The sensor achieves very high sensitivity by coupling the core mode to a mode localized in the adjacent analyte-filled waveguide at the frequency near the modal cut-off. The experimental demonstrated sensitivity of this refractometer was as high as 30100 nm/RIU due to a strong field overlap. However, these designs require a complicated high-pressure filling method to introduce the liquid analytes into the porous claddings. Moreover, these sensors only work for analytes with high refractive indices ( $n_{analyte} > n_{silica}$ ), which limits their applications in biological and chemical field where $n_{analyte}$ is ~1.33.

### 2.2.2 Hollow-core PCFs sensors

Hollow-core PCFs present an alternative for sensing applications to their solid-core counterparts. The key functionality of such sensors is their ability to guide light directly in the hollow or liquid-filled cores with a refractive index smaller than that of a surrounding cladding material by photonic bandgap effect. Practically, bandgaps are defined as the frequency regions of enhanced fiber transmission, and they are the result of destructive interference of the core-guided light inside of the microstructured cladding [91]. When launching a spectrally broad light into a HC-PCF, only the spectral components guided by the fiber bandgap will reach the fiber end, while all the spectral components not located within the bandgaps will irradiate out near the fiber-coupling end.

HC-PCFs based sensors typically operate using a spectral-based detection modality. Variations in the refractive index of a liquid analyte inside the fiber core would modify the bandgap position of the HC-PCF, leading to spectral shifts in the fiber transmission maxima. The spectral shifts can be used to deduce the changes in the refractive indices of the analytes filling the fiber core. Such sensors can achieve almost complete modal overlap with the analytes, thus resulting in very high sensitivity to the refractive index changes. In [107, 108], the authors experimentally demonstrated a highly sensitive liquid-core refractive index sensor based on a commercial silica-based HC-PCF that featured a hollow core surrounded by a porous periodic cladding. A sensitivity of ~5000 nm/RIU was reported. However, fabrication of such fibers requires a sophisticated drawing technique, and the fiber is extremely expensive (thousands of dollars per meter). Moreover, these sensors require a very long response time due to the necessity of introducing the test analytes into the micron-sized holes of a PCF [~10 min for 20cm-long PCFs].

As shown in Fig. 2.6(c), there is a special type of hollow-core PCF, i.e., hollow-core photonic bandgap Bragg fiber, which features a large hollow core surrounded by alternating multilayers of high and low refractive index layers. This configuration avoids the problems of long filling time due to the large size of the hollow core and, at the same time, achieves almost complete confinement of light within the test analyte. Moreover, the bandgap guiding mechanism is valid for liquids with refractive indices smaller than that of the cladding material ($n_{cl}$~1.49-1.58). This is important for many industrial and biochemical sensing applications, where $n_{analyte}$ is

~1.33. Due to the possibility of having a large core (~1mm), the response time of the Bragg fiber sensors could be shortened to ~1s, thus allowing for continuous on-line monitoring of liquid samples in a contained, highly integrated manner.

In 2009, our group proposed the possibility of using a hollow-core low-refractive-index-contrast Bragg fiber as a refractive index sensor [15]. It was theoretically predicted that such a Bragg fiber based refractive index sensor could be on the order of 5000nm/RIU, which is comparable to that of most commonly used SPR sensors. In 2012, K. J. Rowland et al. [110] reported a HC high-refractive-index-contrast Bragg fiber sensor with a sensitivity of~330nm/RIU. More recently, our group reported a HC low-refractive-index-contrast Bragg fiber sensor [111]. We showed that such fiber sensors offer outstanding performance in detection of changes in the real part of the analyte refractive index by monitoring the spectral shifts of the fiber transmission peaks. The sensitivity of our sensor, compared to that of the one reported in [110], is considerably improved (~1400nm/RIU). The detection limit of this Bragg fiber sensor can be as small as $7\times10^{-5}$RIU, assuming that a spectral shift of 0.1nm can be detected reliably. We note that the low-refractive-index-contrast Bragg fibers have certain advantages for liquid analyte sensing, compared to their high-refractive-index-contrast counterparts. In fact, we have argued in [111, 113] that the high-refractive-index-contrast Bragg fibers are relatively suitable for gas sensing (n~1), as for most high-refractive-index-contrast Bragg fibers filled with aqueous solutions (n~1.33), the TM band gaps of the Bragg reflector tend to collapse at the light line of aqueous material due to the Brewster angle phenomenon, leading to high loss for the hybrid (HE/EH) modes. In contrast, the low-refractive-index-contrast Bragg fibers show large TM band gaps in the vicinity of the light line of the aqueous core, thus resulting in a good guidance. We note that the drawback of such sensors is that the plastic materials frequently used in Bragg fibers are generally less chemically resistant than their silica counterparts.

### 2.2.3 PCF sensors based surface plasmon resonance

The combination of photonics and plasmonics is an emerging research area that benefits from the improvements in the coating technology, and it attracts growing interest for biosensing applications. Compared to other types of SPR sensors, PCF-based SPR sensing technology has a number of advantages, such as a large mode area, and a wide tuning range of phase matching condition [121-123]. In a PCF-based SPR sensor, plasmons on a thin metal film can be excited by

a Gaussian-like leaky mode of a photonic crystal waveguide. It has been demonstrated that the effective refractive index of the fiber core mode can be designed to be considerably smaller than that of a core material, thereby enabling efficient phase matching with plasmons at any wavelength of choice, while maintaining highly sensitive response to changes in the refractive index of an analyte layer. In 2006, Kuhlmey et al. [124] provided a theoretical model for metal-coated PCFs and showed that such fibers exhibited plasmonic resonances. Later in 2008, Hautakorpi et al. [125] proposed a three-hole PCF based SPR sensor. This configuration offers higher integrity by ingeniously combining analyte, surface plasmons, and the optical fibers. Hassani and Skorobogatiy [126, 127] analyzed in detail the design principles for two different PCFs structures with metallic coating for biosensing applications. In these designs, phase matching was facilitated by the introduction of the hollow microstructure into the fiber core. Improved microfluidics was addressed by the integration of large analyte-filled channels adjacent to the fiber core. Detection limit of the amplitude-based sensor for measuring changes in the aqueous analyte was found to be $5\times10^{-5}$ RIU, assuming a 1% amplitude change detection limit. The detection limit of the same sensor in the wavelength interrogation mode was found to be $3\times10^{-5}$ RIU, assuming a 0.1 nm detection limit in the shift of a plasmonic peak. More recently, Otupiri et al. [128] presented a theoretical investigation of a multi-channel SPR biosensor based on PCFs. The relatively large air holes and fluidic channels of the biosensor would facilitate aqueous sample loading with pressure or capillary action. The structure with metallized channels shows better performance in terms of easy microfluidic flow of test samples and improved mechanical robustness, compared to traditional fiber-based SPR sensor. Unfortunately, in practice, the metallization of these micron-sized holes along the PCF has proved to be experimentally difficult, and most of the work in this area is still in theoretical level [129-133].

To summarize this section, we have reviewed several optical sensors based on PCFs, and we found that a PCF by itself can be used as a platform for the sensing of liquid or gaseous analytes. In fact, the function of a refractive index sensor can also be implemented on PCFs utilizing fiber Bragg gratings [134-137], long period gratings [138-144], fiber interferometry techniques [145-151], as well as non-linear effects [152]. All these techniques significantly enrich the sensing scenarios of PCF-based sensors, and make PCFs very promising for the development of the next generation of fiber-optic sensors.

## 2.3 THz waveguide sensors

Currently, most of the investigations of fiber-optic sensors are limited to the visible and near-IR regions. However, since the probing lengths of the evanescent fields in these spectral ranges are deeply sub-wavelength, detection of larger targets (such as bacteria with sizes of 0.5μm-10μm) is found to be problematic. In order to extend the probing depth of the surface wave to longer distance for macromolecular or bacteria detection, one can pursue biosensors operating at longer wavelengths (such as THz).

The THz range, with frequencies lying between 100 GHz and 10 THz, has strong potential for a wide range of technological and scientific applications including biosensing, imaging, communications, and spectroscopy [116-120, 153, 154]. Among these applications, THz biosensing has attracted wide interest due to many appealing properties of THz waves. First, THz waves are non-ionizing. Therefore, they pose no damage to the biological samples. Second, many molecules have vibrational and rotational modes in the THz regime, resulting in unique absorption spectral signatures. Third, the probing length of THz surface wave is a natural fit for detection of macromolecules, cells, and bacteria of relatively large sizes.

Designing of THz waveguides for flexible delivery of THz radiation with low loss and efficient light-matter interactions is an important step towards practical sensing applications. The concept of using waveguides for sensing is well established in other frequency ranges, but has only recently started maturing in the THz range. One principal difficulty for realizing low-loss THz waveguides is that most materials exhibit large absorption losses in the THz region. In order to circumvent the loss limit imposed by the absorption of fiber material, subwavelength [155-158], porous [159-161], and hollow-core THz waveguides with various structures [162-164], are developed. In particular, hollow-core or porous waveguides are of great interest for biosensing applications. Such configurations allow the test samples to conveniently access to the waveguide core and the evanescent part of the guided waves. Moreover, the relatively large channels could be further functionalized with bio-recognition elements (such as phages) that can bind and progressively accumulate target bacteria, thus enabling detection of specificity. In what follows, we review several up-to-date waveguide platforms operating in the THz range that have been developed for sensing experiments.

### 2.3.1 Anti-resonant reflecting hollow waveguide (ARRHW) sensors

One of the most common configurations of THz waveguides for sensing applications is based on ARRHW, which features a hollow core surrounded by a ring-shaped dielectric cladding. In this configuration, the core modes can oscillate and radiate through the cladding since the refractive index of the waveguide core is smaller than that of the cladding material. The guiding mechanism of these waveguides is similar to the anti-resonant reflecting optical waveguide model [165-167, 170]. The cladding of such waveguides can be considered as a Fabry-Perot (F-P) resonator. For the wavelengths that satisfy the resonance condition, constructive interference occurs, which means that the F-P resonator is highly transparent for these wavelengths; therefore, light cannot be reflected and leak out of the cladding structure (leaky modes). On the other hand, for the wavelengths under the anti-resonant condition of the cladding (i.e., the wavelengths that do not satisfy the resonance condition), destructive interference takes place, light is well reflected by the F-P resonator, and confined in the air core as guided modes. A schematic of a typical THz-ARRHW sensor with a double-layered cladding is illustrated in Fig. 2.7 [168]. A thin film attached to the ring waveguide cladding of the THz-ARRHW results in resonant-frequency shifts. Thus, one can sense the tiny variations in the refractive index or thickness of an adsorbed molecular film near the ring cladding.

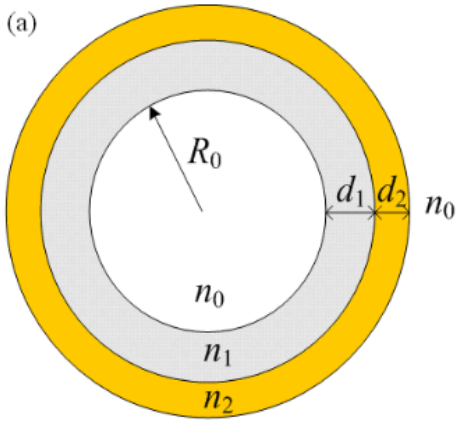


Figure 2.7 Schematic cross-section diagram of a typical THz-ARRHW sensor [Fig. 1 in Ref. 168].

The position of the non-transmission wavelengths can be described by the following equation:

$$\lambda_m = \frac{2(\mathrm{d}_1\sqrt{n_1^2 - n_0^2} + \mathrm{d}_2\sqrt{n_2^2 - n_0^2})}{m} \tag{2.2}$$

where $n_0$, $n_1$ and $n_2$ are the refractive indices of air, waveguide cladding, and sample layer, respectively. $d_1$ and $d_2$ are the thicknesses of the waveguide cladding and the sample layer; $m$ is a positive integer.

From Eq. (2.2), we can see that the resonant wavelengths are determined by the thickness and effective refractive index of the cladding. Based on this mechanism, various sensing applications have been proposed. For example, in [168], the authors experimentally demonstrated the use of a simple hollow tube for the detection of sub-wavelength-thick molecular overlayer adhered to the inner-core surface of tubes. Due to the strongly localized THz evanescent wave at resonant frequency, which is sensitive to the optical-path length of the tube wall, a tiny thickness variation of the molecular layer deposited on the tube would result in an obvious frequency shift of the resonant dip in the transmission spectrum. The demonstrated sensitivity was found to be 0.003mm/μm for a carboxypolymethylene-molecular overlayer. In another implementation [169], the authors demonstrated a similar pipe waveguide as a terahertz refractive index sensor for powder and liquid-vapour sensing. Loading various powders in the ring cladding or inserting different vapours into the hollow core of the pipe waveguide leads to a significant shift of resonant frequency, and the spectral shift is related to the refractive-index changes. The proven detection limit of molecular density was found to be 1.6nano-mole/mm$^3$ and the highest sensitivity to changes in the analyte refractive index was found to be 22.2GHz/RIU. The demonstrated sensors based on ARRHW have the advantages of flexibility and compactness, as well as remote sensing capability. They are potentially suitable for applications, such as biomedical or industrial sensing applications, and environmental pollutant monitoring.

### 2.3.2 Parallel plate waveguide (PPWG) sensors

Parallel plate waveguides [171-180] have also been extensively studied for THz guidance and sensing experiments. PPWG is typically composed of two parallel metal plates separated with an air gap, as shown in Fig. 2.8. One appealing property of such waveguides is that one can selectively excite specific modes with different input polarizations. When the input Gaussian beam is polarized parallel to the plates, one can excite the lowest-order transverse electric ($TE_1$) mode [171]. In contrast, when the input beam is polarized perpendicular to the plate, transverse

electromagnetic (TEM) mode with low-loss and negligible dispersion can be efficiently excited [172]. THz pulses propagating in the PPWG allows characterization of analyte liquids or dielectric films loaded in the vicinity of the waveguide. In such sensors, sensing of thin dielectric films is based on the analysis of resonant frequency or pulse delay in the presence of the test sample. In 2009, the authors [173] described a THz resonator integrated with a parallel-plate waveguide for highly sensitive, and noninvasive liquid refractive index monitoring. The resonator is formed by machining a rectangular groove into one plate of a parallel-plate waveguide, and can be efficiently excited via the transverse-electric ($TE_1$) mode. When the cavity is filled with the dielectric liquid material, the resonance frequency shifts correspondingly. The demonstrated refractive index sensitivity was found to be $3.7\times10^5$nm/RIU. This resonator features an extremely narrow linewidth (3GHz at 0.3THz), which was the narrowest achieved in that frequency range. Such resonators can be easily integrated into microfluidic platforms for real-time monitoring of various samples. Later in 2012, the same research group [174] realized a similar parallel-plate waveguide sensor with two independent integrated resonant cavities. The resonant frequency of each cavity exhibits an approximately linear dependence on the refractive index of the material inside the cavity, and each cavity is demonstrated to respond independently with no measurable crosstalk. In another implementation [175], the authors demonstrated THz sensing of a thin dielectric layer using a parallel-plate waveguide. By inserting a single slit sheet in the waveguide, two channels were thereby formed. When a thin dielectric layer was applied on the upper surface of the channel, changes in the single resonance frequency could be correlated to the layer properties, including length, thickness, and refractive index. The experimental demonstrated sensitivity was found to be 2.4GHz/mm. Moreover, Zhang, et al. [176] demonstrated a waveguide terahertz time-domain spectroscopy for the characterization of nanometer-thick water layers on the surface of a parallel-plate metal waveguide. Both the absorption and refractive index of the water layer were measured by comparing the signal from an empty waveguide with that from the waveguide containing the water layer. This technique has the advantage of simplicity both in the fabrication and implementation. In addition, the open geometries of PPWG are ideal for the sensing of thin films and powder analytes.

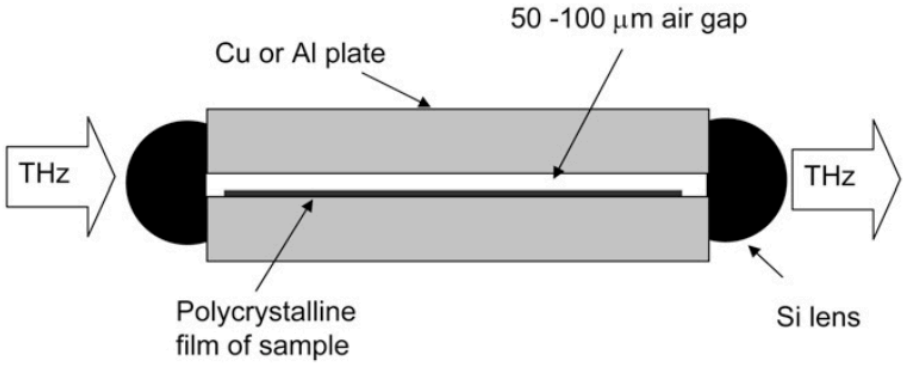


Figure 2.8 Schematics of a parallel plate waveguide sensor [Fig. 3 in Ref. 177].

### 2.3.3 Micro-structured THz waveguide sensors

Another major category of waveguides that have been proposed and developed for THz sensing applications is micro-structured waveguides. These waveguides offer better confinement and lower losses due to less material residing in the core compared to solid-core waveguides, and they have great potential for sensing applications. For example, in Ref. [181], the authors used a suspended core polyethylene THz fiber for the detection of E. coli bacteria based on an amplitude modality. Selective binding of the E. coli bacteria to the surface of the fiber core modifies the THz transmission properties of the suspended core fiber due to enhanced scattering and absorption losses. Changes in the fiber propagation loss can then be correlated to the concentration of the bacteria in the liquid analytes. The sensor is capable of E. coli detection at concentrations in the range of $10^4$-$10^9$ cfu/ml. Presented bacteria detection method is label-free, and it does not rely on the presence of any bacterial "fingerprint" features in the THz spectrum. In another implementation [182], the authors proposed a planar porous dielectric waveguide featuring periodic sequence of deeply sub-wavelength air/dielectric bi-layers for potential applications as low-loss waveguides and sensors in the THz spectral range. The design of this waveguide maximized the fraction of power guided in the air to reduce the waveguide loss due to material absorption, thus providing a conveniently accessible microfluidic channels for sensor measurements. Additionally, authors in [183-185] proposed a hybrid refractometer based on plasmonic THz waveguides that feature two metallic wires inserted into a porous dielectric cladding. The introduction of even lossless analytes into the fiber core leads to significant changes in the modal losses, which is used as a transduction mechanism. Refractive index

sensitivity on the order of $10^{-3}$ RIU is theoretically demonstrated for gaseous analyte based on an amplitude detection modality. Such a sensor is potentially capable of identifying various gaseous analytes and aerosols or measuring the concentration of dust particles in the air.

## 2.4 Conclusion

In this Chapter, we review the main types of the fiber-optic sensors and briefly summarize their advantages and drawbacks. Firstly, we review the fiber-optic sensors based on the evanescent field detection, surface plasmons resonance and fiber Bragg gratings. We then focus on the research and development of PCF-based sensors. Finally, we review several waveguide sensors operating in the THz range. All these techniques, which are summarized in Table 2.1, significantly enrich the sensing scenarios of fiber optic sensors. We find that PCFs, in particular, hollow-core Bragg fibers, offer many advantages for the sensing of liquid analytes.

Table 2.1: Summary of the most commonly used fiber-optic refractive index sensors.

| ***Sensor configuration*** | ***Spectral range*** | ***Sensitivity*** | ***RI range*** | ***Ref.*** |
|---|---|---|---|---|
| **I. Evanescent field detection** | | | | |
| Side-polished/D-shaped fiber | 1480-1580nm | $10^{-3}$ RIU | 1.33-1.45 | [35, 42] |
| Tapered fiber | 850nm | $10^{-5}$ RIU | 1.36-1.46 | [38, 39] |
| U-shaped fiber | 400-1600nm | 10%$\Delta I$/RIU | 1.25-1.45 | [40, 41] |
| **II. Sensors based on SPR** | | | | |
| Based on side-polished fiber | 400-1200nm | $6\times10^{-6}$ RIU | 1.3-1.39 | [50, 51] |
| Based on tapered fiber | 900-1600nm | $7\times10^{-7}$ RIU | 1.44-1.45 | [54] |
| **III. Sensors based on FBGs** | | | | |
| Based on FBGs | 1400-1600nm | 945nm/RIU | 1.3-1.6 | [73] |
| Based on LPGs | 1200-1600nm | 2733nm/RIU | 1.45-1.46 | [81-83] |
| **IV. Sensors based on PCFs** | | | | |

| | | | | |
|---|---|---|---|---|
| Based on solid-core PCFs | 1460-1560nm | $3\times10^{4}$nm/RIU | ~1.5 | [105] |
| Based on hollow-core PCFs | 600-1200nm | 5000nm/RIU | 1.33-1.39 | [107] |
| Based on Bragg fibers | 500-800nm | 1400nm/RIU | 1.33-1.36 | [111] |
| Based on SPR | 500-1500nm | $5\times10^{-5}$ RIU | 1.33-1.34 | [127]* |
| Based on FBG | 1500-1550nm | 1300nm/RIU | ~1.41 | [136] |
| Based on LPG | 1500-1625nm | 2260nm/RIU | 1.33-1.35 | [140] |
| **V. THz waveguide sensors** | | | | |
| Based on ARRHW | 0.1-0.5THz | 22.2GHz/RIU | 1.35-1.5 | [169] |
| Based on PPWG | 0.1-0.5THz | $3\times10^{5}$nm/RIU | 1.39-1.43 | [173] |
| Based on MOFs | 0.5-1THz | $10^{-3}$ RIU | 1-1.5 | [183]* |

$\Delta I$/RIU: Intensity changes per refractive index unit;

* Only theoretical values.

# CHAPTER 3 METHODOLOGY

In Section 3.1, we first summarize the two sensing modalities (i.e., amplitude-based detection modality and spectral-based detection modality) used by the fiber-optic sensors. Then, in Section 3.2, we describe the design principles and the techniques used for the fabrication of the Bragg fibers operating in the visible and the terahertz range. Finally, in Section 3.3, we present the experimental setup used for characterizing the proposed hollow-core Bragg fiber sensors.

## 3.1 Detection strategies of the proposed fiber-optic sensors

In this Section, we describe the amplitude-based modality and spectral-based modality that exploit changes in their transmission spectra in the presence of a target analyte. This section follows closely the contents of the Book Chapter of Prof. Maksim Skorobogatiy [15].

In an amplitude-based detection methodology, one typically operates at a fixed wavelength $\lambda$ and records changes in the amplitude of a signal, which are then re-interpreted in terms of changes in the analyte refractive index. To characterize sensitivity of a fiber-based sensor of length $L$, one employs an amplitude sensitivity function $S_a(\lambda, L)$, which is defined as a relative change in the intensity $P(\delta, \lambda, L)$ of a transmitted light for small changes in the measurand $\delta$. Note that $\delta$ can be any parameter, which influences the transmission properties of the fiber sensor. This includes concentration of absorbing particles in the analyte, thickness of a bio-layer that can change due to capture of specific bio-molecules, as well as real or imaginary parts of the analyte refractive index. Amplitude sensitivity is then defined as:

$$S_a(\lambda, L) = \lim_{\delta \to 0} \frac{P(\delta, \lambda, L) - P(0, \lambda, L)}{\delta \cdot P(0, \lambda, L)} = \frac{\partial P(\delta, \lambda, L) / \partial \delta \big|_{\delta=0}}{P(0, \lambda, L)} \tag{3.1}$$

Denoting, $\alpha(\delta, \lambda)$ to be the fiber propagation loss at a fixed value $\delta$ of a measurand, light intensity at the fiber output can be written as:

$$P(\delta, \lambda, L) = P_{in}(\lambda) \exp(-\alpha(\delta, \lambda) L) \tag{3.2}$$

where $P_{in}(\lambda)$ is the light intensity launched into a fiber. Substituting Eq. (3.2) into Eq. (3.1), amplitude sensitivity function can be then expressed as:

$$S_a(\lambda, L) = -\partial \alpha(\delta, \lambda) / \partial \delta \big|_{\delta=0} \cdot L \tag{3.3}$$

As follows from Eq. (3.3), sensor sensitivity is proportional to the sensor length $L$. In turn, as follows from Eq. (3.2), the maximal sensor length is limited by the absorption loss of a fiber. Defining $P_{det}(\lambda)$ to be the power detection limit at which changes in the light intensity can still be detected reliably, the maximal sensor length allowed by the power detection limit can be calculated from Eq. (3.2) as:

$$L = \frac{\log(P_{in}(\lambda)/P_{det}(\lambda))}{\alpha(0,\lambda)} \tag{3.4}$$

Defining $\eta_{det}(\lambda) = \log(P_{in}(\lambda)/P_{det}(\lambda))$, maximal sensitivity allowed by the power detection limit can be written using (3.3) as:

$$S_a(\lambda) = -\eta_{det}(\lambda)\frac{\partial\alpha(\delta,\lambda)/\partial\delta\big|_{\delta=0}}{\alpha(0,\lambda)} \tag{3.5}$$

Here, we assume that $\eta_{det}(\lambda) = 1$, which allows us to characterize an inherent sensitivity of a sensor system, while separating it from the issue of a power budget that might bring additional sensitivity enhancement. Finally, given sensor amplitude sensitivity, to estimate sensor resolution of a measurand $\delta$, one can use Eq. (3.1). Assuming that the minimal detectable relative change in the signal amplitude is $\left(\Delta P/P\right)_{\min}$ (which is typically on the order of 1% if no advanced electronics is used), then the minimum value of a measurand that can be detected by such a sensor is:

$$\delta_{\min} = \frac{\left(\Delta P/P\right)_{\min}}{S_a(\lambda)} \tag{3.6}$$

Another popular sensing methodology is spectral-based. It uses detection of displacements of spectral singularities in the presence of a measurand with respect to their positions for a zero level of a measurand. This sensing approach is particularly effective in the resonant sensor configurations that feature sharp transmission or absorption peaks in their spectra. Defining $\lambda_p(\delta)$ to be the position of a peak in a sensor transmission spectrum as a function of a measurand value $\delta$, spectral sensitivity function can be defined as:

$$S_\lambda = \partial\lambda(\delta)/\partial\,\delta\big|_{\delta=0} \tag{3.7}$$

Given sensor spectral sensitivity, to estimate sensor resolution of a measurand $\delta$, one can use expression (3.7). Thus, assuming that the minimal detectable spectral shift in the peak

position is $\left(\Delta\lambda_p\right)_{\min}$ (which is typically on the order of $0.1nm$ in the visible spectral range if no advanced optical detection is used), then the minimum value of a measurand that can be detected by such a sensor is:

$$\delta_{\min} = \frac{\left(\Delta\lambda_p\right)_{\min}}{S_\lambda} \tag{3.8}$$

## 3.2 Design and fabrication of the hollow-core Bragg fibers operating in the visible range

As a low-refractive-index-contrast Bragg reflector, we use polystyrene (PS)/polymethyl-methacrylate (PMMA) multilayers with refractive index of 1.58 and 1.49 at 589nm. This material combination is chosen owing to their good thermo-mechanical compatibility. As a result, they can be thermally co-drawn into a multilayer structure without cracking or delamination. Another advantage of using PMMA as the structure material is that many biomolecules can be directly attached to the surface without any chemical functionalization [99], which means that the fabricated Bragg fiber sensor could be conveniently used as a promising platform for a wide range of biochemical sensing applications. Moreover, because of the commercial abundance of these moderately priced polymers, we can build fiber sensors with a relatively low cost.

Bragg fibers confine light in their hollow cores by photonic bandgap effect. When a broadband light is launched into the analyte-filled core of a Bragg fiber, only the light with frequencies within the fiber bandgap of Bragg reflector will be confined and guided in the fiber core, while the light with frequencies outside of the bandgap will irradiate out in the first several centimeters of the fiber. From the basic theory [113] of the Bragg fibers, the resonant center wavelength $\lambda_g$, of the fiber fundamental bandgap can be calculated as:

$$\frac{\lambda_g}{2} = d_l\sqrt{\varepsilon_l^r - \varepsilon_c^r} + d_h\sqrt{\varepsilon_h^r - \varepsilon_c^r} \tag{3.1}$$

where, $d_l$ and $d_h$ are the thicknesses of the low- and high- refractive index layers in the Bragg reflector, $\varepsilon_l^r$, $\varepsilon_h^r$ are the real parts of the corresponding dielectric constants, while $\varepsilon_c^r$ is the real part of the dielectric constant of the core material.

Therefore, by adjusting the thickness of the multilayers in the Bragg reflector, we can target specific bandgap positions. In this project, we fabricate Bragg fibers with their primary bandgaps located in the visible range (600nm-750nm), because the aqueous solutions involved in this work are relatively transparent in this wavelength range.

In order to theoretically verify the resonant sensing mechanism of the Bragg fibers for the detection of analyte refractive index, we calculated the loss spectra of the fundamental $HE_{11}$ mode of the hollow-core Bragg fiber based on the Transfer Matrix Method (TMM) [201, 214]. The geometry of the Bragg fiber is chosen to have its fundamental bandgap located in the visible range (i.e., 680nm), when it is filled with water. In our simulations, the refractive index of the hollow core is changed from 1.33 to 1.355 with a step of 0.005. As shown in Fig. 3.1, the transmission bandgap shows a blue shift as the refractive index of the fiber core increases. This demonstrates that the transmission property of the Bragg fiber can be modified by the refractive index of the fiber core, which constitutes the spectral based sensing modaly of this Bragg fiber for the detection of analyte refractive index.

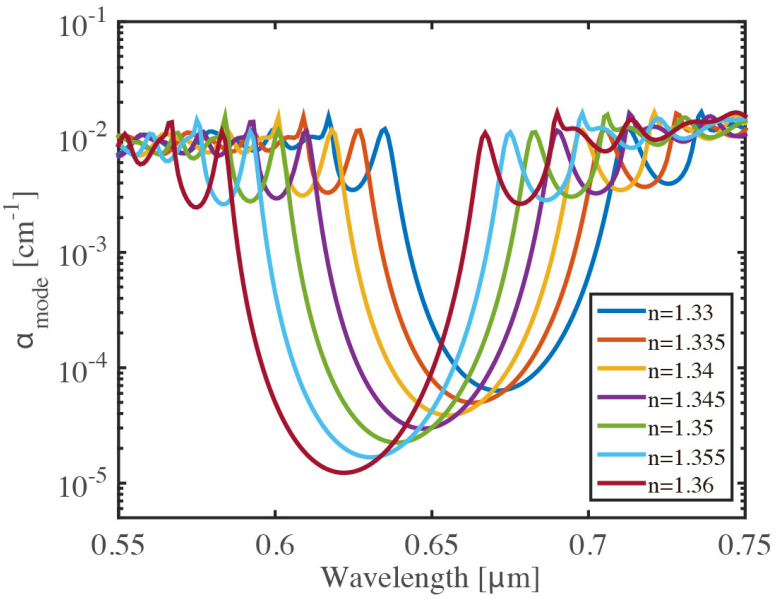


Figure 3.1 Simulated loss spectra of the fundamental mode ($HE_{11}$ mode) of the Bragg fiber filled with solutions with different concentrations.

In Fig. 3.2, we plot the bandgap center (point of lowest propagation loss) as a function of the fiber core refractive index, and a linear dependence is observed, which, at the same time,

shows excellent agreement with the calculation based on Equation 3.1. A spectral sensitivity of 1600nm/RIU is expected from our simulations. This sensitivity will be able to detect analyte refractive index with a resolution of $6\times10^{-5}$RIU, assuming a spectral shift of 0.1nm can be reliably resolved by the spectrometer.

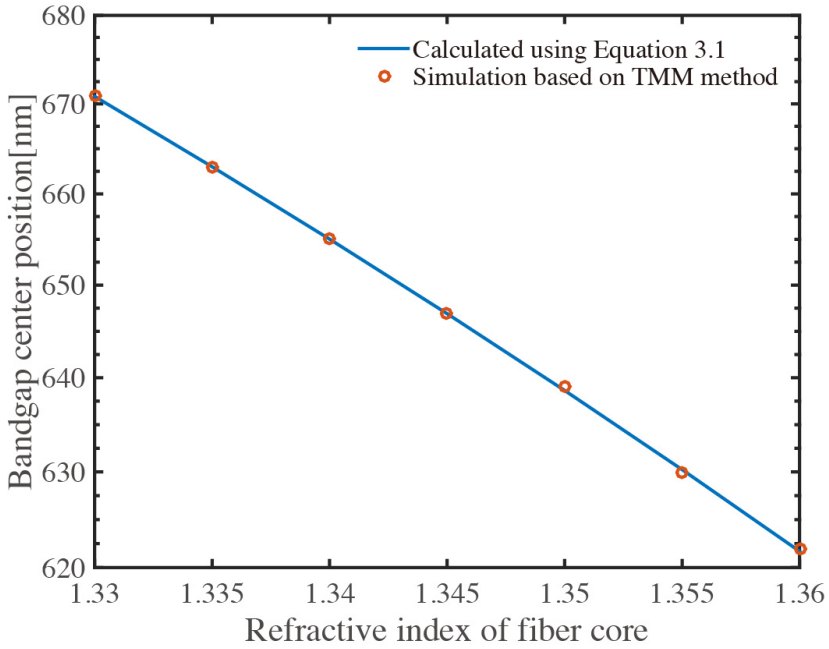


Figure 3.2 Bandgap center (point of lowest propagation loss) of the Bragg fiber obtained from the TMM simulation (red circles) and calculation based on Equation 3.1 (blue line) when the fiber core refractive index is varied from 1.33 to 1.36.

In order to fabricate the hollow-core Bragg fibers, we use a stack-and-draw technique [109]. In particular, we first fabricate a macroscopic preform by co-rolling commercial PMMA/PS films (each film has a thickness of 50μm). To enhance the mechanical robustness, the hollow preform is clad with a thick PMMA tube (thickness: 3mm), and then consolidated by heating it at 80°C under vacuum for one week. After fabrication of the preform, hollow-core Bragg fibers are manufactured by preform heating and drawing in an optical fiber drawing tower. Geometry of the final fiber can be controlled by adjusting the parameters in the drawing process, such as temperature distribution in the furnace, fiber drawing, and preform feed speeds, as well as the pressurization of the hollow core. In our experiment, we find that by simply controlling the drawn-down ratio via changing the drawing speed, we can control the bilayer thicknesses in the Bragg reflector, thus targeting specific bandgap positions. During the fiber drawing process, the

fiber diameter is monitored using a laser micrometer. In Fig. 3.3, we present the bandgap scalability of the hollow-core Bragg fibers (filled with water), by changing the fiber outer diameter from 800μm to 950μm. We note that with the increase of the fiber outer diameter, the bandgap position of the Bragg fiber shifts toward longer wavelengths. Transmission through ~15cm of such hollow-core Bragg fibers (filled with distilled water) is studied by coupling a broadband supercontinuum light source into the fiber core using an objective. Our observations reveal that, upon launching a broadband light, all the spectral components, which are not guided by the reflector bandgap of the Bragg reflector irradiate out in the first 1-3cm along the fiber length. Only a particular colour region guided by the bandgap is propagated to the fiber end, as shown in the bottom panel in Fig. 3.3. Therefore, by changing the periodicity, or equivalently the overall scale to which the fiber is drawn, we can target the bandgap positions at selectable wavelengths.

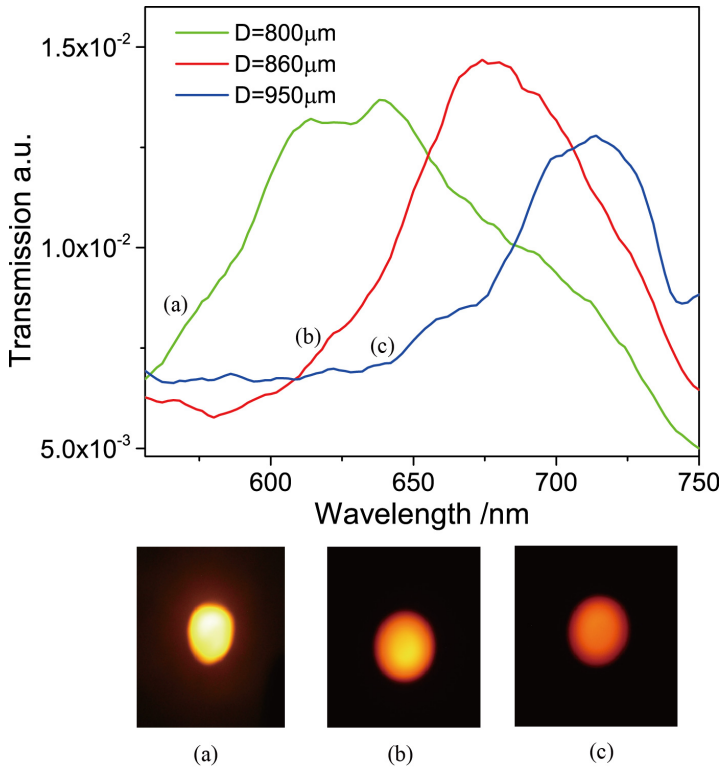


Figure 3.3 Scalability of the bandgap positions of the water-filled Bragg fibers by controlling the outer diameter. Bottom panel: Photographs of the transmitted light for the water-filled Bragg fibers with different outer diameters when they are excited by a supercontinuum light source.

## 3.3 Design and fabrication of THz Bragg waveguides using 3D stereolithography

Figure 3.4 shows the cross section of the THz waveguide used in our work, which features a hollow core surrounded by a periodic sequence of high/low refractive index multilayers, namely, the printing resin and air. The thickness of each layer is designed to be 463μm, with a predicted fundamental bandgap center at 0.2THz, according to the basic theory of Bragg fibers [214]. This frequency region is chosen due to the following reasons: first, there are no water vapor absorption lines in the 0.2-0.3THz region, and waveguide sensors operating in this range are, therefore, less influenced by the environmental conditions; second, a single mode Bragg waveguide operating in this frequency range (the corresponding wavelength is around 1.5mm) has a relatively large core size, which is an asset for practical sensing applications, as it simplifies the introduction of analyte into the waveguide core. Moreover, a relatively large waveguide core size is also essential for the efficient coupling of THz beams. The number of the bilayers in the Bragg reflector is ten. The light blue region in Fig. 3.4 represents a defect layer. The defect layer is formed by a supplementary material deposited on the inner surface of the waveguide core, which effectively modifies the thickness of the first layer in the reflector. In order to maintain the mechanical stability of the Bragg reflector, a set of micro-bridges are introduced into the waveguide cross section, as indicated in Fig. 3.4.

In order to fabricate the THz Bragg waveguides, we used a commercially available 3D printer (Pro 2, Asiga). 3D printing begins with a 3D model of the object, which is then digitized and sliced into model layers with a special software. The objects are built from photopolymer resins, which are liquid chemicals that can be solidified when they are exposed to ultraviolet light. By solidifying successive layers of photopolymer against each other, a physical model is built. This process is also called “stereolithography”. Currently, 3D printing has been widely used for rapid prototyping of microelectronic and optical devices.

The 3D stereolithography system used in this thesis has a transverse resolution of 50μm, and a longitudinal resolution of 1μm (along the waveguide length), which is sufficient for the fabrication of THz Bragg waveguides. This system can print objects with a maximum size of 96mm×54mm×200mm.

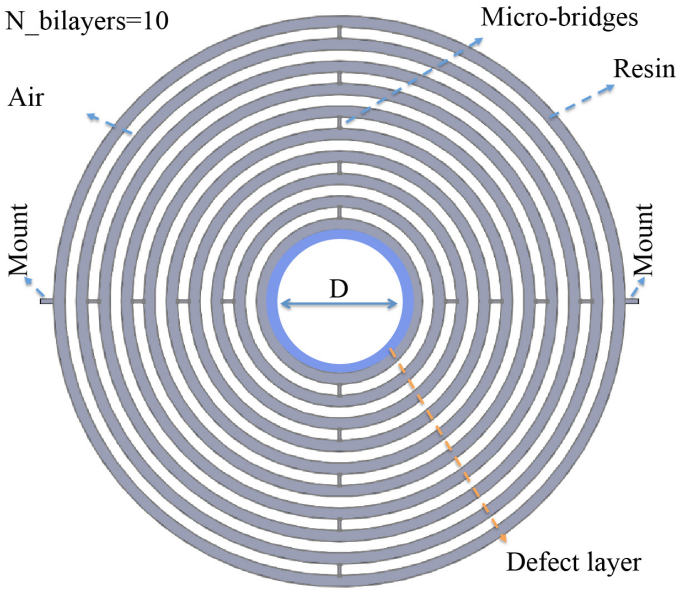


Figure 3.4 Schematic of the THz Bragg waveguide. The gray region and white region represent the high refractive index layer (printing resin) and low refractive index layer (air), respectively. The multilayers are kept together with micro-bridge structures distributed uniformly along the waveguide cross section. The number of bilayers is 10. The light blue region is a defect layer in the Bragg reflector. The defect layer is formed by a supplementary material deposited on the inner surface of a core, which effectively modifies the thickness of the first layer in the reflector.

## 3.4 Experimental setup for the characterization of liquid-core Bragg fiber sensors

The schematic of the experimental setup for the characterization of the liquid-core Bragg fiber sensors operating in the visible range is shown in Fig. 3.5. To integrate the hollow-core Bragg fiber in the setup, we use two opto-fluidic blocks, which enables both optical coupling and the flow of the target analytes. Specifically, the Bragg fiber tip is sealed hermetically in the horizontal channels of the opto-blocks with tread seal tape (or polytetrafluoroethylene tape). A thin glass window is attached at the other end of the horizontal channel to facilitate optical coupling into the fiber core. Each block also features a vertical channel, which is connected to the horizontal channel, thus allowing for a continuous fluidic injection of liquid analyte into the Bragg fiber. A syringe is used to pump the liquid analytes into the Bragg fiber core. During the

experiments, both ends of the fluidic channels are submerged into a water-filled beaker in order to avoid the existence of air bubbles in the sensing system, which would supress the fiber transmission. After pumping the liquid into the hollow-core Bragg fiber, a broadband supercontinuum beam is launched into one end of the liquid-core Bragg fiber using an objective, and the output spectrum of the fiber sensor is registered by a grating monochromator. The Bragg fiber used in the sensor has a core diameter of ~0.7 mm. Such a large core results in a short response time of the sensor, since the flow resistance decreases rapidly as the core radius increases. The experimental response time of the sensor is <1s, which represents an obvious advantage compared to other MOF sensors [107] (typical response time ~1 min/1 cm).

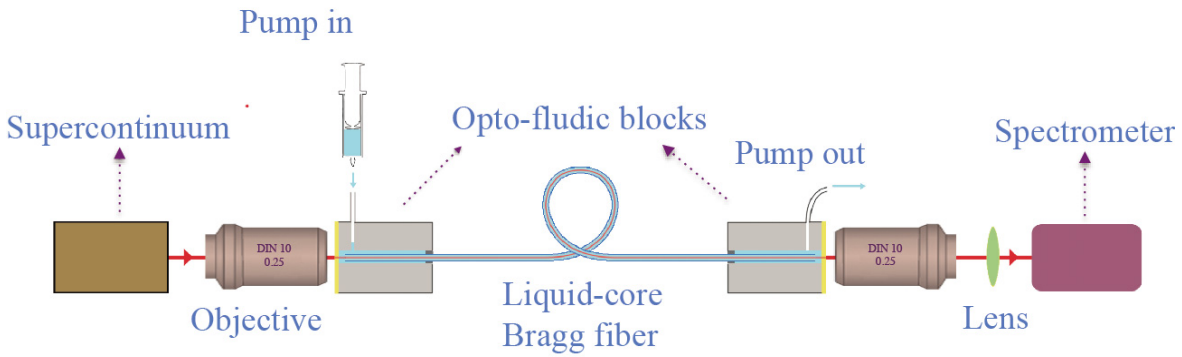


Figure 3.5 Experimental setup for characterizing the liquid-core Bragg fiber sensors operating in the visible range.

## 3.5 Experimental setup for characterizing the 3D printed THz Bragg waveguide sensors

### 3.5.1 Terahertz time domain spectroscopy (THz-TDS)

THz-TDS is emerging as an important tool to characterize the spectroscopic signatures and optical properties of samples in the terahertz range. In our THz-TDS setup, a femtosecond near-infrared (NIR) laser is used as the pump source and two identical low-temperature grown Gallium arsenide (LT-GaAs) photoconductive antennas are used as THz emitter and detector. A photoconductive emitter relies on the generation of photo-carriers, which are accelerated by a DC bias field, the carrier dynamics on a time scale of picosecond results in THz frequency radiation. In our system, we use an antenna with a dipole structure, which consists of two strip lines that are separated by a small gap. When a pump pulse with photon energy larger than the bandgap of the

semiconductor is focused onto the small gap between the electrodes, photo-carriers are excited. The photo-carriers are then accelerated and form a current flowing between the electrodes, thereby generating a linearly polarized light aligned in the direction of the current flow. Photoconductive detection of THz pulses relies on the same physical principles as photoconductive generation, while the only fundamental difference is that the electrodes are not biased. It is, instead, the incoming THz electric field that works as a time dependent bias field, which can be probed by measuring the current when a femtosecond laser pulse excites free carriers in the detector gap. In the setup, the NIR laser pulse is split into two parts by a beam splitter. One part is focused onto the photoconductive emitter to generate the THz pulse. After passing through the sample, the THz beam is recorded by the photoconductive detector. The other part goes through a variable delay line and ultimately terminates on the detector. The delay line allows the THz pulse to be mapped as a function of time. In the measurement, the detector is sensitive to the actual electric field of the THz beam. Both the amplitude and phase information can be retrieved by a point-by-point sampling of the THz pulse with the help of the variable delay line. Properties of the sample, such as absorption and refractive index, can be obtained from the detected amplitude and phase information, respectively. Therefore, THz-TDS provides more information than the conventional Fourier transform spectroscopy, which is only sensitive to the amplitude. More details about the THz-TDS experimental setup are presented in Chapter 6.

### 3.5.2 Continuous wave (CW) spectroscopy

Laser-based continuous-wave sources are recent developments in THz spectroscopy. This method uses two near-infrared lasers having slightly different center wavelengths to generate a beat signal that lies in the THz frequency range. The beat signal is then transformed into THz radiation by a so-called photomixer, which acts as a transmitter. The signal is coherently detected by a second photomixer (i.e., the receiver). This method offers several advantages, such as a broad accessible frequency range, frequency selectivity, and a much higher frequency resolution than that of TDS systems. The setup used in this work has two Distributed Feedback (DFB) lasers with slightly different center wavelengths and balanced power (~30mW for each laser) operating in the telecommunication region. The laser frequency can be tuned by controlling the temperature of the active medium as the period of the Bragg grating changes due to thermal expansion. A 50: 50 coupler combines and splits the two wavelengths equally into the emitter and

detector arm respectively. The generated THz waves, which are the frequency difference of the two lasers, are modulated with a bias voltage for lock-in detection. In order to measure the phase information, each arm is integrated with a fiber stretcher. The two stretchers operate with opposite signs, thus changing the optical path difference. Each fiber stretcher consists of a polarization-maintaining, single-mode fiber wound around a piezo actuator. More details about the CW setup are presented in Chapter 6.

# CHAPTER 4 ARTICLE 1：SIMULTANEOUS MONITORING THE REAL AND IMAGINARY PARTS OF THE ANALYTE REFRACTIVE INDEX USING LIQUID-CORE PHOTONIC BANDGAP BRAGG FIBERS

This chapter is based on the paper “Simultaneous monitoring the real and imaginary parts of the analyte refractive index using liquid-core photonic bandgap Bragg fibers”, which is published on Optics Express in 2015. I am the primary author of this paper, and the co-authors are Hang Qu and Maksim Skorobogatiy.

In this Chapter, we demonstrate simultaneous monitoring of the real and imaginary parts of the liquid analyte refractive index by using a hollow-core Bragg fiber. We apply this two-channel fiber sensor to monitor concentrations of various commercial cooling oils. The sensor operates using spectral monitoring of the fiber bandgap center wavelength, as well as monitoring of the fiber transmission amplitude at mid-bandgap position. The sensitivity of the fiber sensor to changes in the real part of the core refractive index is found to be 1460nm/Refractive index unit (RIU). By using the spectral modality and the effective medium theory, we determine the concentrations of the two commercial fluids from the measured refractive indices with an accuracy of ~0.57% for both low- and high-loss oils. Moreover, using an amplitude-based detection modality allows determination of the oil concentration with accuracy of ~1.64% for low-loss oils, and ~2.81% for the high-loss oils.

## 4.1 Introduction

Refractive index (RI) values of materials are related to their composition. Measurement of analyte refractive index is important in numerous scientific and industry applications, such as biochemical sensing, material purity determination, concentration prediction, physical/chemical process monitoring [1-4]. In particular, on-line monitoring of the solution concentrations, including heat transfer fluids, coolant, or other dilutions, is of significant importance in many industrial processes [5]. Liquid-core optical fibers are a very promising platform for refractive index sensing, as they inherently integrate optical detection with microfluidics, thus allowing for continuous on-line monitoring of liquid samples in a contained, highly integrated manner.

To date, a wide range of liquid-core optical fiber sensors has been developed for RI measurement. For example, several sensors based on liquid-core fibers with total internal reflection (TIR) guidance have been proposed and demonstrated [18, 19]. These sensors typically operate using an amplitude-based sensing modality in which the transmission intensity of the liquid-core fiber is interrogated as a function of changes in the refractive index of a test analyte. While these sensors are advantageous due to their simple structures and sensing principle, the difficulty in finding suitable cladding material with refractive index lower than those of aqueous solutions (n~1.33) limits TIR liquid-core sensors for industrial applications.

Using sensors based on hollow-core (HC) photonic crystal fibers (PCFs) constitutes an alternative to the fibers with TIR guidance [203-205]. A defining feature of the PCFs is the presence of micron-sized air holes running along its entire length, which permits accommodation of the biological and chemical samples in gaseous or liquid forms inside of the air holes in the immediate vicinity of the fiber core [15]. Photonic bandgap fibers (PBGFs), a subset of PCFs, are frequently used to build RI sensors. PBGFs sensors usually operate on a spectral-based detection modality. Variation in the real part of the analyte refractive index modifies the bandgap guidance of a fiber, leading to spectral shifts in the fiber transmission spectrum. The spectral shifts can be used to extract changes in the refractive index of a test analyte. In [107], the authors experimentally demonstrated highly sensitive liquid core RI sensors based on commercial HC-PBGFs that feature a hollow core surrounded by a porous periodic cladding. A sensitivity of ~5000 nm/RIU was reported. However, fabrication of the HC-PBGFs used by the authors requires sophisticated drawing technique, and the fiber is expensive (thousands of dollars per meter). Moreover, these sensors require a relatively long response time for inducing the test analytes into the micron-sized holes of the PBGFs [~10 min for 20cm-long PBGFs].

Hollow-core photonic bandgap Bragg fibers (or simply hollow-core Bragg fibers), which are a subset of PBGFs, could also be used for sensing of refractive index of a liquid analyte. In their cross section, a hollow core is surrounded by a periodic sequence of micron-sized layers of different materials in the cladding. Due to the relatively large core of Bragg fibers, the response time could be shortened to ~1s. In [110], K. J. Rowland et al. reported a HC high-refractive-index- contrast Bragg fiber sensor with the sensitivity ~330nm/RIU. More recently, our group has reported several HC low-RI-contrast Bragg fiber sensors [111]. We showed that such Bragg fiber sensors offer superior performance in detection of changes in the real part of the refractive index

of a liquid analyte by monitoring the spectra shift of the transmission spectrum. The sensitivity of our sensor, compared to that of the sensor reported in [110], is considerably improved (~1400nm/RIU). In fact, we have argued in [111] that low-RI-contrast Bragg fibers are most suitable for liquid-core sensors, while high-RI-contrast Bragg fibers are most suitable for gas-core sensors.

In this paper, we explore the capability of the hollow core Bragg fibers to simultaneously monitor the real and imaginary parts of the analyte refractive index. We then apply our fiber sensor to monitor the concentrations of various commercial cooling oils. The sensing strategy relies on a two-channel sensing modality that simultaneously interrogates the bandgap center position of the Bragg fiber, as well as the fiber transmission amplitude at the bandgap center (the point of fiber lowest propagation loss). Both measurands are highly sensitive to the complex reflective index of the analyte filled in the fiber core, thus enabling efficient determination and cross-correlation with the concentration of cooling oils. The main advantage of the two-channel sensor compared to a single channel sensor is that, in principle, the measurement error can be significantly reduced if the two channels are independent and they offer comparable detection errors.

The fiber sensor is first calibrated using NaCl solutions of different concentrations. By measuring the spectral shift of the fiber bandgap, the sensitivity of the fiber sensor to changes in the real part of the core refractive index is found to be ~1460nm/RIU, which translates into 2.6nm/w% sensitivity to changes in NaCl concentration. Additionally, using changes in the mid-bandgap transmission amplitude of the fiber sensor, sensitivity of 3.55dB/w% for NaCl solutions is demonstrated. We then apply this fiber sensor for monitoring the concentrations of various cooling oils including heat transfer fluid and sawing fluid. By using the spectral modality and the effective medium theory, we determine the concentrations of the two commercial fluids from the measured refractive indices with an accuracy of ~0.57% for both low- and high-loss oils. Moreover, we also demonstrate that using an amplitude-based detection modality allows determination of the oil concentration with an accuracy of ~1.64% for the low-loss oils and an accuracy of ~2.81% for the high-loss oils. The presented fiber sensor can be used for online monitoring of concentration of many industrial fluids such as heat transfer fluids, sawing fluids, and other industrial dilutions with sub-1%v accuracy.

## 4.2 Operation principle of the liquid-core Bragg fiber sensors

### 4.2.1 Sensing mechanism for detection of the real part of an analyte refractive index

The Bragg fiber used in our sensor features a large hollow core (diameter ~700μm) surrounded by periodic sequence of high- and low-refractive index layers, namely polystyrene (PS)/polymethyl-methacrylate (PMMA) Bragg reflector with layer refractive indices of 1.58 and 1.49 at 589nm, respectively. The cross section of the Bragg fiber sensor is shown in Fig. 4.1. The thickness of each PMMA/PS multi-layer is approximately 310nm.

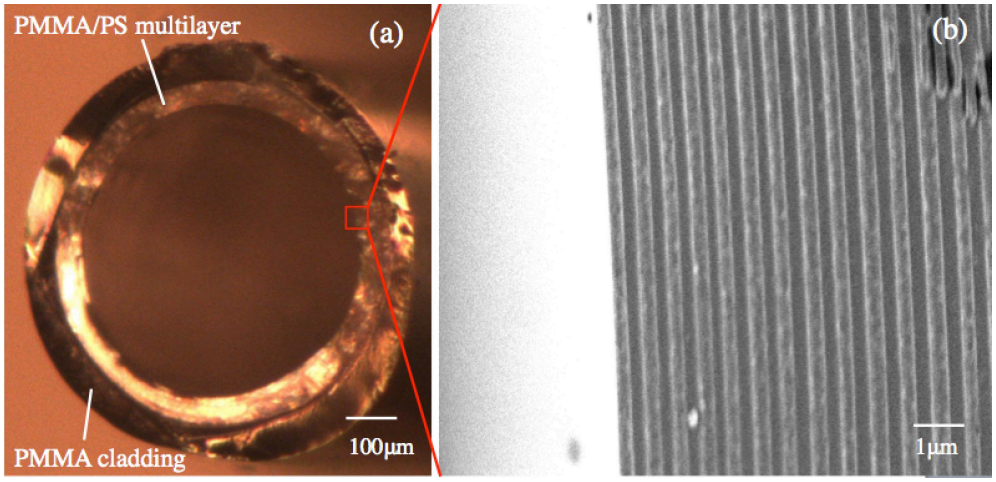


Figure 4.1 (a) Cross section of the fiber sensor under microscope. (b) Cross section of the Bragg reflector taken by a scanning electron microscope (SEM), which features alternating polystyrene (PS) /poly-methacrylate (PMMA) layers, with thickness of approximately 310nm.

Bragg fibers confine light in their hollow cores by photonic bandgap effect. When a broadband light is launched into the analyte-filled core of a Bragg fiber, only the light with frequencies within the fiber bandgap of Bragg reflector will be confined and guided in the fiber core, while the light with frequencies outside of the bandgap will irradiate out in the first several centimeters of the fiber. From the basic theory [113] of the Bragg fibers, the resonant center wavelength $\lambda_g$, of the fiber fundamental bandgap can be calculated as:

$$\frac{\lambda_g}{2} = d_l\sqrt{\varepsilon_l^r - \varepsilon_c^r} + d_h\sqrt{\varepsilon_h^r - \varepsilon_c^r} \tag{4.1}$$

where, $d_l$ and $d_h$ are the thicknesses of the low- and high- refractive index layers in the Bragg reflector, $\varepsilon_l^r$ , $\varepsilon_h^r$ are the real parts of the corresponding dielectric constants, while $\varepsilon_c^r$ is the real part of the dielectric constant of the core material.

Equation (4.1) is valid based on the assumption that the real part of any dielectric constant is much larger than its imaginary part. From Eq. (4.1), it follows that variation in the refractive index of the fiber core would modify spectral position of the Bragg fiber bandgap. In fact, one observes a shift of the fiber transmission spectrum towards shorter wavelengths for larger values of the core dielectric constant. Therefore, changes in the real part of the refractive index of a test analyte filled in the fiber core could be inferred from the displacement of the transmission spectrum, which constitutes the spectral-based sensing principle of a Bragg fiber sensor.

### 4.2.2 Sensing mechanism for detection of the concentration of additives in an analyte

In many practical applications that involve mixtures of fluids, one is not so much interested in the refractive index of a mixture, but rather in the relative concentrations of the constituent fluids. In what follows, we consider a particular problem of monitoring concentration of cooling oils in aqueous mixtures (suspensions). In this case, a small amount of cooling oil together with surfactants is added into water to form a suspension. In such suspensions, spherical oil particles are deeply sub-wavelength. As a result, such suspensions appear clear and without any obvious phase separation, as shown in Fig. 4.2 (a). At the same time, many oils are colored emulsions and have significant frequency-dependent absorption, as shown in Fig. 4.2 (b). In this section, we first show that the oil concentration could be inferred by using the spectral modality for the detection of the mixture refractive index and the effective medium theory for relating the oil concentration to the mixture refractive index. We then demonstrate an amplitude-based detection modality of the Bragg fiber sensor for determining the oil concentration in a suspension by analyzing the transmission amplitude of an analyte-filled Bragg fiber at the bandgap center position.

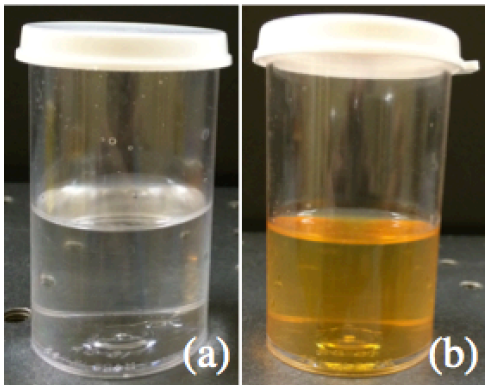


Figure 4.2 (a) Low-loss cooling oil (heat transfer fluid), (b) High-loss cooling oil (sawing fluid).

### 4.2.3 Oil concentration detection using the spectral modality

The effective medium theory relates macroscopic properties of a mixture with its composition, and it has been widely used for the modeling of various optical, electrical, and thermal properties of mixtures [206-210]. According to the effective medium theory, the effective dielectric constant of a mixture can be written as a function of the dielectric constant and the corresponding concentrations of its sub-components. For suspensions featuring small-to-medium concentrations (0-30%) of oil droplets in water, we could use Bruggeman (BG) formulation [20, 211, 213] to describe the dependence of the complex dielectric constant of the suspension on the oil concentration:

$$c \cdot \frac{\varepsilon_o - \varepsilon_{eff}}{\varepsilon_o + 2 \cdot \varepsilon_{eff}} + (1-c) \cdot \frac{\varepsilon_w - \varepsilon_{eff}}{\varepsilon_w + 2 \cdot \varepsilon_{eff}} = 0 \tag{4.2}$$

where $\varepsilon_{eff}$ is the complex effective dielectric constant of the oil suspension in water, $\varepsilon_o$ and $\varepsilon_w$ are the complex dielectric constants of the pure bulk oil and water, respectively, and $c$ is the volume concentration of oil. If the bulk refractive indices of water and oil are known (note that $\varepsilon \approx n^2$, considering that the imaginary part of the dielectric constant is much smaller than the real part of the dielectric constant for the analytes involved in this work), using Eq. (4.2) one can calculate the concentration of oil in a suspension from the effective refractive index of a suspension. In turn, the effective refractive index of a suspension can be measured by using the spectral modality of the Bragg fiber sensor, as discussed in Section 4.2.1.

### 4.2.4 Oil concentration detection using the amplitude modality

When the Bragg fiber is filled with oil suspensions, the propagation loss of the fiber can be considered approximately as the sum of the fiber radiation loss and the absorption loss of the fiber core material.

The radiation loss is a direct consequence of the leaky-mode guidance in a core with refractive index smaller than that of the cladding. The radiation loss of Bragg fibers is frequency dependent. Consider, for example, a Bragg fiber with a certain number of bilayers in its Bragg reflector and a large diameter of a fiber core (much larger than the wavelength of light). According to Eq. 4.47 in [214], at the wavelength corresponding to the bandgap center, the radiation loss coefficient of the fundamental core-guided mode $\alpha_{rad}$ can be written as:

$$\alpha_{rad} = \Re(\mathrm{n}_c^r, \mathrm{n}_h^r, \mathrm{n}_l^r, \mathrm{d}_c, \mathrm{d}_h, \mathrm{d}_l) \tag{4.3}$$

where, $\Re$ is a function dependent on the real part of the refractive index of the fiber core, as well as the geometry parameter and refractive indices of the low- and high- reflective index layers in the Bragg reflector.

When the concentration of a coolant increases, the refractive index of the coolant solution also increases. Consequently, the core refractive index of the liquid-filled Bragg fiber becomes closer to that of the fiber cladding. In the limit when the core refractive index becomes higher than that of the fiber cladding, no radiation losses will occur as the guidance regime will become total internal reflection rather than bandgap guiding. Therefore, the fiber radiation loss would decrease with an increase of the core refractive index; in other words with an increase in the coolant concentration.

Absorption of the fiber core material also affects the fiber propagation loss. Consider, for example, filling the Bragg fiber with an analyte, which is a cooling oil diluted in water at concentration $c$. The effective absorption coefficient of such mixture, $\alpha_{eff}$ can be written as:

$$\alpha_{eff} = \Phi_o(\mathrm{c}) \cdot \alpha_o + \Phi_w(\mathrm{c}) \cdot \alpha_w \tag{4.4}$$

where $\alpha_o$ and $\alpha_w$ are the material absorption coefficients of the pure cooling oil and water, respectively. The detailed expressions for $\Phi_o(c)$ and $\Phi_w(c)$ are presented in the Appendix section.

With the fiber radiation loss and the fiber core absorption given by Eq. (4.3) and Eq. (4.4), we now can write the transmission of an analyte-filled Bragg fiber at the bandgap center as:

$$T(\lambda) = I/I_0 = e^{-(\alpha_{rad}+\alpha_{eff})\cdot L} = e^{-[\Re+\Gamma\cdot(\Phi_o(c)\cdot\alpha_o+\Phi_w(c)\cdot\alpha_w)]\cdot L} \tag{4.5}$$

where $L$ is the length of the Bragg fiber, and $I$ and $I_0$ are the output and input intensities of light related to the fiber sensor. $\Gamma$ is the confinement factor, which is a measure of the overlap between the optical mode and the fiber-core material. For a large-core Bragg fiber in our sensor, the optical mode can be considered completely confined in the core region, and $\Gamma$ is very close to 1.

When the Bragg fiber is filled with a solution of low-loss cooling oil, little or no additional absorption loss occurs when increasing the concentration of the oil. At the same time, the fiber radiation loss decreases when increasing the oil concentration due to an increase in the mixture refractive index. Therefore, the total effect of an increase in the cooling oil concentration would be an enhancement in the Bragg fiber transmission, as shown in Fig. 4.3 (a). However, when using high-loss cooling oils (those with a color tint), an increase in the oil concentration leads to a significant increase in the absorption loss of the liquid core. This, in turn, can be more pronounced than the decrease in the radiation loss, thus leading to suppression of transmission through the liquid-core Bragg fiber, which results in higher attenuation at higher oil concentration, as shown in Fig. 4.3 (b). In both cases, positions of the bandgap centers shift to shorter wavelengths with an increase in the oil concentration, according to Eq. (4.1).

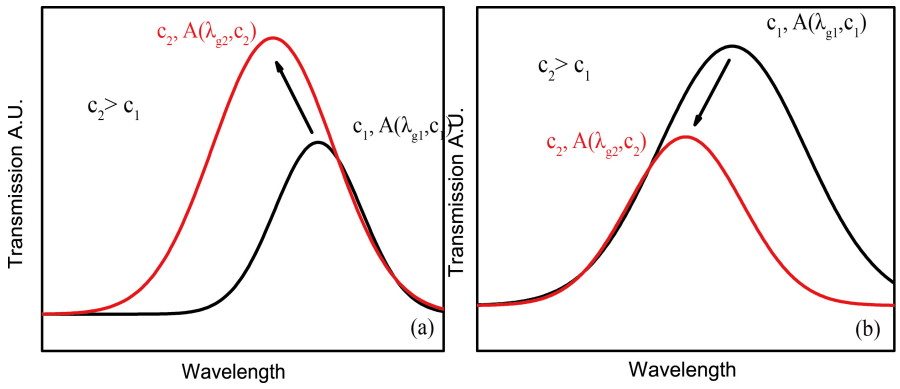


Figure 4.3 Schematic of the two possible behaviors of the Bragg fiber spectra when increasing the concentration of the cooling oil in the liquid-filled fiber core. (a) Low-absorption-loss cooling oil, (b) High-absorption-loss cooling oil.

In order to measure the concentration of an unknown suspension using the amplitude modality, the Bragg fiber sensor should be first calibrated using a set of reference solutions (such as NaCl solutions) with known bulk absorption losses. During calibration, the transmission spectra of the Bragg fiber sensor filled with reference solutions are recorded. After calibration, the sensor can be used to measure the concentration of an oil suspension by comparing the transmission spectrum of the oil-filled Bragg fiber to the spectra of the fiber filled with the reference solutions. If the bandgap center position of the oil-filled Bragg fiber matches that of the Bragg fiber filled with a specific reference solution, the real parts of the refractive index of these two solutions would be identical as follows from Eq. (4.1). Moreover, we note that the radiation losses of the Bragg fiber filled with the oil suspension and the reference solution would be also identical as long as they have the same bandgap center wavelengths, as seen from Eq. (4.3). Therefore, the difference in the transmission intensities of the fiber filled with the oil suspension and the reference solution sharing the same bandgap center wavelength are only attributed to the different absorptions of the liquids filling the fiber core. By comparing the transmission of the Bragg fiber filled with the oil suspension to the transmission of the fiber filled with a reference solution (NaCl solution) for which the bandgap center wavelength $\lambda_g$ is the same, we have:

$$\begin{aligned} T_{ref}(\lambda_g) &= e^{-(\Re+\Gamma\cdot\alpha_{ref})\cdot L} \\ T_{oil}(\lambda_g) &= e^{-[\Re+\Gamma\cdot(\Phi_o(c)\cdot\alpha_o+\Phi_w(c)\cdot\alpha_w)]\cdot L} \\ \Phi_o(c)\cdot\alpha_o + \Phi_w(c)\cdot\alpha_w &= \alpha_{ref} + \frac{1}{\Gamma\cdot L}\cdot In(\frac{T_{ref}(\lambda_g)}{T_{oil}(\lambda_g)}) \end{aligned} \tag{4.6}$$

where, $T_{ref}(\lambda_g)$ and $T_{oil}(\lambda_g)$ refer to the transmission of the Bragg fiber filled with the reference solution and the oil solution to be measured at the same bandgap center wavelength $\lambda_g$, $\alpha_{ref}$ is the absorption of the reference solution, and *c* is the concentration of the test oil. Note that $\alpha_{ref}$, $\alpha_o$ and $\alpha_w$ at wavelength $\lambda_g$ should be measured using, for example, a cut-back method [212]. Based on Eq. (4.6), one could then calculate the concentration of the oil suspension by solving a non-linear equation.

## 4.3 Experimental setup and calibration of the Bragg fiber sensor

### 4.3.1 Experimental setup

The experimental set-up is shown in Fig. 4.4. The fiber sensor is integrated into the set-up using two opto-fluidic blocks, which enable both optical coupling and flow of the target analytes. After pumping liquid analyte into the sensor, a beam from a broadband supercontinuum source is launched into one end of the fiber core using an objective. The transmitted spectrum is registered by a grating spectrometer. The experimental set-up is kept the same in the subsequent measurements to guarantee the same illumination, coupling, and environmental conditions.

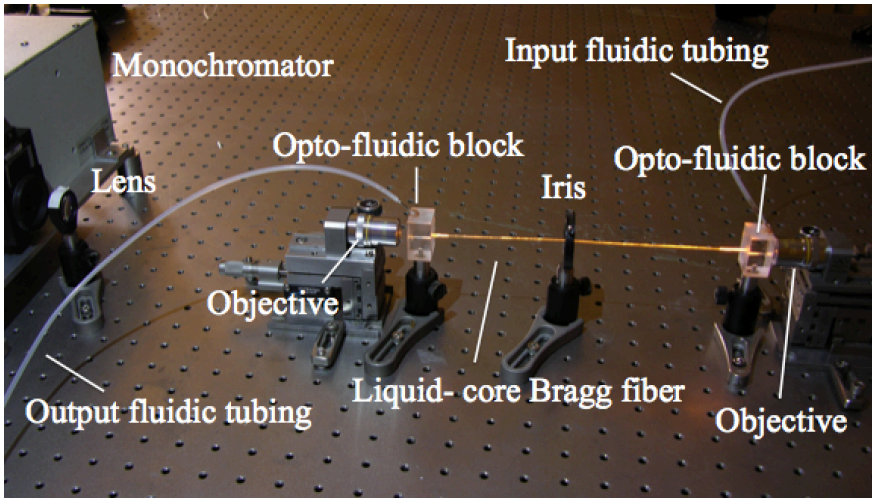


Figure 4.4 Experimental set-up for the characterization of the fiber sensor. The 24cm long Bragg fiber is integrated into the set-up using two opto-fluidic blocks. A broadband supercontinuum beam is launched into one end of the liquid-core Bragg fiber using an objective, and the output spectrum of the fiber sensor is registered by a grating monochromator.

### 4.3.2 Calibration of the Bragg fiber sensor with NaCl solutions

A calibration measurement of the Bragg fiber sensor is first carried out using a set of NaCl solutions with the weight concentrations ranging from 0% to 10% with a 2% increment step. The RIs of NaCl solutions are obtained from [215]. As shown in Fig. 4.5 (a), the experimental transmission spectra feature a blue shift as the RIs of the NaCl solutions filling the core increase with increased concentration of NaCl. This can be easily rationalized using Eq. (4.1) by noting that higher concentrations of NaCl in water lead to higher refractive indices of the resultant

solutions. A spectral shift of around 26 nm is observed when the refractive index of the core material increases from 1.333 to 1.3505 (with corresponding concentration from 0%w to 10%w), as is shown in Fig. 4.5 (b). The spectral sensitivity is thus found to be ~1460nm/RIU, which translates into 2.6nm/w% sensitivity to changes in the NaCl concentration. The demonstrated sensitivity is comparable with those of the recently reported fiber-based refractive index sensors [216-219].

Moreover, the transmission amplitude increases with the increase of the refractive index of the fiber core. Figure 4.5(c) shows the transmission amplitude at the point of the lowest propagation loss as a function of the refractive index of the fiber core. From the linear fit in Fig. 4.5(c), the amplitude sensitivity of the sensor is 301.7 dB/RIU, which translates into a sensitivity of 3.55dB/w% for NaCl solution. In the following sections, we will use the obtained calibration spectra, and the linearly fitted spectral and amplitude data presented in Fig. 4.5, in order to measure the refractive index and concentration of the unknown aqueous mixtures.

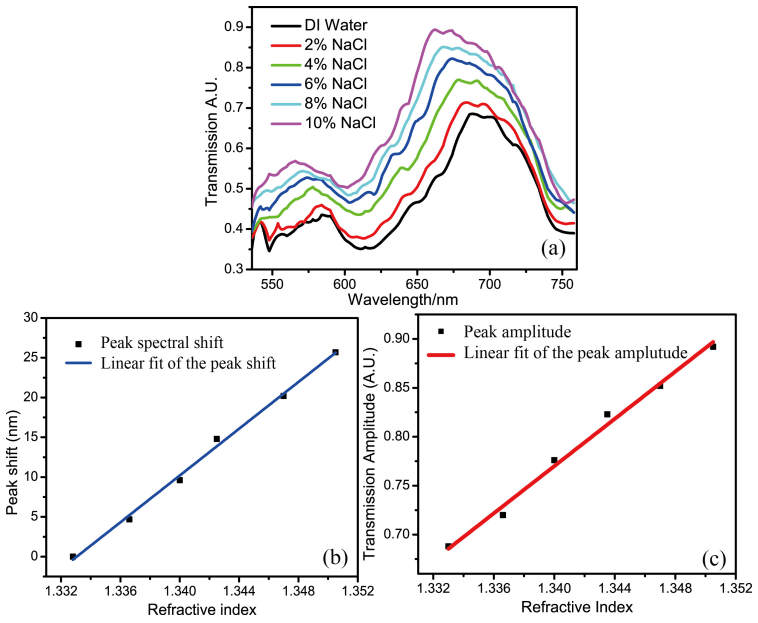


Figure 4.5 (a) Experimental transmission spectra of the ~24cm long Bragg fiber filled with NaCl solutions. The weight concentrations (wt.%) and the corresponding RIs of the NaCl solutions are listed as following. DI water: 1.333, 2%: 1.3366, 4%: 1.3400, 6%: 1.3435, 8%: 1.3470, 10%: 1.3505. (b) Spectral shifts of the fiber maxima transmission peaks obtained from the experimental measurements and their linear fit. (c) Transmission amplitudes at the maxima transmission peaks obtained from the experimental measurements and their linear fit.

### 4.3.3 Measurements of absorption coefficients of pure oil, water and reference solutions

In order to profit from a two-channel modality for the determination of the oil concentration, we have to perform both spectral Eq. (4.1) and amplitude Eq. (4.6) measurements. The latter requires knowledge of the bulk absorptions of the pure oil, water, and NaCl reference solutions. In this section, we present a cut-back technique to measure the required absorption coefficients.

According to a cut-back technique, losses of the two identically prepared material samples of different lengths have to be measured in order to determine the bulk absorption coefficient of the material. Then, the ratio of the transmitted intensities through the samples of different lengths ($L_1, L_2$) at wavelength $\lambda$ is:

$$\frac{I_{liquid}(\mathrm{L}_1,\lambda)}{I_{empty}(\mathrm{L}_1,\lambda)} \Big/ \frac{I_{liquid}(\mathrm{L}_2,\lambda)}{I_{empty}(\mathrm{L}_2,\lambda)} = e^{\alpha_{abs}\cdot(\mathrm{L}_2-\mathrm{L}_1)} \tag{4.7}$$

where the transmitted intensity through the empty tube $I_{empty}$ is used as a reference signal. Rewriting Eq. (4.7), one can calculate the absorption coefficient as:

$$\alpha_{abs}(\lambda) = \frac{In\left(\frac{I_{liquid}(\mathrm{L}_1,\lambda)}{I_{liquid}(\mathrm{L}_2,\lambda)} \cdot \frac{I_{empty}(\mathrm{L}_2,\lambda)}{I_{empty}(\mathrm{L}_1,\lambda)}\right)}{L_2 - L_1} \tag{4.8}$$

The experimental set-up for absorption measurement using a cut-back technique is illustrated in Fig. 4.6 (a). We use three rectangular containers of different lengths (5cm, 10cm, and 15cm) in our measurements. From the transmission spectra for each tube length and the corresponding reference measurements, one can calculate the wavelength dependent absorption coefficient using Eq. (4.8). An average absorption coefficient is calculated from several possible combinations of the different sample lengths in Eq. (4.8).

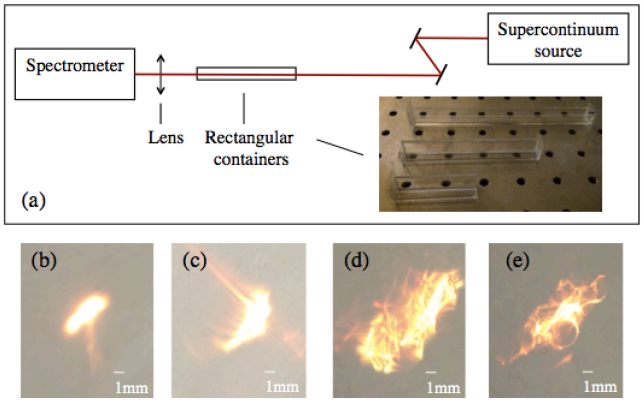


Figure 4.6 (a) Experimental set-up for bulk absorption measurements using a cut-back technique, inset: containers of different length (5cm, 10cm, 15cm). (b) and (c) Optical beam output spot at the end-face of a container filled with the low-loss heat-transfer fluid. (d) and (e) Optical beam output spot at the end-face of a container filled with the high-loss sawing fluid. During measurements, the output spots at the end-face of the container are somewhat distorted and vary with time, the time intervals between (b) and (c), as well as (d) and (e) are both five minutes.

In Fig. 4.7 (a), we plot the measured absorption coefficients of distilled water and a set of NaCl solutions at concentration of 3%, 6%, and 9% (by weight) from 650nm to 700nm with interval of 2nm. We note that the experimental values of absorption coefficients measured using a cut-back method in this work are 1.5 to 1.8 times higher than the values reported in [220-222]. This is probably due to the effect of unequal coupling into the spectrometer when the containers are filled with solutions of different refractive indices.

From Fig. 4.7(a), we can extract the salinity correction coefficient for water absorption. Thus, the absorption coefficient of NaCl solution at any concentration can be calculated [220]. In Figs. 4.7(b) and (c), we plot the absorption coefficients of the low-loss cooling oil (heat transfer fluid), and the high-loss cooling oil (sawing fluid). During the measurement, we notice that the optical beam output spots at the end-face of the container are somewhat distorted and vary with time, as it is shown in Figs. 4.6(b)-(e). This is most probably due to certain microscopic movement, and relaxation dynamics of the cooling oils.

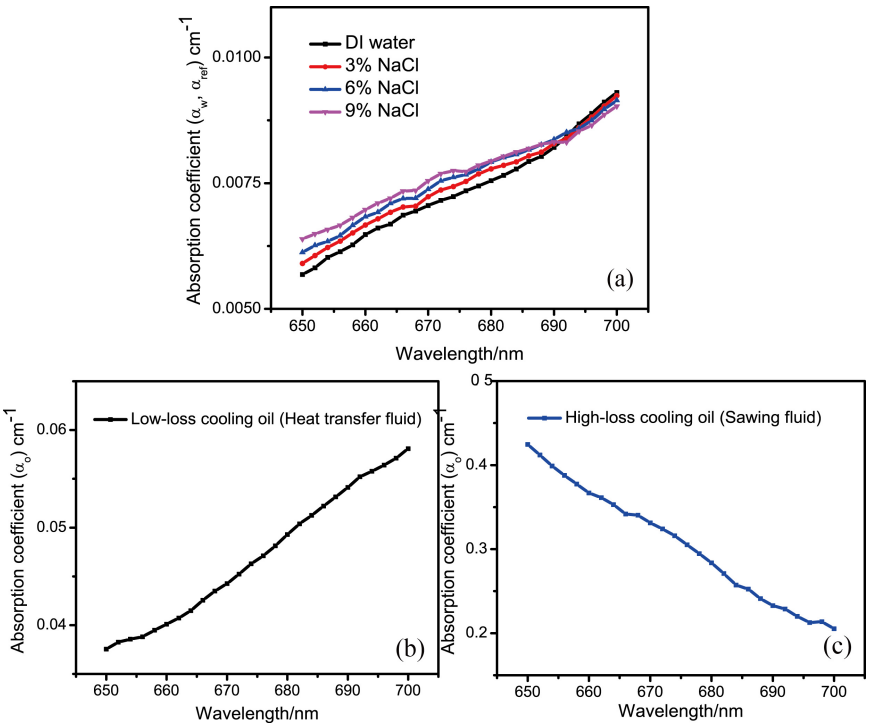


Figure 4.7 (a) Absorption coefficients of distilled water and NaCl solutions at concentrations of 3%, 6%, and 9% (by weight) measured using a cut-back technique. (b) Absorption coefficients of the low-loss-absorption oil (heat-transfer fluid) measured using a cut-back technique and (c) Absorption coefficients of the high-absorption-loss oil (sawing fluid) measured using a cut-back technique.

## 4.4 Two-channel characterization of the concentrations of heat transfer fluids

After the sensor calibrations described in Section 4.3, we use it to first measure the real part of the refractive index of the cooling oil suspension by employing the spectral modality. We choose, as the first analyte, a commercial heat-transfer fluid (Dynalene PG, US, shown in Fig. 4.2 (a)) at three different concentrations 5%, 10% and 15% (by volume). As shown in Fig. 4.8 (a), the transmission spectra show a blue shift of 7.2nm, 17nm and 24.7nm, compared to the transmission spectrum of the Bragg fiber filled with water. Based on the linear fit of the refractive indices of the reference solutions presented in Fig. 4.5 (b), we estimate the real part of the refractive indices of these heat-transfer fluids to be 1.3380, 1.3432, and 1.3492, respectively. These measured values show a good agreement with the reference data provided by the supplier as shown in Fig. 4.8 (b).

We then reconstruct the concentrations of heat-transfer fluids with the algorithm based on the effective medium theory presented in Section 4.2.3. Substituting the refractive indices of the heat-transfer fluids in to Eq. (4.2), we calculate the concentrations of the corresponding analytes based on the BG model. In Fig. 4.8 (c), we plot the experimental concentration and the concentration predicted by the BG model as a function of the refractive index. The reconstruction accuracy in determining the fluid concentration in this case is ~0.42% (relative accuracy of 2.8%).

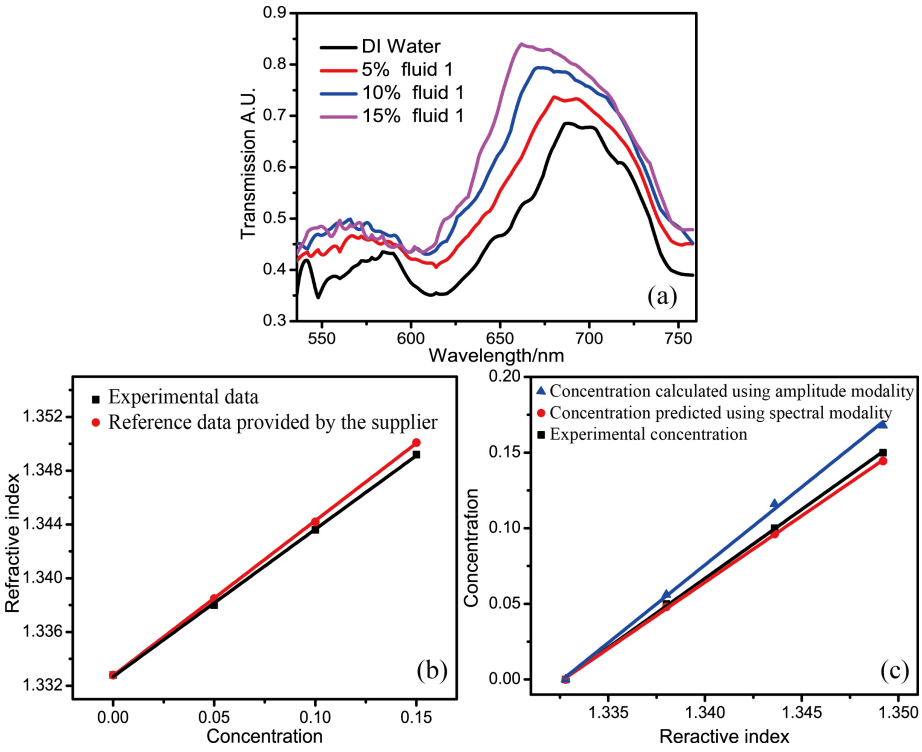


Figure 4.8 (a) Experimental transmission spectra of the 24cm long Bragg fiber filled with heat-transfer fluid at different concentrations (by volume). (b) Comparison of the refractive indices measured in experiment and the reference data provided by the supplier. (c) Comparison of the experimental concentrations with the concentrations predicted using the spectral measurement modality and the BG model, as well as concentrations calculated using the amplitude-based detection modality.

We now analyze the transmission amplitudes of the Bragg fiber filled with the oil suspensions. From the previous experiment, we have established that suspensions of heat-transfer fluid at concentrations of 5%, 10%, and 15% have the same refractive indices as that of NaCl solution at concentrations of 3%, 6.4%, and 9.5%, respectively. Note that the transmission amplitude of the Bragg fiber filled with NaCl solutions could be estimated based on the linear fit

shown in Fig. 4.5 (c). The absorption coefficients of the pure heat-transfer fluid and the reference NaCl solutions have been measured in Section 4.3.3. Using Eq. (4.6), we can now calculate concentrations using the amplitude modality. The data is presented in Fig. 4.8 (c). The accuracy in determination of oil concentration is found to be ~1.64%. We note that the error is mainly due to two reasons. First, in our theoretical calculation, the scattering loss is assumed to be negligible. However, in practice, small particles (such as dust particles) or air bubbles may be introduced during fluid pumping, which leads to errors in the measurement of transmission amplitude. Second, there is a certain error that comes from the cut-back measurement of the absorption coefficient of the cooling oil. As we illustrated in Section 4.3.3, the optical beam output spot at the end-face of the container varies with time when measuring the absorption coefficient, due to certain microscopic movement and relaxation dynamics of the cooling oil.

## 4.5 Two-channel characterization of the concentrations of sawing fluids

Many commercial oils are colored emulsions, which have frequency dependent absorption. In this experiment, we choose as a test analyte commercial sawing fluid (Lenox, US, as shown in Fig. 4.2 (b)) that has a yellow tint upon visual examination. The transmission spectra of the fiber sensor are shown in Fig. 4.9 (a). Despite the strong absorption loss, we see that the spectral features (transmission peaks) in the transmission spectrum remain well pronounced. Using the linear fit in Fig. 4.5 (b), the refractive indices of the emulsions are estimated to be 1.3332, 1.3342, 1.3351, 1.3375, when volume concentrations of sawing fluid are 1%, 3%, 5% and 10%, respectively. These experimentally measured values of the refractive index are in good agreement with the calibration data provided by the fluid suppliers as shown in Fig. 4.9 (b).

Using the effective medium theory, we can then extract sawing fluid concentrations from the measured values of the refractive index by using the BG model. Fig. 4.9 (c) shows the experimental concentrations and concentrations predicted by the BG model as a function of the refractive index. The reconstructed accuracy in this case is ~0.57%.

We then apply the amplitude modality to determine the concentrations of sawing fluids using the same methodology as presented in Section 4.4. In Fig. 4.9 (c), we plot the calculated concentrations by the amplitude modality and the experimental concentrations as a function of the refractive index. The accuracy in this case is found to be ~2.81%, which is worse than that for

a low-loss heat-transfer fluid. The primary reason is due to low precision in the measured value of the bulk absorption loss of the sawing fluid when using a cut-back method.

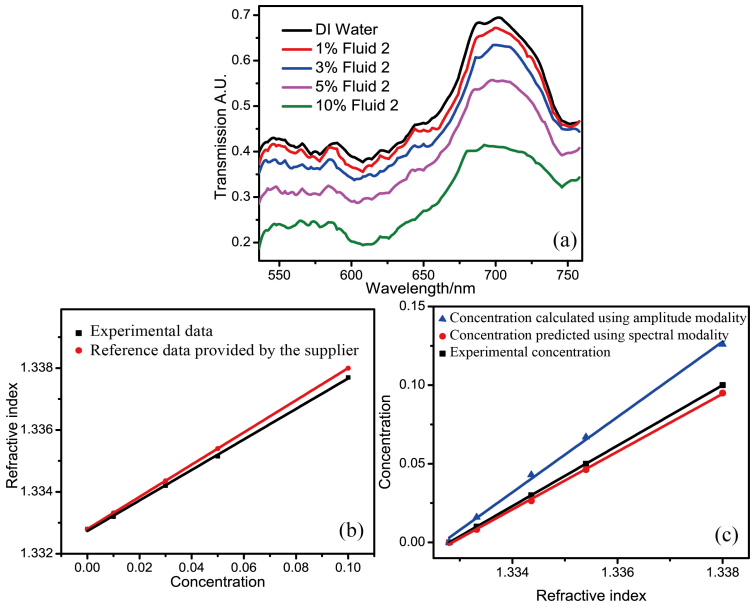


Figure 4.9 (a) Experimental transmission spectra of the 24cm long Bragg fiber filled with sawing fluids at different concentrations (by volume). (b) Comparison of the refractive indices measured in experiment and the reference data provided by the supplier. (c) Comparison of the experimental concentrations with the concentrations predicted by the spectral modality and the BG model, as well as the concentrations calculated using the amplitude-based detection modality.

## 4.6 Discussion

In this paper, we proposed two detection modalities for monitoring the concentrations of commercial cooling oils by analyzing the bandgap center position and transmission amplitude at the mid-bandgap of the analyte-filled Bragg fiber. First, when using the spectral-based detection modality, oil concentration could be inferred from the suspension refractive index by using the Bruggeman effective medium theory. Alternatively, when using the amplitude detection modality, oil concentration could be found by fitting changes in the suspension absorption losses and comparing them to the loss of a reference solution.

In principle, using multiple-channel detection modalities for measuring an experimental value could enhance the detection accuracy, since the measurement uncertainty could become smaller by a factor of $1/\sqrt{N}$, when $N$ detection channels with comparable detection errors are

used. However, because of unstable optical output of the cooling oils when measuring the absorption coefficients using a cut-back technique, the accuracy of the amplitude detection modality is much worse than that of the spectral modality, therefore, the accuracy of our sensor for monitoring the oil concentration cannot be enhanced by using the two detection modalities. In our future work, we will have to balance the accuracies of the two sensing channels in order to enhance the overall accuracy of the two-channel Bragg fiber sensor.

## 4.7 Conclusion

In summary, we demonstrate simultaneous monitoring of the real and imaginary parts of the liquid analyte refractive index by using a hollow-core Bragg fiber, and we apply this fiber sensor to monitor concentrations of various commercial liquids by monitoring of the fiber bandgap center wavelength, as well as the fiber transmission amplitude at the point of fiber lowest propagation loss (bandgap center). The fiber sensor is first calibrated using NaCl solutions of different concentrations. By measuring spectral shift of the fiber bandgap, the sensitivity to changes in the real part of the core refractive index is found to be 1460nm/RIU, which translates into a sensitivity of 2.6nm/w% to changes in the concentration of a NaCl solution. Additionally, using changes of the transmission amplitude at the point of lowest propagation loss of the Bragg fiber, a concentration sensitivity of 3.55dB/w% for NaCl solutions is obtained. By using the spectral modality and the effective medium theory, we determine the concentrations of the two commercial fluids from the measured refractive indices with accuracy of ~0.57% for both low- and high-loss oils. Moreover, we demonstrate that using the amplitude-based detection modality allows determination of the oil concentration with an accuracy of ~1.64% for low-loss oils and an accuracy ~2.81% for the high-loss oils. The proposed Bragg fiber sensor has the advantages such as simple structure, fast response, and low cost. One practical application of the proposed sensor is precision monitoring of the cooling oil concentration in cooling solutions and sawing liquids, where real time monitoring of oil concentration with sub-1%v accuracy is desired.

# CHAPTER 5 ARTICLE 2: SQUEEZED HOLLOW CORE PHOTONIC BRAGG FIBER FOR SURFACE SENSING APPLICATIONS

This chapter is based on the paper "Squeezed hollow core photonic Bragg fiber for surface sensing applications", which is published on Optics Express in 2016. I am the primary author of this paper, and the co-authors are Hang Qu and Maksim Skorobogatiy.

In this Chapter, we propose to use squeezed hollow-core photonic bandgap Bragg fibers for surface sensing applications. We demonstrate theoretically and confirm experimentally that squeezing a section of the Bragg fiber core increases overlap between the optical fields of the core-guided modes and the modes bound to the sensing layer, thus significantly enhancing their interaction via anticrossing phenomenon, which, in turn, enhances surface sensitivity of the fiber sensor. As a practical demonstration, we apply our fiber sensor for *in situ* monitoring of the dissolution dynamics of a sub-micron-thick polyvinyl butyral (PVB) film coated on the surface of the liquid-filled Bragg fiber core. Strong spectral shift is observed during the dissolution of the PVB film, and a surface spectral sensitivity of ~70pm/nm is achieved experimentally with aqueous analytes. The proposed fiber sensor offers a new sensing modality and opens new sensing applications for photonic bandgap fibers, such as real-time detection of binding and affinity, study of kinetics, etc., for a range of chemical and biological samples.

## 5.1 Introduction

Precise detection of bio-layer thickness, trace amounts of biomolecules, and identification of bacteria pathogens is important in numerous biochemical applications including diagnostics, genomics, proteomics, microbiology, and surface chemistry [3, 8, 225-226]. Optical biosensors are powerful analysis tools to address these applications by means of fluorescence-based techniques or label-free detection. Compared to fluorescence-based techniques, label-free biosensors forgo the need of laborious labeling of samples and can detect target molecules in their natural forms by measuring changes in the analyte refractive index [227], optical absorption [228], or Raman scattering [229] in the presence of the biological agents. The label-free sensing modality allows *in situ* monitoring of surface kinetics and affinity, as well as other surface interactions.

Optical fibers constitute a very promising platform for label-free biosensing applications, as they offer miniaturization, a high degree of integration, and continuously quantitative and qualitative analysis. To date, a wide range of optical fiber-based biosensors have been proposed and developed. One common implementation for surface sensing is by using an evanescent coupling of the total internal reflection (TIR) guided modes to the bio-layer. This sensing strategy has been applied in various configurations, such as tapered microfibers [230], U-shaped fiber [231], side-polished fiber [232], and long period fiber grating (LPFG) [233]. However, in such sensors, in order to ensure efficient overlap between the bio-layer and the evanescent fields of the optical modes, certain fiber modifications have to be first carried out, such as stripping off a section of the fiber cladding or tapering the fibers into microfibers, which undermine the mechanical robustness of these fiber sensors and limit the interaction length between the optical modes and the analyte.

Another popular implementation of the fiber sensors for surface sensing is based on the phenomenon of surface plasmon resonance (SPR), which involves resonant excitation of the electromagnetic surface waves at the metal-dielectric interface. Being extremely sensitive to the refractive index changes of the surrounding medium, these sensors are particularly suitable for biosensing applications such as monitoring molecule interactions, DNA hybridization, and antigen-antibody reactions [234-236]. However, this technique requires a complicated fabrication process, including fiber cladding stripping and precisely controlled metal-layer deposition. Furthermore, the probing length of surface plasmon in the visible range is only on the order of 100nm [237], which limits its utility when detection of larger targets (such as bacteria with sizes of 0.5μm-10μm) is required.

In order to extend the probing depth of the surface wave to longer distances for macromolecular or bacteria detection, one can pursue biosensors operating at longer wavelengths (such as THz). Thus, in [181] the authors used a suspended core polyethylene THz fiber for the detection of E. coli bacteria. The highly porous structure of the suspended core fiber allows the target analytes to conveniently access to the fiber core and the evanescent part of the guided wave. It was demonstrated that selective binding of the E. coli bacteria to the surface of the fiber core can significantly influence the THz transmission properties of the suspended core fiber due to enhanced scattering and absorption losses caused by the bacteria. Changes in the fiber propagation loss can then be correlated to the concentration of the bacteria in the liquid analyte.

Additionally, You et al. reported a polypropylene hollow-tube based on an anti-resonant reflecting hollow waveguidance (ARRHW) mechanism for the sensing of molecular overlayers adhered to the inner surface of the tube [168, 169]. The strongly localized THz evanescent wave enables detection of the subwavelength-thick overlayers (several microns to tens of microns) attached on the inner surface of the hollow tube. Nevertheless, the strong absorption of THz waves in water limits the sensor application in aqueous environment.

Using sensors based on hollow-core photonic bandgap Bragg fibers operating in the visible-near infrared spectral range constitutes a viable alternative for surface sensing applications in aqueous analytes, as Bragg fibers inherently integrate optical detection with microfluidics, and water is relatively transparent in this spectral range. Due to the possibility of having a large fiber core (~1mm), the response time of the liquid-filled Bragg fiber sensor could be reduced to under 1s, thus allowing for continuous online monitoring of biological and chemical samples in a contained, highly integrated manner. Furthermore, the large fiber core could be further functionalized with bio-recognition elements that can bind and progressively accumulate target biomolecules or bacteria, thus enabling detection of specificity. In general, one distinguishes two types of Bragg fibers, namely low-refractive index (RI)-contrast Bragg fibers and high-RI-contrast Bragg fibers. We note that low-RI-contrast Bragg fibers have certain advantages for liquid analyte sensing, compared to their high-RI-contrast counterparts. In fact, we have argued in [111, 113], that high-RI-contrast Bragg fibers show superior guidance in the gaseous cores ($n_c$~1), which makes them highly suitable for gas sensing applications. Meanwhile, when these high-RI-contrast Bragg fibers are filled with aqueous solutions ($n_c$~1.33), the TM bandgaps of the Bragg reflectors tend to collapse at the light line of aqueous material due to the Brewster angle phenomenon, leading to high loss of the guided modes. In contrast, the low-RI-contrast Bragg fibers show large TM bandgaps in the vicinity of the light line of an aqueous solution-filled fiber core, thus resulting in good guidance of all the polarizations. Therefore, the use of low-RI-contrast Bragg fibers is preferred in the case of detecting aqueous analytes.

In our previous work, we have demonstrated using hollow-core Bragg fibers for bulk refractive index sensing of liquid samples [112, 115]. The operation principle of such sensors relies on the spectral modality, according to which variations in the analyte refractive index modify the bandgap guidance of the fiber, leading to spectral shifts in the fiber transmission

spectra. In this paper, we demonstrate a novel application of the hollow-core Bragg fibers for surface sensing applications. The fiber used in this work is an all-polymer hollow-core low-RI-contrast Bragg fiber, which features a hollow core surrounded by a periodic sequence of high/low refractive index multilayers, namely, polystyrene (PS)/polymethyl-methacrylate (PMMA) Bragg reflector. We then deposit a thin polyvinyl butyral (PVB) analyte layer on the inner surface of the fiber core. The analyte layer supports its own-guided modes with their optical properties strongly affected by the layer refractive index and thickness. Due to the phenomenon of avoided crossing in the vicinity of the phase matching wavelength between a particular pair of the core-guided and the analyte layer bound modes, fiber transmission spectra (bandgap shape) can be significantly modified, thus allowing for monitoring of changes in the analyte layer properties. It is, in fact, the hybridization of the core-guided modes of the Bragg fiber with the analyte layer bound modes in the vicinity of their corresponding phase matching points that enables the surface sensing modality of the Bragg fiber. One of the design challenges when using Bragg fibers for surface sensing is a weak overlap between the modal fields of the core-guided and the analyte layer bound modes. This is due to the fact that the fields of the core-guided modes of the Bragg fiber decrease rapidly from the core center towards the core inner surface where the analyte layer is located. In order to increase the modal overlap and promote the hybridization between the core-guided modes and the analyte layer bound modes, we propose squeezing of the Bragg fiber. Squeezing of the fiber decreases the fiber core size in one dimension, which, in turn, leads to the modal overlap enhancement in the direction of squeezing. As a demonstration of the surface sensing modality, we apply our sensor to monitor the dissolution dynamics of the polyvinyl butyral film coated on the inner surface of the fiber core. Furthermore, we demonstrate that the surface sensitivity of the fiber sensor could be greatly enhanced by squeezing a section of the Bragg fiber, thus increasing the modal overlap between the core-guided modes and the modes bound to the thin PVB film. Simulations based on the transfer matrix method are conducted to validate the experimental results. The proposed fiber sensor opens a new approach for a wide range of application, such as detection of molecular interaction and the study of surface kinetics, as well as bacteria detection and other applications involving surfaces.

## 5.2 Theoretical analysis of using Bragg fiber for surface sensing applications

Bragg fibers are well known for their ability to confine light in the core filled with analytes having refractive indices lower than those of the fiber cladding materials. When a broadband light source is launched into the Bragg fiber core, only the light with frequencies within bandgap of the Bragg reflector will be confined and guided in the fiber core, while the light with frequencies outside of the bandgap will irradiate out.

In order to theoretically study the surface sensing mechanism, we simulate the modal refractive indices and the propagation losses of the guided modes inside of the Bragg fibers by using the transfer matrix method (TMM) [210, 214], with an analyte layer deposited onto the core inner surface. In our simulations, we approximate the circular Bragg fibers as planar Bragg stacks with the same material composition and layer thickness. First, we consider a Bragg fiber with a bilayer featuring refractive indices of $n_h$, $n_l$, and having corresponding layer thicknesses of $d_h$, $d_l$. The core is assumed to be filled with water ($n_c$=1.33) and has a diameter of $D$. The number of bilayers in the fiber reflector is $N$. In Fig. 5.1, the green region represents an analyte layer with a thickness of $d_a$ and refractive index of $n_a$.

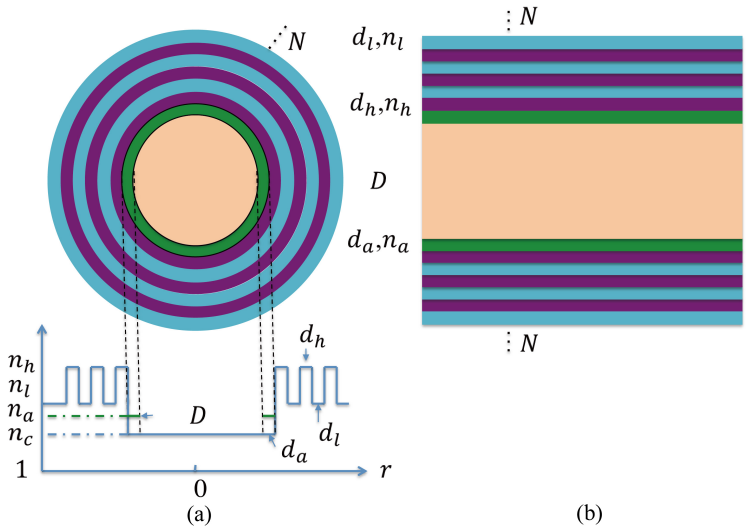


Figure 5.1 Schematic of the Bragg fiber (a) and the corresponding planar Bragg waveguide (b) with the same material composition and layer thickness. The Bragg reflectors feature alternating polystyrene (PS) /polymethyl-methacrylate (PMMA) layers. The green region represents the analyte layer.

### 5.2.1 Influence of the analyte layer thickness on the Bragg fiber spectral features

In our first set of simulations of the Bragg fibers, we calculate the modal refractive indices and the radiation losses of the $TM_1$ and $TE_1$ modes guided in the water-filled fiber core that features a thin analyte layer with thickness ranging from 0nm to 200nm. The thicknesses of PMMA/PS bilayer are obtained from the scanning electron microscopy graphs of the cross section of the Bragg fiber used in our experiments ($d_{PMMA}$=210nm. $d_{PS}$=210nm), as shown in Fig. 5.5. The number of bilayers $N$ in the Bragg reflector is twenty. The refractive indices of the PMMA, PS, and water are ($n_{PMMA}$=1.49, $n_{PS}$=1.58, $n_{water}$=1.33). The fiber core diameter is set to be $D$ =600μm. The refractive index of the analyte layer is set to be 1.46, which is a typical value for many biomaterials [100], as well as for the PVB layer used in our experiments.

Figures 5.2(a)-(d) illustrate the simulated modal refractive indices and the radiation losses of the $TM_1$ and $TE_1$ modes guided in the Bragg fiber as a function of wavelength. We note that introduction of an analyte layer into the fiber core results in the anticrossing phenomenon when the fundamental mode of the Bragg fiber (closest to the light line of the core material) hybridizes with the modes guided predominately in the analyte layer. This phenomenon happens in the vicinity of the phase matching wavelength between the dispersion relations of the two modes, and it results in apparent discontinuities in the modal dispersion curves, corresponding to the anticrossings between the core-guided modes of the Bragg waveguide and the so-called defect modes [238-240] guided in the analyte layer.

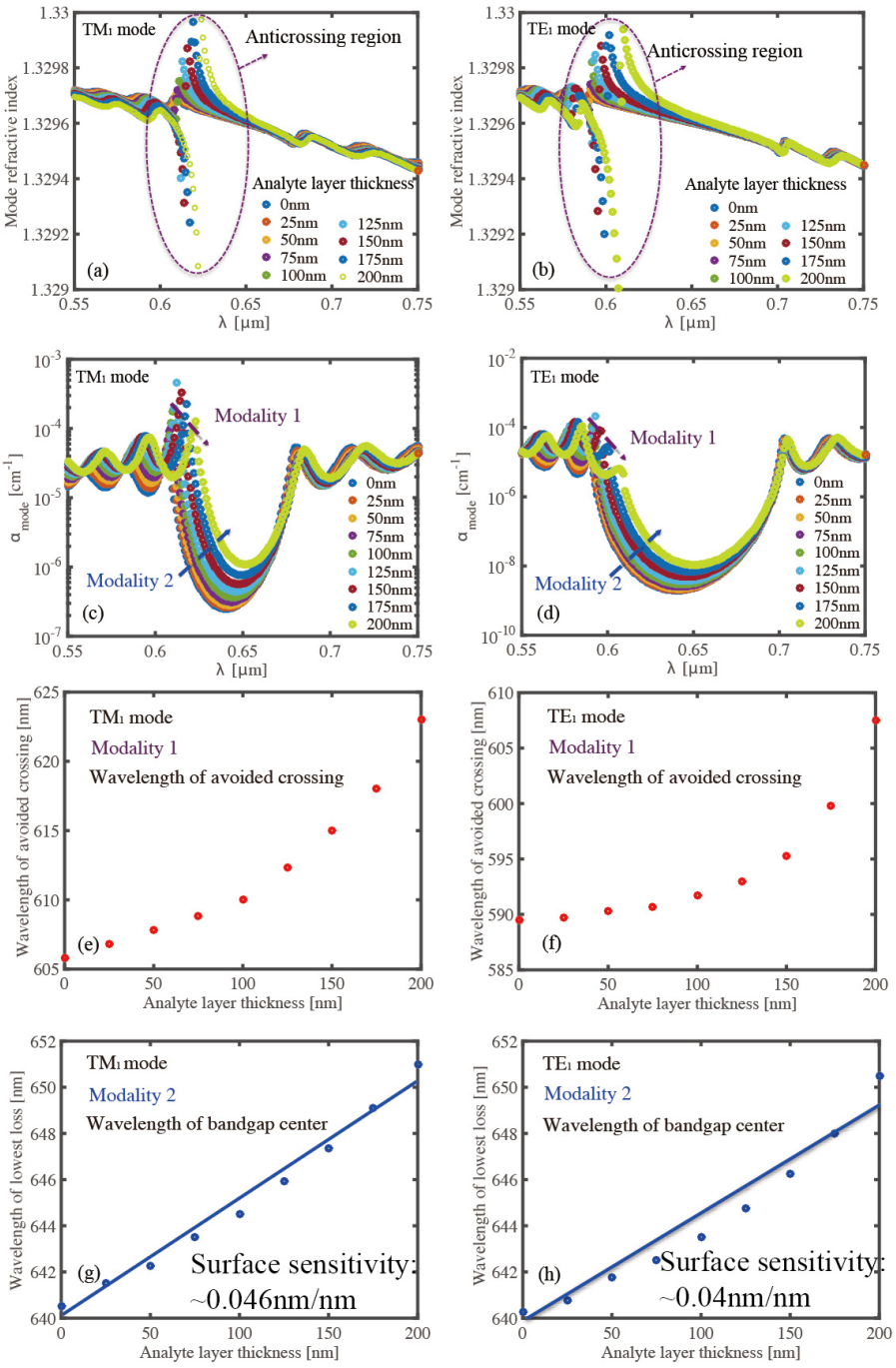


Figure 5.2 Simulated modal dispersion relations of $TM_1$ (a) and $TE_1$ (b) modes in the water-filled Bragg fiber featuring an analyte layer with thickness ranging from 0nm to 200nm. Corresponding radiation losses of the $TM_1$ (c) and $TE_1$ (d) modes. Dependence of the wavelength of avoided crossing of the $TM_1$ (e) and $TE_1$ (f) modes (obtained from (c) and (d)) as a function of the analyte layer thickness. Dependence of the wavelength of the lowest radiation loss of the $TM_1$ (g) and $TE_1$ (h) modes (obtained from (c) and (d)) as a function of the analyte layer thickness.

A schematic view of anticrossing between a particular pair of a core-guided mode and an analyte layer bound defect mode is illustrated in Fig. 5.3. The dispersion relation of a core-guided mode of a Bragg fiber (without analyte layer) is shown as a blue dotted line. Similarly, the dispersion relation of an analyte layer bound mode (mode of a step-index slab waveguide) is shown as a purple dotted line. The wavelength of crossing between the two dispersion relations is called the phase match point between the two modes. When plotting the corresponding modes of a Bragg fiber with analyte layer we observe anticrossing of the dispersion relations corresponding to the core-guided and analyte bound mode in the vicinity of the phase matching point. In the vicinity of the phase matching point (also wavelength of avoided crossing), there is a resonant power transfer from the core-guided mode of a Bragg fiber into the defect mode of an analyte layer. In turn, the defect mode in the analyte layer is phase matched with the radiation continuum of the fiber cladding, thus resulting in a significant increase of the fiber propagation losses in the vicinity of the wavelength of the avoided crossing.

The wavelength of the avoided crossing depends strongly on the analyte layer thickness. When increasing the analyte layer thickness, the anticrossing wavelength shows a red shift. This is easy to rationalize by noting that dispersion relation of the fundamental mode of the Bragg waveguide (with analyte layer) shows red shift when the analyte layer thickness increases.

Moreover, we note that, upon introduction of the analyte layer, the original bandgap of the Bragg fiber (without the analyte layer) becomes fractured due to the appearance of the loss peak near the wavelength of anticrossing. This new structure of the bandgap suggests two modalities for the detection of changes in the analyte layer thickness. The most direct modality (modality 1 in Fig. 5.2(e) and (f)) is to track the wavelength of the avoided crossing that appears as a transmission dip inside of the original fiber bandgap (region of high transmission). From Figs. 5.2(e) and (f), one finds a nonlinear dependence of the wavelength shift with respect to the analyte layer thickness. However, in practice, this modality is difficult to realize as the large core Bragg fibers are highly multimode, so there is no single anticrossing wavelength. Thus, in place of a single transmission dip, one typically observes a change in the bandgap shape. This phenomenon is clearly observed in Figs. 5.2(c) and (d). Due to the avoided crossing, a transmission loss peak appears inside of the bandgap. This peak splits the bandgap into two smaller bandgaps. By tracking the shift in the wavelength of the lowest loss of the large bandgap (modality 2 in Figs. 5.2(c) and (d)), one can indirectly track the changes in the position of the

anticrossing wavelength (transmission dip in the fiber bandgap). We find in the following that modality 2 is more relevant experimentally. In order to characterize the surface sensitivity of this modality, we thus plot the wavelengths of the lowest propagation loss of the $TM_1$ and $TE_1$ modes as a function of the analyte layer thickness, as shown in Figs. 5.2(g) and (h). An approximately linear dependency with analyte layer thickness is found for both modes. The surface sensitivity of the spectral method can be then defined as $S_\lambda = \partial\lambda_c / \partial d_a$, where $\partial\lambda_c$ is the wavelength shift when the analyte layer thickness is changed by $\partial d_a$. According to this definition, the simulated surface sensitivities using modality 2 are found to be 0.046nm/nm and 0.04nm/nm for the $TM_1$ and $TE_1$ modes, respectively. We note that the simulated surface sensitivity is mostly valid for the Bragg fiber operating in the single mode or a few modes regime. In our experiments, the hollow-core Bragg fiber features a relatively large core diameter (~600μm) and a relatively small length of 8cm, which allows thousands of modes propagating in the fiber core. As a result, many higher-order modes are excited when the light beam is launched into the fiber. These higher-order modes have somewhat different modal overlap with the analyte layer, as well as different anticrossing wavelengths and transmission bandgaps. Therefore, we expect that the surface sensitivity measured experimentally would be a result of the combined contribution of many higher-order modes, rather than only the fundamental $TE_1$ and $TM_1$ modes. At the same time, we note that another effect of the multimode operation on the fiber transmission is in the broadening of the transmission window and the overall increase in the propagation loss.

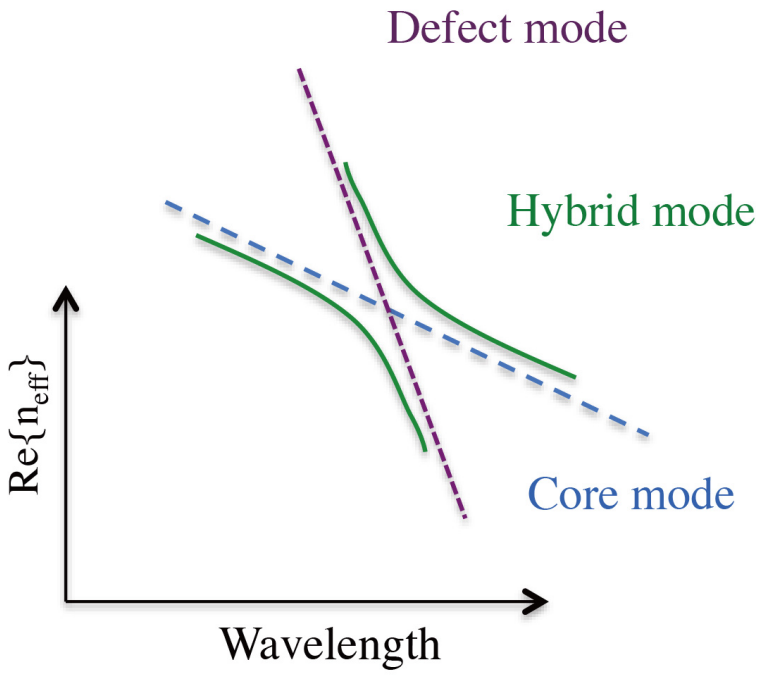


Figure 5.3 Schematic of the modal dispersion relations of the core-guided (blue dotted line) and the analyte layer bound modes (purple dotted line), as well as the dispersion relations of the hybridized modes in a Bragg fiber with an analyte layer (green solid lines) near the point of phase matching (anticrossing wavelength).

### 5.2.2 Effect of the fiber core size (degree of squeezing) on the surface sensitivity

Now, we study the effect of the squeezed fiber core on the surface sensitivity of our sensor. When dealing with the squeezed Bragg fibers, we approximate them as planar Bragg stacks with the same material composition and layer thickness. When the fiber is squeezed, it can be considered that the distance between the planar stacks ( $D$ ) is reduced. In the following simulation, we keep the analyte layer thickness constant (100nm) and calculate the surface sensitivity of 10 possible even-symmetric TE and TM modes (closest to the light line) of the squeezed fiber when $D$ is decreased from 600μm to 20μm. In Figure 5.4, we plot the surface sensitivities of the 10 TE and TM modes as a function of the squeezed core size $D$. One can make several interesting observations from the simulation results. First, the higher order modes show higher surface sensitivity compared to the fundamental modes, due to a higher modal overlap with the analyte layer coated on the fiber inner surface. Second, when reducing the fiber

core size, the surface sensitivity of the fiber sensor increases. This enhancement is especially pronounced when the squeezed core size becomes smaller than 100µm. This remarkable improvement of the surface sensitivity is attributed to an enhanced modal overlap between the core-guided modes and the analyte layer. This demonstrates that, indeed, the surface sensitivity of the fiber sensor can be enhanced dramatically by squeezing a section of the Bragg fiber core so as to increase the modal overlap with the analyte layer. From the simulation results, one can find that the largest sensitivity enhancement of the 10 TE and TM modes is ~52% when the fiber core size is reduced from 600µm to 100µm. Furthermore, this enhancement could reach up to ~12-fold when the fiber core size is reduced to 20µm. We note that, in practice, our fiber sensor operates in a multimode regime. The extent of the surface sensitivity enhancement would be a result of the combined contribution of a great number of optical modes propagating in the fiber core, with higher order modes being more sensitive to changes in the fiber core size.

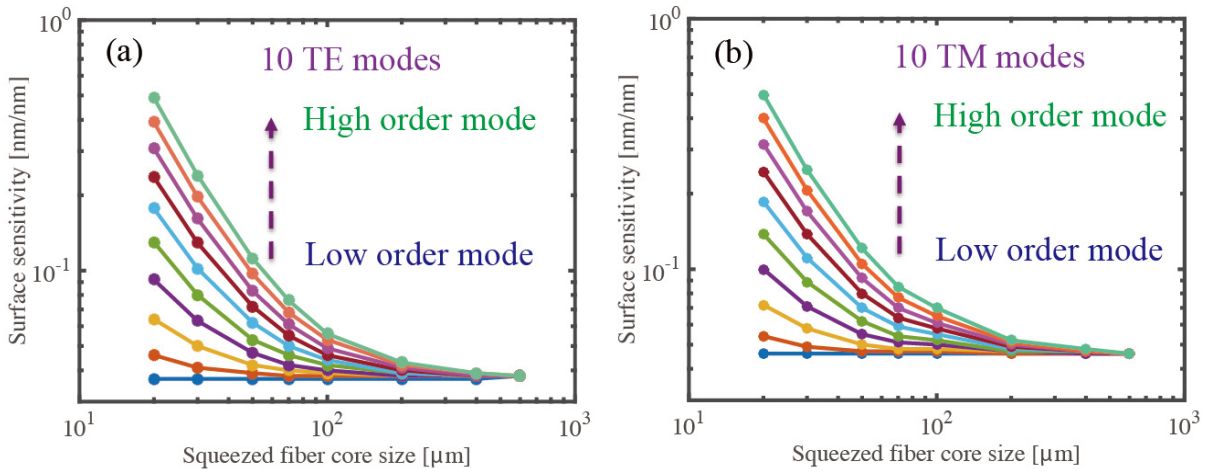


Figure 5.4 Simulated surface sensitivity of 10 even symmetric TE (a) and TM (b) modes (closest to the light line) when the fiber core size D is reduced from 600µm to 20µm. The PVB layer thickness is kept constant and equals to 100nm in all the simulations.

## 5.3 Experimental realization of the Bragg fiber sensor

### 5.3.1 Deposition of the PVB layer

In order to experimentally study the squeezed Bragg fiber sensors and assess their potential for surface sensing applications, we undertake the study of dissolution dynamics of a thin analyte film deposited on the fiber core inner surface. A thin layer of polyvinyl butyral resin (Butvar® B-

98, Sigma-Aldrich) is chosen as the analyte material in this demonstration because it is transparent in the visible spectral range and a PVB layer deposited onto the fiber core inner surface can be easily dissolved using ethyl alcohol without damaging the PS/PMMA reflector. A PVB layer fabricated using a solution-based method has a refractive index in the range of 1.45-1.47, which is close to that of many practical biomaterials.

In order to deposit a thin PVB film on the inner surface of the Bragg fiber, 1.5g PVB is first dissolved in 10 mL ethyl alcohol and mixed thoroughly. Then, the mixture is pumped into the Bragg fiber via applying a negative pressure. Subsequently, the 8cm long fiber section is fixed on the chuck of a spin coater (WS-400-6NPP, Laurel) and rotated at a speed of 3000RPM for 60s. The cross section of the obtained fiber with a PVB layer inside is shown in Figs. 5.5(a) and (b). From the SEM micrograph, the thickness of the PVB layer is estimated to be ~500nm, while the thicknesses of the individual PMMA and PS layers are both ~210nm.

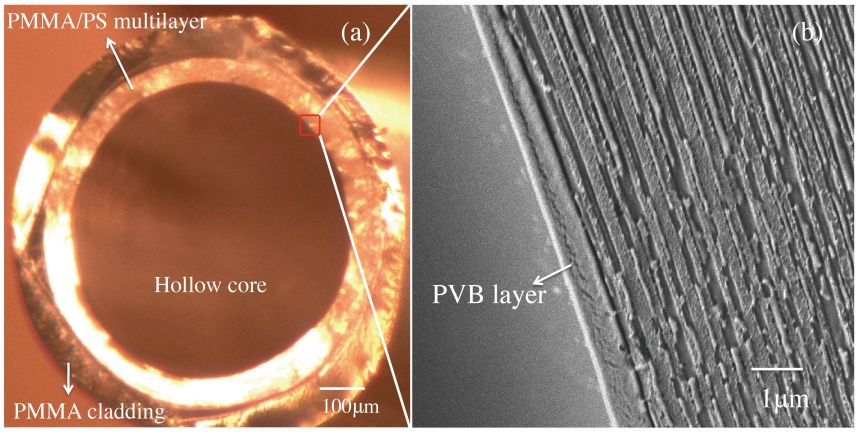


Figure 5.5 (a) Cross section of the hollow-core PMMA/PS Bragg fiber with a PVB layer under optical microscope. (b) Cross section of the Bragg reflector taken by a scanning electron microscope (SEM), featuring the alternating polystyrene (PS) and poly-methacrylate (PMMA) layers with individual thickness of ~210nm, as well as a ~500nm-thick PVB layer.

### 5.3.2 Experimental setup

Experimentally, we use two opto-fluidic blocks to integrate the Bragg fiber sensor into the setup, as shown in Fig. 5.6. The two opto-fluidic blocks enable both optical coupling and flow of the target analytes, which are detailed in our prior work [112]. After pumping liquid analyte into the hollow core Bragg fiber, a beam from a broadband supercontinuum source (500nm-1700nm) is

launched into one end of the fiber core using an objective (×10). The transmitted spectrum is registered by a grating-based monochromator (Oriel, 1/8m cornerstone, Newport). In order to enhance the surface sensitivity of the Bragg fiber sensor, we increase the modal overlap between the core-guided modes and the analyte film by squeezing the fiber using a metallic rod fixed on a micro-positioning stage. The fiber can be squeezed in increments of 50μm.

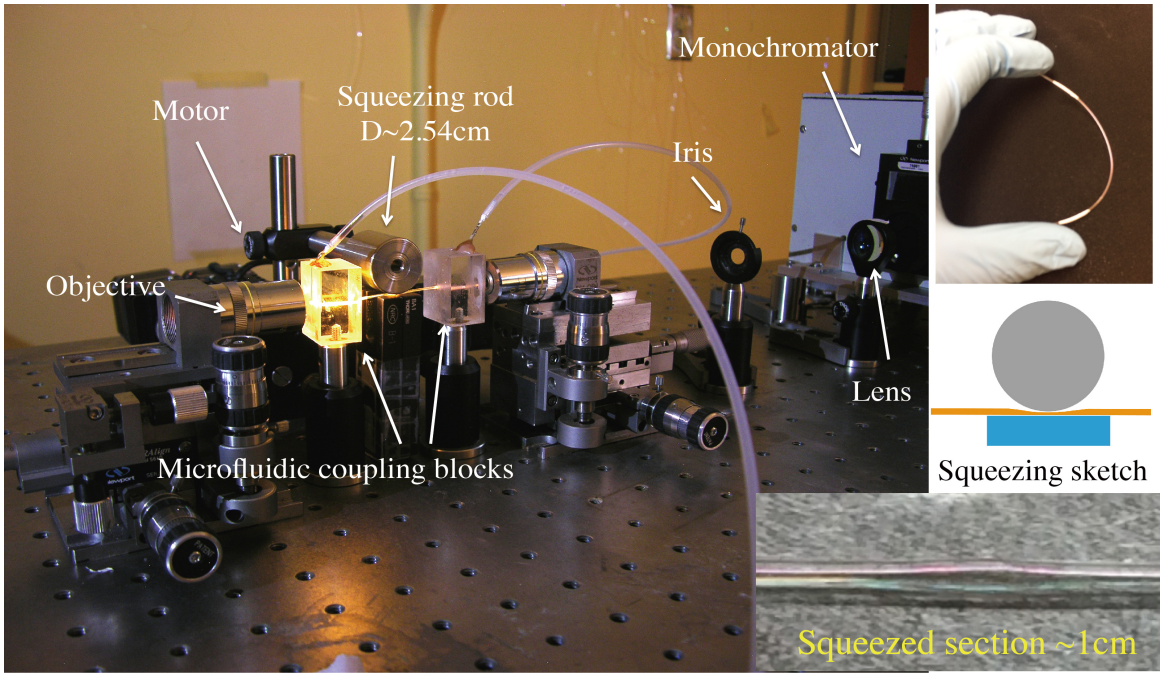


Figure 5.6 Experimental setup for the optical characterization of the surface sensitivity of the squeezed Bragg fiber sensor. The 8cm-long Bragg fiber with a thin PVB coated on the inner surface is integrated into the setup using two opto-fluidic blocks. A broadband supercontinuum beam is launched into one end of the liquid-core Bragg fiber using an objective, while the output spectrum of the fiber sensor is registered by a monochromator. The metallic rod (diameter: 2.54cm) is fixed on a micro-positioning stage and is used to squeeze a section of the fiber in increments of 50μm. Inset: ~8cm Bragg fiber used in this experiment (top), squeezing sketch of our setup (middle), as well as the squeezed section of the Bragg fiber (bottom).

### 5.3.3 Characterization of dissolution dynamics of the PVB analyte layer

First, we characterize the surface sensitivity of the Bragg fiber sensor without squeezing. The fiber features a PVB analyte layer (with a thickness of ~500nm) at the start. We note that since a grating based spectrometer is used to register the transmission spectra, each scan of the spectral

region of interest (550-750nm) is relatively large, and it takes ~60 seconds. When introducing ethyl alcohol into fiber, the analyte layer starts dissolving immediately and the Bragg fiber spectra change continuously. Therefore, before pumping ethyl alcohol into the fiber (in order to dissolve the PVB layer), we first register the reference transmission spectrum using chemically inert 16%wt NaCl solution in water. This NaCl solution is chosen because it has the same refractive index (n~1.36) as ethyl alcohol and thereby the fiber has the same bandgap position as the one filled with ethyl alcohol. After acquiring the reference spectrum, the ethyl alcohol is introduced into the fiber core in order to dissolve the thin PBV layer deposited onto the fiber core inner surface. The time varying transmission spectra are then acquired every minute. As shown in Fig. 5.7, with the dissolution of a PVB layer, the transmission spectra have an obvious blue shift towards shorter wavelengths. The direction of the spectral shift is consistent with that found in our numerical simulations. Moreover, as the PVB film (RI~1.46) dissolves in ethyl alcohol (RI~1.36), we expect that the bulk refractive index of the fiber core should gradually increase, which induces an additional blue spectral shift [112]. This assumption is well verified by noting that when we purge the fiber with pure ethyl alcohol after the PVB layer is dissolved, a red shift of ~5nm is observed, which is due to the decrease of the refractive index of pure ethyl alcohol compared to that of the PVB-alcohol mixture. Therefore, based on the observed results, we can make the following statement; the surface sensitivity of a Bragg fiber is made of two contributions. The first contribution is due to a true surface sensing modality owing to the thickness variation of an analyte layer attached to the inner surface of the fiber core, while the second contribution is due to the changes of the bulk refractive index of the fiber core with the dissolution of the analyte layer in the liquid material of a fiber core (assuming that the core liquid is not continuously pumped through the fiber core).

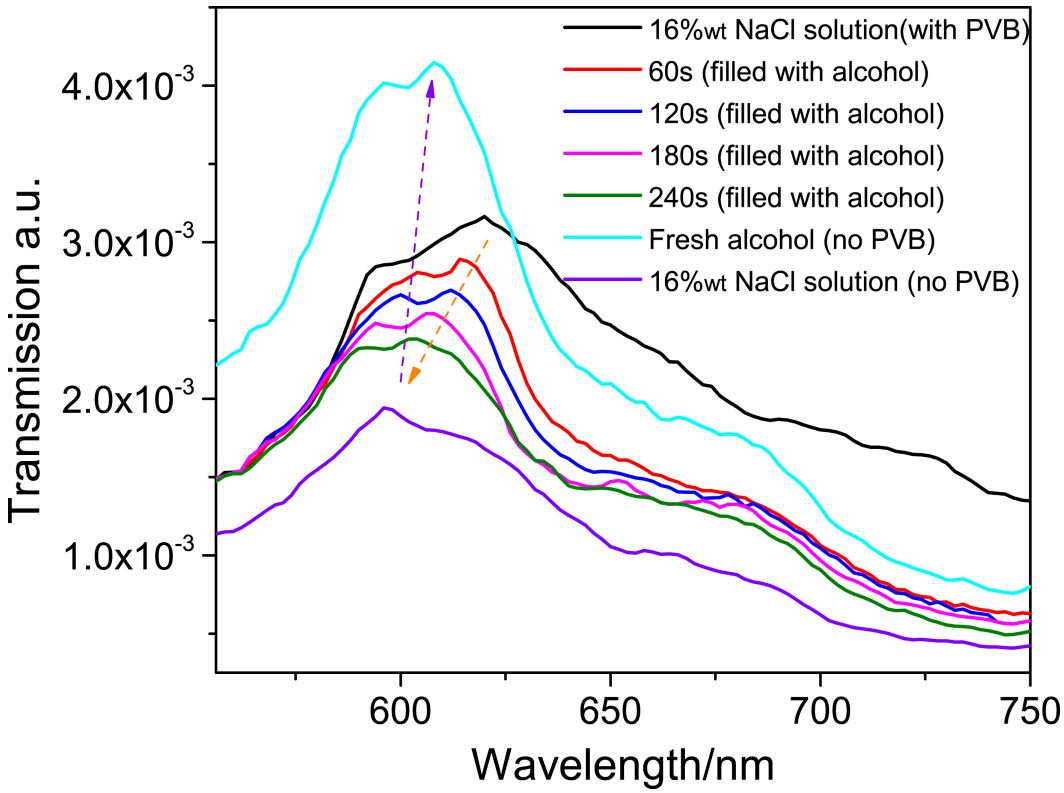


Figure 5.7 Experimental transmission spectra of the Bragg fiber during the dissolution process of a thin PVB layer (thickness~500nm) coated on the inner surface of the fiber core. A blue shift is observed with dissolution of the PVB film. After the PVB layer is dissolved, the fiber is purged with fresh ethyl alcohol, and a red shift of ~5nm is observed, which is attributed to the fact that the RI of ethyl alcohol is somewhat lower than that of the PVB-alcohol mixture.

Finally, we refill the fiber used in the prior experiment with 16%wt NaCl solution in distilled water, and acquire their spectra after a complete removal of the PVB layer. Comparison with the initial transmission peak positions that are measured before the dissolution process allows us to calculate the surface sensitivity of the Bragg fiber. In Fig. 5.8, we plot the spectra of the Bragg fiber filled with 16%wt NaCl in water before and after the PVB film dissolution. We find that the presence of a ~500nm thick PVB layer leads to 23nm red shift in the fiber transmission spectrum, compared to the spectrum of the fiber without a PVB layer. The corresponding surface sensitivity of our sensor to changes in the layer thickness is then estimated to be 0.046nm/nm. For completeness, we also present in Fig. 5.8(a) the transmission spectra of a Bragg fiber with and without PVB layer when the fiber core is filled with distilled water. In this case, we also observe a ~26nm shift of the transmission peak, thus resulting in a surface

sensitivity of 0.052nm/nm. The experimentally demonstrated surface sensitivity is comparable to that found in the numerical simulations. Additionally, from the time dependent date of Fig. 5.7, we can estimate that the dissolution rate the PVB layer is ~2nm/s. We note that in the spectra of a Bragg fiber with a PVB layer, a pronounced transmission dip at the left edge of the fiber transmission window is well observed both in the case of water and 16%wt NaCl solution (see Figs. 5.8(a) and (b)). The presence of this transmission dip is probably attributed to anticrossing between the fiber core modes and the modes confined to the analyte PVB layer, as we have observed in the simulated spectra in Section 5.2.

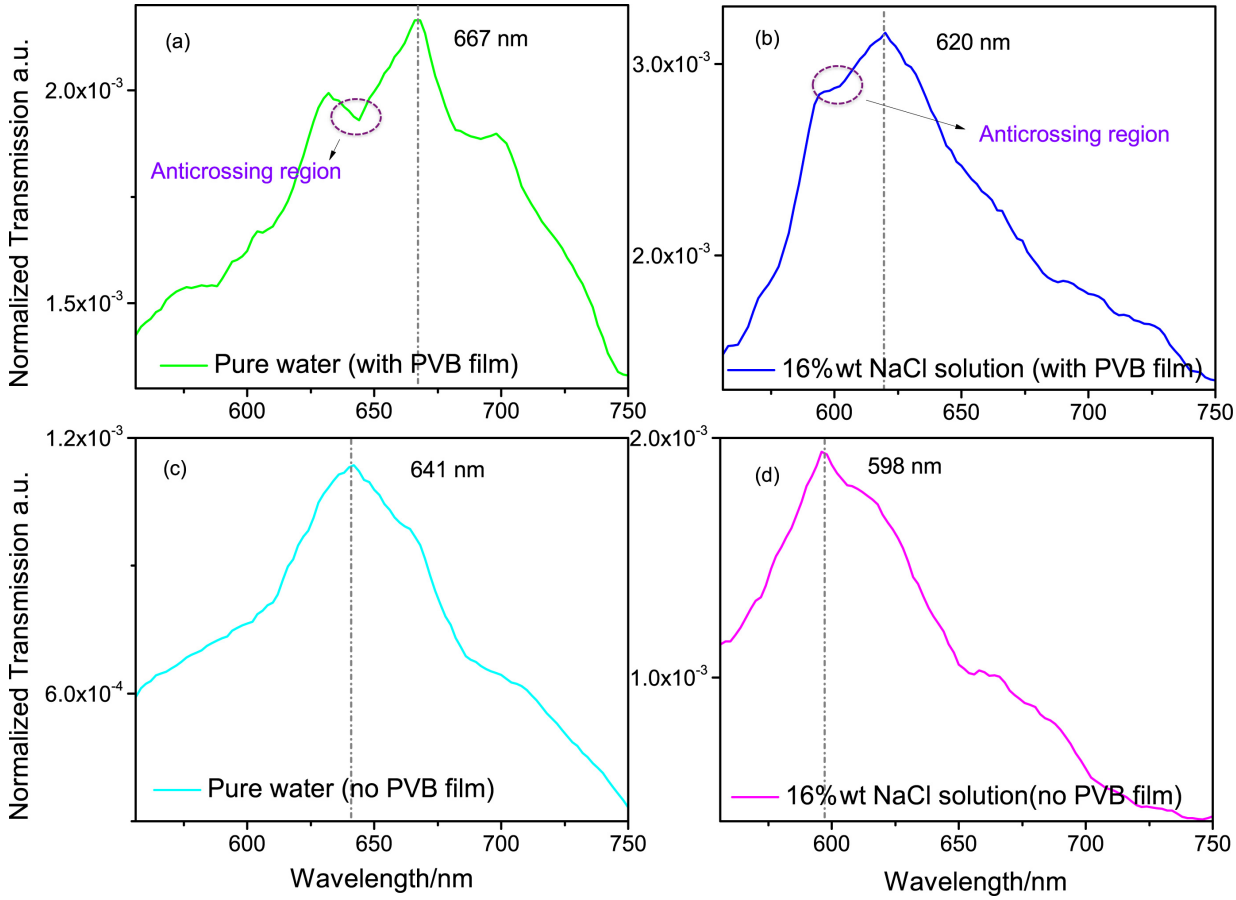


Figure 5.8 (a) Experimental transmission spectra of the ~8cm-long Bragg fiber filled with distilled water (a), (c), and 16%wt NaCl in water (b), (d), before and after the PVB film dissolution. The ~500nm PVB film induces a red shift of 26nm and 23nm in the transmission peak, respectively, when compared to transmission of the same fiber without a PVB layer.

## 5.4 Enhancement of the surface sensitivity by squeezing the Bragg fiber

Due to the large core of the Bragg fiber (significantly larger than the wavelength of light and the analyte layer thickness), only a small fraction of the power of the core-guided mode is present in the vicinity of the inner surface of the fiber core, thus leading to a poor modal overlap with the PVB analyte layer; therefore, only a moderate surface sensitivity is observed experimentally. In order to enhance the surface sensitivity, numerical simulations of Section 5.2 suggest that one has to reduce the fiber core size. To verify this experimentally, we repeate the surface sensitivity characterization experiment, when a section of the Bragg fiber is squeezed, thus, effectively reducing the fiber core size. The advantage of a fiber squeezing technique versus drawing fiber of a smaller diameter is that, in the case of a fiber squeezing, one can explore the tradeoff between sensitivity enhancement and sensor response time increase observed for smaller fiber core sizes. More importantly, such a fiber-squeezing technique can also serve as a flexible and independent "knob" to adjust the surface sensitivity and the response time, in order to suit particular needs for different applications.

The experimental setup for the squeezed fiber experiment is shown in Fig. 5.6. The metallic rod with a diameter of 2.54cm is fixed on the micro-positioning stage, which enables squeezing a one-centimeter-long section of the fiber (as shown in Fig. 5.6) in increments of 50μm. We choose the same Bragg fiber, as well as the same recipe for the PVB film deposition in order to guarantee similar transmission properties of the Bragg fiber and similar PVB layer thicknesses as in the case of experiments with non-squeezed fiber detailed in Section 5.3.

In Fig. 5.9, we plot the transmission spectra of the Bragg fiber filled with distilled water when a section of the fiber is squeezed by displacements ranging from 0μm to 500μm. The fiber has a PVB layer with a thickness of ~500nm. We can see that although the transmission amplitude of the fiber is decreased with the increase of the squeezing displacement, the transmission peak positions are well conserved during the squeezing process.

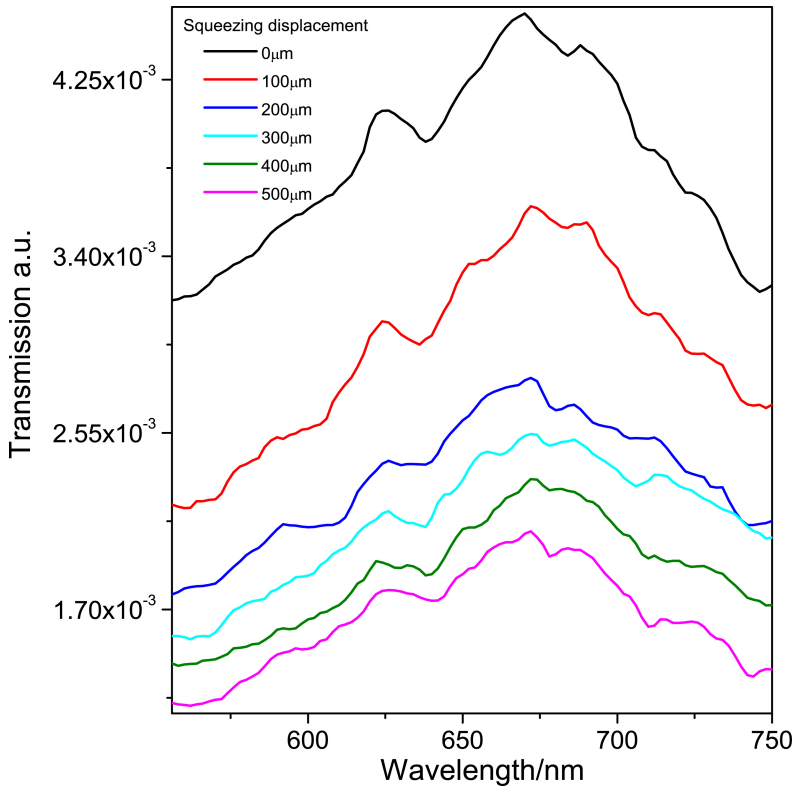


Figure 5.9 Experimental transmission spectra of the ~8cm long Bragg fiber filled with distilled water before PVB layer dissolution, when a section of fiber is squeezed by displacements ranging from 0μm to 500μm using a 2.54cm diameter cylinder. The fiber has a PVB layer with thickness of 500nm.

Then, we register the time-varying spectra of the Bragg fiber during the dissolution of the PVB layer using ethyl alcohol when a section of the fiber is squeezed. Two squeezing displacements of 250μm and 500μm are used in our preliminary experiments. In Fig. 5.10, we present the spectra of the Bragg fiber filled with distilled water and 16%wt NaCl solution in water before and after the complete dissolution of the PVB layer with a goal of characterizing the overall surface sensitivities and their enhancement due to the fiber squeezing. We remind the reader that the refractive index of the 16%wt NaCl solutions in water is the same as that of ethyl alcohol that we use for dissolution of the PVB layer. Moreover, the PVB film is not dissolvable in NaCl solutions, which motivates us to use such a solution for the reference measurements before and after the PVB layer dissolution. Measurement with pure distilled water is presented in lieu of the potential applications of our sensor with aqueous analytes and bio-functional layers.

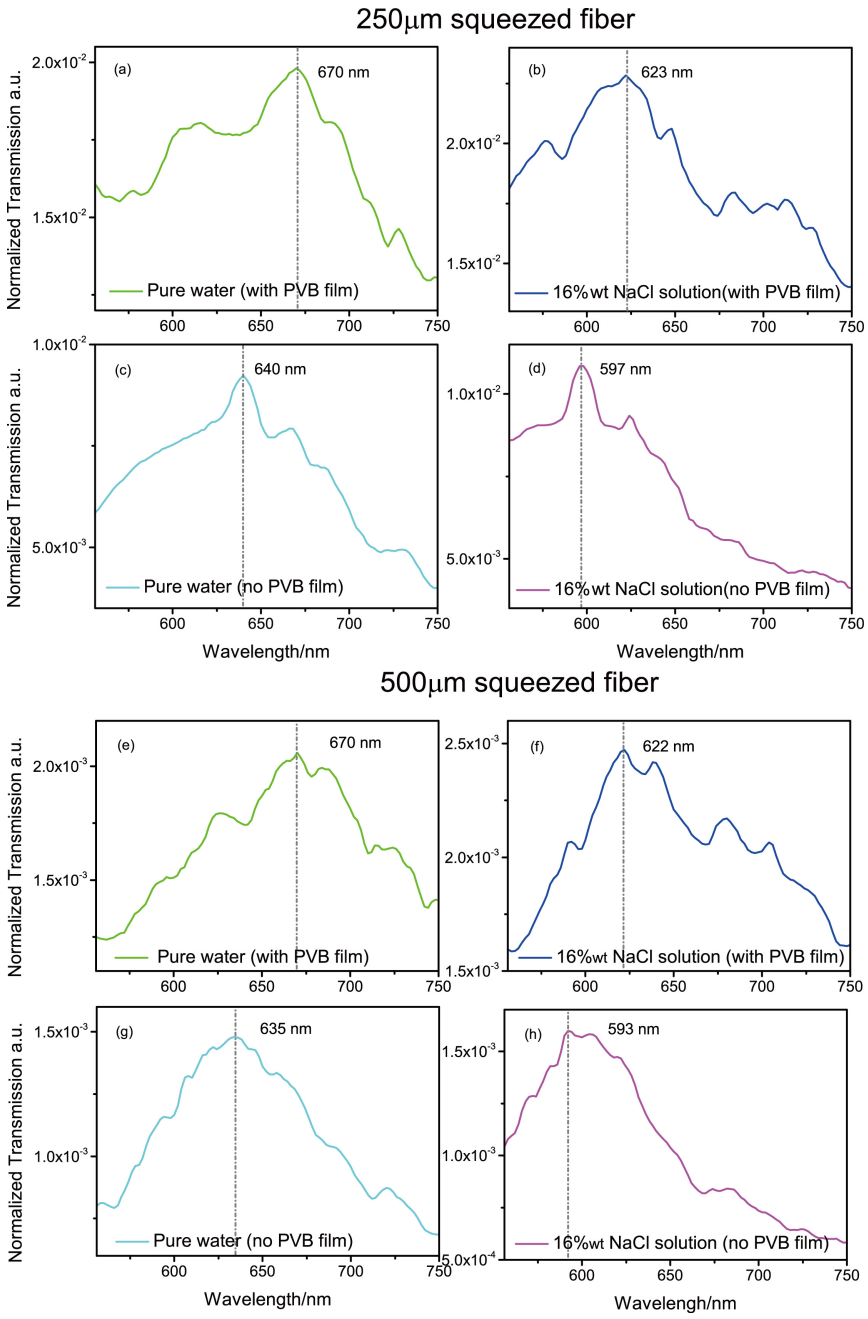


Figure 5.10 Experimental transmission spectra of the ~8cm long Bragg fiber filled with distilled water and 16%wt NaCl solution in water before and after the PVB film dissolution. The fiber is squeezed by the depths of 250μm and 500μm using a 2.54cm diameter cylinder. In the case of a 250μm-squeezed fiber (D~350μm), a ~500nm PVB film induces a red shift of 30nm (filled with pure water), and 26nm (filled with 16%wt NaCl solution). In the case of a 500μm-squeezed fiber (D~100μm), the 500nm PVB film induces a red shift of 35nm (filled with pure water), and 29nm (filled with 16%wt NaCl solution).

By comparing the transmission peak positions of the fiber filled with distilled water and 16%wt NaCl solution before and after the PVB film is fully dissolved, we can calculate the surface sensitivities of the Bragg fiber at those two different degrees of squeezing. As shown in Fig. 5.11, the surface sensitivities of the squeezed fiber are enhanced by ~35% and ~30%, when the fiber is filled with distilled water and 16%wt NaCl solution, respectively, compared to that of a non-squeezed fiber. The extent of sensitivity enhancement shows reasonable agreement with our simulation results. The mechanism of the sensitivity enhancement is due to increased overlap between the core modes and the PVB analyte layer when the fiber is squeezed.

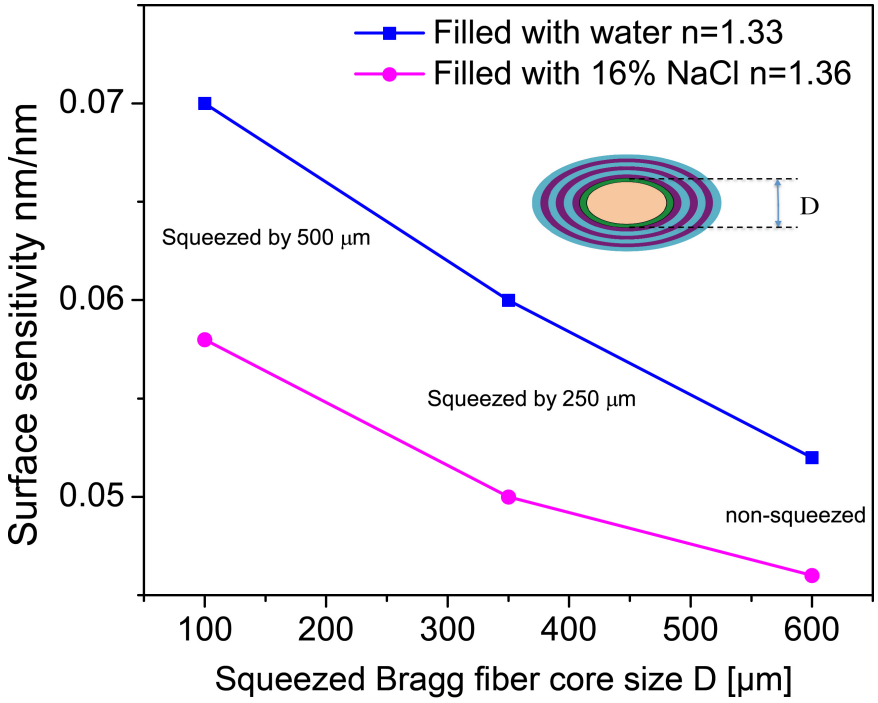


Figure 5.11 Surface sensitivities of the squeezed hollow-core Bragg fiber sensor filled with distilled water and 16%wt NaCl solution for various degrees of squeezing. The circular fiber core has a diameter of ~600μm. Inset: Schematic of the squeezed Bragg fiber with core size of D.

## 5.5 Discussion

In this paper, we propose using squeezed hollow-core Bragg fibers for surface sensing applications. As a demonstration, we apply the fiber sensor to monitor the thickness variations of a thin analyte layer deposited on the inner surface of the fiber core. When a thin film is introduced onto the fiber inner surface, anticrossings between the core-guided modes and the modes confined to the analyte layer are observed both theoretically and experimentally. In the

vicinity of anticrossings, the optical energy is resonantly transferred from the fiber core modes to the analyte layer modes, followed by a strong increase in the fiber propagation loss. The wavelength of the modal anticrossing depends strongly on the analyte layer thickness, thus allowing for monitoring of changes in the analyte layer thickness. The presence of the attenuation peaks induced by the anticrossing phenomenon deforms the shape of the original bandgap of the Bragg fiber and results in changes in the shape of a transmission spectrum. Experimentally, it is easier to monitor spectral shift of the point of the lowest transmission loss than the anticrossing wavelength (transmission dip). This spectral modality for monitoring of the analyte layer optical properties is suitable for a wide range of surface sensing applications.

Due to the large size of the Bragg fiber core (which is much larger than the thickness of the analyte layer), only a poor modal overlap between the core-guided modes and the analyte layer modes is achieved, thereby leading to a moderate surface sensitivity. In order to enhance surface sensitivity, we explore squeezing a section of the Bragg fiber, which enhances the core-guided modes/analyte layer overlap. Numerical simulations show that squeezing the hollow-core Bragg fiber could significantly enhance the surface sensitivity. This enhancement is especially pronounced when the squeezed core size becomes smaller than 100μm. However, due to the moderate mechanical robustness and chemical resistivity of the all-polymer Bragg fiber when it is filled with ethyl alcohol, the fiber breaks or cracks if it is squeezed by a displacement of more than 500μm (the resultant core size ~100μm). As a result, only a moderate sensitivity enhancement (~35%) is achieved in our experimental demonstration, when the core size is reduced from 600μm to 100μm. Despite the limited degrees of squeezing, we can still clearly observe enhancement of the surface sensitivity when we squeeze the Bragg fiber. In our future work, we will study the ways of increasing the mechanical robustness of the polymer Bragg fibers to squeezing in order to further enhance the surface sensitivity.

## 5.6 Conclusion

In summary, we study, both theoretically and experimentally, the use of hollow-core Bragg fibers for surface sensing applications. The fiber sensor operates using a spectral sensing modality to monitor changes in the thickness of an analyte layer deposited on the inner surface of the Bragg fiber core. As a practical demonstration, we have applied this sensor to monitor the dissolution dynamics of a thin PVB layer coated on the fiber inner surface. A surface sensitivity of

0.052nm/nm is experimentally achieved with aqueous analyte. Moreover, we have also experimentally demonstrated that squeezing a section of the Bragg fiber effectively increases the overlap between the core-guided modes and the analyte layer, thus enhancing the surface sensitivity of the fiber sensor. The highest surface sensitivity achieved in our work is 0.07nm/nm with the squeezed fiber core size of 100μm. The experimental observations are validated by theoretical simulation based on the transfer matrix method. The proposed liquid-core Bragg fiber sensor is applicable to a wide range of surface sensing applications including molecular recognition, bacteria detection, and monitoring of the biolayer thickness variation and others, with the advantages of simplicity in sensing mechanism, short response time, ease of fabrication, and relatively high sensitivity.

# CHAPTER 6 ARTICLE 3: 3D PRINTED HOLLOW CORE TERAHERTZ BRAGG WAVEGUIDES WITH DEFECT LAYERS FOR SURFACE SENSING APPLICATIONS

This chapter is based on the paper "3D printed hollow core terahertz Bragg waveguides with defect layers for surface sensing applications", which is published on Optics Express in 2017. I am the primary author of this paper, and the co-authors are Katirvel Nallappan, Hichem Guerboukha, and Maksim Skorobogatiy.

In this Chapter, we study a 3D-printed hollow core terahertz (THz) Bragg waveguide for resonant surface sensing applications. We demonstrate theoretically and confirm experimentally that by introducing a defect in the first layer of the Bragg reflector, thereby causing anticrossing between the dispersion relations of the core-guided mode and the defect mode, we can create a sharp transmission dip in the waveguide transmission spectrum. By tracking changes in the spectral position of the narrow transmission dip, one can build a sensor, which is highly sensitive to the optical properties of the defect layer. To calibrate our sensor, we use PMMA layers of various thicknesses deposited onto the waveguide core surface. The measured sensitivity to changes in the defect layer thickness is found to be 0.1 GHz/μm. Then, we explore THz resonant surface sensing using α-lactose monohydrate powder as an analyte. We employ a rotating THz Bragg fiber and a semi-automatic powder feeder to explore the limit of the analyte thickness detection using a surface modality. We demonstrate experimentally that powder layer thickness variations as small as 3μm can be reliably detected with our sensor. Finally, we present a comparative study of the time-domain spectroscopy versus continuous wave THz systems supplemented with THz imaging for resonant surface sensing applications.

## 6.1 Introduction

Optical fibers have been extensively studied for biochemical sensing applications due to numerous advantages, such as small footprint, high degree of integration, and continuously quantitative and qualitative analysis. To date, a wide range of fiber-optic biochemical sensors based on various configurations have been proposed and developed [3, 8, 226]. One common fiber-based implementation for surface sensing is using an evanescent coupling of the total internal reflection (TIR) guided modes to the analyte layer. This sensing strategy has been

applied in various configurations, such as tapered microfibers [230], U-shaped fiber [231] and side-polished fiber [232], as well as long period fiber grating (LPFG) [233]. Another popular implementation of the fiber sensors for surface sensing is based on the phenomenon of surface plasmon resonance (SPR). However, the probing length of those surface waves in the visible range is only on the order of 100nm [237], which limits its utility when trying to detect of larger targets (such as bacteria with sizes of 0.5μm-10μm).

In order to extend the probing depth of the surface waves to longer distances for macromolecular or bacteria detection, one can pursue biosensors operating at longer wavelengths (such as THz). For example, in [181], the authors used a suspended-core polyethylene THz waveguide for the detection of E. coli bacteria based on an amplitude modality. Selective binding of the E. coli bacteria to the surface of the waveguide core modifies the THz transmission properties of the suspended core waveguide due to enhanced scattering and absorption losses. Changes in the waveguide propagation loss can then be correlated to the concentration of the bacteria in the liquid analyte. Hollow tubes or dielectric pipes based on the anti-resonant reflecting optical waveguide (ARROW) mechanism [168, 169] constitute an alternative to the THz micro-structured waveguide sensors based on the amplitude modality. The strongly localized THz evanescent wave enables detection of the subwavelength-thick analyte layers attached to the inner surface of the hollow tube. By tracking the spectral shift of the resonant wavelength, one can monitor changes in the analyte layer thickness. However, most of those sensors typically have relatively broad spectral features, which dramatically reduce the sensitivity and detection limit.

By employing sensors with narrow resonances, much higher sensitivities could be achieved. For example, in [257, 258], the authors demonstrated thin film sensing by exciting high-Q Fano resonances in planar terahertz metamaterials. Metamaterial structures have the advantage of being able to support resonances at any desired frequency based on their structural geometry, and these resonances are responsive to the changes in the thickness and the effective refractive index at their surface. Such resonances with extremely narrow linewidths enable measuring minute spectral shift caused by small changes in the thickness and refractive index of the surrounding media. In another example [259], multipolar plasmonic resonances at terahertz frequencies have been reported for designing ultra-sensitive sensors.

In this work, the relatively broad transmission spectrum of Bragg waveguide (45GHz) is modified by introducing a narrow spectral loss peak (3GHz). This is accomplished by introducing a geometrical defect in the first layer of the Bragg reflector. The spectral position of the loss peak is found to be highly sensitive to the optical properties of the defect layer, such as thickness and refractive index. The present work is inspired by our recent report using hollow-core Bragg fiber operating in the visible range for surface sensing applications [114]. It was demonstrated that a thin analyte layer deposited on the inner surface of the fiber core results in avoided crossing in the vicinity of the phase matching wavelength between the core-guided mode and the analyte layer bound mode. The wavelength of anticrossing, and as a consequence, fiber transmission spectra is strongly dependent on the analyte layer thickness, thus allowing monitoring of changes in the analyte layer thickness.

In order to improve the detection limit of such sensors, we employ a THz Bragg waveguide operating in an effectively single mode regime. By directly tracking the anticrossing frequency between the core-guided mode and the defect mode, which manifests itself as a sharp transmission dip within the relatively broad transmission window, we have significantly improved the detection limit compared to the THz waveguide sensors reported in the literature [168, 169]. In order to realize such sensors operating in the THz range, we use 3D stereolithography. The Bragg waveguide used in this work features a hollow core surrounded by a periodic sequence of high- and low-refractive index multilayers, namely, printing resin (PlasClear, Asiga) and air. The thickness of each bilayer is 512μm, with a predicted fundamental bandgap centered at 0.18THz. The waveguide core size of 4.5mm is chosen to ensure an effectively single mode operation within the fundamental bandgap region. In order to introduce a transmission dip with narrow linewidth inside of the original bandgap, we increase the thickness of the first layer in the Bragg reflector, thus introducing anticrossing (hybridization) between the core-guided mode and the lossy modes confined in the vicinity of the defect layer. For sensor calibration, we use PMMA films with different thicknesses attached to the inner surface of the waveguide core. Then, an example of THz resonant surface sensing using α-lactose monohydrate powder as the analyte is demonstrated experimentally. Simulations based on the finite element method (FEM) are conducted to validate the experimental results. The anticrossing phenomenon between the core-guided mode and defect mode is confirmed by imaging the modes propagated in the waveguide using a fiber-coupled THz microscopy setup. The Bragg waveguide sensor is

characterized using both time domain spectroscopy (TDS) and continuous wave (CW) spectroscopy setup, and we conclude that the CW setup with higher frequency resolution is more suitable for applications that require high sensitivities. The ability to tailor the spectral properties of the sensors by properly designing their geometric parameters means that our Bragg waveguides become a viable platform for a wide range of application, such as detection of molecular and bacterial interactions, study of surface kinetics, monitoring of powder analytes, etc.

It is important to highlight several advantages of the proposed sensing system, which uses resonant phenomenon in the THz waveguides versus more traditional ways for layer thickness and composition monitoring such as the free space transmission mode spectroscopy. In particular, compared to the free space transmission mode spectroscopy which monitors thin film properties by observing the phase variations in the THz wave passing through an analyte film, our waveguide sensor rather uses resonant interaction between its various guided and leaky modes in the alayte layer while employing an amplitude (not phase) detection modality. Amplitude detection requires considerably simpler (and cheaper) THz systems, at the same time, offer a comparable sensitivity compared to the state-of the art phase detection modality employed in the free space transmission mode spectroscopy. This is the major advantage for the development of practical THz systems for industrial monitoring and sensing applications. Secondly, we note that most of the current resonant THz sensors have relatively broad spectral features, thus, resulting in lower sensitivities. In our photonic bandgap THz waveguide-based sensors, the modal field in the hollow core is resonantly coupled to the field in the defect mode concentrated in the analyte layer. This coupling is strongly wavelength dependent as it relies on the modal anticrossing phenomenon. Moreover, the strength of the intermodal coupling (hence, the spectral width of the transmission peak) can be designed to be as small as desired by simply displacing the analyte layer into the reflector region away from the core. As a result, the resonant dip with narrow linewidth in the waveguide transmission spectrum can be used to resolve minute spectral shifts in the resonant dip positions caused by small changes in the defect layer thickness or refractive index, which allows an improved detection limit, compared other conventional setups. Note that in our system detection sensitivity is fundamentally limited only by the spectral resolution of the detector rather than by that of the resonant waveguide sensor. In particular, we demonstrate that for the same waveguide sensor designed to feature a ~3GHz transmission dip, when employing a CW THz system that offers sub-GHz spectral resolution, we get considerably higher detection

sensitivities compared to the case of using a standard TDS-THz system with >3GHz resolution. We note that, by using a CW THz setup [259] capable of 4MHz spectral resolution, the waveguide sensors discussed in this paper can be, in principle, designed for the detection of sub-100nm changes in the layer thickness. To our knowledge, this is virtually impossible to achieve with other more standard approaches. Thirdly, we note that waveguide-based sensing system offers an opportunity for seamless integration of various conduits for the delivery of analytes (e.g. liquids, powders, gases) into the optical setup. As an example, in this work, we demonstrate that the spinning hollow core waveguide with minor modifications in its geometry can be used to produce (via centrifugal force) and hold thin layers of powders for the detection of changes in their mass (thickness), which, to our best knowledge, has never been reported before. This sensing strategy is especially relevant for many practical applications, such as environmental monitoring, among others applications. Finally, we note that by adjusting the waveguide geometry, one can target specific frequency range of interest, and enrich the sensing scenarios. For example, as proposed in our manuscript, by designing the operation frequency of the sensor near the absorption peak of α-lactose monohydrate (at 0.53THz), one can simultaneously monitor the layer thickness and the lactose concentration in the powders using the anticrossing frequency and the absorption peak strength, respectively. Again, to our knowledge, this multi-parameter sensing modality has never been reported before, and it is beneficial for the design of versatile, and highly integrated sensors, which enables a comprehensive multi-parameter material characterization by a single device.

## 6.2 Design of an effectively single-mode THz Bragg waveguide

Single-mode operation gives many advantages for signal processing and sensing applications. The $HE_{11}$ mode in a Bragg fiber has a Gaussian-like field distribution, and is generally favored over the lowest loss $TE_{01}$ mode [224], because the $HE_{11}$ mode can be easily excited with a linearly polarized THz input beam. In this section, we start by designing a THz Bragg waveguide operating in an effectively single mode regime.

Figure 6.1(a) shows the cross section of the waveguide used in our work, which features a hollow core surrounded by a periodic sequence of high/low refractive index multilayers, namely, the printing resin and air. The thickness of each layer is designed to be 512μm, with a predicted fundamental bandgap center at 0.18THz, according to the basic theory of Bragg fibers [214]. This

frequency region is chosen due to the following reasons: first, there are no water vapor absorption lines in this region, and waveguide sensors operating in this range are, therefore, less influenced by the environmental conditions; second, a single mode Bragg waveguide operating in this frequency range (the corresponding wavelength is around 1.5mm) has a relatively large core size, which is an asset for practical sensing applications, as it simplifies the introduction of analyte into the waveguide core. Moreover, a relatively large waveguide core size is also essential for the efficient coupling of THz beams. The number of the bilayers in the Bragg reflector is ten. In order to maintain the mechanical stability of the Bragg reflector, a set of micro-bridges are introduced into the waveguide cross section, as indicated in Fig. 6.1(a). In order to guarantee consistent alignment of the Bragg waveguide sections during the cutback measurements, U-shaped holders (see Fig. 6.3) are used.

The most straightforward method to achieve an effectively single-mode operation is to reduce the waveguide core diameter until only one core-guided mode is supported. Reduction in the core size results in increase in the waveguide propagation loss, because the fields of the guided modes extend more into the waveguide cladding. Thus, not only the radiation loss due to finite number of bilayers in the reflector, but also the absorption loss due to the loss in the cladding material has to be considered. In order to achieve an effectively single-mode operation at the fundamental bandgap, we compute the band diagram of the Bragg waveguide at different core diameters using a commercial finite element software COMSOL. We note that the Bragg waveguide used in this section features a perfectly periodic reflector (no defect layer). For the frequency dependent refractive index and absorption loss of the reflector material, we use the polynomial fits in Eq. (B. 2) and Eq. (B. 3) (See Appendix B).

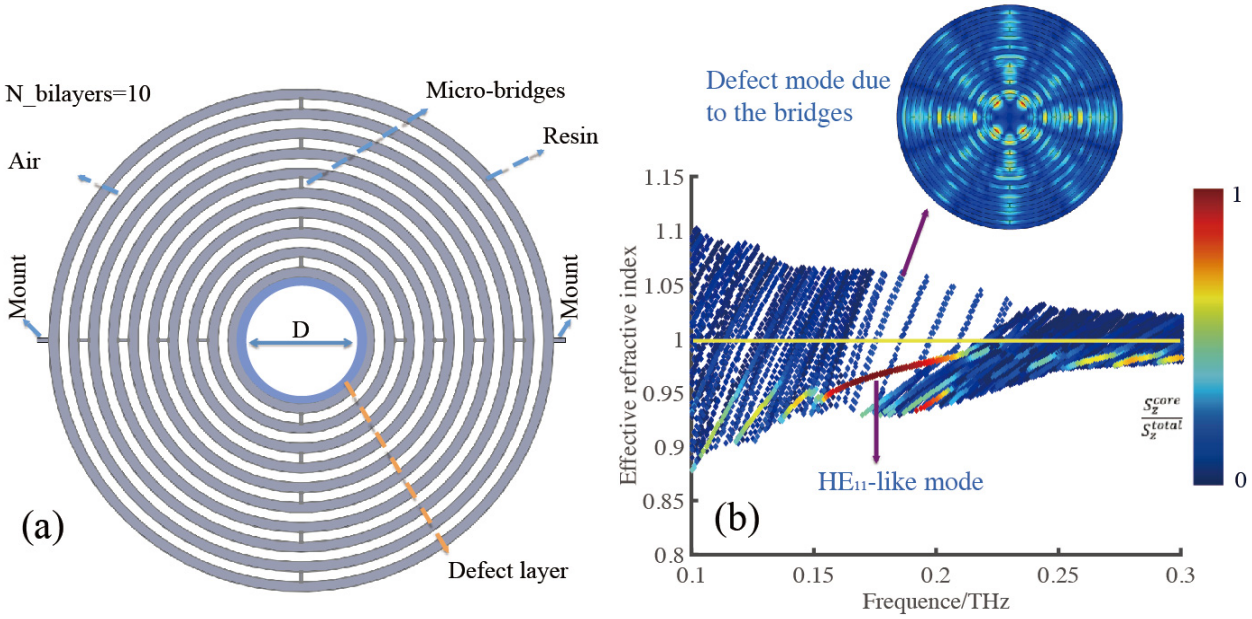


Figure 6.1 (a) Schematic of the THz Bragg waveguide. The gray region and white region represent the high refractive index layer (printing resin) and low refractive index layer (air), respectively. Both the resin and air layer have a thickness of 512μm. The multilayers are kept together with micro-bridge structures distributed uniformly along the waveguide cross section. The number of bilayers is 10. Two mounts at the waveguide periphery are introduced for convenient loading and aligning of the waveguide in the U-shaped holder. The light blue region is a defect layer in the Bragg reflector. (b). Band diagram of the Bragg waveguide with a core diameter of 4.5mm. The yellow solid line illustrates the air light line. Color of each dot indicates the fraction of power guided in the hollow core. The red-colored curve represents the $HE_{11}$-like mode. A typical defect mode due to the presence of the bridges is shown in the insert.

We start by computing the band diagram of the Bragg waveguide with a core diameter much larger than the operation wavelength (1.5mm at 0.2THz), and gradually reduce the core diameter until only the $HE_{11}$ mode is guided in the waveguide. In our simulations, the computational cell is terminated by a circular perfect-electric-conducting boundary located at the waveguide periphery. To exclude the modes of a continuum that are concentrated in the vicinity of the numerical boundary, we only present the modes that have more than 30% of the total power confined to an area delimited by a radius equal to the 2/3 of that of the waveguide outer boundary. We find that when the waveguide core diameter is reduced to 4.5mm, an effectively single $HE_{11}$ mode propagation can be achieved in the fundamental bandgap region (centered at

~0.18THz). In Fig. 6.1(b), we plot the modal effective refractive indices of the guided modes as a function of frequency in the range of 0.1-0.3THz. The color code indicates the fraction of the modal power guided within the hollow core. The blue color defines the modes with power localized mostly outside of the waveguide core, and the red color signals strong presence of the modal fields in the hollow core. The yellow solid line in the diagram is the light line of air with n= 1. As shown in Fig. 6.1(b), the bandgap, in fact, features several types of modes that can be identified as core-guided modes and defect modes. The core-guided modes are the two almost degenerate polarizations of the Gaussian-like $HE_{11}$ modes [red-colored curves in Fig. 6.1(b). The degeneracy is lifted due to the presence of bridges in the reflector structure. The same bridges lead to appearance of radiation modes that are present within the fundamental bandgap. Such modes have less than 20% of their modal power in the core, and they are difficult to excite [see the inset of Fig. 6.1(b), for example]. Therefore, the Bragg waveguide operates in an effectively single mode regime, when using a linearly polarized Gaussian beam. All the Bragg waveguides used in the following sections have a diameter of 4.5mm, in order to ensure an effectively single-$HE_{11}$ mode operation.

## 6.3 Bragg waveguide with a defect layer

It is well known that one can introduce narrow loss peaks into the bandgap region by introducing geometrical defects into the structure of a Bragg reflector [243, 244]. The geometrical defects in the reflector can confine localized states (defect modes) whose frequencies lie within the reflector bandgap. The defect modes can be considered as lossy Fabry-Perot (FP) cavity states localized in the vicinity of the geometrical defects. The optical properties of the FP cavity states are highly sensitive to the thickness of the geometrical defect. Thus, thicker defects (longer FP cavities) result in resonant states at lower frequencies. Similarly, thinner defects result in resonances at higher frequencies. In Bragg waveguides, the geometrical defects can be realized either by thinning a particular reflector layer or by making it thicker. In our experiments, we pursue the latter approach, as thicker layers are easier to realize experimentally due to finite resolution of our 3D printer, as well as mechanical stability considerations when dealing with very thin waveguide layers. As shown in Fig. 6.1(a), the light blue region represents a defect layer. It is formed by adding material on the inner surface of the waveguide core, which modifies the thickness of the first reflector layer.

To demonstrate this phenomenon, we compute the band diagram of a Bragg waveguide featuring a defect in the form of a thicker first reflector layer (thickness increase of 300μm). In the simulation, we limit the frequency region to 0.1THz to 0.3THz, where the Bragg waveguide operates in an effectively single $HE_{11}$ mode regime. As shown in Fig. 6.2(a), the introduction of a defect layer into the waveguide core results in anticrossing between the core-guided $HE_{11}$ mode and the modes guided predominately in the defect layer. We note that the defect modes are bound to the core/reflector interface, and thus, exhibit significant presence in the lossy cladding material [see mode C in Fig. 6.2(c)]. Meanwhile, the core-guided mode [see mode A in Fig. 6.2(c)] has most of the power guided in the low loss air-core region; therefore, its propagation loss is relatively small. Over a certain frequency range, the core-guided mode hybridizes with the defect mode. A hybridized mode is shown as mode B in Fig. 6.2(c), which is known as the anticrossing phenomenon. Owing to the anticrossing, the dispersion relation of the core-guided mode is significantly altered, as shown in the inset of Fig. 6.2(a). In the vicinity of the anticrossing frequency, there is a resonant power transfer from the core-guided mode into the defect mode, thus resulting in a significant increase in the waveguide propagation loss, and thereby resulting in a narrow resonant transmission dip inside the waveguide transmission bandgap. In Fig. 6.2(b), we present the loss spectrum of the fundamental $HE_{11}$ mode. As expected, the spectrum features two loss peaks inside of the waveguide bandgap, which correspond to the two anticrossing regions shown in Fig. 6.2(a).

Thus, by increasing the thickness of the first layer of the reflector, one can introduce guided modes into the defect layer. At the point of anticrossing between the dispersion relations of a lossy defect mode and that of a low-loss core-guided $HE_{11}$ mode, strong modal hybridization is observed, thereby resulting in strong increase in the propagation loss of the $HE_{11}$ mode in the vicinity of the anticrossing frequency. The frequency of avoided crossing depends strongly on the defect layer thickness [114]. Therefore, by tracking the shift in the anticrossing frequency (spectral position of the resonant dip), one can build THz waveguide sensors for monitoring changes in the physical/chemical state of the waveguide core surface.

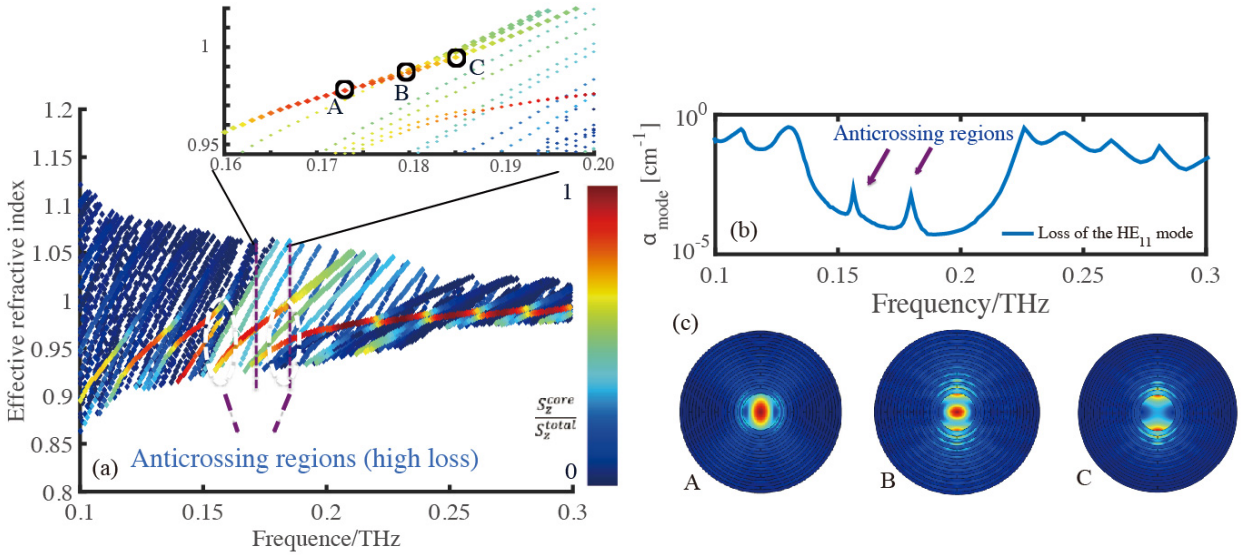


Figure 6.2 (a) Band diagram of the Bragg waveguide with a defect layer (thickness: 300μm). The two white dashed ellipses highlight the anticrossing regions between the core-guided mode and the defect modes. Insert: magnified view of the anticrossing region. In order to show the anticrossing phenomenon clearly, we use bigger dots to represent the core-guided $HE_{11}$ mode and the defect modes. The black circles refer to the different types of modes guided in the bandgap. (b) Propagation loss of the $HE_{11}$ mode. The two sharp loss peaks inside of the bandgap correspond to the two anticrossing regions highlighted as dashed white ellipses in (a). (c) The longitudinal flux distributions for those modes highlighted in the band diagram. A: Core-guided $HE_{11}$ mode. B: Hybridized mode. C: Defect modes localized in the immediate vicinity of the defect layer at the waveguide core/reflector interface.

## 6.4 THz Bragg waveguides with a perfectly periodic reflector (no defect)

We fabricate the THz Bragg waveguides using a 3D stereolithography system (Pro 2, Asiga), which has a transverse resolution of 50μm and a longitudinal resolution of 1μm (along the waveguide length). We first fabricate five sections of Bragg waveguides with a perfectly periodic reflector (without a defect). Each section has a length of 2.5cm [see Figs. 6.3(b-d)].

The transmission spectra are characterized using a terahertz Time Domain Spectroscopy (TDS) setup shown in Fig. 6.3(a) and detailed in [241]. The setup comprises a frequency doubled femtosecond laser (Ti: Sapphire laser, 90fs, repetition rate of 100MHz, Menlo System) used as a

pump source and two identical low-temperature grown GaAs photoconductive antennas used as the THz emitter and detector. A near infrared (NIR) laser pulse is split into two parts by a beam splitter. One part is focused onto a photoconductive emitter for the generation of THz pulse. The THz pulse is then collimated and focused onto the sample by a pair of parabolic mirrors. After passing through the sample, the THz beam is re-collimated and focused onto the detector. The other part of the NIR laser goes through a variable delay line and ultimately terminates on the detector. The delay line allows the THz pulse to be mapped as a function of time. The photocurrent in the detector is measured with a lock-in amplifier to ensure a good signal-to-noise ratio. The operating frequency range is 0.1-3.0THz. The parabolic mirror that collimates the beam after the sample is mounted on the translation rails. This arrangement allows easy insertion of the THz waveguides and guarantees that both the input facet and the output facet are placed at the focal points of the parabolic mirrors. The Bragg waveguide under test is fixed in a U-shaped holder of equivalent length [see Figs. 6.3(b) and 3(c)]. The cross section of the fabricated Bragg waveguide with a perfectly periodic reflector is shown in Fig. 6.3(d). The experimentally measured average thicknesses of the high refractive index resin layer and the micro-bridge are 512μm and 145μm [see Figs. 6.3(e) and 3(f)], respectively, which are in good agreement with the designed values. The U-shaped holders are mounted on a sliding track, which is placed between the two parabolic mirrors. To prevent excitation of the cladding modes, an iris with a hole-diameter of 4.5mm is fixed at the waveguide input end, and an aluminum foil with a hole-diameter of 4.5mm is glued on the holder at the output facet. The first holder section is fixed in the focal point of the stationary parabolic mirror (PM1), thereby ensuring that the input facet of the Bragg waveguide is also at the focal point of PM1.

In the experiment, five holder sections, each hosting a 2.5cm-long waveguide, are removed one by one. During each measurement, the output facet of the holder section (together with the Bragg waveguide) is always fixed in the focal point of the PM2 by adjusting the movable stage. Therefore, waveguides of 12.5cm, 10cm, 7.5cm, 5cm, and 2.5cm are measured. The reference is acquired by removing all the holder sections (together with the waveguide sections), and then moving the PM2 so that the aperture becomes in its focal point.

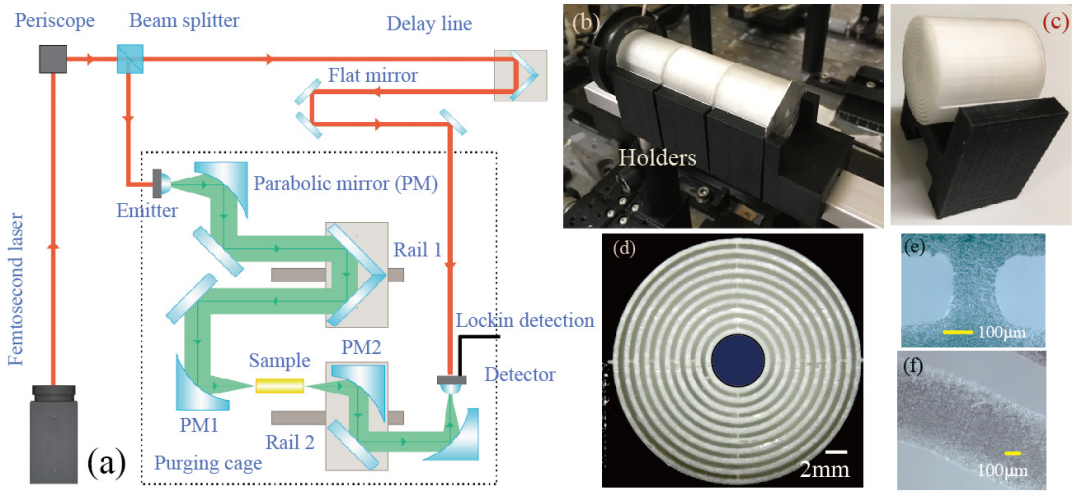


Figure 6.3 (a) Schematic of the THz-TDS setup for characterizing the transmission properties of the THz Bragg waveguides. A mirror assembly (rail 2) can translate the output focal plane to accommodate the waveguides of various lengths. The femtosecond laser pulse is shown in red and the THz pulse is shown in green. PM1: fixed parabolic mirror with a focus at the waveguide input facet. PM2: movable parabolic mirror, which is displaced every time when the waveguide section is removed in order to keep the focal point at the waveguide output facet. (b) Three sections of the Bragg waveguides (white) mounted in the U-shaped holders (black). Both the input facet and the output facet of the Bragg waveguides feature an aperture with the size equal to that of the waveguide core. (c) Close-up view of one section of Bragg waveguide mounted in the U-shaped holder. (d) Cross section of the printed Bragg waveguide with a uniformly periodic reflector. (e) Magnified view of the micro-bridge. (f) Magnified view of the high refractive index resin layer.

In Fig. 6.4, we present the cutback measurements of the transmission spectra through the Bragg waveguides with different lengths. The experimentally measured fundamental bandgap is centered at 0.18THz, which is in good agreement with that of the simulation. Next, the transmission loss of the Bragg waveguide with a uniform reflector is found by comparing the transmission spectra through waveguides of different lengths (cutback method). In Fig. 6.4(b), we plot the calculated propagation loss of the hollow-core Bragg waveguide in the frequency region between 0.1THz and 0.5THz. We note that, at the fundamental bandgap gap center position (0.18THz), the propagation loss is ~0.12 $cm^{-1}$, which is significantly smaller than the corresponding bulk absorption loss of the reflector material at the same frequency (~1 $cm^{-1}$).

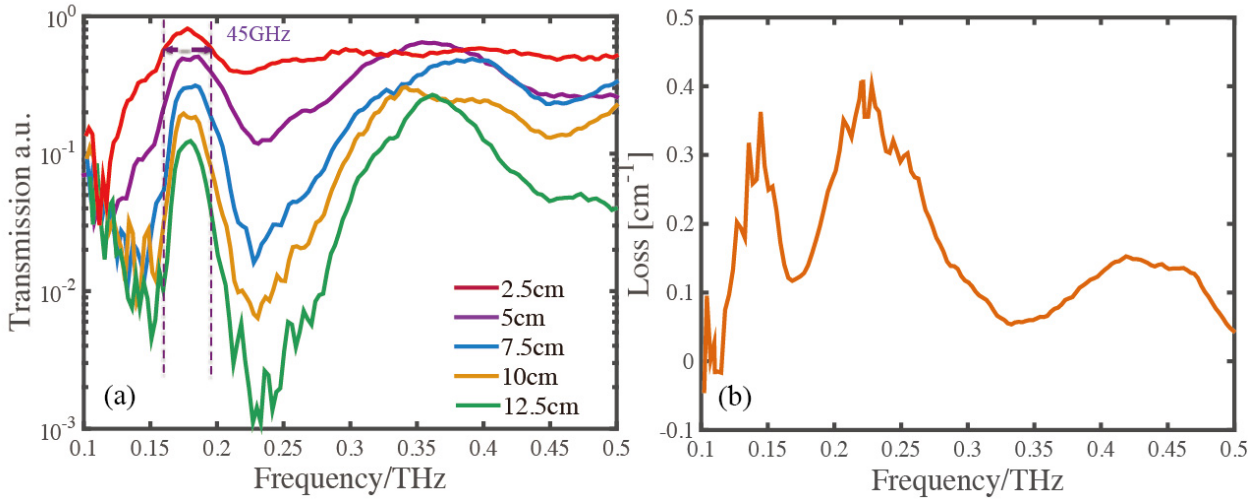


Figure 6.4 (a) Measured transmission spectra of the THz Bragg waveguides with uniform periodic reflector for different waveguide lengths (2.5cm, 5cm, 7.5cm, 10cm, and 12.5cm). The bandwidth (FWHM) of the fundamental bandgap of a Bragg waveguide is ~45GHz. (b) Calculated propagation loss of the hollow-core Bragg waveguide using the cutback method.

## 6.5 THz Bragg waveguides with a defect layer in the reflector

Next, we introduce narrow resonant loss peaks into the Bragg waveguide transmission spectra by introducing a defect layer with thicknesses of 200μm, 300μm, and 400μm, respectively. Each Bragg waveguide has a length of 2.5cm. Then, we characterize the transmission spectra of the fabricated waveguides with defect layers using the same setup and methodology as presented in Section 6.4. In Fig. 6.5(a), we plot the experimentally measured transmission spectra for the Bragg waveguides featuring defect layers of different thicknesses. As predicted, the introduction of a defect layer results in pronounced anticrossings between the core-guided mode and the defect modes localized in the vicinity of the defect layer. The two sharp transmission dips observed in the transmission spectra can be well interpreted by the two anticrossing regions as presented in Fig. 6.2. When the thickness of the defect layer is increased from 200μm to 400μm, the anticrossing frequency shows a blue frequency shift. We note that the two resonant dips in the waveguide transmission spectra correspond to anticrossing of the core-guided mode with the two different defect modes. Generally, due to distinct electric field distributions in these two defect states, we expect that sensitivity of the two resonant peaks to changes in the analyte layer parameters will also be different. In Fig. 6.5(b), we plot frequency of the two resonant dips found

at the right edge (dip 1) and the left edge (dip 2) of the bandgap as a function of the defect layer thickness, and a linear dependency is well observed for both cases. The experimentally obtained surface sensitivity to changes in the thickness of the first reflector layer is found to be 0.12GHz/μm and 0.115GHz/μm for the resonant dip 1 and dip 2, respectively. The experimental results agree well with the theoretically calculated surface sensitivities of $HE_{11}$ mode [see dotted lines in Fig. 6.5(b)]. In what follows, we use the resonant dip 1 with higher sensitivity in order to perform the sensing of different analytes. Nevertheless, we note that there is alternative sensing modality according to which, one could track changes in the inter-peak spectral separation, rather than the spectral position of one of the two individual peaks. The advantage of the two-peak methodology is that one of the peaks serves as a natural reference for the other one, thus allowing for mitigating various sources of spectral noise. However, in order to make this sensing scheme effective, one has to ensure that the two peaks have significantly different sensitivities to changes of the measurand, thus resulting in appreciable inter-peak spectral changes when analyte optical properties are varied. This implies that the structure of the sensor has to be judiciously designed to realize this condition. Currently, we are investigating the two-peak modality in more details, and we will present our findings in the future works.

The two resonant dips feature narrow linewidths. For example, the linewidth of the transmission dip of the Bragg waveguide with a defect thickness of 300μm is 9GHz, which is five times smaller than that of the bandgap bandwidth. Additionally, we note that the quoted linewidth of the resonant dip is inferred from the measurements performed using the TDS system, which has a spectral resolution of 3GHz for our system. As we will present later in Section 6.9, by using a continuous wave THz spectroscopy setup with sub-1GHz spectral resolution, the actual resonant dip linewidth is much narrower.

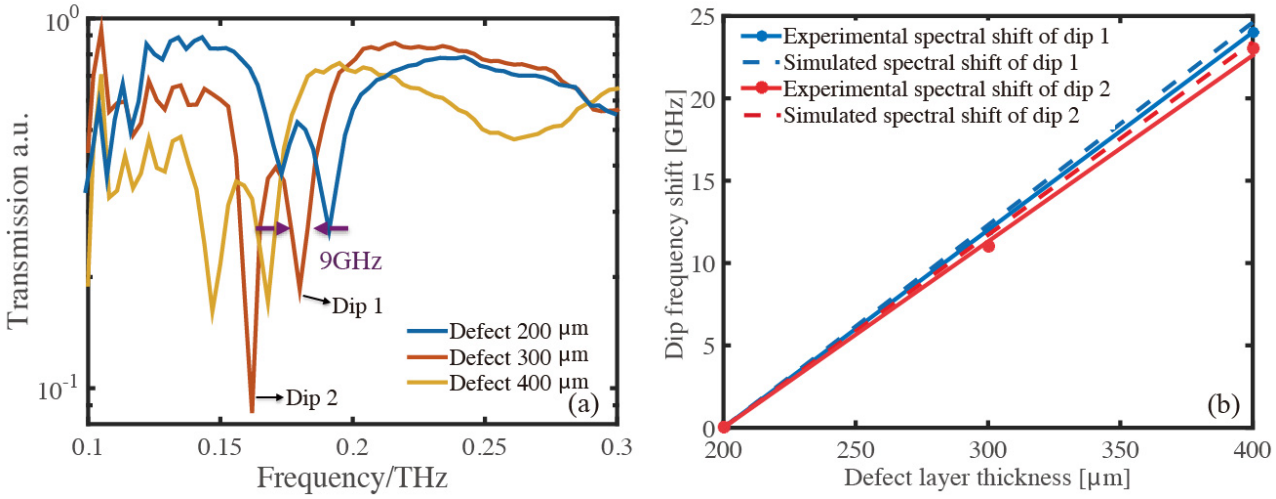


Figure 6.5 (a) Measured transmission spectra of the THz Bragg waveguide featuring a defect layer of different thicknesses (200μm, 300μm, and 400μm). (b) Experimental and theoretical spectral shifts of the two transmission dips as a function of the defect layer thickness.

## 6.6 THz Bragg waveguides for monitoring of the optical properties of thin films

As a practical demonstration, we apply the proposed THz Bragg waveguide to detect changes in the thickness of a PMMA film attached onto the waveguide inner surface. This is accomplished by tracking the spectral position of the narrow resonance within the Bragg waveguide bandgap. This sensor type can be used, for example, to study degradation of the analyte layer properties due to flow of the reagent vapors or other reactive substances.

We choose the THz Bragg waveguide with a defect layer of 300μm in the Bragg reflector as the sensing platform. In our experiment, PMMA films with two different thicknesses (50μm and 100μm) are manually inserted into the waveguide core. In order to avoid the air gap between the PMMA film and the waveguide core inner surface, we use a rectangular piece of the PMMA film with the length equal to that of the waveguide and the width matched closely to the perimeter of the waveguide core. The PMMA films used in this work are rigid enough to maintain their shapes and adhere tightly to the core inner surface under the stress caused by the round shape of the core. In Fig. 6.6(a), we plot the experimental transmission spectra of the Bragg waveguides with a PMMA film of different thickness, revealing that, with the increase of

the PMMA film thickness, the dip spectral position features a blue frequency shift. In Fig. 6.6(b), we plot frequency of the resonant dip found at the right edge of the bandgap as a function of the PMMA layer thickness, and a linear dependency is observed. The experimentally achieved surface sensitivity, in this case, is found to be 0.1GHz/μm. We also calculated the surface sensitivity of the $HE_{11}$ mode by assuming that the value of the PMMA film refractive index is 1.61 [260]. As shown in Fig. 6.6(b), the experimental achieved results show a good agreement with our simulation results.

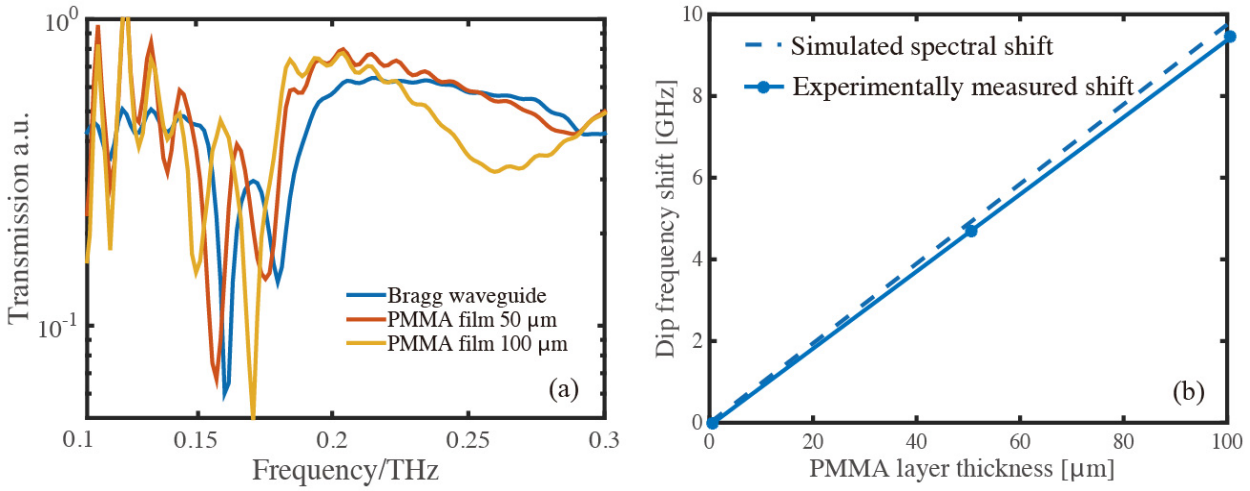


Figure 6.6 (a) Measured transmission spectra of the THz Bragg waveguide (with a 300μm defect layer), when PMMA films of different thicknesses (50μm and 100μm) are inserted into the waveguide core. (b) Experimental and theoretical spectral shift of the transmission dip found at the right edge of the bandgap as a function of the PMMA layer thickness.

We note that the anticrossing frequency depends on both the thickness and the refractive index of the target analyte. So far, we have investigated the effect of the analyte layer thickness on the sensor response, considering that the analate refractive index is fixed. An interesting question is whether the current sensor can be modified for the direct measurement of the analyte refractive index. In fact, in order to effectively and reliably extract the refractive index of the target analyte, one would first need to fix the analyte layer thickness and then, calibrate the sensor with various values of analyte refractive indices. However, the major challenge in this approach is how to maintain the same thickness for various analytes during calibration. We note that for liquid and gaseous analytes, their thickness can be fixed via introduction of the well-defined, analyte-filled microfluidic channels into the sensor structure. This is, in fact, a work in

progress that we are currently undertaking in our lab, and, we are planning to report on the results in the nearest future.

## 6.7 THz Bragg waveguides for monitoring of the optical properties of powders

Here, we apply our waveguide sensor to detect thickness changes in the powder analyte, namely, α-lactose monohydrate (density: ~1.59g/cm2, 5989-81-1, Sigma-Aldrich), which is a common excipient in the pharmaceutical and food industry [245]. In the experiment, we choose the THz Bragg waveguide with a defect thickness of 300μm in the first layer of the Bragg reflector as the sensing platform (length: 2.5cm). We employ the centrifugal force to disperse the lactose powder analyte onto the waveguide core surface by rotating the waveguide. In particular, as shown in Fig. 6.7(a), the Bragg waveguide is first clad with a 3D printed tube [black region in Fig. 6.7(a)] to enhance the mechanical robustness and stability during the fast rotation. The tube is inserted into a bearing (inner diameter: 1 inch; outer diameter: 2 inches), which is fixed into a standard lens mount (inner diameter: 2 inches, LMR2). The rotation of the Bragg waveguide is accomplished by connecting it to a motor via a strap (see Supplementary Visualization 1). During the experiment, in order to prevent the leakage of the lactose powder from the waveguide core during the rotation, an aluminum foil with a hole diameter of 4.2mm is glued on both the waveguide input and output facets, which is somewhat smaller than the core diameter of the Bragg waveguide (4.5mm).

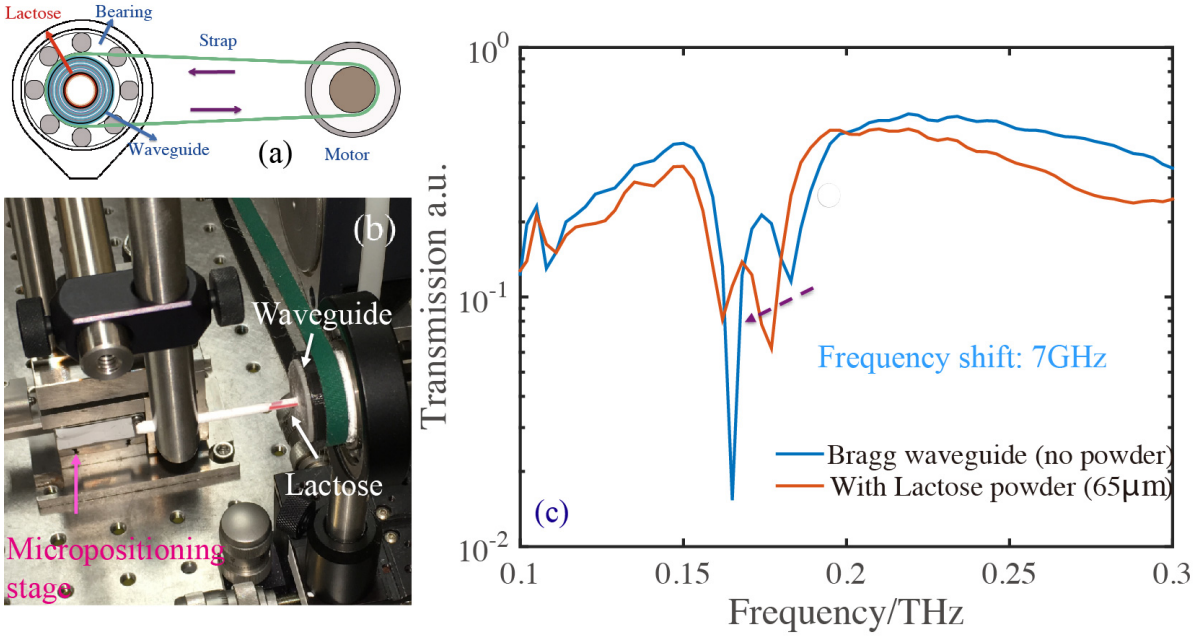


Figure 6.7 (a) Schematic of the setup used for monitoring of the thickness of powder analytes deposited on the inner surface of a rotating Bragg waveguide (see Visualization 1). (b) Semi-automatic loader used for feeding lactose powders into the rotating waveguide (see Visualization 2). (c) Measured transmission spectra of the THz Bragg waveguide (with a 300μm defect layer), when 0.042g α-lactose monohydrate powder analyte (thickness of ~65μm) is deposited uniformly onto the waveguide inner surface.

In order to ensure formation of uniform lactose films on the waveguide inner surface, we, therefore, pursue several approaches. First, in our setup, we carefully align the waveguide to be as horizontal as possible. Then, during the measurements, we load the lactose powder along the axis of the rotating waveguide using a semi-automatic feeder. During the waveguide rotation, we visually check that the powder has been uniformly dispersed along the waveguide. Beyond the visual inspection we have no means of direct confirmation that the lactose powder is dispersed uniformly. Nevertheless, we are still confident that the resultant film is uniform using an indirect observation method based on the resonant dip width. Particularly, we note that in case of a significant thickness variation of the analyte layer along the waveguide length, the transmission spectrum would feature transmission dips at variable spectral locations related to the local analyte layer thickness. This would result in considerable broadening of the transmission dip. In our experiments both with the low-resolution TDS and the high-resolution CW setups, we do not

observe any reliably measurable dip broadening compared to the reference measurement with an empty waveguide. This makes us to conclude that the thus realized power analyte layers are uniform.

In our experiment, we fill the Bragg waveguide core with 0.042g lactose powders, and then, we characterize the transmission spectrum of the waveguide when it is rotated at a speed of 1500RPM (revolutions per minute). As very small amounts of powder are used in the experiment, and the waveguide core size is relatively small, we supplement the basic sensor design with a semi-automatic feeder system [see Fig. 6.7(b)] that comprises a 3D micro-positioning stage and a straw-like delivery attachment (see Supplementary Visualization 2). The use of such a feeder is necessary in order to realize a reliable and consistent powder analyte delivery into the sensor. In Fig. 6.7(c), we present the transmission spectra of the Bragg waveguide sensor before and after dispersing the powder analyte onto the waveguide inner surface. We find that the presence of 0.042g lactose powders causes a frequency shift of 7GHz in the resonant dip position, which reveals a spectral sensitivity of 166GHz/g. In fact, by assuming that the lactose powder is uniformly dispersed onto the waveguide inner surface, the resultant thickness of the lactose film is estimated to be 65μm, considering that the waveguide has a core diameter of 4.5mm and a length of 2.5cm. In this case, the spectral sensitivity of the Bragg waveguide to changes in the thickness of lactose powders is found to be 0.11GHz/μm.

In practical industrial applications, in order to capture the target powder analyte onto the waveguide inner surface, one can also pursue the following two approaches: one is to modify the waveguide inner surface with an absorbing layer, which can bind and accumulate specific targets; another alternative is to introduce porous structures into the defect layer. Efficient trapping of micro-particles or powders in the porous structures results in refractive index changes in the defect layer, which can be correlated to the spectral shifts in the resonant dip positions. Furthermore, to enable specific detection of analytes, one can track the specific absorption features that “fingerprint” the analytes. In our case, by designing the operation frequency of the sensor near the absorption peak of α-lactose monohydrate (at 0.53THz), one could possibly simultaneously monitor the layer thickness and the lactose concentration in the powders using the anticrossing frequency and the absorption peak strength, respectively. This modality, however, has to be further researched.

## 6.8 Imaging of the modes propagating in the THz Bragg waveguides

To confirm excitation of the defect modes in the vicinity of the anticrossing frequency, we perform the modal imaging at the waveguide output end using a fiber-coupled THz microscopy setup. The schematic of the modal imaging setup is illustrated in Fig. 6.8(a).

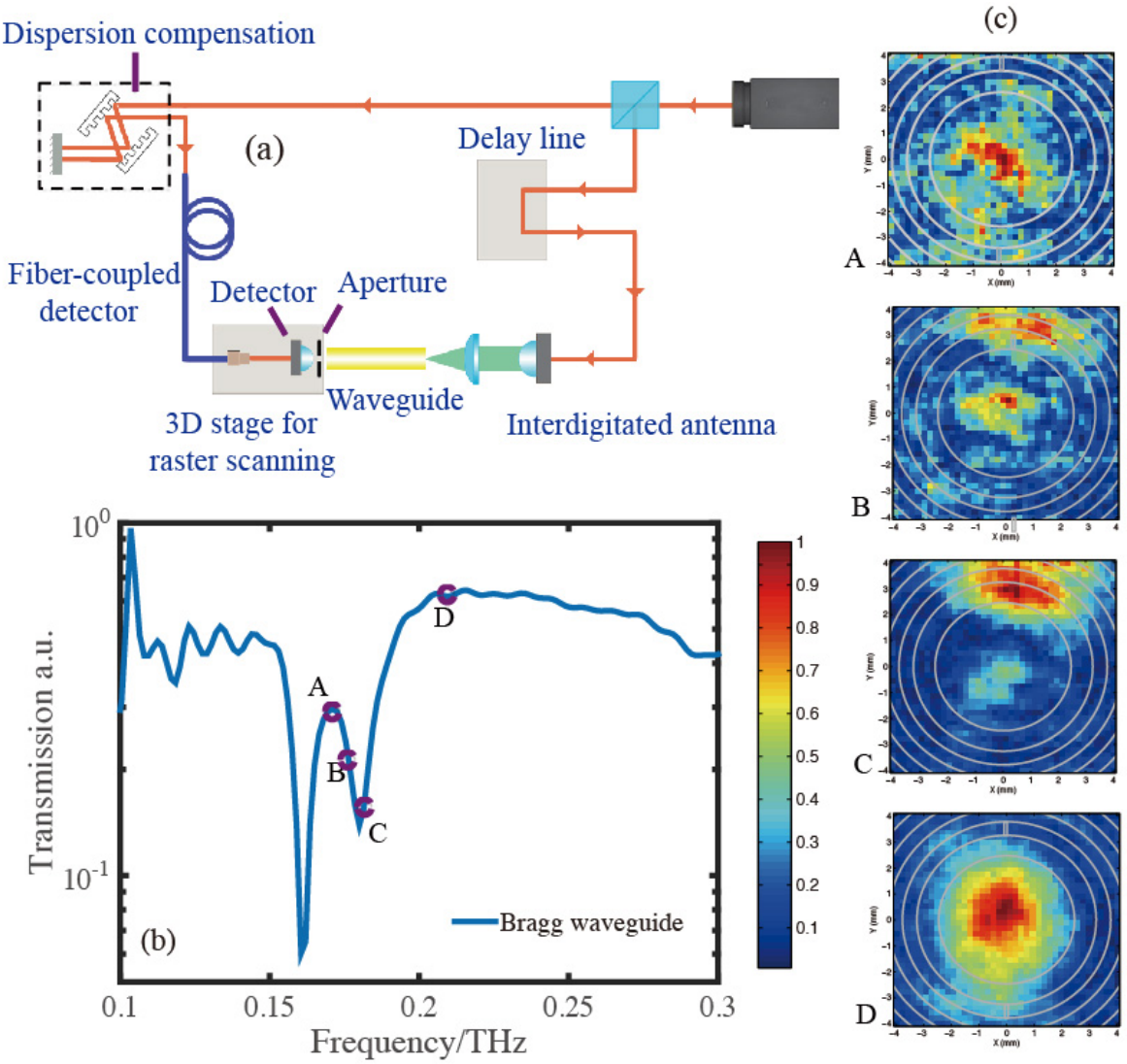


Figure 6.8 (a) Schematic of the fiber-coupled THz modal imaging system. (b) Transmission spectrum of the Bragg waveguide (with a 300μm defect layer). (c) Spatial electric field distribution $|E_x|$ of the four modes marked in (b) acquired at the output of the waveguide.

A photoconductive antenna is used as the detector, and a free space coupled high power interdigitated antenna is used as the emitter. The photoconductive antenna has a silicon lens and

an aperture of 1mm mounted in front of the lens. In order to compensate the pump pulse broadening due to the dispersion in the fiber, a grating-based, dispersion-compensation system is used before coupling the near-infrared pulse into the polarization-maintaining fiber [246]. The output end of the fiber is placed on a 3D stage, and a fiber collimator is used to couple the output of the fiber into free space to excite the detection antenna. The detection antenna is raster scanned with a step resolution of 250μm across the output end of a waveguide to perform the modal imaging. Because the photoconductive antenna is only sensitive to the polarization parallel to the dipole electrode, we only measure the spatial electric field distributions ($|E_x|$) in this experiment.

A Bragg waveguide (with a defect thickness of 300μm) is used in this experiment. In Fig. 6.8(b), we plot the transmission spectrum of the waveguide measured using the TDS system. In Fig. 6.8(c), we plot the spatial electric field distributions of the four modes marked in Fig. 6.8(b). As expected from the simulation results, in the vicinity of the anticrossing frequency, the core-guided mode (mode A) hybridizes with the defect mode (mode C). Mode B is a hybridized mode. We note that the asymmetric profile of the defect mode is probably due to a misalignment and off-center coupling of the THz beam to the Bragg waveguide in the experiment. As the frequency moves far from the anticrossing region, the modal profile becomes a Gaussian shape in the electric field distribution, which agrees well with the $HE_{11}$ mode structure. This confirms an effectively single-$HE_{11}$-mode propagation in the fundamental bandgap region of the Bragg waveguide.

## 6.9 Resolution enhancement using continuous wave THz spectroscopy

In a THz-TDS setup, the frequency resolution of the Fourier transform of a THz waveform is fundamentally limited by the span of the time delay sweep, which, in turn, is typically limited to 200-300ps due to appearance of echoes in the THz time trace. These are caused by the multiple reflections in the silicon lens and antenna substrates. In a typical THz-TDS setup, the resolution is, therefore, limited to ~1-3GHz [192], thus setting the sensor detection limit.

Continuous wave terahertz spectroscopy systems based on the photo-mixing effect constitute a viable alternative to the TDS systems for high-resolution spectral characterizations. The CW-terahertz generation process is based on heterodyne difference frequency generation in

the high-bandwidth photoconductors: The beat signal of the two lasers is converted into a CW-terahertz wave exactly at the difference frequency of the lasers. In comparison to time-domain terahertz systems, a CW-terahertz setup enables spectrally selective measurements and, at the same time, offers a significantly improved frequency resolution and signal power. The frequency resolution of CW systems is determined by the linewidth of the laser sources, which is typically in the 10MHz range [247, 248]. Finally, the cost of such systems is comparable to the cost of the TDS systems.

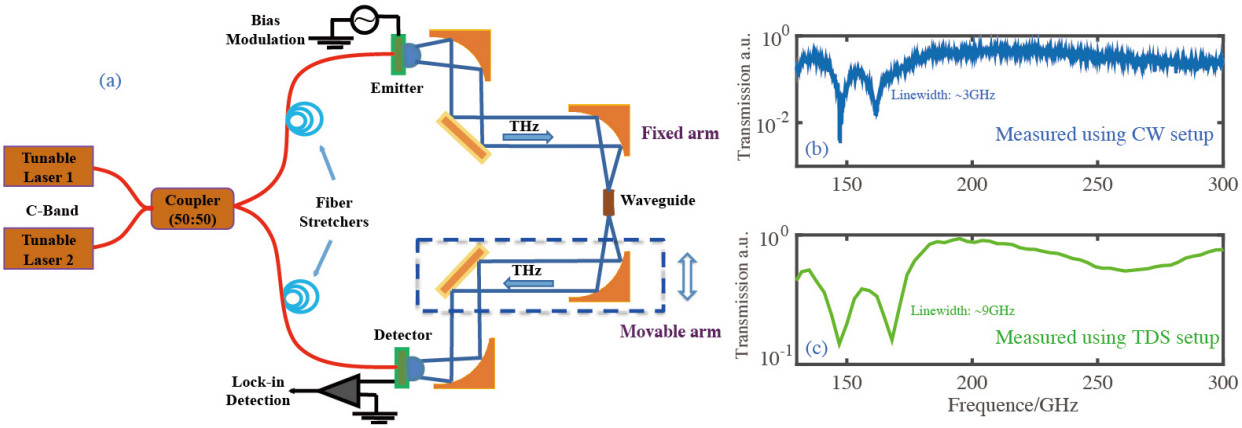


Figure 6.9 (a) Schematic of the THz-CW spectroscopy setup for characterizing the transmission spectra of the THz Bragg waveguides. Comparison of the transmission spectra of the Bragg waveguide (with a 400μm defect layer) measured using (b) THz-TDS and (c) THz-CW setups.

For comparison, in this section we characterize the transmission spectra of the hollow-core Bragg waveguide sensor using a continuous wave terahertz spectroscopy system from Toptica Photonics. The schematic illustration of this setup is shown in Fig. 6.9(a). The setup has two distributed feedback (DFB) lasers with slightly different center wavelengths and balanced power (~30mW for each laser) operating in the telecommunication range. A 50:50 coupler combines and splits the two wavelengths equally into the emitter and detector arms. In order to measure the phase information, each arm features a fiber stretcher. The two stretchers operate with opposite signs, thus enhancing the optical path difference. Each fiber stretcher consists of a polarization-maintaining single-mode fiber wound around a piezo actuator. The generated THz waves are modulated with a bias voltage for lock-in detection.

In Fig. 6.9(b), we plot the transmission spectrum of a Bragg waveguide (with defect thickness of 400μm) measured using the CW system with a reliable resolution of 40MHz. For

comparison, we also plot the spectrum of the same waveguide characterized using the TDS setup in Fig. 6.9(c) with time traces of 300ps. Overall, the spectrum of the Bragg waveguide sensor measured using the CW setup shows good agreement with that measured using the TDS setup. More importantly, we note that the linewidth of the resonant dip characterized by the CW setup is only 3GHz, which is much narrower than that measured using the TDS setup (9GHz). The corresponding Q factor of the sensor is therefore 55. Although the quality factor of the resonant dip is not the highest for a sensor operating in the THz range [249], the 3GHz linewidth, to the best of our knowledge, is among the narrowest measured for any resonator in the THz range [250-252]. With the experimentally demonstrated sensitivity of 0.1GHz/μm and narrow linewidth of the spectral features, our Bragg waveguide sensor can be used for the detection of targets with size ranging from ~100nm to hundreds of microns by considering that the practical frequency resolution of a continuous wave THz setup is in the 10MHz range. This is of great significance for biosensing applications, when precision detection of targets, such as bacteria, cell, and other macro-molecular layers, is needed

## 6.10 Sensor detection limit for powder analytes using the THz-CW setup

We now evaluate the detection limit of the resonant Bragg waveguide sensors when used for monitoring thickness of the powder analytes. In this study, we employ the continuous wave THz setup that offers high spectral resolution in order to resolve minute changes in the sensor spectral response when loading small amounts of lactose powders. Particularly, the powder is introduced in small amounts with mass increments of 0.002g (corresponding thickness increase is 3μm) into the rotating Bragg waveguide using a semi-automatic feeder described earlier. Totally, three measurements are performed for the net masses of the lactose powder equal to 0.002g, 0.004g, and 0.008g that correspond to the analyte layer thicknesses of the 3μm, 6μm, and 12μm on the inner core surface.

In Fig. 6.10(a), we present the transmission spectra of the Bragg waveguide sensor before and after dispersing the powders onto the waveguide inner surface. We note that in order to resolve the minute spectral shifts caused by the small amounts of lactose powders, we perform the Fourier transform of the transmission spectra of the waveguide sensor and remove the high

frequency fluctuations in the signal that arises due to the standing waves between the waveguide facet and the detector. We find that the increase of lactose powder mass causes a continuous frequency shift in the resonant dip positions. In Fig. 6.10(b), we plot frequency of the resonant dip found at the right edge of the bandgap as a function of the lactose layer thickness, and a linear dependency is observed. The experimentally achieved surface sensitivity is found to be 0.14GHz/μm, which is somewhat higher than that we have achieved using the TDS setup. This is probably due to the enhanced spectral resolution of the CW setup. Moreover, in order to theoretically validate the experimental results, we also calculate the surface sensitivity of the $HE_{11}$ mode. The refractive index of the α-lactose monohydrate is found in [264] as is taken to be 1.78 in our simulations. The theoretical surface sensitivity of the Bragg waveguide sensor is shown in Fig. 6.10(b) and we observe a good agreement between the theoretical and experimental results.

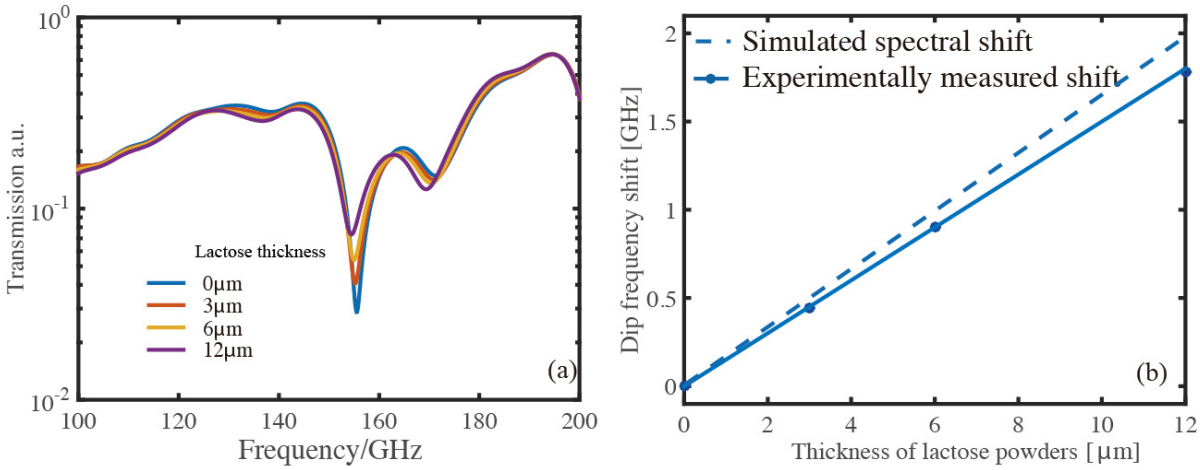


Figure 6.10 (a) Measured transmission spectra of the THz Bragg waveguide (with a 300μm defect), when different amounts of lactose powders are loaded into the core (corresponding analyte layer thicknesses are 0μm, 3μm, 6μm, 12μm). (b) Experimental and theoretical spectral shift of the transmission dip found at the right edge of the bandgap as a function of the layer thickness.

## 6.11 Discussions

### 6.11.1 Comparison of the sensor to free space transmission mode THz spectroscopy

Thin film characterization using THz waves is recognized as an important technique, which has many practical applications. Thin films that are particularly relevant in the development of high-speed electronics [253] include epitaxial semiconductors, dielectric insulators, and graphene, among others. Biosensing is another field where thin film detection is of great significance. Target substances such as bacteria, cells, monolayers, or ligands, are typically studied in the form of thin films on top of functionalized substrates [254].

One of the simplest configurations used for THz thin film sensing is based on a free space transmission mode spectroscopy [255]. Changes in a thin dielectric film can be detected by observing the phase variations in the transmission spectrum. However, this technique has many fundamental and practical challenges. Since thin samples offer a very short interaction length in such configurations, they only impart little modifications to the waves passing through it. The measurement accuracy is significantly reduced, when the measurement uncertainties become relatively strong compared to the phase changes induced by the samples. Only if the confidence intervals of the sample and reference measurement are well separated, can it then be inferred that a sample is reliably detected [255]. It is reported that a THz transmission mode spectroscopy system can be used to detect thin polymer films with thickness down to ~2μm by observing the phase change between the averaged reference and sample measurements. However, in practice, for reasonable accurate characterization, it is recommended that the thin film thickness be at least ten times above this limit.

The lack of resonant interaction between the THz waves and the samples is the principal factor that limits the resolution of conventional transmission mode spectroscopy. In our THz waveguide sensor, the modal field in the core is resonantly coupled to the field in the defect mode in the anticrossing spectral region. The resonant dip with narrow linewidth in the waveguide transmission spectrum can be used to resolve minute spectral shifts in the resonant dip positions caused by small changes in the defect layer thickness or refractive index, which allows an improved detection limit, compared to that of the conventional transmission mode spectroscopy

setups. With the experimental demonstrated sensitivity of 0.1GHz/μm and a reliable spectral resolution of 40MHz in our CW setup, the THz Bragg waveguide sensor can be used for the sensing of thin films with sub-micron thicknesses (400nm).

### 6.11.2 Practical applications of the THz waveguide sensors

Currently, THz sensing of powder analytes has been extensively applied for the discovery of illicit drugs [12], and explosive or hazardous powders [13] via their fingerprint THz spectra. The presented THz Bragg waveguide sensor could potentially distinguish various powders if a selective binding of specific powders to the waveguide inner surface could be realized, or, when the sensor is operated in the vicinity of the spectral "fingerprint" absorption lines. Other potential applications of the waveguide sensors include industrial or environmental pollution detection, as well as monitoring of dynamical generation of solid or liquid compounds in chemical reactions. For example, ammonia gas interacts with hydrochloric acid, producing particles of chloride ammonium. Moreover, such waveguide sensors can be used for monitoring the precipitation of objects on the core surface, thickness variations due to flow of reagent vapors, and changes in the layer refractive index caused by chemical process. Finally, the proposed THz Bragg waveguide sensor could also be used as a viable platform for efficient and label-free detection of bacteria pathogens. By functionalizing the surface of the waveguide core with specific phages, selective detection of pathogenic bacteria could be realized with the proposed THz Bragg waveguide sensor. Changes in the resonant dip positions could be directly correlated with the concentration of bacteria samples. These are all the new exciting directions that we are currently exploring in our laboratories.

## 6.12 Conclusions

In this paper, we propose using 3D printed hollow-core THz Bragg waveguides with defect layers for resonant surface sensing applications. It is demonstrated that by introducing a defect into the first layer of the Bragg reflector, a strong and spectrally narrow dip appears in the waveguide transmission spectrum. The dip is due to the anticrossing phenomenon between the core-guided mode and a mode localized in the defect of the Bragg reflector. By tracking the anticrossing frequency, which manifests itself as a transmission dip with narrow linewidth in the waveguide transmission spectrum, one can detect changes in the geometrical or optical properties

of the defect layer. Both the THz-TDS and THz-CW setups are used in our work, and we conclude that CW setup with higher frequency resolution is more suitable for applications that require high sensitivities. The experimentally achieved linewidth of the resonant dip (with a THz CW setup) is only 3GHz, which is among the narrowest measured for any resonator in the THz range. As a practical demonstration, we apply this sensor for detecting PMMA films with different thicknesses loaded on the inner surface of the waveguide core. Target film thickness can be directly correlated to the position of the anticrossing frequency. A surface sensitivity of 0.1GHz/μm is achieved experimentally. Moreover, an example of THz resonant surface sensing using α-lactose monohydrate powder as the analyte is demonstrated experimentally using a setup with rotating waveguide, where the powders are spread uniformly on the waveguide core surface via the action of centrifugal force. We demonstrate that our sensor is capable of reliable detection of 3μm change in the analyte layer thickness, which is among the lowest ever reported for THz sensing. Finally, the anticrossing phenomenon between the core-guided mode and the defect mode is directly confirmed by imaging the modes propagated in the waveguide using a THz microscopy setup.

# CHAPTER 7 GENERAL DISCUSSIONS

In the previous chapters, we have proposed and experimentally demonstrated hollow-core photonic Bragg fibers for bulk refractometry of commercial liquids and surface sensing applications including *in situ* monitoring of surface dynamics, as well as thickness detection of bio-layers and powder analytes. Both theoretical analysis and experimental demonstrations have been performed to characterize the proposed sensors. In this chapter, we would like to reiterate the distinctive features of the proposed Bragg fiber sensors, present some additional experimental and theoretical results that are not included in previous chapters, discuss their potential applications, indicate the challenges and limitations of the proposed sensors, and suggest future research directions for this project.

## 7.1 Liquid-core photonic Bragg fiber sensors for bulk refractometry of liquid analytes

We first emphasize that hollow-core Bragg fiber sensors presented in this work are genuinely sensitive to the "bulk" changes of the liquid analyte refractive index, while most fiber-based refractive index sensors are only sensitive to changes in the analyte refractive index within the penetration depth of the evanescent field of the propagating modes. This advantage makes the presented hollow-core Bragg fiber sensor a natural candidate for monitoring the refractive indices or relative concentrations of various commercial liquids.

In Chapter 4, we proposed two detection modalities for monitoring the concentrations of commercial cooling oils by analyzing the bandgap center position and transmission amplitude at the mid-bandgap of the analyte-filled Bragg fiber. First, when using spectral-based detection modality, oil concentration could be inferred from the suspension refractive index by using the Bruggeman effective medium theory. Alternatively, when using amplitude-based detection modality, oil concentration could be found by fitting changes in the suspension absorption losses and comparing them to the losses of a reference solution. Both measurands are highly sensitive to the complex reflective index of the analyte filling the fiber core, thus enabling efficient determination and cross-correlation with the concentration of cooling oils. In the following, we will discuss in more details about the challenges of the two channel modalities and the corresponding approaches we have employed to improve the sensing performances.

### 7.1.1 Amplitude-based detection modality

When the Bragg fiber sensor operates in the amplitude-based detection modality, its signal is negatively affected by many factors, such as intensity fluctuations of the optical source, deviations in the mechanical/optical alignment during the analyte loading or unloading, bending of the fiber, and existence of micro particles or air bubbles in the sensing system. All these factors would influence the detection accuracy and repeatability of the fiber sensor.

In order to reduce these negative influences, we performed the following optimizations during the experiments. First, to improve the stability of the supercontinuum light source, we integrate an optical isolator after the pump laser (diode pumped passively Q-switched Nd: YAG laser). An optical isolator is a passive magneto-optic device that only allows light to travel in one direction. It is used to protect an optical source from back reflections or signals, which may cause instabilities in the light source. We note that the instability of the light source after integrating the optical isolator in the setup is less than 0.4% in a ten-minute period.

In order to ensure a consistent mechanical and optical coupling condition of the Bragg fiber sensor, the Bragg fiber tip is sealed hermetically into the horizontal channels of the opto-block with tread seal tape. The light beam from the supercontinuum source is coupled into the center of the fiber input facet using an objective, as shown in Fig. 7.1. The Bragg fiber is kept still in the experimental setup during the fiber calibration and subsequent measurements of various commercial cooling oil suspensions, in order to guarantee the same coupling conditions. A syringe is used to pump liquid analytes into the core of the fiber.

In order to eliminate the influence of air bubbles in the experiments, we submerge both ends of the fluidic channels and the pumping syringe into a water-filled beaker (1L) during the experiments. With all these conditions satisfied, we have virtually achieved a stable opto-fluidic setup for sensing applications.

To verify the repeatability and stability of the amplitude-based detection modality, we repeat the transmission spectra characterization of one Bragg fiber with a length of 15cm 60 minutes after its first round of characterization. In Fig. 7.2, we present the results of the two consecutive experiments. The dotted curves represent the transmission spectra of the second measurements, which match well with the results of the first measurement shown as the solid curves. The fluctuations in the transmission amplitude are found to be no more than 2%.

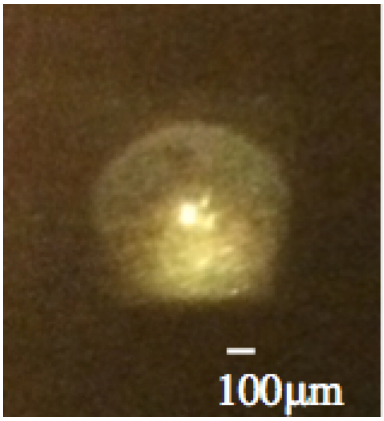


Figure 7.1 Input coupling facet of the liquid-core Bragg fiber sensor. Light beam from the supercontinuum source is focused onto the center of the liquid-filled fiber core using an objective.

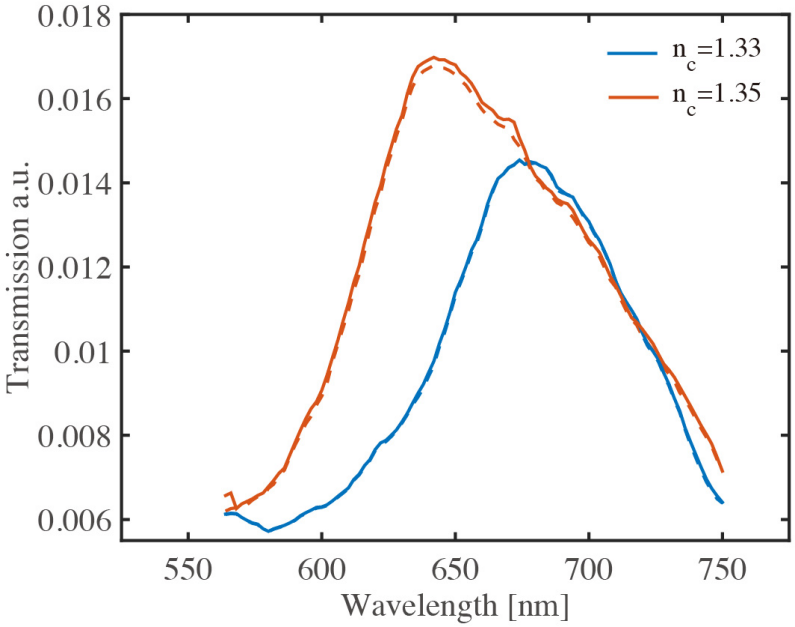


Figure 7.2 Experimental transmission spectra of a ~15 cm long Bragg fiber when the core is filled with analytes with different refractive indices (solid curves). The dotted curves indicate a repeat of the first experiment after 60 minutes, which demonstrate a good repeatability and stability of the Bragg fiber sensor.

### 7.1.2 Spectral-based detection modality

The sensors using spectral-based detection modality are immune to those negative influences as mentioned in Section 7.1.1, because the measurand in this case is the peak position in the fiber

transmission spectrum (or the bandgap position of the Bragg fiber), which is mostly determined by the refractive index of the liquid analyte filled in the fiber core. As we have observed in the repeatability test (see Fig. 7.2), the peak position in the fiber transmission spectrum barely changes in several consecutive measurements regardless of somewhat amplitude fluctuations. We, therefore, conclude that the spectral-based detection modality with higher detection accuracy and stability is more suitable for instrumentation of the Bragg fiber sensors to realize real time refractometry of commercial liquids.

Next, we would like analyze the factors that could influence the sensitivity of a Bragg fiber sensor using the spectral-based detection modality. We, therefore, derive the analytical expression of the spectral sensitivity of a Bragg fiber sensor by substituting Eq. (4.1) into Eq. (3.7), and thus we have the spectral sensitivity as:

$$S = \left|\frac{\partial \lambda_g}{\partial n_c}\right| = 2[d_h(\frac{n_h^2}{n_c^2} - 1)^{-1/2} + d_l(\frac{n_l^2}{n_c^2} - 1)^{-1/2}] \tag{7.1}$$

From Eq. (7.1), one finds that the spectral sensitivity of a Bragg fiber sensor is a function of the real part of the refractive index of the liquid analyte filling the fiber core, as well as the refractive indices and thicknesses of the individual layers in the Bragg reflector. We note that in the derivation, we use the following approximation $\varepsilon_r = n^2$, due to the imaginary part of the dielectric constant being much smaller than the real part of the dielectric constant for the liquid analytes involved in this paper.

Apparently, the spectral sensitivity of a Bragg fiber sensor increases with the refractive index of the analyte filling the fiber core. Consequently, the shift of the resonant wavelength should have a polynomial dependence on the analyte refractive index. However, since our Bragg fiber sensors operate within a relatively small dynamic range ($n_c$: 1.333-1.360), the spectral shift of the resonant wavelength is considered to be virtually linear to increment of the refractive index of the fiber core.

Besides, Eq. (7.1) indicates that the closer the value of refractive index of the fiber core to those of the individual layers in the reflector, the more sensitive the sensor will be. As a result, low-refractive-index-contrast Bragg fibers are generally more sensitive than their high-refractive-index-contrast counterparts in sensing of the liquid analytes refractive indices. In fact, in this

thesis, we choose low-refractive-index-contrast PS and PMMA layers as the reflector materials mostly due to their thermo-mechanical compatibility.

Additionally, Eq. (7.1) suggests that the spectral sensitivity of the fiber sensor increases with the thicknesses of the high- and low-refractive index layers. As a result, Bragg fibers with thicker bilayers in the reflector generally have higher spectral sensitivity. However, it is important to realize that simultaneously increasing the thicknesses of both the high- and low-refractive index layer would also shift the bandgap position of the Bragg fiber towards longer wavelengths, according to Eq. (4.1). Currently, we routinely fabricate Bragg fibers with their primary bandgaps located in the visible range, because aqueous solutions are relatively transparent in this range.

In fact, even when the bandgap positions of the Bragg fibers are fixed, one can still possibly enhance the spectral sensitivity by optimizing the bilayer thickness contrast in the reflector, which is define as $d_h / d_l$. To verify this theoretically, we investigate the dependence of the fiber spectral sensitivity on the bilayer thickness contrast based on Eq. 7.1. In order to keep the bandgap center of the Bragg fiber constant (e.g. 680nm), when we change the thickness of the high-RI layer, the thickness of the low-RI layer is also changed according to Eq. 4.1, and the bilayer layer thickness contrast is thus determined. In Fig. 7.3, we plot the spectral sensitivity of the Bragg fiber sensor as a function of the bilayer thickness contrast. Our simulation results suggest that by using a Bragg reflector with smaller bilayer thickness contrast, higher spectral sensitivity could be achieved. As a matter of fact, this observation can be easily rationalized by noting that coefficient of $d_l$ in Eq. (7.1) is somewhat larger than that of $d_h$ because $n_l$ is closer to $n_c$ than $n_h$.

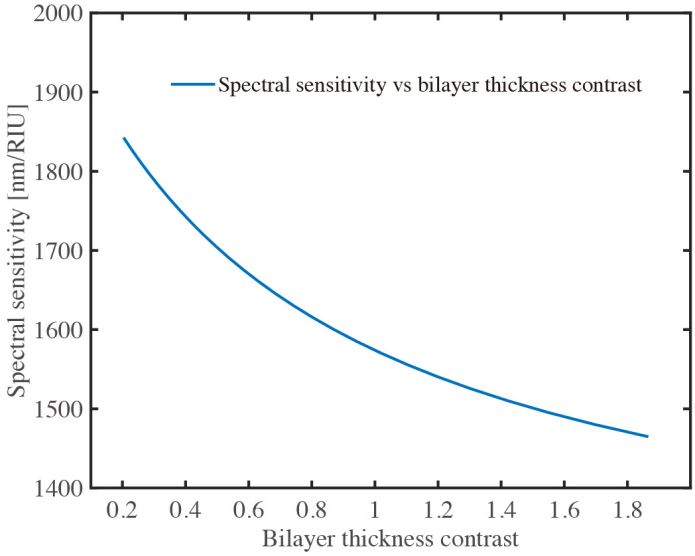


Figure 7.3 Dependence of the spectral sensitivity of the Bragg fiber on the bilayer thickness contrast in the Bragg reflector.

Experimentally, to verify the dependence of the spectral sensitivity on the bilayer thickness contrast, we design and draw Bragg fibers with similar bandgap positions but with different bilayer thickness contrasts, and carry out the characterizations of their spectral sensitivities. In Fig. 7.4, we present the transmission spectra of two Bragg fibers with almost identical bandgap positions (centered at around 680nm when $n_c$=1.33). The bilayer thickness contrast of each fiber is determined from the SEM graphs. We find that the fiber with smaller bilayer thickness contrast (~0.3) in the reflector has a higher spectral sensitivity of 1900nm/RIU, which is more than 30% higher than that of the other fiber (1460nm/RIU) with bilayer thickness contrast of ~1. The spectral sensitivity of 1900nm/RIU is the highest value achieved experimentally for refractive index sensors based on Bragg fibers. Therefore, by optimizing the geometry parameters in the Bragg reflector, one can enhance the spectral sensitivity of the Bragg fiber sensor, which, in turn, improves its detection accuracy for refractive index measurement and concentration prediction of commercial liquids.

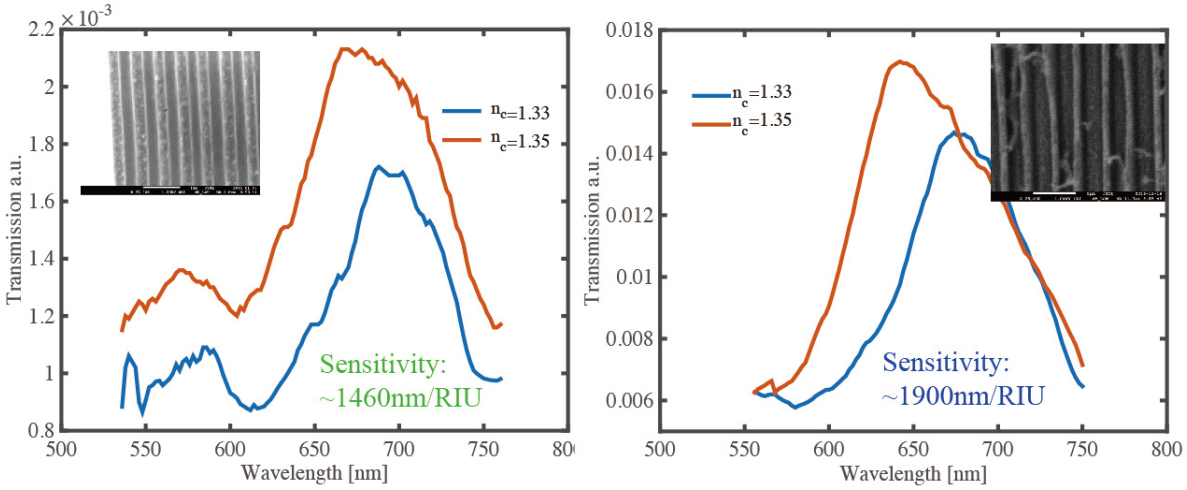


Figure 7.4 (a) Experimental characterization of the spectral sensitivity of a Bragg fiber with bilayer thickness contrast of ~1. (b) Experimental characterization of the spectral sensitivity of a Bragg fiber with a bilayer thickness contrast of ~0.3.

### 7.1.3 Dependence of the spectral sensitivity on the fiber length

In order to study the dependence of the spectral sensitivity on the length of a Bragg fiber, we experimentally characterize the spectral sensitivities of Bragg fibers with different lengths (10cm and 8cm). In this experiment, we first measure the spectral sensitivity of a Bragg fiber with a length of 10cm, and we then cut the fiber into 8cm and repeat the same characterization. In Fig. 7.5, we plot the transmission spectra of the Bragg fibers with a length of 10cm and 8cm. At each fiber length, the fiber is filled with liquid analytes with refractive indices of 1.333 and 1.360, respectively. In both cases, pronounced spectral shifts are well observed when the fiber core refractive index is increased. The bandgap positions of the two fibers show good agreement with each other. The differences in the transmission spectrum shapes are probably caused by the different coupling conditions in two separate characterizations. By comparing the spectral shifts of the transmission peaks in the fiber transmission spectra, we estimate that the spectral sensitivities of the 10 cm long fiber and 8cm long fiber are ~1610 nm/RIU and 1600 nm/RIU, respectively. Moreover, we note that the liquid-core Bragg fibers should have a minimal (threshold) length to ensure sufficient attenuation at the wavelengths in the vicinity of bandgap edges in order to allow the formation of spectral features (such as transmission peaks) in the fiber transmission spectrum. We experimentally find the threshold length to be ~5 cm for most Bragg

fibers. We, therefore, conclude that once the fiber length is longer than the threshold value, the spectral sensitivity of a Bragg fiber sensor is virtually independent on the fiber length. Practically, shorter Bragg fibers are more favorable for the development of refractive index sensors than the longer counterparts, because the as-developed sensors feature smaller footprints and are easier to maintain.

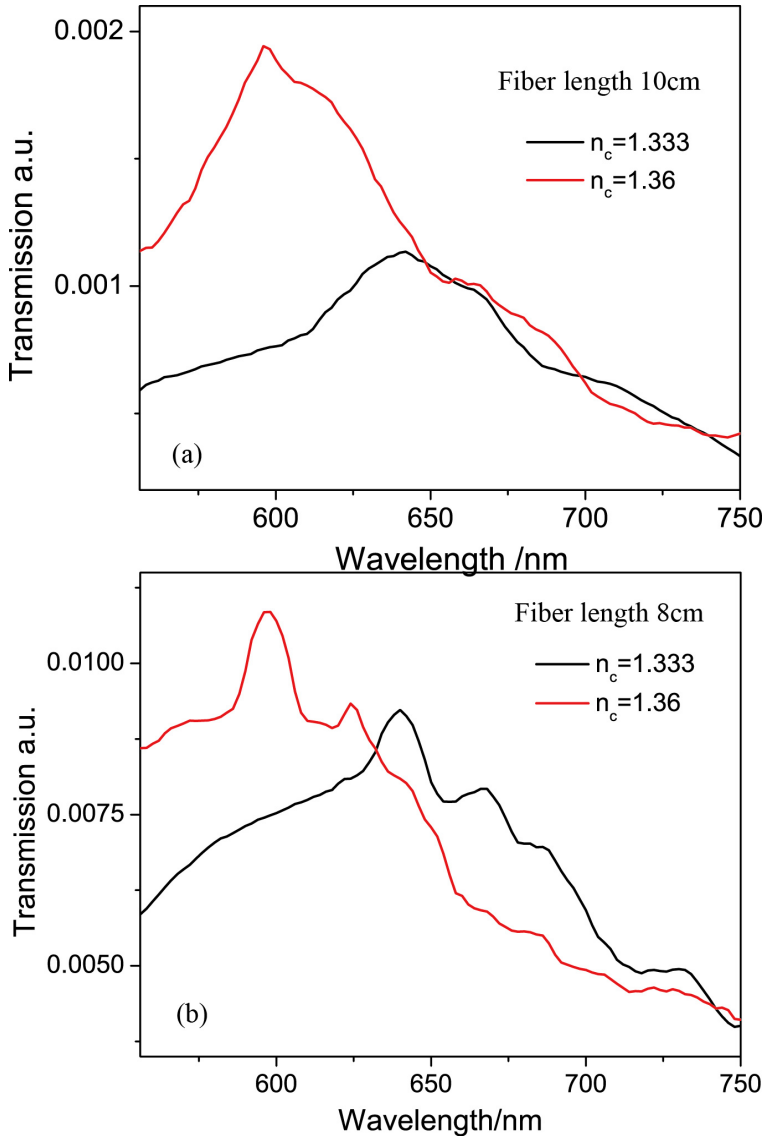


Figure 7.5 Transmission spectra of liquid-core Bragg fibers with different lengths: (a) 10 cm, (b) 8 cm, when the refractive index of the analyte filling the fiber core is changed from 1.333 to 1.360.

### 7.1.4 Temperature stability of the Bragg fiber sensor

The performance of most refractive index sensors is frequently affected by the temperature variations because of the thermo-optic effect of the fiber materials [191]. In this section, we discuss how the thermal variations would influence the performance of the proposed Bragg fiber sensors. Since the glass transition temperature of PS and PMMA in the range of 75°C-110°C [187, 188], our Bragg fiber sensor cannot operate in temperatures higher than this range. Below the glass transition temperature, an increase in the environmental temperature leads to the thermal expansion of the multilayers and the refractive index changes of the fiber materials. Both of them would result in displacement of the transmission peak (bandgap position) of the Bragg fiber. In order to evaluate the effect of the temperature changes on the fiber transmission spectrum, we theoretically calculate the normalized transmission spectra of the fundamental $HE_{11}$ mode in a 10cm long Bragg fiber at different temperatures. The temperature dependent refractive index of PMMA and PS can be found in [187, 188]. The linear thermal expansion coefficient for PMMA and PS are $7\times10^{-5}$m/m·°C and $9\times10^{-5}$ m/m·°C, respectively [189]. The fiber core is assumed to be filled with water, which has a temperature dependent refractive index of $-1\times10^{-4}$/°C [190]. The thickness of individual layer in the Bragg reflector is extracted from the SEM graph of Bragg fiber in Chapter 4. The simulated transmission spectra of the Bragg fiber at different environmental temperatures are shown in Fig. 7.6(a). A red shift in the bandgap center positions is observed with the increase of the temperature. In Fig. 7.6(b), we plot the bandgap center positions as a function of the ambient temperatures, and a linear dependence is found. The temperature response of our Bragg fiber sensor with aqueous solutions in the fiber core is only 45pm/°C.

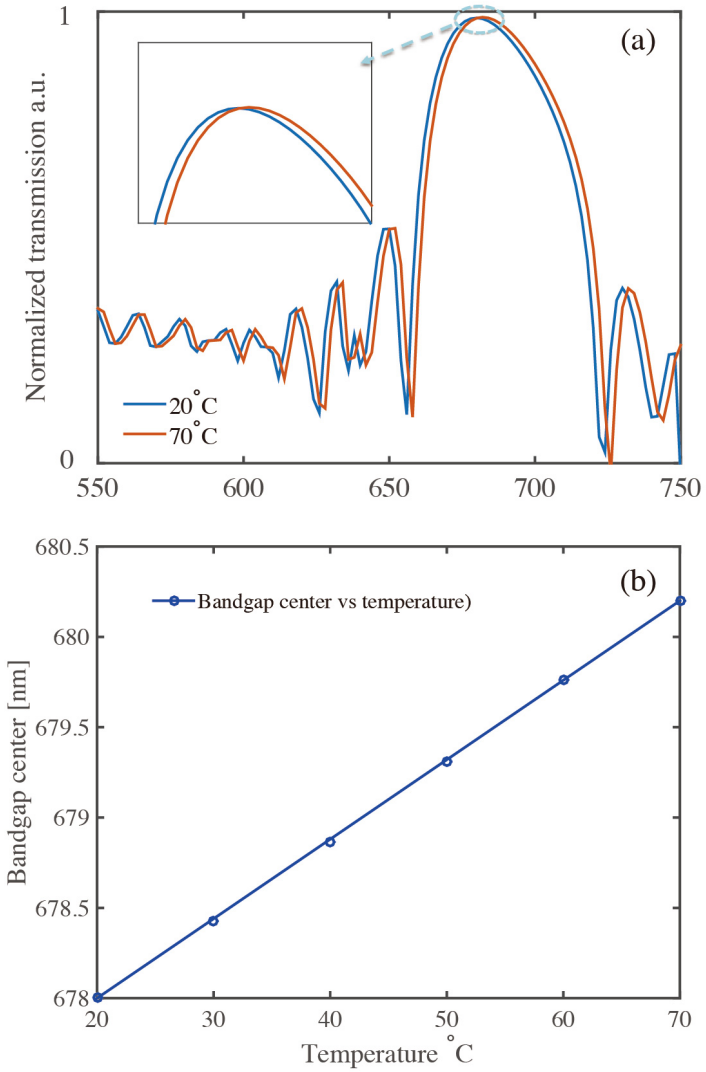


Figure 7.6 (a) Simulated transmission spectra of a water-filled Bragg fiber sensor at different temperatures. (b) Spectral positions of the transmission peak at various temperatures.

## 7.2 Liquid-core Bragg fibers for surface sensing applications

In Chapter 5, we demonstrate the surface sensing capability of the liquid-core Bragg fiber sensor. We then apply the fiber sensor to monitor the thickness variations of a thin analyte layer deposited on the inner surface of the fiber core. We observe both theoretically and experimentally that the introduction of a thin film onto the fiber inner surface results in obvious anticrossings between the core-guided modes and the modes confined to the thin film. In the vicinity of anticrossings, the optical energy is resonantly transferred from the fiber core modes to the analyte

layer modes, followed by a strong increase in the fiber propagation loss. The wavelength of modal anticrossing depends strongly on the analyte thickness, thus allowing for the monitoring of changes in the analyte layer thickness. The presence of the attenuation peaks induced by anticrossing phenomenon deforms the shape of the original bandgap of the Bragg fiber and results in changes in the shape of a transmission spectrum. Experimentally, we find it is easier to monitor spectral shift of the point of the lowest transmission loss than the anticrossing wavelength (transmission dip), since the Bragg fiber sensor is highly multimode. Further insight regarding the multimode operation of the Bragg fiber sensor can be obtained by calculating the modal dispersions and loss spectra of the guided modes in the Bragg reflector, as illustrated in the following section.

### 7.2.1 Liquid-core Bragg fiber sensor operating in a multimode regime

In previous simulations in Chapter 5, we have detailed the theoretical behavior of the fundamental TM and TE modes having the lowest propagation losses in response to changes of the analyte layer thickness. These results are mostly valid for Bragg fiber operating in the single mode or a few modes regime. In our experiments, the hollow-core Bragg fiber features a relatively large core diameter (~600μm), and a relatively small length of 8cm, which allows thousands of modes propagating in the fiber core. As a result, many higher-order modes are excited when the light beam is launched into the fiber. These higher-order modes have somewhat different modal indices, anticrossing wavelengths, and transmission bandgaps. To illustrate this, in Fig. 7.7 we present the modal dispersion relations and the attenuation loss spectra of 10 TM modes closest to the light line of the core material for the fiber without analyte layer [Figs. 7.7(a), (c)], and with a 200nm-thick analyte layer [Figs. 7.7(b), (d)]. As is clear from the figures, the overall effect of the multimode operation on the fiber transmission is in the broadening of the transmission window and overall increase in the propagation loss. Therefore, the surface sensitivity measured experimentally would be a result of combined contribution of many higher-order modes, rather than only the fundamental $TM_1$ and $TE_1$ modes. We note that for lower-order modes, the mode fields are tightly concentrated near the center of the core, with relatively moderate overlap with the analyte layer, while for higher-order modes, the fields are distributed more towards the edges of the waveguide and thereby more sensitive to the changes in the analyte layer thickness, as we have also observed in Chapter 5.

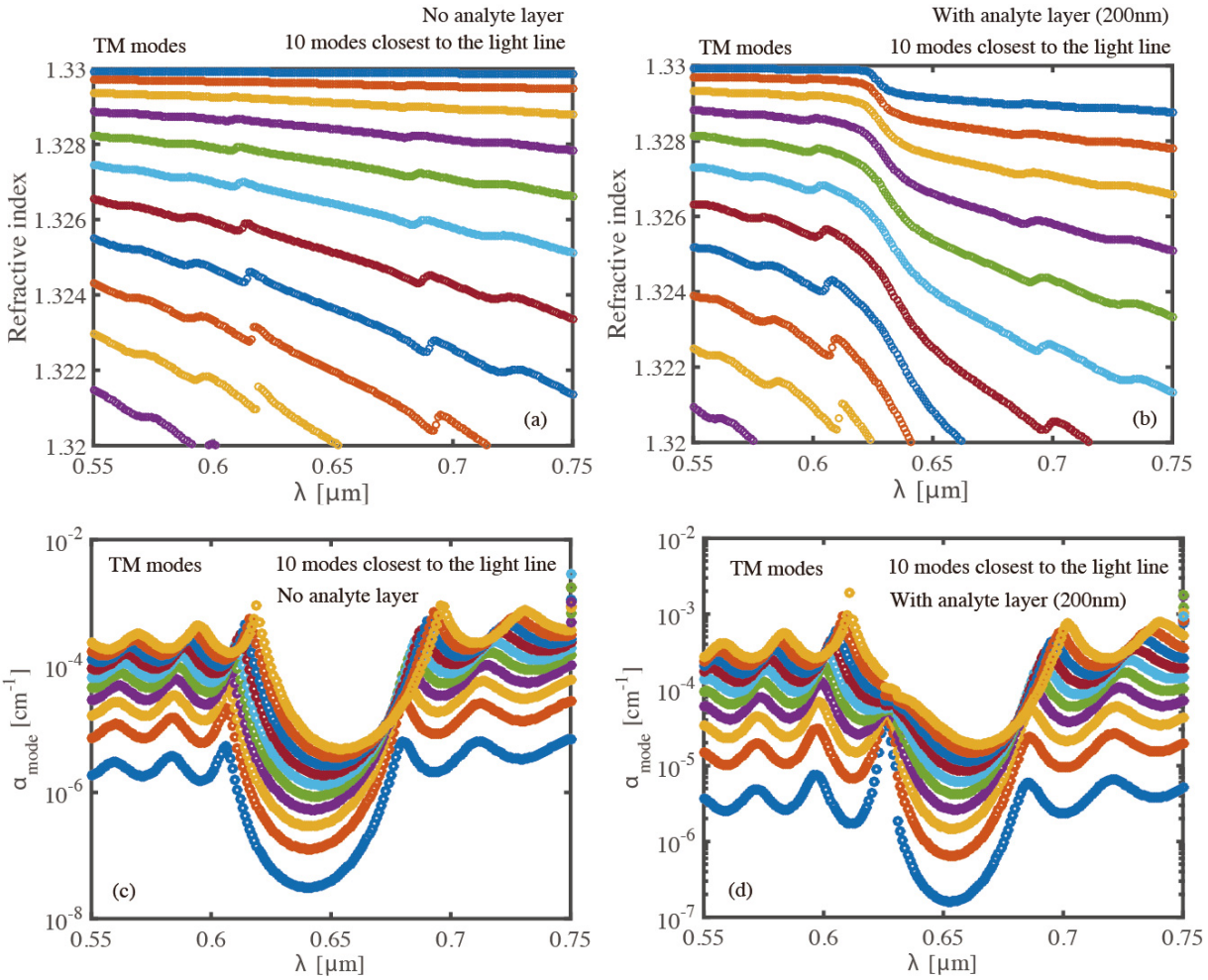


Figure 7.7 Modal dispersion relations of 10 TM modes closest to the light line of a core material for the Bragg fiber (core size: 600μm) without analyte layer (a), and with 200nm thick analyte layer (b). Attenuation loss spectra of the 10 TM modes for the Bragg fiber without analyte layer (c), and with 200nm-thick analyte layer (d).

### 7.2.2 Influence of the analyte layer refractive index on the fiber spectral features

In Chapter 5, we have studied the influence of the analyte layer thickness on the Bragg fiber spectral features, and we demonstrated both theoretically and experimentally that the fiber sensor can be used to monitor thickness variations of a biolayer attached on the fiber inner surface. In fact, the proposed Bragg fiber sensor can also be used to detect variations in the analyte layer refractive index. This type of sensing scheme could be used to monitor changes in the refractive index of an analyte layer caused by chemical process.

In this section, we theoretically study the influence of changes in the analyte layer refractive index on the anticrossing wavelength and the fiber spectral features. In our simulation, the refractive index of the biolayer is varied from 1.33 to 1.58 with a step of 0.05, while the biolayer thickness is kept constant (100nm). Figures 7.8(a)-(d) show the simulated modal dispersions and radiation losses of the $TM_1$ and $TE_1$ modes guided in the Bragg fiber as a function of wavelength. The spectra show similar resonant behaviors as shown in Fig. 5.2 in Chapter 5 due to the anticrossings between the core-guided modes and the defect modes. In the anticrossing region, the modes exhibit very large dispersions and relatively large radiation losses, which deform the shape of the original bandgap. With the increase of the analyte layer refractive index, a red shift is observed in the anticrossing wavelength. This can be easily rationalized by noting that dispersion relations of the waveguide exhibit a red shift when the refractive index of the analyte layer is increased. In Fig. 7.8 (e) and (f), we plot the anticrossing wavelength of $TM_1$ and $TE_1$ modes as a function of the analyte layer refractive index. It is shown that changes in the analyte layer refractive indices are unambiguously correlated with the anticrossing wavelength. Additionally, we notice that the overall attenuation spectra of both the $TM_1$ and $TE_1$ modes also show a red shift with the increase of the analyte layer refractive index. This is due to the fact that highly lossy resonant peak (region of anticrossing) is shifting towards longer wavelengths when increasing the analyte layer refractive index.

In Figs. 7.8 (g) and (h), we plot the wavelength of the lowest propagation loss of the $TM_1$ and $TE_1$ modes as a function of the analyte layer refractive index, and find an effectively linear dependence of such a wavelength on the effective refractive index of the ananlyte layer. Based on this finding, we conclude that the proposed fiber sensor could also be used to detect variations in the analyte layer refractive index, with a sensitivity of 36nm/RIU and 33nm/RIU for $TM_1$ and $TE_1$ modes, respectively. The surface sensitivity to changes in the RI of the analyte layer is relatively moderate due to a low overlap between the fields of the core-guided modes and a mode localized in the analyte layer. We note that this sensitivity can also be improved by squeezing the fiber core, so as to increase the modal overlap with the analyte layer.

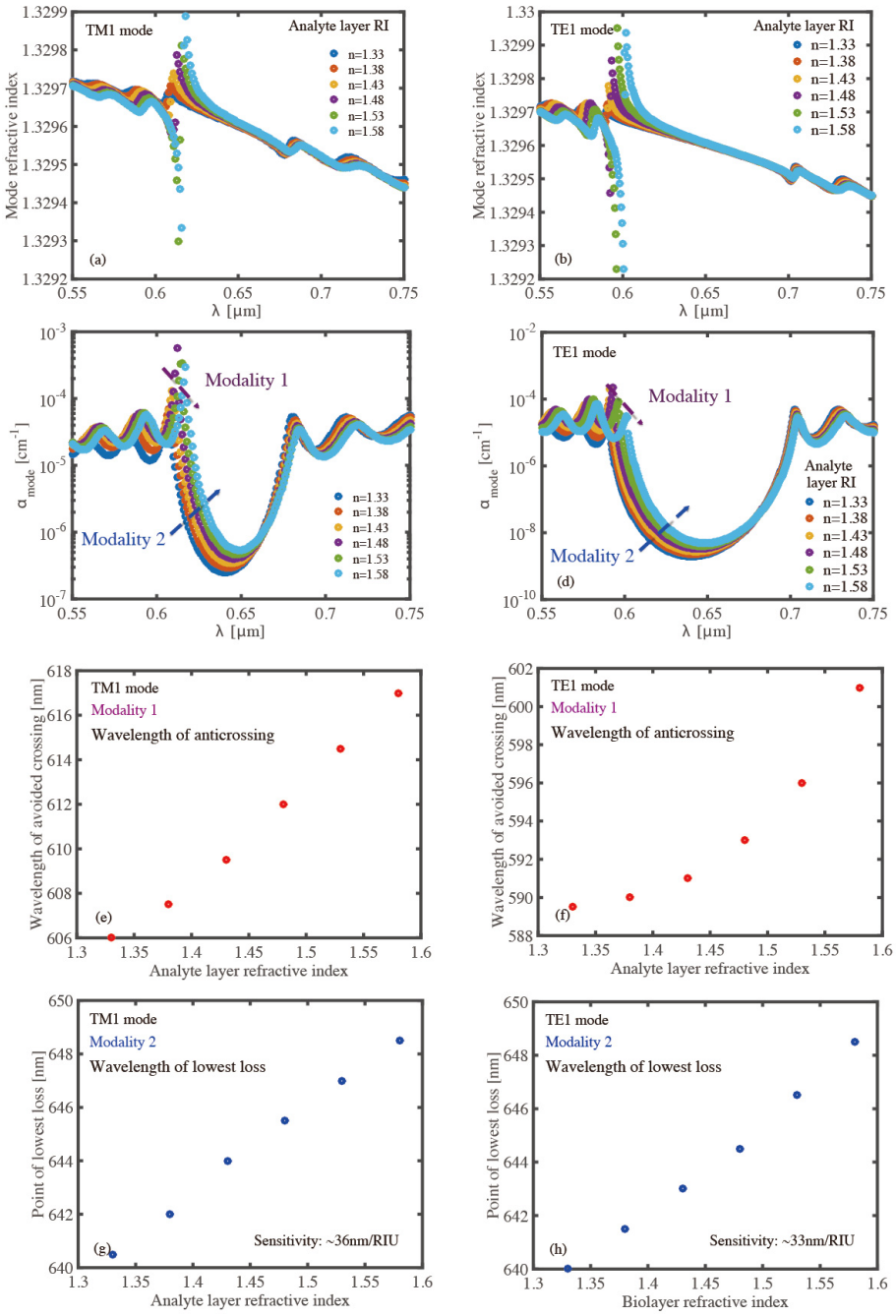


Figure 7.8 Simulated modal dispersion relations of the $TM_1$ (a) and $TE_1$ modes (b) in the water-filled fiber for different values of the analyte layer RI ranging from 1.33 to 1.58. Corresponding radiation losses of the $TM_1$ (c) and $TE_1$ modes (d). Wavelengths of avoided crossing of the $TM_1$ (e) and $TE_1$ modes (f) obtained from (c) and (d) as a function of the analyte layer refractive index. Wavelengths of lowest radiation loss of the $TM_1$ (g) and $TE_1$ modes (h) obtained from (c) and (d) as a function of the analyte layer refractive index.

### 7.2.3 Enhancement of the surface sensitivity of the liquid-core Bragg fiber sensor

Due to the large size of the Bragg fiber core, only a poor modal overlap between the core-guided modes and the analyte layer bound modes is achieved, leading to a moderate surface sensitivity. In order to enhance the surface sensitivity, we squeezed a section of the Bragg fiber to enhance the modal overlap between the core-guided modes and the analyte layer. Limited by the mechanical robustness and chemical resistivity of the all-polymer Bragg fiber when it is filled with ethyl alcohol, only a moderate sensitivity enhancement (~35%) is achieved experimentally when the core size is reduced from 600μm to 100μm. Despite the limited degrees of squeezing, we have still clearly observed an enhancement of the surface sensitivity when the fiber core is squeezed.

By increasing mechanical robustness of the Bragg fibers to squeezing, or using established fiber drawing techniques to directly fabricate desired fiber structure (such as tapered fibers), one could potentially further enhance the surface sensitivity. However, there is a tradeoff between sensitivity enhancement and response time increase for smaller fiber core sizes. We note that one advantage of fiber-squeezing technique proposed in this thesis is that it can serve as a flexible “knob” to adjust the surface sensitivity and the response time, to suit particular needs for different applications.

Another alternative to enhance the modal overlap between the core-guided modes and the analyte layer is by introducing a porous network of thin bridges that can be biologically or chemically functionalized. This can also increase the overlap between the core modes and the analyte layer; however, fabrication of such fibers operating in the visible range could be challenging.

## 7.3 Limitations of the liquid-core Bragg fiber sensors and future directions

While our Bragg fiber sensors offer numerous advantages such as high sensitivity, fast response, and low cost, they also have some limitations. First, since the Bragg fiber sensors use all-polymer structure, they are less resistant to aggressive chemicals and high temperature than silica fibers. However, we note that this does not affect their primary applications for fast refractometry of various commercial oils and other aqueous solutions. Moreover, since biomolecules can be

directly bound to the PMMA surface without any further chemical functionalization [99], the presented Bragg fiber sensors could also be conveniently used as a promising platform for a wide range of bio/chemical sensing applications.

Another drawback of the Bragg fiber sensors is related to their relatively broad transmission bands, compared to sensors based on Bragg gratings. This may lead to difficulty in determination of minute spectral shift caused by small changes in the analyte refractive indices or the coated biolayer thicknesses. To address this problem, we would like to explain why the Bragg fibers have relatively broad transmission windows. First, we find that the multilayers in the Bragg reflector fabricated by the commercial fiber-drawing technique are not perfectly uniform. The variations in the bilayer thicknesses may lead to broadening in the fiber transmission band. Second, the Bragg fibers used in this work are only several centimeters long; as a result, the transmission spectra are relatively broad due to reduced fiber attenuation at the bandgap edges because of short fiber lengths. Third, the presented Bragg fiber sensors operate in a multimode regime, and many high-order modes with different bandgap positions have also been excited and propagated.

Despite the relatively broad transmission windows of the Bragg fibers, the spectral features (peaks or dips) in their transmission spectra can still be easily differentiated under our experimental conditions. Clear shifts of spectral peaks can also be observed in response to changes in the refractive index of the fiber core or the biolayer thickness, even when the Bragg fiber sensor is greatly squeezed (see Fig. 5.9).

In order to achieve narrower transmission bands of the Bragg fibers, one could pursue the following approaches in future work. To begin with, one could use longer fibers with more precisely controlled bilayer thicknesses and increase the number of bilayers in the Bragg reflector, thus enabling a stronger confinement of the optical modes and achieving narrower bandgaps; alternatively, one could also use fibers operating in a single mode regime or few modes regime. To do this, one could use Bragg fibers with smaller diameters to eliminate the influence of higher order modes, or coil fibers into circles with diameter of several centimeters to strip out the high-order modes. Moreover, one could achieve a single $TE_{01}$ mode operation in the large-core Bragg fibers with the modal filter effect [202]. Finally, another attractive approach would be modifying

the broad transmission window with resonant dip with narrow linewidth via the introduction of a defect in the Bragg reflector, as we have demonstrated in Chapter 6.

## 7.4 Practical applications of the liquid-core Bragg fibers

Due to the advantages of the liquid-core Bragg fibers such as high sensitivity, short response time, simplicity in structure, small footprint, and the possibility of cost-effective mass production, we believe that the proposed Bragg fiber sensors could be a very attractive platform for a variety of scientific and industrial sensing applications.

We now propose several potential applications of the liquid-core Bragg fiber sensors. Firstly, as we have demonstrated in Chapter 5, the Bragg fiber sensor can be used for online monitoring of the concentrations of many industrial fluids, such as heat transfer fluids, sawing fluids, and other industrial dilutions. This is of significant importance in various indurtrial processes. Second, the Bragg fiber sensor can be used in food industry and medicine. For example, the refractive indices of glucose solutions (or syrup) are monotonically dependent on the glucose concentration. Considering the resolution of the demonstrated Bragg fiber sensor to be $7\times10^{-5}$ RIU, this fiber sensor is able to resolve variations in the glucose concentratio of 0.05% by weight. Thirdly, the sensor could also be used as a platform to detect the bio-layer thickness, study the surface dynamics and molecular interactions, as well as antigen-antibody conjugations, thus making the proposed all-plastic, hollow core Bragg fibers a promising component for the development of a new generation of the fiber-based biosensors. One advantage of using PMMA based structure is that many biomolecules can be directly attached to the surface without any chemical functionalization [99], which means that the fabricated Bragg fiber sensor could be conveniently used as a promising platform for a wide range of biochemical sensing applications. The demonstrated “one fiber” solution for both bulk and surface sensing applications will open up important commercialization opportunities for sensor-system instrumentation. Finally, the demonstrated Bragg fiber sensors can be simply used as absorption-based sensors for bio-chemical detection. Compared to those absorption-based sensors which frequently use “leaky modes” of fiber capillaries, the Bragg fibers in this work offer much lower propagation loss, thus enabling longer sensing length and, therefore, higher sensitivity.

## 7.5 3D printed THz Bragg fiber for resonant surface sensing applications

In Chapter 6, we demonstrated 3D-printed THz Bragg waveguides with defect layers for resonant surface sensing applications. Such waveguide sensors operate in an effectively single mode regime. The relatively broad transmission spectrum of a Bragg waveguide is modified by a spectrally narrow loss peak, which is accomplished by introducing a geometrical defect in the first layer of the Bragg reflector. The spectral position of the resonant loss peak is found to be highly sensitive to the optical properties of the defect layer, such as thickness and refractive index. By directly tracking the anticrossing frequency, which manifests itself as a transmission dip with narrow linewidth in the waveguide transmission spectrum, we have significantly improved the sensitivity and limit of detection of such sensors. As a practical demonstration, we applied this sensor to detect targets in the form of thin films and powder analyte.

### 7.5.1 Spectral resolution of TDS spectroscopy and CW spectroscopy

The desirable characteristic in spectroscopy is high spectral resolution, which is critical for observing resonances with narrow line widths. In TDS, the THz spectrum is calculated by numerical Fourier transformation of the measured temporal waveform. From the Fourier theory, the spectral resolution of a TDS system is determined from the span of the time delay sweep, and is given by $c/2L$, where $L$ is the physical length of the mechanical delay line. A higher spectral resolution can be obtained by extending the temporal window, which corresponds to the scanning distance. In a noise-free system with an unlimited delay line, the resolution would be limited by the pulse repetition rate of the pump laser. The longest duration that can be sampled is equal to the time between the two consecutive pulses. However, in the presence of a noise, the achievable frequency resolution is much poorer and is determined by the signal-to-noise ratio (SNR) of the system in time domain. This is because as the signal amplitude diminishes with an increased delay from the main pulse, the SNR approaches unity. From a certain point onwards, scanning to longer delay spans gives no further data. Therefore, the usable delay span is limited by the SNR of the system. In practice, it is advisable to limit the scan length to the region where the SNR is higher than 2.

On some occasions, it is common practice to increase the frequency resolution of a TDS measurement by zero-padding [192, 193]. This is accomplished by extending the time-domain data set with a string of zeros. Zero-padding uses the information contained in the existing time span and interpolate additional frequency data points, which trace out the spectra with greater resolution. In fact, the additional supplementary data points carry no additional information, but rather interpolate the existing information. When the measured spectrum lacks narrow-resonant features, this technique works well and produces spectra that are negligibly different from high-resolutions ones. However, when the spectra of interest feature narrow-resonant features such as the sharp transmission dips in Chapter 6, the zero-padded spectrum does not entirely succeed in reproducing the detailed long-scan spectrum, because that narrow spectral features require extended time data in order to be determined accurately. To explicitly illustrate the effects of zero-padding, in Fig, 6.9, we plot the spectrum of a Bragg waveguide with two sharp transmission dips obtained with high resolution and low resolution, as well as that with zero-padding. It is well observed that for the region with broad spectral features (e.g., 0.2THz-0.4THz), the zero-padding technique with interpolated data points has refined the spectral profile. However, the zero-padded spectrum fails to reproduce the two sharp dips as shown in the detailed long-scan spectrum.

In contrast, in a continuous wave (CW) spectroscopy setup, the frequency resolution is determined by the quality of the laser beat. Therefore, it is dependent on the frequency stability and linewidth of the lasers sources. In such systems, Distributed Feedback (DFB) lasers, which feature a grating structure within the active region of the semiconductor, are frequently used to restrict the emission spectrum to a single longitudinal mode. In general, a typical CW system can achieve a frequency resolution on the 10MHz range. This is of great significance for industrial sensing applications, when precise detection of small volume of target analytes is required.

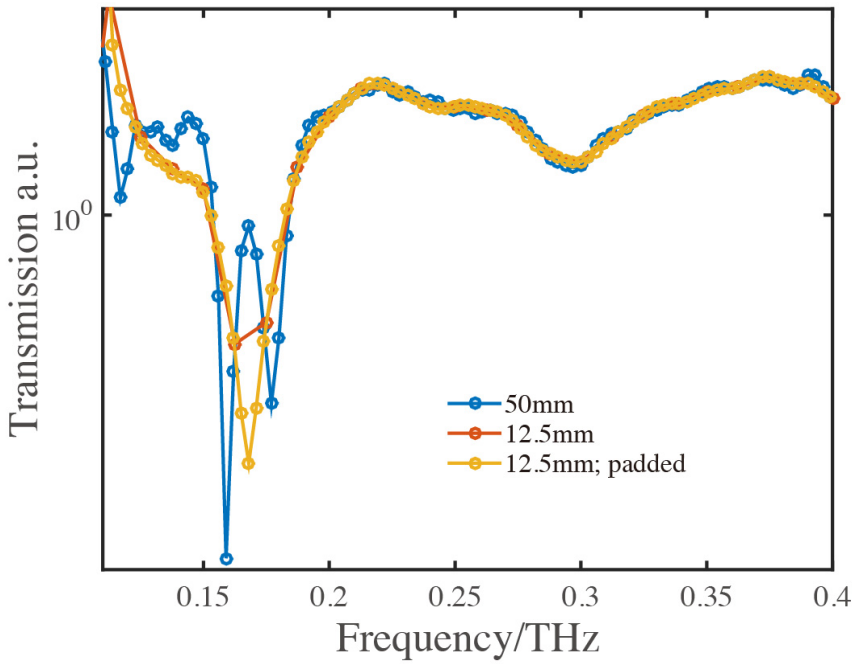


Figure 7.9 Spectral characterization of a Bragg waveguide (with a defect of 300μm). The measurements are conducted with a 50mm scan with 3 GHz resolution, a 12.5 mm scan with 12 GHz resolution, a 12.5mm scan with zero-padding to 50 mm with a nominal resolution of 3 GHz.

### 7.5.2 Reproducibility of the 3D printed THz Bragg waveguide sensors

To verify the reproducibility and stability of the spectral-based sensing modality of the 3D printed Bragg waveguide sensors, we fabricate several sections of Bragg waveguides (length: 2.5cm) with different defect layer thickness (i.e., 300μm and 400μm) in the first layer of the reflector, and we characterize their transmission spectra using THz-TDS setup. As illustrated in Fig. 7.10, the Bragg waveguides with same geometrical parameters show excellent reproducibility in the spectral positions of the resonant dips. This suggests a good stability and consistency when using 3D printing technology to fabricate the THz Bragg waveguides. Moreover, we note that such waveguide sensors are potentially capable of realizing parallelism sensing (the ability to interrogate more than one sample simultaneously and independently). This could be accomplished by employing a relatively long waveguide, which includes several sections of Bragg waveguides with different defect layer thicknesses and different resonant dip positions in the transmission spectra. Each section could be biologically or chemically

functionalized to selectively detect specific analytes. By tracking each independent resonant dip in the overall transmission spectrum of the long waveguide, one can thereby monitor changes in the thickness or quantity of different analytes by exploiting a single-cycle terahertz pulse.

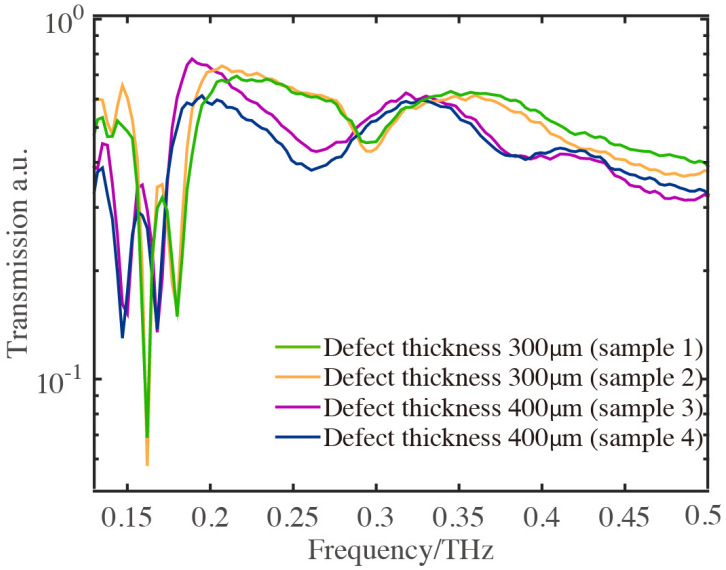


Figure 7.10 Transmission spectra of several sections of 3D printed THz Bragg waveguides with different defect layer thickness in the first layer of the reflector, which demonstrates a good reproducibility of the Bragg waveguide sensor.

### 7.5.3 Repeatability of the 3D printed THz Bragg waveguide sensors

To verify the repeatability of the spectral-based sensing modality of the 3D printed Bragg waveguide sensor, we repeat the experimental characterization of the waveguide sensor for the detection of lactose powders using high-resolution CW setup (shown in Fig. 6.10). In this experiment, we choose the same Bragg waveguide as the sensing platform, and measured the transmission spectra of the rotating waveguide when different amount of lactose powders are loaded into the waveguide core using the semi-automatic feeder presented in Chapter 6. Three measurements are performed for the net masses of the lactose powder equal to 0.002g, 0.004g, and 0.008g that correspond to the analyte layer thicknesses of the 3μm, 6μm, and 12μm on the inner core surface. At each mount of lactose powers, the measurements are repeated by 4 times. As shown in Fig. 7.11, the Bragg waveguides with same amount of lactose powders show very

good agreement in the spectral positions of the resonant dips. This suggests an excellent repeatability of our Bragg waveguides sensor for the detection of powder analytes.

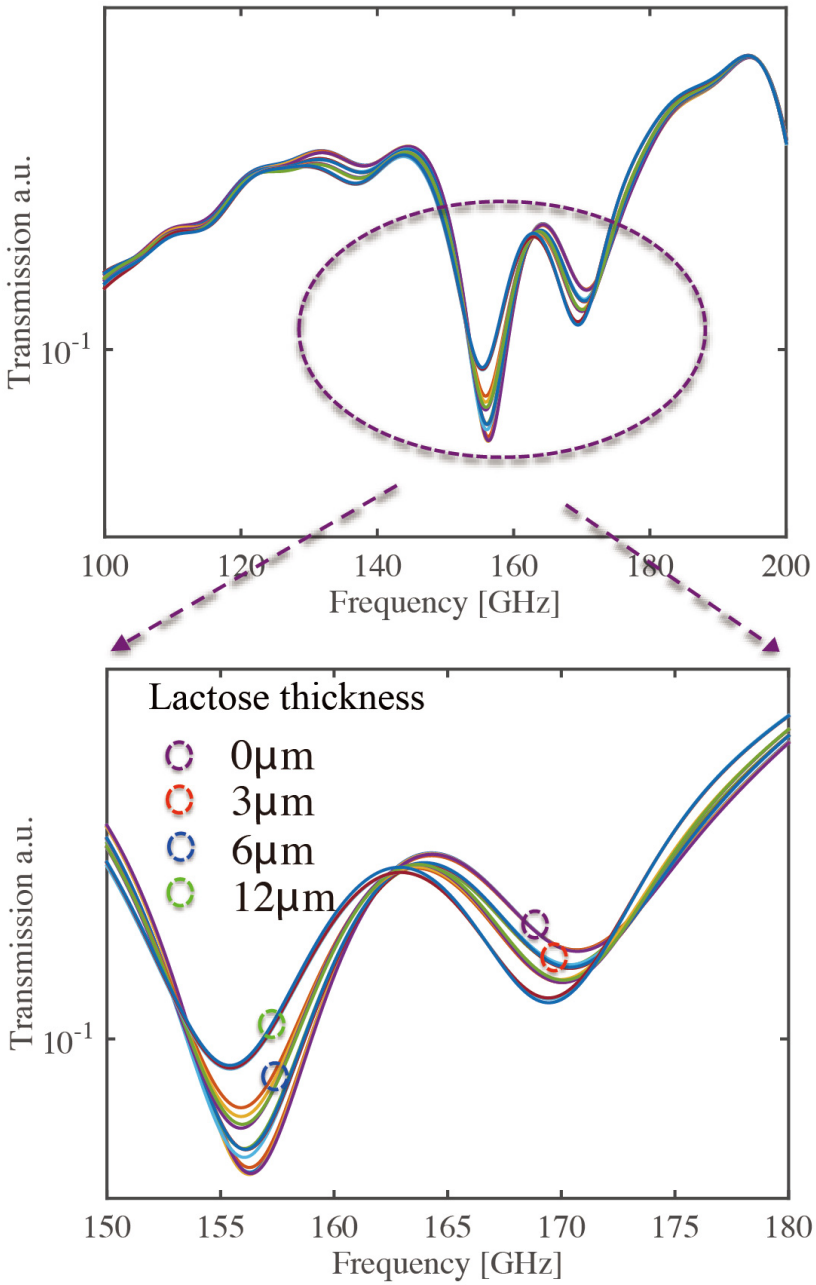


Figure 7.11 Transmission spectra of several sections of 3D printed THz Bragg waveguides with different defect layer thickness in the first layer of the Bragg reflector.

### 7.5.4 Practical applications of 3D printed THz Bragg waveguide sensors

Due to the advantages of the proposed 3D printed THz Bragg waveguides such as high sensitivity, flexibility to tailor the spectral features, and low cost, as well as simplicity in the structure and fabrication, we believe our Bragg waveguide sensors could be used as a very promising platform for a variety of scientific and industrial application. As we have demonstrated in Chapter 6, the THz Bragg waveguide sensors can be used to detect thin films with different thicknesses, or small quantities of analytes in powder forms. This sensing strategy can be used for industrial or environmental pollution detection, as well as monitoring of dynamical generation of solid or liquid compounds in chemical reactions.

We would like to highlight several advantages of the proposed sensing system, which uses resonant phenomenon in the THz waveguides versus more traditional ways for layer thickness and composition monitoring (e.g., free space transmission mode spectroscopy). The free space transmission mode spectroscopy measures thin film properties by monitoring the phase variations of the THz waves transmitting through the analyte film. Such systems typically suffer from a relatively moderate interaction length of the THz waves with the target analyte film, as well as a complicated sensing setup. Our waveguide sensor rather uses resonant interaction between its various guided and leaky modes in the alayte layer while employing an amplitude detection modality. Amplitude detection requires considerably simpler and cheaper THz systems, at the same time, offer a comparable sensitivity compared to the state-of-art phase detection method used in the free space transmission mode spectroscopy. This is a major advantage for the development of practical THz systems for industrial monitoring and sensing applications. Secondly, we note that most of the current resonant THz sensors have relatively broad spectral features, thus, resulting in lower sensitivity and resolution. In our THz waveguide-based sensors, the modal field in the hollow core is resonantly coupled to the field in the defect mode located in the analyte layer. The resonant dip with narrow linewidth in the waveguide transmission spectrum can be used to resolve minute spectral shifts in the resonant dip positions caused by small changes in the defect layer thickness or refractive index, which allows an improved detection limit, compared other conventional setups. We note that, by using a CW THz setup [259] capable of 4MHz spectral resolution, the waveguide sensors discussed in this paper can be, in principle, designed for the detection of sub-100nm changes in the layer thickness. To our

knowledge, this is virtually impossible to achieve with other more standard approaches. Thirdly, we note that waveguide-based sensing system offers an opportunity for seamless integration of various conduits for the delivery of analytes (e.g. liquids, powders, gases) into the optical setup. As an example, in this work, we demonstrate that the spinning hollow core waveguide with minor modifications in its geometry can be used to produce (via centrifugal force) and hold thin layers of powders for the detection of changes in their mass (thickness), which, to our best knowledge, has never been reported before. This sensing strategy is especially relevant for many practical applications, such as environmental monitoring, among others applications. Finally, we note that by adjusting the waveguide geometry, one can target specific frequency range of interest, and enrich the sensing scenarios. For example, as proposed in our manuscript, by designing the operation frequency of the sensor near the absorption peak of α-lactose monohydrate (at 0.53THz), one can simultaneously monitor the layer thickness and the lactose concentration in the powders using the anticrossing frequency and the absorption peak strength, respectively. Again, to our knowledge, this multi-parameter sensing modality has never been reported before, and it is beneficial for the design of versatile, and highly integrated sensors, which enables a comprehensive multi-parameter material characterization by a single device.

In this section, we would like to propose some other potential application scenarios of the 3D printed THz hollow-core Bragg waveguide sensors.

#### 7.5.4.1 Online monitoring of water content in crude oil

The accurate measurement of water content of crude oil in an oil tank, oil well, and oil pipeline is of great importance, and it has a direct impact on mining and dehydration, as well as refining of the crude oil. The existence of water in crude oil can introduce serious problems in the petroleum refining process, and other related chemical or petroleum engineering processes. Currently, most of the measurements of the water content of crude oil are based on offline methods. The basic principle of offline analysis is by separating the moisture from crude oil and analyzing the mass fraction of water [196, 197]. With the increase of automation in the process of oilfield production, online measurement is more desirable to monitor continuously the relative concentrations of water in the treated mixtures to ensure that the water contents remain below a certain level.

The limitation of THz wave propagation through water does enable one of the most useful applications of THz waves: the detection of moisture or water content in materials. What makes

this application such a natural fit for THz sensing is that water is highly absorptive in the THz range, while many materials are either transparent or reasonably transparent to THz (i.e., paper, plastics, and crude oil). Consequently, by monitoring the variations in transmission amplitude of test samples, one can potentially extract the corresponding water contents.

Hollow core THz Bragg waveguides can be used as a viable platform for such applications, as they could inherently integrate the THz detection with microfluidics, thus allowing for continuous online monitoring the water content of crude oil in a contained, highly integrated manner. With the amplitude and phase information of samples obtained from the coherent measurements of a THz-TDS characterization, one can pursue two approaches to deduce the relative concentrations of water in the crude oils; first, the water contents in the crude oils can be interrogated with the variations in the transmission amplitude of the THz Bragg waveguide when the core is filled with crude oil suspensions; second, by using a spectral-based detection modality, water contents can be inferred from the refractive indices of the oil suspensions by using the Bruggeman effective medium theory, as we have demonstrated in Chapter 3. We note that when the waveguide core is used as the fluidic channel, the dynamic range of such sensors for monitoring the water contents in crude oils is limited to below 10% for sensing cells with centimeter length, because of high attenuation of THz propagation in water. However, this problem could be possibly circumvented by employing the air gap between the high refractive index layers with a sub-millimeter size as the fluidic channel to accommodate the liquid samples. In this sensing configuration, since most of the THz power is guided in the low-loss air-core region, the propagation loss is kept low. Changes in the analytes refractive indices flowing through the gap will modify the anticrossing frequency between the core-guide mode and the defect modes. By tracking the shift in the anticrossing frequency due to the changes of the analytes refractive indices, one can then estimate the water contents by using the Bruggeman effective medium theory. This configuration could be used as an alternative when monitoring of crude oil samples with high water contents is needed.

#### 7.5.4.2 Detection of bacteria

Billions of people around the world are infected with bacteria every year. Detection of pathogen bacteria has been an area of prime interest in the field of food and water safety, as well as public health. Conventionally, pathogen bacteria are detected using a plate count technique [198],

enzyme-linked immunosorbent assay (ELISA) [199], biochemical tests and/or polymerase chain reaction (PCR) [200]. However, these techniques are time-consuming and labor-intensive. Therefore, there is a need for alternate rapid, sensitive, and affordable pathogen detection platforms. The THz Bragg waveguide sensors proposed in this work could be used for efficient, label-free detection of bacteria pathogens. By functionalizing the surface of the fiber core with specific phages, selective detection of pathogenic bacteria can be realized with the proposed THz Bragg fiber sensor. Changes in the fiber anticrossing frequency can be correlated with the concentration of bacteria samples. This detection method is label-free and it does not rely on the presence of any bacterial "fingerprint" features in the THz spectrum.

### 7.5.5 Limitation of the THz Bragg waveguide sensors and future directions

One drawback of the currently demonstrated THz waveguide sensors is the relatively poor modal overlap with the target analytes, when the spectral region is far from the anticrossing frequency. Over this spectral region, the modal fields interact weakly with the analyte layer. Therefore, it is relatively impractical for unique identification of the target analytes by their spectral fingerprints.

In order to enable specific detection of the analytes, one can optimize the waveguide design, so that the operation frequency is near the fingerprint of target analyte. The enhanced light-matter interactions that occur in the vicinity of the anticrossing frequency between the core-guided mode and the analyte layer open the door towards a spectroscopic approach for THz sensing using the proposed waveguide sensors. In such configurations, one can simultaneously monitor the analyte layer thickness and the concentration (e.g., in powder analytes) using the anticrossing frequency and the absorption peak strength, respectively. This modality, however, has to be further researched. Another way to enhance the modal overlap is reducing the waveguide core size. However, a reduction in the core size also results in an increase in the fiber propagation loss, because the core mode would penetrate deeper into the cladding material. As a result, there is a trade-off between the enhancement of the modal overlap with the test analyte and an increase in the fiber attenuation loss. Moreover, a viable approach to enhance the modal overlap between the core modes and the analyte layer is to introduce a porous network of thin bridges that can be biologically or chemically functionalized. Porous-core waveguides offer better confinement and lower losses, due to less material residing in the core compared to solid-core waveguides. These waveguides have great potential for sensing applications. Such THz

porous waveguide sensors can be conveniently fabricated using 3D printing technologies. We note that currently, a 100μm lateral resolution is standard in 3D stereolithography systems. Some commercial systems even offer sub-10μm lateral resolution. Compared to the traditional fiber drawing techniques, even when supplemented by methods including stacking [201], drilling [242], and extrusion moulding [202] for the preform fabrication, 3D printing technologies enable the fabrication of waveguides with significantly complex transverse profiles, which means that this method could have a considerable impact on the developments of practical terahertz waveguides and enrich their application scenarios in numerous industrial fields.

Additionally, we would like to highlight the flexibility of tailoring the spectral features of the THz waveguides by properly designing their geometric parameters. This could be considered as a very promising research direction for the development of THz Bragg waveguide sensors in order to suit particular needs in different industrial applications. In what follows, we indicate three possible independent "knobs" (the location of the defect, the size of the defect, and the overall scaling of the structure) that can be used to tailor the spectral properties of the waveguide in intuitively predictable ways.

The first knob is the depth of the defect within the Bragg reflector, which controls the interaction strength of the core-guided mode and the defect mode. According to the coupled-mode theory [223], the magnitude of the frequency range over which the modal interaction takes place depends on the strength of the interaction between the core-guided mode and the defect mode (or in other words the degree of overlap between the fields of the two modes). In this thesis, we have demonstrated the waveguide for resonant surface sensing when the defect layer is located in the first layer of the Bragg reflector. In this case, the defect modes have relatively strong interactions with the core-guided mode. In fact, when the interaction is weaker, which will be the case if the defect is located further from the waveguide core, the frequency range over which the avoided crossing occurs will be narrower, resulting in even sharper loss peaks in the waveguide transmission spectrum. This is highly attractive for resonant sensing applications if the target analytes could be loaded in the vicinity of the defect layer.

The second knob is the structure of the defect, and in particular the size of the defect layer, which controls the anticrossing frequency between the core-guided mode and the defect modes.

One can shift the frequency of modal interaction up or down by decreasing or increasing the size of the defect, respectively.

A third knob is the overall scaling of the waveguide structure. By changing the periodicity or, equivalently, the individual layer in the Bragg reflector, one can perform sensing at selectable wavelengths. We note that although the materials of the cladding may be highly lossy at these wavelength regions, these properties can be suppressed by many orders of magnitude for the core-guided modes, which have almost all of their fields within the hollow core. This knob is particularly useful when designing waveguide for the detection target analytes, which have absorption signatures over certain frequency regions.

Finally, another area in which additional research can be carried out is waveguide dispersion tailoring based on the modal interaction between the core-guided mode and the defect modes [243]. We note that, in the hollow-core THz Bragg waveguide, the intrinsic material dispersion is negligible, so the waveguide dispersion could be controlled entirely by controlling the geometric parameters. This can be accomplished via adjusting the three independent “knobs” as mentioned before. This strategy could be useful for applications such as accurate dispersion compensation and dispersion-less transmission in the THz range.

# CHAPTER 8 CONCLUSION AND PERSPECTIVE

To conclude, in this thesis we have proposed and experimentally demonstrated hollow-core photonic Bragg fibers for bulk refractometry of commercial liquid analytes and surface sensing applications including *in situ* monitoring of surface dynamics, and detection of thickness variations of bio-layers and powder analytes attached to the waveguide inner surface. Both sensing schemes can be used for a wide range of industrial sensing applications.

The first project undertaken in this thesis explores the capability of the liquid-core Bragg fibers to simultaneously monitor the real and imaginary parts of the analyte refractive index by interrogating the bandgap center position of the Bragg fiber and the fiber transmission amplitude at the bandgap center. The fiber features a large hollow core surrounded by an alternating PMMA/PS multilayer, and it operates in the visible range. We then apply this fiber sensor to monitor concentrations of various commercial cooling oils by employing a two-channel sensing modality. Right from the outset of this project, the aim of investigating the amplitude-based detection modality is to forgo the need of bulky spectrometers and build more compact refractometer for industrial sensing applications. Moreover, in principle, using multiple-channel detection modalities for measuring an experimental value could reduce the detection errors. However, because of unstable optical output of the cooling oils when measuring the absorption coefficients using a cut-back technique, the accuracy of amplitude detection modality is much worse than that of the spectral modality, the overall detection error of the fiber sensor is not reduced. In our future work, we will have to balance the accuracies of the two sensing channels in order to enhance the overall accuracy of the two-channel Bragg fiber sensor. In practice, we find that the spectral-based detection modality with higher accuracy and stability is sufficient for the instrumentation of the Bragg fiber sensor for industrial sensing applications. In order to further increase the spectral sensitivity and improve the detection accuracy, we have investigated the factors that could influence the spectral sensitivity of the Bragg fiber sensor. We find that by optimizing the fiber geometry parameters (i.e., bilayer thickness contrast), we have enhanced the spectral sensitivity of the sensor by more than 30% compared to the experimental values we have achieved before. The highest spectral sensitivity achieved experimentally in this thesis is 1900nm/RIU, which is the highest value that for the Bragg fiber based refractometers. The presented fiber sensor can inherently integrate optical detection with microfluidics, thus allowing

for online monitoring of the concentration of many industrial fluids such as heat transfer fluids, sawing fluids, and other industrial dilutions with sub-1%v accuracy. Moreover, since the spectral sensitivity is virtually independent on the fiber length, the centimeters-long Bragg fiber pieces can be used to produce ultra-compact sensing systems. As a practical example, we have described a compact smartphone-based sensing system, in which the LED acts as the light source and the camera, together with a diffracting grating, is used to interrogate the transmission spectra of the liquid-filled Bragg fiber sensor. The proposed cost-effective and portable smartphone-based refractive index sensor can be used for fast refractometry of commercial liquids, point-of-care diagnostics, and environmental monitoring, as well as numerous healthcare and other bio-sensing applications.

In the second part of the thesis, we demonstrate the hollow-core Bragg fibers operating in the visible range for surface sensing applications. The fiber sensor operates using a spectral-based detection modality to monitor changes in the thickness of an analyte layer deposited on the inner surface of the fiber core. Due to the phenomenon of avoided crossing in the vicinity of the phase matching wavelength between the core-guided and the analyte layer bound modes, fiber transmission spectra are significantly modified, thus allowing for the monitoring of the changes in the analyte layer properties. It is, in fact, the hybridization of the core guided modes of a Bragg fiber with the analyte layer bound modes that enables the surface sensing modality of the Bragg fibers. One of the design challenges of using the Bragg fibers for surface sensing is a moderate overlap between the core-guided modes and the analyte layer bound modes, because the fields of core-guided modes decrease rapidly from the core center towards the fiber core inner surface. In order to increase the modal overlap between the core-guided modes and the analyte layer bound modes, we propose squeezing a section of the Bragg fiber, thus significantly enhancing their interaction via anticrossing phenomenon, which, in turn, enhances surface sensitivity of the fiber sensor. Due to the moderate mechanical robustness and chemical resistivity of the all-polymer Bragg fiber when it is filled with ethyl alcohol, the fiber breaks or cracks if squeezed by a displacement of more than 500μm (the resultant core size ~100μm). As a result, only a sensitivity enhancement (~35%) is achieved in our experimental demonstration when the core size is reduced from 600μm to 100μm. As a practical demonstration, we apply our fiber sensor to *in situ* monitoring of the dissolution dynamics of a sub-micron-thick polyvinyl butyral (PVB) film coated on the surface of the liquid-filled Bragg fiber core. Strong spectral shift is observed during

the dissolution of the PVB film, and a surface spectral sensitivity of ~0.07nm/nm is achieved experimentally with aqueous analytes. The proposed fiber sensor offers a new sensing modality and opens new sensing applications for photonic bandgap fibers, such as real time detection of binding and affinity and study of kinetics for a range of chemical and biological samples.

The first two projects demonstrate a "one fiber" solution operating in the visible range for both bulk refractometry of liquid analytes and surface sensing applications. The hollow-core Bragg fibers fabricated using a commercial fiber-drawing tower can be directly integrated into the opto-fluidic setup without any fiber modifications, such as fiber tapering, cladding stripping, or grating inscriptions, which significantly simplifies the practical sensing implementation, and greatly enhances the robustness of the system. Other advantages of the proposed sensor include high sensitivity, short response time, label-free detection, good repeatability and stability, cost-effective mass production, and re-usability.

In the third part of the thesis, we propose using 3D printed hollow-core THz Bragg waveguides with defect layers for resonant surface sensing applications. It is demonstrated that by introducing a defect layer into the first layer of the Bragg reflector structure, a strong and spectrally narrow dip appears in the waveguide transmission spectrum. The dip is due to the anticrossing phenomenon between the core-guided mode and a mode localized in the defect layer of the Bragg reflector. By tracking the anticrossing frequency, which manifests itself as a transmission dip with narrow linewidth in the waveguide transmission spectrum, one can detect changes in the geometrical or optical properties of the defect layer. The experimentally achieved linewidth of the resonant dip is only 3GHz, which is among the narrowest measured for any resonator in the THz range. As a practical demonstration, we apply this sensor for the detection of thin PMMA films with different thicknesses loaded on the waveguide inner surface. The thickness of the target film can be directly correlated to the position of the anticrossing frequency. A surface sensitivity of 0.1GHz/μm is achieved experimentally. Moreover, an example of THz resonant surface sensing using α-lactose monohydrate powder as the analyte is demonstrated experimentally. The efficient excitation of defect mode is directly verified by measuring the mode structure at the output fact of the waveguide using a modal imaging technique. The Bragg waveguide sensor is characterized using both TDS setup and CW setup, and we conclude that CW setup with higher frequency resolution is more suitable for applications that require high sensitivities. The ability to tailor the spectral properties of the sensors by properly designing their

geometric parameters means that the Bragg waveguide become a viable platform for a wide range of applications, such as detection of various powder analytes (e.g., illicit drugs, hazardous powders, suspended powder pollutants), as well as bacteria detection and other applications.

# BIBLIOGRAPHY


1. J. Beuthan, O. Minet, J. Helfmann, M. Herrig, and G. Muller, "The spatial variation of the refractive index in biological cells," Physics in Medicine and Biology, vol. 41, pp. 369-382, 1996.
2. S. Singh, "Refractive index measurement and its applications," Physica Scripta, vol. 65, pp. 167-180, 2002.
3. X. Fan, I M. White, S I. Shopova, H. Zhu, J D. Suter, Y. Sun, "Sensitive optical biosensors for unlabeled targets: A review," Analytica Chimica Acta, vol. 620, pp. 8-26, 2008.
4. A. B. Dahlin, Plasmonic Biosensors: An integrated view of refractometric detection, IOS Press, 2012.
5. H. Yu, L. Xiong, Z. Chen, Q. Li, X. Yi, Y. Ding, F. Wang, H. Lv, and Y. Ding, "Solution concentration and refractive index sensing based on polymer microfiber knot resonator," Applied Physics Express, vol. 7, no. 2, pp. 022501, 2014.
6. P. Berini, "Bulk and surface sensitivities of surface plasmon waveguides," New Journal of Physics, vol. 10, pp. 105010-37, 2008.
7. F. DellOlio and V. M. N. Passaro, "Optical sensing by optimized silicon slot waveguides," Optics Express, vol. 15, no. 8, pp. 4977-17, 2007.
8. M. Zourob, S. Elwary, A. Turner, Principles of bacterial detection: biosensors, recognition receptors and microsystems, Springer, 2008.
9. D. A. Krohn, Fiber optic sensors: fundamentals and applications, 3rd Edition, Instrument Society of America, 1992.
10. M. A. Cooper, "Label-free biosensors: techniques and applications," Cambridge University Press, 2009.
11. R. E. Kunz. K. Cottier, "Optimizing integrated optical chips for label-free bio-chemical sensing," Analytical and Bioanalytical Chemistry, vol. 384, pp. 180-190, 2006.

12. K. Kawase, Y. Ogawa, Y. Watanabe, and H. Inoue, "Non-destructive terahertz imaging of illicit drugs using spectral fingerprints," Optics Express, vol. 11, no. 20, pp. 2549-2554, 2003.

13. J. F. Federici, B. Schulkin, F. Huang, D. Gary, R. Barat, F. Oliveira and D. Zimdars, "THz imaging and sensing for security applications-explosives, weapons and drugs," Semiconductor Science and Technology, vol. 20, pp. S266, 2005.

14. A. Davies, "Terahertz spectroscopy of explosives and drugs," Materials Today, vol. 11, no. 3, pp. 18-26, 2008.

15. M. Skorobogatiy, "Resonant bio-chemical sensors based on Photonic Bandgap waveguides and fibers" in Optical guided-wave chemical and biosensors II, Springer Series on Chemical Sensors and Biosensors, edited by A. Lakhtakia and Z. Mohammod, Springer-Verlag Berlin Heidelberg, 2010.

16. M. Y. Ye, M. X. Shen, X. M. Lin, "Ringing phenomenon based whispering-gallery-mode sensing," Scientific Report, vol. 6, pp. 19597, 2016.

17. A. Boleininger, T. Lake, S. Hami and C. Vallance, "Whispering gallery modes in standard optical fibres for fibre profiling measurements and sensing of unlabelled chemical species," Sensors, vol. 10, pp. 1765-1781, 2010.

18. R. Manor, A. Datta, I. Ahmad, M. Holta, S. Gangopadhyay, and T. Dallsa, "Microfabrication and characterization of liquid core waveguide glass channels coated with teflon AF," IEEE Sensors Journal, vol. 3, no. 6, pp. 687-692, 2003.

19. V. Benoit and M. C. Yappert, "Effect of capillary properties on the sensitivity enhancement in capillary/fiber optical sensors," Analytical Chemistry, vol. 68, no. 1, pp. 183-188, 1996.

20. M. Skorobogatiy, Nanostructured and subwavelength waveguides, Wiley, 2012.

21. T. E. Hirschfeld, "Total reflection fluorescence," Canadian Journal of Spectroscopy, vol. 10, pp. 128, 1965.

22. C. R. Taitt, G. P. Anderson, F. S. Ligler, "Evanescent wave fluorescence biosensors," Biosensors and Bioelectronics," vol. 20, pp. 2470-2487, 2005.

23. A. Leung, P. M. Shankar, R. Mutharasan, “A review of fiber-optic biosensors,” Sensors and Actuators B, vol. 125, pp. 688-703, 2007.

24. C. R. Taitt, G. P. Anderson, F. S. Ligler, “Evanescent wave fluorescence biosensors: Advances of the last decade,” Biosensors and Bioelectronics, vol. 76, pp. 103-112, 2016.

25. M. E. Bosch, A. J. Sanchez, F. S. Rojas, and C. B. Ojeda, Recent Development in Optical Fiber Biosensors, Sensors, 7(6), 797-859, 2007

26. A. Banerjee, S. Mukherjee, R. K. Verma, B. Jana, T. K. Khan, M. Chakroborty, R. Das, S. Biswas, A. Saxena, V. Singh, R. M. Hallen, R. S. Rajput, P. Tewai, V. Singh, A. K. Ghosh, J. John, H. Wannare, and P. Gupta-Bhaya, “Fiber optic sensing of liquid refractive index,” Sensors and Actuators: B, 123, 594-605, 2007

27. G. P. Anderson, J. P. Golden, F. S. Ligler, “An evanescent-wave biosensor Fluorescent signal acquisition from step-etched fiber optic probes,” IEEE Transazations on Biomedical Engineering, vol. 41, no. 6, pp. 578-584, 1994.

28. M. Mehrvar, C. BIS, J. M. SCHARER, M. M. Young, and J. H. Luong, “Fiber-Optic Biosensors-Trends and Advances,” Analytical Sciences, vol. 16, pp. 677-694, 2000.

29. M. Yasuda, T. Akimoto, “High-contrast fluorescence microscopy for a biomolecular analysis based on polarization techniques using an optical interference mirror slide,” Biosensors, vol. 4, no. 4, pp. 513-522, 2014.

30. F. Longa, C. Gao, H.C. Shi, M. He, A.N. Zhu, A.M. Klibanov, A.Z. Gu, “Reusable evanescent wave DNA biosensor for rapid, highly sensitive, and selective detection of mercury ions,” Biosensors and Bioelectronics, vol. 26, pp. 4018-4023, 2011.

31. K. Bhavsar, R. Prabhu and P. Pollard, “Development of dithizone based fibre optic evanescent wave sensor for heavy metal ion detection in aqueous environments,” Journal of Physics: Conference Series, vol. 450, pp. 012011-6, 2013.

32. H. Qiu, S. Gao, P. Chen, Z. Li, X. Liu, C. Zhang, Y. Xu, S. Jiang, C. Yang, Y. Huo, W. Yue, “Evanescent wave absorption sensor based on tapered multimode fiber coated with monolayer graphene film,” Optics Communications, vol. 366, pp. 275-281, 2016.

33. M. Sheeba, M. Rajesh, C. P. G. Vallabhan, V. P. N. Nampoori, and P. Radhakrishnan, "Fibre optic sensor for the detection of adulterant traces in coconut oil," Measurement Science and Technology, vol. 16, pp. 2247-2250, 2005.

34. J. Villiatoro, D. Hernadex, and D. Talavera, "High resolution refractive index sensing with cladded multimode tapered optical fiber," Electronic Letters, vol. 40, pp. 106-107, 2004.

35. K. R. Sohna, K. T. Kimb, J. W. Song, "Optical fiber sensor for water detection using a side-polished fiber coupler with a planar glass-overlay-waveguide," Sensors and Actuators A, vol. 101, pp. 137-142, 2002.

36. A. Mukherjee, D. Munsi, V. Saxena, R. Rajput, P. Tewari, V. Singh, A. K. Ghosh, J. John, H. Wannare, and P. Gupta-Bhaya, "Characterization of a fiber optic liquid refractive index sensor," Sensors and Actuators: B, vol. 145, pp. 265-271, 2010.

37. K. Cherif, S. Hleli, A. Abdelghani, N. Jaffrezic-Renault and V. Matejec, "Chemical detection in liquid media with a refractometric sensor based on a multimode optical fibre," Sensors, vol. 195, pp. 204-210, 2002.

38. W. B. Ji, S. C. Tjin, B. Lin, and C. L. Ng, "Highly sensitive refractive index sensor based on adiabatically tapered microfiber long period gratings," Sensors, vol. 13, no. 10, pp. 14055-14063, 2013.

39. D. M. Hernandez, J. Villatoro, D. Lunamoreno, "Miniature optical fiber refractometer using cladded multimode tapered fiber tips," Sensors and Actuators: B, vol. 110, pp. 36-40, 2005.

40. A. Iadicicco, D. Paladino, S. Campopiano, W. J. Bock, A. Cutolo, and A. Cusano, "Evanescent wave sensor based on permanently bent single mode optical fiber," Sensors and Actuators B, vol. 155, no.2, pp. 903-908, 2011.

41. N. Zhong, M. Zhao, and Y. Li, "U-shaped, double-tapered, fiber-optic sensor for effective biofilm growth monitoring," Biomedical Optics Express, vol. 7, no. 2, pp. 335-351, 2016.

42. A. Dudus, R. Blue, and D. Uttamchandani, "Comparative study of microfiber and side-polished optical fiber sensors for refractometry in microfluidics," IEEE Sensors Journal, vol. 13, no. 5, pp. 1594-1601, 2013.

43. C. Caucheteur, T. Guo, J. Albert, "Review of plasmonic fiber optic biochemical sensors: improving the limit of detection," Analytical Bioanalytical Chemistry, vol. 407, pp. 3883-3897, 2015.

44. A. K. Sharma, R. Jha, and B. D. Gupta, "Fiber-optic sensors based on surface plasmon resonance: a comprehensive review," IEEE Sensors Journal, vol. 7, pp. 1118, 2007.

45. A. Hassani and M. Skorobogatiy, "Design criteria for microstructured-optical-fiber-based surface-plasmon-resnoance sensors," Journal of the Optical Society of America B, vol. 24, pp. 1423, 2007.

46. P. Englebienne, A. V. Hoonacker, and M. Verhas, "Surface plasmon resonance: principles, methods and applications in biomedical sciences," Spectroscopy, vol. 17, pp. 255-273, 2003.

47. Y. Chen, R. Zheng, Y. Lu, P. Wang, and H. Ming, "Fiber-optic surface plasmon resonant sensor with low-index anti-oxidation coating," Chinese Optics Letters, vol. 9, pp. 100605, 2011.

48. Y. S. Dwivedi, A. K. Sharma, B. D. Gupta. "Influence of design parameters on the performance of a SPR based fiber optic sensor," Plasmonics, vol. 3, pp. 79-86, 2008.

49. P. Englebienne, A. V. Hoonacker, and M. Verhas, "Surface plasmon resonance: principles, methods and applications in biomedical sciences," Spectroscopy, vol. 17, pp. 255-273 (2003).

50. Y. Lin, "Characteritics of optical fiber refractive index sensor based on surface plasmon resonance," Microwave and Optical Technology Letters, vol. 55, pp. 574, 2013.

51. N. Cennamo, D. Massarotti, L. Conte, and L. Zeni, "Low cost sensors based on SPR in a plastic optical fiber for biosensor implementation," Sensors, vol. 11, pp. 11752-11760, 2011.

52. P. Bhatia, and B. D. Gupta, "Surface plasmon resonance based fiber-optic refractive index sensor: sensitivity enhancement," Applied Optics, vol. 50, pp. 2032, 2011.

53. J. H. Ahn, T. Y. Seong, W. M. Kim, T. S. Lee, I. Kim and K. Lee, "Fiber-optic waveguide coupled surface plasmon resonance sensor," Optics Express, vol. 20, pp. 21729, 2012.

54. D. M. Hernandez, and J. Villatoro, "High-resolution refractive index by means of a multiple-peak surface plasmon resonance optical fiber sensor," Sensors and Actuators: B, vol. 115, pp. 227-231, 2006.

55. M. Mar, R. C. Jorgenson, S. Letellier, and S. S. Yee, "*In-situ* characterization of multilayered Langmuir-Blodgett films using a surface plasmon resonance fiber optic sensor," Proceedings 15th Annual International Conference of the IEEE, pp. 1551-1552, 1993.

56. Y. C. Tsao, W. H. Tsai, W. C. Shih, and M. S. Wu, "An *in-situ* real-time Optical fiber sensor based on surface plasmon resonance for monitoring the growth of TiO2 thin films," Sensors, vol. 13, no. 7, pp. 9513-9521, 2013.

57. Y. Shevchenkoa, N. U. Ahamadb, G. Galwayb, A. Ianoul b and J. Alberta, "Surface plasmon resonance fiber sensor for *in situ* monitoring of the deposition of nm-scale polymer films," Proceeding of SPIE, 20th International Conference on Optical Fibre Sensors, vol. 7503, pp. 11, 2009.

58. Y. Shevchenko, N. U. Ahamad, A. Ianoul and J. Albert, "*In situ* monitoring of the formation of nanoscale polyelectrolyte coatings on optical fibers using Surface Plasmon Resonances," Optics Express, vol. 18, no. 19, pp. 20409-20421, 2010.

59. P. Englebienne, A. V. Hoonacker, and M. Verhas, "Surface plasmon resonance: principles, methods and applications in biomedical sciences," Spectroscopy, vol. 17, pp. 255-273, 2003.

60. S B. D. Gupta and R. K. Verma, "Surface plasmon resonance-based fiber optic sensors: principle, probe design, and some applications," Journal of Sensors, vol. 2009, pp. 979761, 2009.

61. J. Homola, S. S. Yee, G. Gauglitz, "Surface plasmon resonance sensors: review," Sensors and Actuators: B, vol. 54, pp. 3-15, 1999.

62. T. C. Chang, C. C. Wu, S. C. Wang, L. K. Chau, and W. H. Hsieh, "Using a fiber optic particle plasmon resonance biosensor to determine kinetic constants of antigen-antibody binding reaction," Analytical Chemistry, vol. 85, no. 1, pp. 245-250, 2013.

63. J. Pollet, F. Delport, K. P. Janssen, K. Jans, G. Maes, H. Pfeiffer, M. Wevers, and J. Lammertyn, "Fiber optic SPR biosensing of DNA hybridization and DNA-protein interactions," Biosensors and Bioelectronics, vol. 25, no. 4, pp. 864-869, 2009.

64. D. Ciprian, and P. Hlubina, "Theoretical model of the influence of oxide overlayer thickness on the performance of a surface plasmon fibre-optic sensor," Measurement Science and Technology, vol. 24, no. 2, pp. 1-17, 2013.

65. Y. Wang, S. Meng, Y. Liang, L. Li, W. Peng, “Fiber-optic surface plasmon resonance sensor with multi-alternating metal layers for biological measurement,” Plasmonic Sensors, vol. 3, no. 3, pp. 202-207, 2013.

66. V.V. R. Sai, T. Kundu, C. Deshmukh, S. Titus, P. Kumar, S. Mukherji, “Label-free fiber optic biosensor based on evanescent wave absorbance at 280 nm,” Sensors and Actuators B, vol. 143, pp. 724-730, 2010.

67. A. P. Zhang, S. Gao, G. Yan, and Y. Bai, “Advances in optical fiber Bragg grating sensor technology,” Photonic Sensors, vol. 2, pp. 1-13, 2012.

68. D. A. Pereira, O. Frazao, J. L. Santos, “Fiber Bragg grating sensing system for simultaneous measurement of salinity and temperature,” Optical Engineering, vol. 43, pp. 299, 2004.

69. T. Wang, Z. Yuan, Y. Gong, Y. Wu, Y. Rao, L. Wei, P. Guo, J. Wang, F. Wan, “Fiber Bragg grating strain sensors for marine engineering,” Photonic Sensors, vol. 3, no. 3, pp. 267-271, 2013.

70. W. Liang, Y. Huang, Y. Xu, R. K. Lee, and A. Yariv, “Highly sensitive fiber Bragg grating refractive index sensors, Applied Physics Letters, vol. 86, pp. 151122-151124, 2005.

71. A. Asseh, S. Sandgren, H. Ahlfeldt, B. Sahlgren, R. Stubbe, and G. Edwall, “Fiber optical Bragg grating refractometer,” Fiber and Integrated Optics, vol. 17, pp. 51-62, 1998.

72. A. N. Chryssis, S. M. Lee, S. B. Lee, S. S. Saini, and M. Dagenais, “High sensitivity evanescent field fiber Bragg grating sensor,” IEEE Photonics Technology Letters, vol. 17, pp. 1253, 2005.

73. K. Zhou, Y. Lai, X. Chen, K. Sugden, L. Zhang, I. Bennion, “A refractometer based on a micro-slot in a fiber Bragg grating formed by chemically assisted femtosecond laser processing,” Optics Express, vol. 15, pp. 15848, 2007.

74. A. N. Chryssis, S. S. Saini, S. M. Lee, H. M. Yi, W. E. Bentley, and M. Dagenais, “Detecting hybridization of DNA by highly sensitive evanescent field etched core fiber bragg grating sensors,” IEEE Journal of Selected Topics in Quantum Electronics, vol. 11, no. 4, pp. 864-872, 2005.

75. S. Maguis, G. Laffont, P. Ferdinand, B. Carbonnier, K. Kham, T. Mekhalif, and M. C. Millot, "Biofunctionalized tilted Fiber Bragg Gratings for label-free immune-sensing," Optics Express, vol. 16, no. 23, pp. 19049-19062, 2008.

76. T. Guo, F. Liu, X. Liang, X. Qiu, Y. Huang, C. Xie, P. Xu, W. Mao, B. O. Guan, J. Albert, "Highly sensitive detection of urinary protein variations using tilted fiber grating sensors with plasmonic nanocoatings," Biosensors and Bioelectronics, vol. 78, pp. 221-228, 2016.

77. V. Bhatia, D. K. Compbell, T. D'Alberto, G. A. T. Eyck, D. Sherr, K .A. Murphy, R. O. Claus, "Standard optical fiber long-period gratings with reduced temperature sensitivity for strain and refractive index sensing," Proceedings of Optical Fiber Communication, vol. 97, pp. 346-347, 1997.

78. V. Bhatia, T. D'Alberto, N. Zabaronick, and R. O. Claus, "Temperature-insensitive long-period gratings for strain and refractive index sensing," Proceeding of SPIE, vol. 3042, pp. 194, 1997.

79. S. M. Tripathi, E. Marin, A. Kumar, and J-P. Meunier, "Refractive index sensing characteristics of dual resonance long period gratings in bare and metal-coated D-shaped fibers," Applied Optics, vol. 48, pp. G53, 2009.

80. A. Iadicicco, D. paladino, P. Pilla, S. Campopiano, A. Cutolo and A. Cusano, "Long period gratings in new generation optical fibers," Recent Progress in Optical Fiber Research, edited by M. Yasin, InTech, 2012.

81. Z. Yin, X. Zhang, Y. Liu, F. Pang, and T. Wang, "Refractive index sensitivity characteristics of fiber taper long-period grating," in Asia Communications and Photonics Conference, Guangzhou, China, 2013.

82. A. N. Chryssis, S. M. Lee, S. B. Lee, S. S. Saini, and M. Dagenais, "High sensitivity evanescent field fiber Bragg grating sensor," IEEE Photonics Technology Letters, vol. 17, pp. 1253, 2005.

83. J. L. Kou, M. Ding, J. Feng, Y. Q. Lu, F. Xu, and G. Brambilla, "Microfiber-based Bragg gratings for sensing applications: a review sensors," Sensors, vol. 12, no. 7, pp. 8861-8876, 2012.

84. Z. Wang, J. R. Heflin, R. H. Stolen, S. Ramachandran, "Analysis of optical response of long period fiber gratings to nm-thick thin-film coatings," Optics Express, vol. 13, no. 8, pp. 2808, 2005.

85. C. Ribaut, V. Voisin, V. Malachovska, V. Dubois, P. Megret, R. Wattiez, C. Caucheteur, "Small biomolecule immunosensing with plasmonic optical fiber grating sensor," Biosensors and Bioelectronics, vol. 77, pp. 315-322, 2016.

86. J. N. Wang. "A microfluidic long-period fiber grating sensor platform for chloride ion concentration measurement," Sensors, vol. 11, no. 9, pp. 8550-8568, 2011.

87. M. P. Delisa, Z Zhang, M. Shiloach, "Evanescent wave long-period fiber Bragg grating as an immobilized antibody biosensor," Analytical Chemistry, vol. 72, no. 13, pp. 2895, 2000.

88. S. W. Harun and H. Arof, Current developments in optical fiber technology, InTech, 2013.

89. S. W. James and R. P Tatam, "Optical fibre long-period grating sensors: characteristics and application," Measurement Science and Technology, vol. 14, pp. R49-R61, 2003.

90. K. T. V. Grattan, T. Sun, "Optical Fiber Sensor Technology," Sensors and Actuators A, vol. 82, pp. 40-61, 2000.

91. H. Qu, M. Skorobogatiy, "Resonant bio- and chemical sensors using low-refractive-index-contrast liquid-core Bragg fibers," Sensors and Actuators B, vol. 161, pp. 261-268, 2012.

92. T. M. Monro, D. J. Richardson and P. J. Bennett, "Developing holey fibres for evanescent field devices," Electron Letters, vol. 35, pp. 1188-9, 1999.

93. T. M. Monro, D. J. Richardson, N. G. R. Broderick and P. J. Bennett, "Modeling large air fraction holey optical fibers," Journal of Lightwave Technology, vol. 18, pp. 50-6, 2000.

94. G. Pickeral, W. Peng, and A. Wang, "Random-hole optical fiber evanescent-wave gas sensing," Optics Letters, vol. 29, pp. 1476-1478, 2004.

95. X. Yu, Y. Zhang, Y. C. Kwok, P. Shum, "Highly sensitive photonic crystal fiber based absorption spectroscopy," Sensors and Actuators B, vol. 145, pp. 110-113, 2010.

96. J. B. Jensen, L. H. Pedersen, P. E. Hoiby, L. B. Nielsen, T. P. Hansen, J. R. Folkenberg, J. Riishede, D. Noordegraaf, K. Nielsen, A. Carlsen, and A. Bjarklev, "Photonic crystal fiber

based evanescent wave sensor for detection of biomolecules in aqueous solution," Optics Letters, vol. 29, no. 1, pp. 974-1976, 2004.

97. M. A. van Eijkelenborg, M. C. J. Large, A. Argyros, J. Zagari, S. Manos, N. A. Issa, I. Bassett, S. Fleming, R. C. McPhedran, C. Martijn de Sterke, and N. A. P. Nicorovici, "Microstructured polymer optical fibre," Optics Express vol. 9, pp. 319-327, 2001.

98. M. C. J. Large, A. Argyros, F. Cox, M. A. Eijkelenborg, S. Ponrathnam, N. S. Pujari,I. M. Bassett, R. Lwin, and G. W. Barton, "Microstructured polymer optical fibres: New opportunities and challenges," Molecular Crystals and Liquid Crystals, vol. 446, pp. 219-231 (2006).

99. J. B. Jensen, P. E. Hoiby, G. Emiliyanov, O. Bang, L. H. Pedersen, and A. Bjarklev, "Selective detection of antibodies in microstructured polymer optical fibers," Optics Express, vol. 13, pp. 5883-5889, 2005.

100. L. Rindorf, J. B. Jensen, M. Dufva, L. H. Pedersen, P. E. Hoiby, and O. Bang, "Photonic crystal fiber long-period gratings for biochemical sensing," Optics Express, vol. 14, pp. 8224-8231, 2006.

101. L. Rindorf and O. Bang, "Sensitivity of photonic crystal fiber grating sensors: biosensing, refractive index, strain, and temperature sensing," Journal of the Optical Society of America B, vol. 25, pp. 310-324, 2008.

102. L. Rindorf and O. Bang, "Highly sensitive refractometer with a photonic- crystal-fiber long-period grating," Optics Letters, vol. 33, no. 6, pp. 563-565, 2008.

103. N. M. Litchinitser, E. Poliakov, "Antiresonant guiding microstructured optical fibers for sensing applications," Applied Physic B, vol. 81, pp. 347-351, 2005.

104. X. Yu, P. Shum, G. B. Ren, and N. Q. Ngo, "Photonic crystal fibers with high index infiltrations for refractive index sensing," Optics Communication, vol. 281, pp. 4555-4559, 2008.

105. D. K. Wu, B. T. Kuhlmey, and B. J. Eggleton, "Ultrasensitive photonic crystal fiber refractive index sensor," Optics Letters, vol. 34, pp. 322-324, 2009.

106. C. Markos, W. Yuan, K. Vlachos, G. E. Town, and O. Bang, "Label-free biosensing with high sensitivity in dual-core microstructured polymer optical fibers," Optics Express, vol. 19, no. 8, pp. 7790-7798, 2011.

107. J. Sun, and C. C. Chan, "Photonic bandgap fiber for refractive index measurement," Sensors and Actuators B, vol. 128, pp. 46-50, 2007.

108. H. F. Xuan, W. Jin, J. Ju, H. L. Ho, M. Zhang, Y. B. Liao, "Low-contrast photonic bandgap fibers and their potential applications in liquid-base sensors," Proceeding of SPIE, in 3rd European Workshop on Optical Fiber Sensors, vol. 6619, pp. 661936, 2007.

109. E. Pone, C. Dubois, N. Guo, Y. Gao, A. Dupuis, F. Boismenu, S. Lacroix, M. Skorobogatiy, "Drawing of the hollow all-polymer Bragg fibers," Optics Express, vol. 14, no. 13, pp. 5838-5852, 2006.

110. K. J. Rowland, S. Afshar, A. Stolyarov, Y. Fink, and T. M. Monro, "Bragg waveguides with low-index liquid cores," Optics Express, vol. 20, pp. 48-62, 2012.

111. H. Qu, and M. Skorobogatiy, "Liquid-core low-refractive-index-contrast Bragg fiber sensor," Applied Physics Letters, vol. 98, pp. 201114, 2011.

112. J. Li, H. Qu, and M. Skorobogatiy, "Simultaneous monitoring the real and imaginary parts of the analyte refractive index using liquid-core photonic bandgap Bragg fibers", Optics Express, vol. 23, no. 18, pp. 22963, 2015.

113. M. Skorobogatiy, "Efficient antiguiding of TE and TM polarizations in low-index core waveguides without the need for an omnidirectional reflector," Optics Letters, vol. 30, no. 22, pp. 2991-2993, 2005.

114. J. Li, H, Qu, M. Skorobogatiy, "Squeezed Squeezed hollow-core photonic Bragg fiber for surface sensing applications," Optics Express, vol. 24, no. 14, pp. 15687-15691, 2016.

115. H. Qu, J. Li, M. Skorobogatiy, "Photonic bandgap fibers: a roadway to all-fiber refractometer systems for monitoring of liquid analytes" in Optofluidics, sensors and actuators in microstructured optical fibres, Woodhead Publishing, 2015.

116. H. Liu, H. Zhong, N. Karpowicz, Y. Chen and X. Zhang, "Terahertz spectroscopy and iImaging for defense and security applications," Proceeding of IEEE, vol. 95, pp. 1514, 2007.

117. S. Wang and X. C. Zhang, “Pulsed terahertz tomography,” Journal of Physics D: Applied Physics, vol. 37, pp. R1-R36, 2004.

118. M. Tonouchi, “Cutting edge terahertz technology,” Nature photonics, vol. 1, pp. 97-105, 2007.

119. Y. S. Lee, Principles of terahertz science and technology, Springer Publishing, 2008.

120. D. Mittleman, “Sensing with terahertz radiation,” Springer Series in Optical Sciences (Springer, 2010).

121. A. A. Rifat, R. Ahmed, “A simple photonic crystal fiber based plasmonic biosensor,” International OSA Network of Students, 2016.

122. X. Zhang, R. Wang, F. M. Cox, B. T. Kuhlmey, and M. C. J. Large, “Selective coating of holes in microstructured optical fiber and its application to in-fiber absorptive polarizers,” Optics Express, vol. 15, no. 24, pp. 16270-9, 2007.

123. P. Zhang, J. Yao, H. Cui, Y. Lu, “A surface plasmon resonance sensor based on a multi-core photonic crystal fiber,” Optoelectronics Letter, vol. 9, no. 5, pp. 342-345, 2013.

124. B. T. Kuhlmey, K. Pathmanandavel, and R. C. Mcphedran, “Multipole analysis of photonic crystal fibers with coated inclusions,” Optics Express, vol. 14, pp. 10851-10864 2006.

125. M. Hautakorpi, M. Mattinen, and H. Ludvigsen, “Surface-plasmon-resonance sensor based on three-hole microstructured optical fiber,” Optics Express, vol. 16, pp. 8427-32, 2008.

126. A. Hassani and M. Skorobogatiy, “Design criteria for microstructured-optical-fiberbased surface-plasmon-resonance sensors,” Journal of the Optical Society of America B, vol. 24, no. 6, pp. 1423-1429, 2007.

127. A. Hassani and M. Skorobogatiy, “Design of the microstructured optical fiber-based surface plasmon resonance sensors with enhanced microfluidics,” Optics Express, vol.14, no. 24, pp. 11616-11621, 2006.

128. R. Otupiri, E. K. Akowuah, and S. Haxha, “Multi-channel SPR biosensor based on PCF for multi-analyte sensing applications,” Optics Express, vol. 23, no. 12, pp. 15716-15727, 2015.

129. S. I. Azzam, M. O. Hameed, R. A. Shehata, A. M. Heika, S. S. A. Obayya, "Multichannel photonic crystal fiber surface plasmon resonance based sensor," Optical and Quantum Electronics, vol. 48, no. 2, pp.1-11, 2016.

130. J. N. Dash, R. Jha, "Highly sensitive D shaped PCF sensor based on SPR for near IR," Optical and Quantum Electronics, vol. 48, pp. 137, 2016.

131. H. Li, S. Li, H. Chen, J. Li, G. An, J. Zi, "A Polarization Filter Based on Photonic Crystal Fiber with Asymmetry Around Gold-Coated Holes," Plasmonics, vol. 11, pp.103-108, 2016.

132. D. F. Santos, A. Guerreiro, and J. M. Baptista, "SPR microstructured D-type optical fiber sensor configuration for refractive index measurement," IEEE Sensors Journal, vol. 15, no. 10, pp. 5472-5477, 2015.

133. C. Liu, L. Yang, W. Su, F. Wang, T. Sun, Q. Liu, H. Mu, P. K. Chu, "Numerical analysis of a photonic crystal fiber based on a surface plasmon resonance sensor with an annular analyte channel," Optics Communications, vol. 382, pp. 162-166, 2017.

134. M. C. P. Huy, G. Laffont, Y. Frignac, V. D. Marty, P. Ferdinand, P. Roy, J. Blondy, D. Pagnoux, W. Blanc, B. Dussardier, "Fiber Bragg grating photowrting in microstructured optical fibers for refractive index measurement, " Measurement Science and Technology, vol. 17, pp. 992-997, 2006.

135. M. C. P. Huy, G. Laffont, V. Dewynter, P. Ferdinand, P. Roy, J. Auguste, D. Pagnoux, W. Blanc, and B. Dussardier, "Three-hole microstructured optical fiber for efficient fiber Bragg grating refractometer," Optics Letters, vol. 32, pp. 2390, 2007.

136. M. C. P. Huy, G. Laffont, V. Dewynter, L. Labonte, P. Ferdinand, P. Roy, J. Auguste, D. Pagnoux, W. Blanc, and B. Dussardier, "Tilted fiber Bragg grating photowritten in microstructured optical fiber for improved refractive index measurement," Optics Express, vol. 14, pp. 10359, 2006.

137. A. P. Zhang, G. Yan, S. Gao, S. He, B. Kim, J. Im, and Y. Chung, "Microfluidic refractive- index sensors based on small-hole microstructured optical fiber Bragg gratings," Applied Physics Letters, vol. 98, pp. 221109-4, 2011.

138. X. Yu, P. Shum, and G. B. Ren, "Highly sensitive photonic crystal fiber-based refractive index sensing using mechanical long-period grating," IEEE Photonics Technology Letters, vol. 20, pp. 1688, 2008.

139. X. Yu, Pshum, G. B. Ren, and Y. Zhang, "Refractive index sensing using mechanical long- period grating in photonic crystal fiber," in Conference of Photonics Global at Singapore, no. 4781448, 2008.

140. Z. He, Y. Zhu, and H. Du, "Long-period gratings inscribed in air- and water- filled photonic crystal fiber for refractometric sensing of aqueous solution," Applied Physics Letters, vol. 92, pp. 044105-4, 2008.

141. H. Dobb, K. Kalli, and D. J. Webb, "Measured sensitivity of arc-induced long-period grating sensors in photonic crystal fiber," Optics Communication, vol. 260, pp. 184-191, 2006.

142. F. Tian, Z. He, and H. Du, "Numerical and experimental investigation of long-period gratings in photonic crystal fiber for refractive index sensing of gas media," Optics Letters, vol. 37, pp. 380, 2012.

143. L. Rindorf. J. B. Jensen, M. Dufva, L. H. Pedersen, P. F. Hoiby, and O. Bang, "Photonic crystal fiber long-perod gratings for biochemical sensing," Optics Express, vol. 14, pp. 8224, 2006.

144. M. Smietana, M. L. Korwin-Pawlowski, W. J. Bock, G. R. Pickrell, and J. Szmidt, "Refractive index sensing of fiber optic long-period grating structures coated with a plasma deposited diamond-like carbon thin film," Measurement Science and Technology, vol. 19, pp. 085301, 2008.

145. J. L. Lim, D. J. J. Hu, P. P. Shum and Y. wang, "Cascaded photonic crystal fiber interferometers for refractive index sensing," IEEE Photonics Journal, vol. 4, pp. 1163, 2012.

146. D. J. J. Hu, J. L. Lim, M. Jiang, Y. Wang, F. Luan, P. P. Shum, H. Wei, and W. Tong, "Long period grating cascaded to photonic crystal fiber modal interferometer for simultaneous measurement of temperature and refractive index," Optics Letters, vol. 37, pp. 2283, 2012.

147. J. Villatoro, M. P. Kreuzer, R. Jha, V. P. Minkovich, V. Finazzi, G. Badenes, and V. Prunery, "Photonic crystal fiber interferometer for chemical vapour detection with high sensitivity," Optics Express, vol. 17, pp. 1447, 2009.

148. M. Deng, C-P. Tang, T. Zhu, Y-J. Rao, L-C. Xu, and M. Han, "Refractive index measurement using photonic crystal fiber based Fabry-Perot interferometer," Applied Optics, vol. 49, pp. 1593, 2010.

149. Q. Li, and Q. Wang, "Refractive index sensor based on taperd PCF in-line interferometer," Chinese Optics Letters, vol. 10, pp. 090601-4, 2012.

150. J. Villatoro, V. P. Minkovich, and J. Zubia, "Photonic crystal fiber interferometer vector bending sensor," Optics Letters, vol. 40, no. 13, pp. 3113-3116, 2015.

151. R. Jha, J. Villatoro, G. Badenes, and V. Pruneri, "Refractometry based on a photonic crystal fiber interferometer," Optics Letters, vol. 34, pp. 617-620, 2009.

152. M. H. Frosz, A. Stefani, and O. Bang, "Highly sensitive and simple method for refractive index sensing of liquids in microstructured optical fibers using four-wave mixing," Optics Express, vol. 19, no. 11, pp. 10471-10484, 2011.

153. M. J. Fitch, R. Osiander, "Terahertz waves for communications and sensing," Johns Hopkins APL Technology Digest, vol. 25, no. 4, pp. 348-355, 2004.

154. Y. C. Shen, "Terahertz pulsed spectroscopy and imaging for pharmaceutical applications: A review," International Journal of Pharmaceutics, vol. 417, no. 1-2 pp. 48-60, 2011.

155. L. J. Chen, H. W. Chen, T. F. Kao, J. Y. Lu, and C. K. Sun, "Low-loss subwavelength plastic fiber for terahertz waveguiding," Optics Letters, vol. 31, no. 3, pp. 308-310, 2006.

156. M. Rozé, B. Ung, A. Mazhorova, M. Walther, and M. Skorobogatiy, "Suspended core subwavelength fibers: towards practical designs for low-loss terahertz guidance," Optics Express, vol. 19, no. 10, pp. 9127-9138, 2011.

157. A. Hassani, A. Dupuis, and M. Skorobogatiy, "Low loss porous terahertz fibers containing multiple subwavelength holes," Applied Physics Letters, vol. 92, no. 7, pp. 071101-4, 2008.

158. A. Dupuis, A. Mazhorova, F. Désévédavy, M. Rozé, and M. Skorobogatiy, "Spectral characterization of porous dielectric subwavelength THz fibers fabricated using a microstructured molding technique," Optics Express, vol. 18, no. 13, pp. 13813-13828, 2010.

159. S. Atakaramians, S. Afshar, B. M. Fisher, D. Abbott, and T. M. Monro, "Low loss, low dispersion and highly birefringent terahertz porous fibers," Optics Communications, vol. 282, no. 1, pp. 36-38, 2009.

160. A. Dupuis, J. F. Allard, D. Morris, K. Stoeffler, C. Dubois, and M. Skorobogatiy, "Fabrication and THz loss measurements of porous subwavelength fibers using a directional coupler method," Optics Express, vol. 17, no. 10, pp. 8012-8028, 2009.

161. S. Atakaramians, S. Afshar V, B. M. Fischer, D. Abbott, and T. M. Monro, "Porous fibers: a novel approach to low loss THz waveguides," Optics Express, vol. 16, no. 12, pp. 8845-8854, 2008.

162. S. Atakaramians, S. Afshar, T. M. Monro, and D. Abbott, "Terahertz dielectric waveguides," Advances in Optics and Photonics, vol. 5, no. 2, pp. 169-215, 2013.

163. B. Bowden, J. A. Harrington, and O. Mitrofanov, "Silver/polystyrene-coated hollow glass waveguides for the transmission of terahertz radiation," Optics Letters, vol. 32, no. 20, pp. 2945-2947, 2007.

164. A. Dupuis, K. Stoeffler, B. Ung, C. Dubois, and M. Skorobogatiy, "Transmission measurements of hollow-core THz Bragg fibers," Journal of the Optical Society of America B, vol. 28, no. 4, pp. 896-907, 2011.

165. A. M. Zheltikov, "Ray-optic analysis of the (bio)sensing ability of ring-cladding hollow waveguides," Applied Optics, vol. 47, no. 3, pp. 474-479, 2008.

166. C. H. Lai, Y. C. Hsueh, H. W. Chen, Y. J. Huang, H. C. Chang, and C. K. Sun, "Low-index terahertz pipe waveguides," Optics Letters, vol. 34, no. 21, pp. 3457-3459, 2009.

167. C. H. Lai, B. You, J. Y. Lu, T. A. Liu, J. L. Peng, C. K. Sun, and H. C. Chang, "Modal characteristics of antiresonant reflecting pipe waveguides for terahertz waveguiding," Optics Express, vol. 18, no.1, pp. 309-322, 2010.

168. B. You, J. Y. Lu, J. H. Liou, C. P. Yu, H. Z. Chen, T. A. Liu, J. L. Peng, "Subwavelength film sensing based on terahertz anti-resonant reflecting hollow waveguides," Optics Express, vol. 18, no. 1, pp. 19353-19360, 2010.

169. B. You, J. Y. Lu, C. P. Yu, T. A. Liu, and J. L. Peng, "Terahertz refractive index sensors using dielectric pipe waveguides," Optics Express, vol. 20, no. 1, pp. 5858-5866, 2010.

170. B. You, J. Y. Lu, "Remote and *in situ* sensing products in chemical reaction using a flexible terahertz pipe waveguide," Optics Express, vol. 24, no. 16, pp. 18013-18023, 2016.

171. R. Mendis and D. M. Mittleman, "An investigation of the lowest-order transverse-electric TE1 mode of the parallel-plate waveguide for THz pulse propagation," Journal of the Optical Society of America B, vol. 26, no. 9, pp. A6-A13, 2009.

172. R. Mendis and D. Grischkowsky, "Undistorted guided-wave propagation of subpicosecond terahertz pulses," Optics Letters, vol. 26, no. 1, pp. 846-849, 2001.

173. R. Mendis, V. Astley, J. Liu, and D. M. Mittleman, "Terahertz microfluidic sensor based on a parallel-plate waveguide resonant cavity," Applied Physics Letters, vol. 95, no. 17, pp. 171113-4, 2009.

174. V. Astley, K. S. Reichel, J. Jones, R. Mendis, and D. M. Mittleman, "Terahertz multichannel microfluidic sensor based on parallel-plate waveguide resonant cavities," Applied Physics Letters, vol. 100, 231108-4, 2012.

175. H. S. Bark, J. Zha, E. S. Lee, and T. I. Jeon, "Thin layer terahertz sensing using two-channel parallel-plate waveguides," Optics Express, vol. 22, no. 14, pp. 16738-16744, 2014.

176. J. Zhang and D. Grischkowsky, "Waveguide terahertz time-domain spectroscopy of nanometer water layers," Optics Letters, vol. 29, no. 14, pp. 1617-1619, 2004.

177. N. Laman, S. S. Harsha, D. Grischkowsky, and J. S. Melingery, "High-resolution waveguide THz spectroscopy of biological molecules," Biophysical Journal, vol. 94, pp. 1010-1020, 2008.

178. S. Sree Harsha, N. Laman, and D. Grischkowsky, "High-Q terahertz Bragg resonances within a metal parallel plate waveguide," Applied Physics Letters, vol. 94, pp. 091118-4, 2009.

179. E. S. Lee, J. K. So, G. S. Park, D. S. Kim, C. S. Kee, and T. I. Jeon, "Terahertz band gaps induced by metal grooves inside parallel-plate waveguides," Optics Express, vol. 20, no. 6, pp. 6117-6124, 2012.

180. J. S. Melinger, N. Laman, S. S. Harsha, and D. Grischkowsky, "Line narrowing of terahertz vibrational modes for organic thin polycrystalline films within a parallel plate waveguide," Applied Physics Letters, vol. 89, pp. 251110-4, 2006.

181. A. Mazhorova, A. Markov, A. Ng, R. Chinnappan, O. Skorobogata, M. Zourob, and M. Skorobogatiy, "Labelfree bacteria detection using evanescent mode of a suspended core terahertz fiber," Optics Express, vol. 20, pp. 5, pp. 5344-5355, 2012.

182. A. Markov, A. Mazhorova, and M. Skorobogatiy, "Planar porous THz waveguides for low-loss Guidance and sensing applications," IEEE Transactions on Terahertz Science and Technology, vol. 3, no.1, pp. 96-102, 2013.

183. A. Markov and M. Skorobogatiy, "Hybrid plasmonic terahertz fibers for sensing applications," Applied Physics Letters, vol. 103, pp. 181118-3, 2013.

184. A. Markov, M. Skorobogatiy, "Two-wire terahertz fibers with porous dielectric support," Optics Express, vol. 21, no. 10, pp. 12729-12743, 2013.

185. Y. Yu, X. Li, K. He, and B. Sun, "Terahertz multi-metal-wire hybrid-cladding hollow waveguide for refractive index sensing," Chinese Physics B, Vol. 25, no. 2, pp. 028703-028709, 2016.

186. T. Schubert, N. Haase, H. Kuck, R. Gottfried-Gottfried, "Refractive index measurements using an integrated Mach-Zehnder interferometer," Sensors and Acutuators A, vol. 60, pp. 108-112, 1997.

187. Karuse and Z. H. Lu, "Refractive index-temperature measurements on anionically polymerized polystyrene," Journal of Polymer Science, vol.19, pp. 1925-1928, 1981.

188. H. Lin, D. E. Day, K. D. Weaver, and J. O. Stoffer, "Temperature and wavelength dependent transmission of optically transparent glass fiber poly(methyl methacrylate) composites," Journal of Material Science, vol. 29, pp. 5193-5198, 1994.

189. H. Qu, T. Brastaviceanu, F. Bergeron, J. Olesik, I. Pavlov, and M. Skorobogatiy, "Photonic bandgap Bragg fiber sensors for bending/displacement detection," Applied Optics, vol. 52, pp. 6344-6349, 2013.

190. S. K. Mitra, Narsingh Dass, and N. C. Varshneya, "Temperature Dependence of the Refractive Index of Water," The Journal of Chemical Physics, vol. 57, pp. 1798-1799, 1972.

191. J. Grochowski, M. Mysliwiec, P. Mikulic, W. J. Bock, M. Smietana, "Temperature cross-sensitivity for highly refractive index sensitive nanocoated long-period gratings," Acta Physica Polonica A, vol. 124, no. 3, pp. 421-424, 2013.

192. W. Withayachumnankul, and M. Naftaly, "Fundamentals of Measurement in Terahertz Time-Domain Spectroscopy," Journal of Infrared, Millimeter, and Terahertz Waves, vol. 35, pp. 610-637, 2014.

193. S. P. Mickan, J. Xu, J. Munch, X. C. Zhang, and D. Abbott, "The limit of spectral resolution in THz time-domain spectroscopy," in SPIE Microelectronics, MEMS, and Nanotechnology, International Society for Optics and Photonics, pp. 54-64, 2004.

194. A. Ishikawa, S. Zhang, D. A. Genov, G. Bartal, and X. Zhang, "Deep sub-wavelength THz waveguides using gap magnetic plasmon," Physics Review Letters, vol. 102, pp. 043904, 2009.

195. S. Atakaramians, A. Argyros, S. C. Fleming, and B. T. Kuhlmey, "Hollow-core waveguides with uniaxial metamaterial cladding: modal equations and guidance conditions," Journal of the Optical Society of America B, vol. 29, pp. 2462-2477, 2012.

196. Y. Song, H. L. Zhan, K. Zhao, X. Y. Miao, Z. Q. Lu, R. M. Bao, J. Zhu, and L. Z. Xiao, "Simultaneous characterization of water content and distribution in high-water-cut crude oil," Energy Fuels, vol. 30, pp. 3929-3933, 2016.

197. W. Jin, K. Zhao, C. Yang, C. Xu, H. Ni, and S. Chen, "Experimental measurements of water content in crude oil emulsions by terahertz time-domain spectroscopy," Applied Geophysics, vol. 10, no. 4, pp. 506-509, 2013.

198. A. Bajwa, S. T. Tan, R. Mehta, B. Bahreyni, “Rapid detection of viable microorganisms based on a plate count technique using arrayed microelectrodes,” Sensors, vol. 13, no. 7, pp. 8188-8198, 2013.

199. H. J. Lee, G. Shan, T. Watanabe, D. W. Stoutamire, S. J. Gee, and B. D. Hammock, “Enzyme-linked immunosorbent assay for the pyrethroid deltamethrin,” Journal of Agriculture and Food Chemistry, vol. 50, pp. 5526−5532, 2002.

200. F. T. Ishmael, C. Stellato, “Principles and applications of polymerase chain reaction: basic science for the practicing physician,” Ann Allergy Asthma Immunol, vol. 101, no. 4, pp. 60323-60329, 2008.

201. V. Setti, L. Vincetti, and A. Argyros, “Flexible tube lattice fibers for terahertz applications,” Optics Express, vol. 21, no. 3, pp. 3388-3399, 2013.

202. J. Wang, X. Yang, and L. Wang, “Fabrication and experimental observation of monolithic multi-air-core fiber array for image transmission,” Optics. Express, vol. 16, no. 11, pp. 7703. 2008.

203. Y. Han, M. K. Khaing, Y. Zhu, L. Xiao, M. S. Demohan, W. Jin, H. Du, “Index-guiding liquid-core photonic crystal fiber for solution measurement using normal and surface-enhanced Raman scattering,” Optics Engineering, vol. 47, pp. 040502, 2008.

204. Y. Zhang, C. Shi, C. Gu, L. Seballos, J. Zhang, “Liquid core photonic crystal fiber sensor based on surface enhanced Raman scattering,” Applied Physics Letters, vol. 90, pp. 193504, 2007.

205. H. F. Xuan, W. Jin, J. Ju, H.L. Ho, M. Zhang, Y.B. Liao, “Low-contrast photonic bandgap fibers and their potential applications in liquid-base sensors,” Proceeding of SPIE, vol. 6619, pp. 661936-661939, 2007.

206. G. A. Niklasson, C. G. Granqvist, O. Hunderi, “Effective medium models for the optical properties of inhomogeneous materials,” Applied Optics, vol. 20, pp. 26-30, 1981.

207. N. J. Hutchinson, T. Coquil, A. Navid, L. Pilon, “Effective optical properties of highly ordered mesoporous thin films,” Thin Solid Films, vol. 518, pp. 2141-2146, 2010.

208. A. Sihvola, J. A. Kong, “Effective permittivity of dielectric mixtures,” In Proceeding of IEEE on Trans. Geoscience and Remote Sensing, pp. 420-429, 1988.

209. V. Janicki, J. Sancho-Parramon, H. Zorc, “Refractive index profile modeling of dielectric inhomogeneous coatings using effective medium theories,” Thin Solid Films, vol. 10, pp. 3368-3373, 2008.

210. F. J. Gordillo-Vazquez, C. Pecharroman, “A effective-medium approach to the optical properties of heterogeneous materials with nonlinear properties,” Journal of Modern Optics, vol 50, no. 1, pp. 113-135, 2003.

211. Tuck C. Choy, Effective Medium Theory: Principles and Applications, Oxford University Press, 1999.

212. S. Kedenburg, M. Vieweg, T. Gissibl, H. Giessen, “Linear refractive index and absorption measurements of nonlinear optical liquids in the visible and near-infrared spectral region,” Optical Material Express, vol. 2, pp. 1588-1611, 2012.

213. G. A. Niklasson, C. G. Granqvist, O. Hunderi, “Effective medium models for the optical properties of inhomogeneous materials,” Applied Optics, vol. 20, pp. 26-30, 1981.

214. M. Skorobogatiy, J. Yang, Fundamentals of photonic crystal guiding, Cambridge university press, 2009.

215. W. M. Haynes, CRC Handbook of Chemistry and Physics, CRC Press, 2010.

216. L. Rindorf and O. Bang. “Highly sensitive refractometer with a photonic- crystal-fiber long-period grating,” Optics Letters, vol. 33, pp. 563-565, 2008.

217. T. Wieduwilt, J. Dellith, F. Talkenberg, H. Bartelt, M. A. Schmidt. “Reflectivity enhanced refractive index sensor based on a fiber-integrated Fabry-Perot microresonator,” Optics Express, vol. 22, no. 21, pp. 25333-25346, 2014.

218. K. J. Lee, X. Liu, N. Vuillemin, R. Lwin, S. G. Leon-Saval, A. Argyros, B. T. Kuhlmey. "Refractive index sensor based on a polymer fiber directional coupler for low index sensing," Optics Express, vol. 22, no. 14, pp. 17497-17507, 2014.

219. T. K Yadav, R. Narayanaswamy, M. H. Abu Bakar, Y. Mustapha Kamil, M. A. Mahdi. "Single mode tapered fiber-optic interferometer based refractive index sensor and its application to protein sensing," Optics Express, vol. 22, no. 19, pp. 22802-22807, 2014.

220. R. Röttgers, D. McKee, C. Utschig, "Temperature and salinity correction coefficients for light absorption by water in the visible to infrared spectral region," Optics Express, vol. 22, pp. 25093-25108, 2014.

221. W. Scott Pegau, D. Gray, J. Ronald V. Zaneveld, "Absorption and attenuation of visible and near-infrared light in water: dependence on temperature and salinity," Applied Optics, vol. 36, pp. 6035-6046, 1997.

222. J. M. Sullivan, M. S. Twardowski, J. R. V. Zaneveld, C. M. Moore, A. H. Barnard, P. L. Donaghay, B. Rhoades, "Hyperspectral temperature and salt dependencies of absorption by water and heavy water in the 400- 750 nm spectral range," Applied Optics, vol. 45, pp. 5294-5309, 2006.

223. W. P. Huang, "Coupled-mode theory for optical waveguides: an overview," Journal of Optical Society A, vol. 11, pp. 963-983, 1994.

224. S. G. Johnson, M. Ibanescu, M. Skorobogatiy, O. Weisberg, T. D. Engeness, M. Soljacic, S. A. Jacobs, J. D. Joannopoulos, and Y. Fink, "Low-loss asymptotically single-mode propagation in large-core OmniGuide fibers," Optics Express, vol. 9, no. 13, pp. 748-779 2001.

225. G. Gauglitz, "Direct optical sensors: principles and selected applications," Analytical Bioanalytical Chemistry, vol. 381, no. 1, pp. 141-155, 2005.

226. X. D. Wang, O. S. Wolfbeis, "Fiber-optic chemical sensors and biosensors," Analytical Chemistry, vol. 85, no. 2, pp. 487-508, 2013.

227. E. Chow, A. Grot, L. Mirkarimi, M. Sigalas, and G. Girolami, “Ultracompact biochemical sensor built with two-dimensional photonic crystal microcavity,” Optics Letter, vol. 29, no. 10, pp. 1093-1095, 2004.

228. B. Jensen, L. H. Pedersen, P. E. Hoiby, L. B. Nielsen, T. P. Hansen, J. R. Folkenberg, J. Riishede, D. Noordegraaf, K. Nielsen, A. Carlsen, and A. Bjarklev, “Photonic crystal fiber based evanescent-wave sensor for detection of biomolecules in aqueous solutions,” Optics Letters, vol. 29, no. 17, pp. 1974-1976, 2004.

229. T. W. Koo, S. Chan, and A. A. Berlin, ”Single-molecule detection of biomolecules by surface-enhanced coherent anti-stokes Raman scattering,” Optics Letters, vol. 30, no. 9, pp. 1024, 2005.

230. W. B. Ji, S. C. Tjin, B. Lin, C. L. Ng, “Highly sensitive refractive index sensor based on adiabatically tapered microfiber long period gratings,” Sensors, vol. 13, no. 10, pp. 14055, 2013.

231. A. Ladicicco, D. Paladino, S. Campopiano, W. J. Bock, A. Cutolo, and A. Cusano, “Evanescent wave sensor based on permanently bent single mode optical fiber,” Sensors and Actuators B, vol. 155, no. 2, pp. 903-908, 2011.

232. A. Dudus, R. Blue, and D. Uttamchandani, “Comparative study of microfiber and side-polished optical fiber sensors for refractometry in microfluidics,” IEEE Sensors Journal, vol. 13, no. 5, pp. 1594-1601, 2013.

233. M. P. DeLisa, Z. Zhang, M. Shiloach, S. Pilevar, C. C. Davis, J. S. Sirkis, and W. E. Bentley, “Evanescent wave long-period fiber bragg grating as an immobilized antibody biosensor,” Analytical Chemistry, vol. 72, no. 13, pp. 2895-2900, 2000.

234. A. K. Sharma, R. Jha, and B. D. Gupta, “Fiber-optic sensors based on surface plasmon resonance: a comprehensive review,” IEEE Sensors Journal, vol. 7, no. 8, pp. 1118-1129, 2007.

235. T. C. Chang, C. C. Wu, S. C. Wang, L. K. Chau and W. H. Hsieh, "Using a fiber optic particle plasmon resonance biosensor to determine kinetic constants of antigen-antibody binding reaction," Analytical Chemistry, vol. 85, no. 1, pp. 245-250, 2013.

236. J. Polleta, F. Delporta, K. F. Janssena, K. Jansb, G. Maesc, H. Pfeifferd, M. Wsversd, J. Lammertyna, "Fiber optic SPR biosensing of DNA hybridization and DNA-protein interactions," Biosensors and Bioelectronics, vol. 25, no. 4, pp. 864-869, 2009.

237. A. Hassani, and M. Skorobogatiy, "Photonic crystal fiber-based plasmonic sensors for the detection of biolayer thickness," Journal of Optical Society of America B, vol. 26, no. 8, pp. 1550-1557, 2009.

238. J. Y. Lu, C. P. Yu, H. C. Chang, H. W. Chen, Y. T. Li, C. L. Pan, and C. K. Sun, "Terahertz air-core microstructure fiber," Applied Physics Letters, vol. 92, pp. 064105, 2008.

239. A. Argyros, I. M. Bassett, M. A. Van Eijkelenborg, M. C. J. Large, "Analysis of ring-structured Bragg fibres for single TE mode guidance," Optics Express, vol. 12, no. 12, pp. 2688-2698, 2004.

240. J. A. West, C. M. Smith, N. F. Borrelli, D. C. Allan, and K. W. Koch, "Surface modes in air-core photonic band-gap fibers," Optics Express, vol. 12, no. 8, pp. 1485-1496, 2004.

241. A. Dupuis, A. Mazhorova, F. Desevedavy, M. Roze, and M. Skorobogatiy, "Spectral characterization of porous dielectric subwavelength THz fibers fabricated using a microstructured molding technique," Optics Express, vol. 18, no.13, pp. 13813-13828, 2010.

242. T. Ma, H. Guerboukha, M. Girard, A. D. Squires, R. A. Lewis, and M. Skorobogatiy, "3D printed hollow-core terahertz optical waveguides with hyperuniform disordered dielectric reflectors," Advanced Optical Material, vol. 6, pp. 1-10, 2016.

243. T. D. Engeness, M. Ibanescu, S. G. Johnson, O. Weisberg, M. Skorobogatiy, S. Jacobs, and Y. Fink, "Dispersion tailoring and compensation by modal interactions in OmniGuide fibers," Optics Express, vol. 11, no. 10, pp. 1175-1196, 2003.

244. D. Chen, T. J. Yang, J. J. Wu, L. Shen, K. L. Liao, and S. He, "Band-rejection fiber filter and fiber sensor based on a Bragg fiber of transversal resonant structure," Optics Express, vol. 16, no. 21, pp. 16489-16496, 2008.

245. E. Pickwell and V. P. Wallace. "Biomedical applications of terahertz technology." Journal of Physics D: Applied Physics, vol. 39, pp. R301, 2006.

246. F. Ellrich, T. Weinland, D. Molter, J. Jonuscheit, and R. Beigang, "Compact fiber-coupled terahertz spectroscopy system pumped at 800 nm wavelength," Review of Scientific Instrument, vol. 82, pp. 053102, 2011.

247. M. Yahyapour, N. Vieweg, A. Roggenbuck, F. Rettich, O. Cojocari, and A. Deninger, "A flexible phase-insensitive system for broadband CW-terahertz spectroscopy and imaging," IEEE Transactions on Terahertz Science and Technology, vol. 6, no. 5, pp. 670-673, 2016.

248. A. Roggenbuck, K. Thirunavukkuarasu, H. Schmitz, J. Marx, A. Deninger, I. C. Mayorga, R. Güsten, J. Hemberger, M. Grüninger, "Using a fiber stretcher as a fast phase modulator in a continuous wave terahertz spectrometer," Journal of Optical Society of America B, vol. 29, no. 4, pp. 614-620, 2012.

249. R. Mendis, V. Astley, J. Liu, and D. M. Mittleman, "Terahertz microfluidic sensor based on a parallel-plate waveguide resonant cavity," Applied Physics Letters, vol. 95, pp. 171113-171116, 2009.

250. R. Mendis, D. M. Mittleman, "Comparison of the lowest-order transverse-electric ($TE_1$) and transverse-magnetic (TEM) modes of the parallel-plate waveguide for terahertz pulse applications," Optics Express, vol. 17, no. 17, pp. 14839-14850, 2009.

251. A. L. Bingham and D. Grischkowsky, "Terahertz two-dimensional high-Q photonic crystal waveguide cavities," Optics Letters, vol. 33, no. 4, pp. 348-350, 2008.

252. C. M. Yee, M. S. Sherwin, "High-Q terahertz microcavities in silicon photonic crystal slabs," Applied Physics Letters, vol. 94, pp. 154104-154107, 2009.

253. K. S. Lee, T. M. Lu, and X. C. Zhang, “Tera tool,” IEEE Circuits and Devices Magazine, vol. 18, pp. 23-28, 2002.

254. H. B. Liu, G. Plopper, S. Earley, Y. Chen, B. Ferguson, and X. C. Zhang, “Sensing minute changes in biological cell monolayers with THz differential time-domain spectroscopy,” Biosensors and Bioelectronics, vol. 22, pp.1075-1080, 2007.

255. W. Withayachumnankul, J. F. O’Hara, W. Cao, I. A. Naib, and W. Zhang, “Limitation in thin-film sensing with transmission-mode terahertz time-domain spectroscopy,” Optics Express, vol. 22, no.1, pp. 972-986, 2014.

256. B. H. Oconnor and D. Y. Li, "Attaining 1% accuracy in absolute phase composition levels by rietveld analysis," Advances in X-ray Analysis 2000, vol.43, pp. 305-312.

257. R. Singh, W. Cao, I. A. Naib, L. Cong, W. Withayachumnankul, and W. Zhang, “Ultrasensitive terahertz sensing with high-Q Fano resonances in metasurfaces,” Appl. Phys. Lett. 105, 171101 (2014).

258. R. Singh, A. I. Al-Naib, M. Koch, and W. Zhang, "Sharp Fano resonances in THz metamaterials," Opt. Express 19, 6312-6319 (2011).

259. L. Chen, Y. Wei, X. Zang, Y. Zhu, and S. Zhuang, “Excitation of dark multipolar plasmonic resonances at terahertz frequencies,” Scientific Reports 6, 22027 (2016).

260. M. Naftaly, R. E. Miles, “Terahertz time-domain spectroscopy for material characterization,” Proc. IEEE 95, 1658-

261. W. Withayachumnankul, and M. Naftaly, “Fundamentals of measurement in terahertz time-domain spectroscopy,” J. Infrared Milli. Terahertz Waves 35, 610–637 (2014).

262. P. U. Jepsen, D. G. Cooke, and M. Koch, "Terahertz spectroscopy and imaging-modern techniques and applications," Laser Photonics Rev. 5, 124–166 (2011).

263. P. Kužel, H. Němec, F. Kadlec, C. Kadlec, P. Kuzel, H. Nemec, F. Kadlec, and C. Kadlec, "Gouy shift correction for highly accurate refractive index retrieval in time-domain terahertz spectroscopy," Opt. Express 18, 15338-15348 (2010).

264. A. Roggenbuck, H. Schmitz, A. Deninger, "Coherent broadband continuous wave terahertz spectroscopy on solid-state samples," New J. Phys., 12, 043017 (2010).

# APPENDIX A – EFFECTIVE MEDIUM THEORY

In the appendix, we provide derivation of the expression for the effective absorption coefficient of a two-component mixture suspension (cooling oil diluted in water at concentration $c$) using effective medium theory.

The effective absorption coefficient of a suspension is related to the imaginary part of its effective dielectric constant. The dependence of the complex dielectric constant of a suspension on the oil concentration can be described using Bruggeman (BG) model for suspensions featuring small-to-medium concentrations (0-30%) of oil droplets in water. To extract the relation between the imaginary part of the effective dielectric constant and the oil concentration, we write the BG formulation Eq. (4.2) using complex values of the dielectric constants:

$$c\cdot\frac{\varepsilon_o^r+i\cdot\varepsilon_o^i-\left(\varepsilon_{eff}^r+i\cdot\varepsilon_{eff}^i\right)}{\varepsilon_o^r+i\cdot\varepsilon_o^i+\left(\varepsilon_{eff}^r+2i\cdot\varepsilon_{eff}^i\right)}=\left(c-1\right)\cdot\frac{\varepsilon_w^r+i\cdot\varepsilon_w^i-\left(\varepsilon_{eff}^r+i\cdot\varepsilon_{eff}^i\right)}{\varepsilon_w^r+i\cdot\varepsilon_w^i+\left(\varepsilon_{eff}^r+2i\cdot\varepsilon_{eff}^i\right)} \tag{A.1}$$

where $\varepsilon_{eff}$ is the complex effective dielectric constant of the oil suspension in water, $\varepsilon_o$ and $\varepsilon_w$ are the complex dielectric constants of the pure bulk oil and water, respectively. Manuscripts $r$ and $i$ refer to the real and imaginary parts of the dielectric constants.

Assuming that the imaginary part of any dielectric constant is much smaller than the real part of any dielectric constant for the analytes involved in this paper, the imaginary part of the dielectric constant of the effective medium in Eq. (A.1) can be considered as a small correction to its real part. We then expand Eq. (A.1), and only retain the first-order terms, thus obtaining:

$$\varepsilon_{eff}^i=\varepsilon_o^i\cdot\frac{\varepsilon_{eff}^r-3c\cdot\varepsilon_{eff}^r-\varepsilon_w^r}{3c\varepsilon_o^r-\varepsilon_o^r+2\varepsilon_w^r-3c\varepsilon_w^r-4\varepsilon_{eff}^r}+\varepsilon_w^i\cdot\frac{-\varepsilon_o^r+3c\varepsilon_{eff}^r-2\varepsilon_{eff}^r}{3c\varepsilon_o^r-\varepsilon_o^r+2\varepsilon_w^r-3c\varepsilon_w^r-4\varepsilon_{eff}^r} \tag{A.2}$$

Then, using $\varepsilon^i=2n^r\cdot n^i=2n^r\cdot\frac{\lambda\cdot\alpha_{abs}}{4\pi}$ into Eq. (A.2), we get:

$$\alpha_{eff}=\alpha_o\cdot\frac{n_o^r}{n_{eff}^r}\cdot\frac{\varepsilon_{eff}^r-3c\cdot\varepsilon_{eff}^r-\varepsilon_w^r}{3c\varepsilon_o^r-\varepsilon_o^r+2\varepsilon_w^r-3c\varepsilon_w^r-4\varepsilon_{eff}^r}+\alpha_w\cdot\frac{n_w^r}{n_{eff}^r}\cdot\frac{-\varepsilon_o^r+3c\cdot\varepsilon_{eff}^r-2\varepsilon_{eff}^r}{3c\varepsilon_o^r-\varepsilon_o^r+2\varepsilon_w^r-3c\varepsilon_w^r-4\varepsilon_{eff}^r} \tag{A.3}$$

Based on Eq. (A.3), we then write $\alpha_{eff}$ as:

$$\alpha_{eff} = \Phi_o(\mathrm{c}) \cdot \alpha_o + \Phi_w(\mathrm{c}) \cdot \alpha_w$$

$$\Phi_o(\mathrm{c}) = \frac{n_o^r}{n_{eff}^r} \cdot \frac{\varepsilon_{eff}^r - 3c \cdot \varepsilon_{eff}^r - \varepsilon_w^r}{3c\varepsilon_o^r - \varepsilon_o^r + 2\varepsilon_w^r - 3c\varepsilon_w^r - 4\varepsilon_{eff}^r} \tag{A.4}$$

$$\Phi_w(\mathrm{c}) = \frac{n_w^r}{n_{eff}^r} \cdot \frac{-\varepsilon_o^r + 3c \cdot \varepsilon_{eff}^r - 2\varepsilon_{eff}^r}{3c\varepsilon_o^r - \varepsilon_o^r + 2\varepsilon_w^r - 3c\varepsilon_w^r - 4\varepsilon_{eff}^r}$$

# APPENDIX B – THZ OPTICAL PROPERTIES OF THE RESIN USED IN 3D STEREOLITHOGRAPHY

The refractive index and absorption losses of the reflector material used in the Bragg waveguide fabrication are characterized using a THZ-TDS setup. Cutback measurements are performed using three printed resin slices of 6mm thickness. In the experiment, the printed resin slices are fixed on a holder [see Fig. B.1(a)], which is placed between the two parabolic mirrors. The resins slices have the same thickness with flatness on the sub-50μm scale. During the cutback measurements, the slices are placed tightly close to each other so as to minimize the air gap between them (due to surface roughness), which in any case remains deeply sub-wavelength. Also, we note that on the top of each slice a small notch is present in order to simplify the removal of the slides during measurements. The outmost left resin slice is fixed in the focal point of the parabolic mirror (PM1), while the outmost right resin slice is fixed at the focal point of the parabolic mirror (PM2). To ensure constant coupling conditions during measurements, resin slices are removed one by one from the right. Thus, transmission spectra through resin samples with different thicknesses (18mm, 12mm, 6mm) are measured.

We note that PM2 is fixed in this measurement. In each measurement, 20 traces are recorded and averaged in order to enhance the signal-to-noise ratio. The real part of the resin refractive index and the absorption coefficient are extracted from the measured complex transmission data. Following [242, 261-263], the measured complex transmission is given by:

$$\begin{aligned} T(\omega,\mathrm{L}) &= \frac{E_t}{E_r} = \left|T(\omega,\mathrm{L})\right| \cdot \exp[\mathrm{i}\,\varphi(\omega,\mathrm{L})] \\ \left|T(\omega,\mathrm{L})\right| &= C_{in} \cdot C_{out} \cdot \exp[-\frac{\alpha(\omega)\cdot \mathrm{L}}{2}] \\ \varphi(\omega,\mathrm{L}) &= -\frac{\omega}{c}(\mathrm{n}_r(\omega)-1)\cdot \mathrm{L} \end{aligned} \quad . \tag{B. 1}$$

where $E_t$ and $E_r$ are the complex transmission spectra measured with a sample of length $L$ and a reference (all samples removed). $C_{in}$ and $C_{out}$ represent the input and output coupling coefficients of the THz light, which are assumed to be same during all the measurements. $n(\omega)$, and $\alpha(\omega)$ are the real part of the reflective index, and the absorption coefficient of the samples.

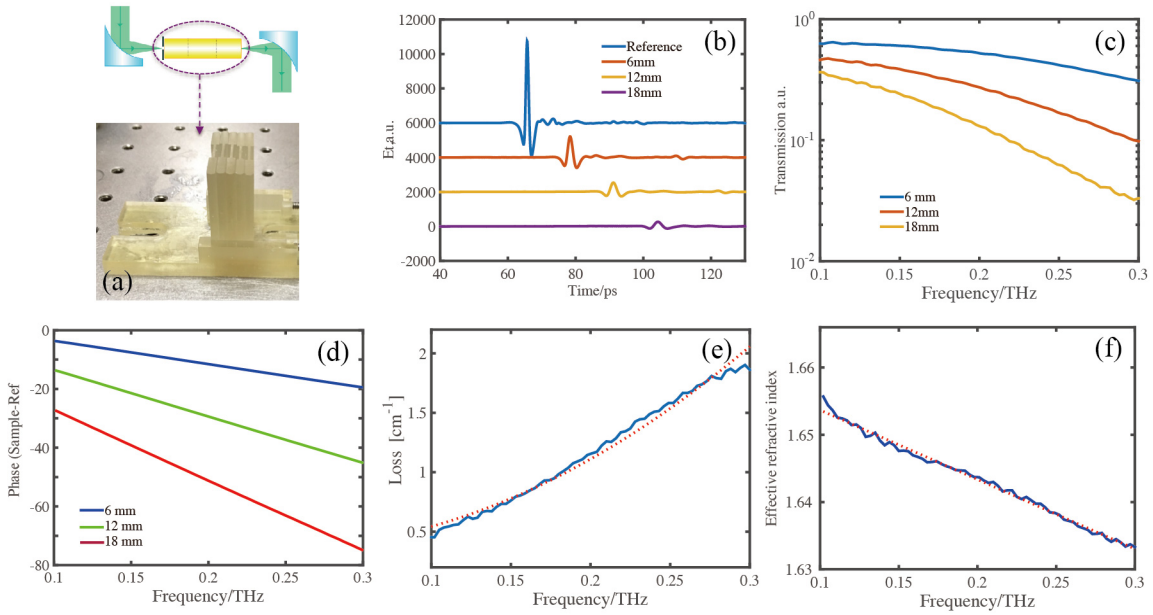


Figure B.1 Optical characterizations of the photosensitive resin using cutback method. (a) 3D printed resin samples of various lengths mounted in the holder. (b) Temporal traces of the THz pulses at the output of the resin slices (plotted with a vertical offset for clarity), (c) transmission spectra, (d) unwrapped phases (relative to the reference), (e) resin absorption loss and the polynomial fit (p=2), (f) resin refractive index and the polynomial fit (p=1).

We note that, the THz spectroscopic measurements are performed in focused beam geometry, while the standard routine for the retrieval of the sample refractive index assumes plane-wave approximation, we therefore, use the model proposed in [263], in order to correct the Gouy shift for a more accurate determination of the refractive index of the resin. In Fig. B.1(b), we show the temporal traces of the THz pulses guided through the resin slices with different thicknesses (traces are plot with a vertical offset for clarity). For each slice with a different length, the temporal delay compared to the reference pulse is proportional to the slice thickness. In Figs. B.1(c) and B.1(d), we plot the transmission spectra and the unwrapped phases relative to the reference of the tested samples of different thicknesses. Our analysis is limited to the frequency range of 0.1-0.3THz, where all the spectra are well above the noise level. In this frequency range, the absorption coefficient and the refractive index can then be fitted using second order and first order polynomials as:

$$\alpha(\omega)[\mathrm{cm}^{-1}] = 0.64 + 13.44 \cdot (\omega[\mathrm{THz}])^2 \,, \qquad \text{(B. 2)}$$

$$n(\omega) = 1.654 - 0.07\omega[THz] \ . \qquad \text{(B. 3)}$$

# APPENDIX C – LIST OF PUBLICATIONS

The work presented in this thesis has been published in the following peer-reviewed journals:

**Peer-reviewed journals:**

1. **Jingwen Li**, Hang Qu, and Maksim Skorobogatiy, “Simultaneous monitoring the real and imaginary parts of the analyte refractive index using liquid-core photonic bandgap Bragg fibers”, Optics Express, vol. 23, no. 18, pp. 22963, 2015.
2. **Jingwen Li**, Hang Qu, Maksim Skorobogatiy, “Squeezed Squeezed hollow-core photonic Bragg fiber for surface sensing applications,” Optics Express, vol. 24, no. 14, pp. 15687-15691, 2016.
3. **Jingwen Li**, Katirvel Nallappan, Hichem Guerboukha, and Maksim Skorobogatiy, “3D printed hollow core terahertz Bragg waveguides with defect layers for surface sensing applications,” Optics Express, vol. 25, no. 4, pp. 4126-4144, 2017.

The results were also reported in the following scientific conference proceedings:

**Conference proceedings:**

1. **Jingwen Li**, Hang Qu, and Maksim Skorobogatiy, “Detection of analyte refractive index and concentration using liquid-core photonic Bragg fibers,” 9702-27,Oral Presentation. SPIE Photonic West, Feb, California, 2016.
2. **Jingwen Li**, Maksim Skorobogatiy, "Hollow-core photonic Bragg fiber for bulk and surface sensing applications," (BIOS, 34, 30), Oral Presentation, SPIE Photonics North, May, Quebec city, Quebec, Canada, 2016.
3. **Jingwen Li**, Maksim Skorobogatiy, "Hollow-core photonic Bragg fiber for bulk and surface sensing applications," Oral Presentation, Canadian Association of Physicists Congress, June, Ottwa, Canada, 2016

4. **Jingwen Li**, Hang Qu, Maksim Skorobogatiy, "Squeezed Squeezed hollow-core photonic Bragg fiber for surface sensing applications," Fiber Photonics, CLEO, May, San Jose, 2017, 2687810, under review.
5. **Jingwen Li**, Katirvel Nallapan, Hichem Guerboukha, and Maksim Skorobogatiy, "3D printed hollow core terahertz Bragg waveguides with defect layers for surface sensing applications," Terahertz Science and Technology, CLEO, May, San Jose, 2017, 2687828, under review.
6. **Jingwen Li**, Hang Qu, Maksim Skorobogatiy, "Squeezed Squeezed hollow-core photonic Bragg fiber for surface sensing applications," SPIE Photonics North, June, Ottawa, Canada 2017, 255-LPqi-412, under review.
7. **Jingwen Li**, Katirvel Nallapan, Hichem Guerboukha, and Maksim Skorobogatiy, "3D printed hollow core terahertz Bragg waveguides with defect layers for surface sensing applications," SPIE Photonics North, June, Ottawa, Canada 2017, 255-GXHU-412, under review.

Other publications (not included in the thesis):

**Book chapters:**

1. Hang Qu, **Jingwen Li**, Maksim Skorobogatiy, "Photonic bandgap fibers: a roadway to all-fiber refractometer systems for monitoring of liquid analytes" in Optofluidics, sensors and actuators in microstructured optical fibres, Woodhead Publishing, 2015.